



Degradation of Solar Cells Comprising both Organic and Inorganic Materials

Andreasen, Birgitta

Publication date:
2015

Document Version
Publisher's PDF, also known as Version of record

[Link back to DTU Orbit](#)

Citation (APA):
Andreasen, B. (2015). *Degradation of Solar Cells Comprising both Organic and Inorganic Materials*. Technical University of Denmark.

General rights

Copyright and moral rights for the publications made accessible in the public portal are retained by the authors and/or other copyright owners and it is a condition of accessing publications that users recognise and abide by the legal requirements associated with these rights.

- Users may download and print one copy of any publication from the public portal for the purpose of private study or research.
- You may not further distribute the material or use it for any profit-making activity or commercial gain
- You may freely distribute the URL identifying the publication in the public portal

If you believe that this document breaches copyright please contact us providing details, and we will remove access to the work immediately and investigate your claim.

Degradation of Solar Cells Comprising both Organic and Inorganic Materials

PhD Thesis

Birgitta Andreassen



January 2015

PhD thesis title:

Degradation of Solar Cells Comprising both Organic and Inorganic Materials

Author:

Birgitta Andreasen

Supervisors:

Senior scientist Kion Norrman

Technical University of Denmark

Department of Energy Conversion and Storage

Imaging and Structural Analysis

Prof. Frederik C. Krebs

Technical University of Denmark

Department of Energy Conversion and Storage

Solar Energy

Assessment committee:

Eugene A. Katz, Ben-Gurion University of the Negev, Israel

Nils-Krister Persson, University of Borås, Sweden

Louise Theil Kuhn, Technical University of Denmark, Denmark

Date of defence:

13 April 2015

Funding:

Danish National Research Foundation and the National Natural Science Foundation of China (grant no. 51011130028)

Address:

Technical University of Denmark

Department of Energy Conversion and Storage

Frederiksborgvej 399

DK-4000 Roskilde, Denmark

Phone + 45 4677 5800

Info@enerdy.dtu.dk

www.energy.dtu.dk

ISBN:

Preface

This PhD thesis represents the main result of the work I carried out as a PhD student in the Solar Energy Section at the Department of Energy Conversion and Storage at the Technical University of Denmark. The PhD study commenced in October 2010 and finishes in January 2015, which includes a year maternity leave. The PhD was conducted as part of the Danish-Chinese Centre for Organic-based Photovoltaic Cells with Morphology Control which consists of four partners, two Danish (Technical University of Denmark and Aalborg University) and two Chinese (Zhejiang University and Institute of Chemistry, Chinese Academy of Science). The centre is financed by the Danish National Research Foundation and the National Natural Science Foundation of China (Grant no. 51011130028) under the supervision of Kion Norrman and Prof. Frederik C. Krebs

Six months of the PhD were carried out in China, 3 months at Zhejiang University, Hangzhou (Apr-Jul 2012) under the supervision of Prof. Hongzheng Chen and 3 months at Suzhou Institute of Nano-Tech and Nano-Bionic, Suzhou (Sep-Dec 2012) under the supervision of Prof. Liwei Chen. I also participated in different summer schools and conferences (where I both presented posters and gave talks) in Europe and China.

The thesis is based on a number of papers that I have authored/co-authored in the duration of the PhD along with some unpublished work. The work has allowed me to really get in to the depths of some of the larger studies and to help others with smaller characterisation studies, of which I have found both enjoyable.

First of all I would like to thank my supervisor Kion Norrman, he has taught me everything I know about TOF-SIMS both the good and the bad. For keeping his cool when I was on my first solo venture with the TOF-SIMS when suddenly smoke starting seeping out of the electronics! Also, thank you to Frederik C. Krebs for always having time to answer my silly questions. Thank you to everyone in the Solar Energy group, these past years have been a blast, it is all of you that make it a great place to work. And thank you all for trying to keep my mood up when I was throwing up for six months of my pregnancy!

To my family at home in Faroe Islands, and my friends all around, thank you.

Finally, to my little family Pætur and Mia, thank you for all your love and support. Especially during the final month before thesis submission, thank you for not going crazy!

Abstract

The organic photovoltaic (OPV) research field has made a remarkable advance in the past decades, evident by an impressive amount of work being published. Even though OPV research has come a long way since its beginning there is however still some way to go before commercialisation becomes a possibility. There are three main challenges in OPV research, efficiency, processability, and stability. These challenges have to be addressed both individually and, more importantly, in unification before commercialisation of OPVs can be realised.

This thesis primarily focuses on the challenge area of stability, more specifically the characterization of chemical degradation of both OPV devices and OPV materials. The secondary focus was on characterization in general of OPV devices and OPV materials. The characterization was conducted using time-of-flight secondary ion microscopy (TOF-SIMS) and atomic force microscopy (AFM).

A large inter-laboratory study, involving six distinct sets of OPV devices, was conducted. The devices were degraded under identical conditions. The devices were thereafter analysed at different laboratories using different analysis techniques, herein the results from TOF-SIMS analysis are reported and discussed.

Degradation analysis of an active layer polymer and polymer blend was also conducted. The samples were degraded as a function of exposed light dose and afterwards analysed by TOF-SIMS and x-ray photoelectron spectroscopy (XPS). Some of the results were analysed using multivariate analysis to get further insight into the chemistry of the active layer degradation.

The last part of the thesis are smaller TOF-SIMS and AFM studies, characterization studies of both OPV devices and OPV materials conducted in the duration of the PhD.

Resumé

Forskning inden for organiske solceller (OSC) har is de seneste årtier haft en imponerende fremgang som tydeligt ses af en imponerende mængde studier der er blevet udgivet. Selvom OSC forskning er kommet langt siden dens begyndelse, er der dog stadig et stykke vej før en mulig kommercialisering. Der er tre udfordringer i OSC feltet, effektivitet, bearbejdelighed, og stabilitet. Disse udfordringer skal både behandles individuelt og, endnu vigtigere, i forening før en kommercialisering af OSC kan realiseres.

Denne afhandling fokuserer primært på stabilitet udfordringen, mere specifikt karakterisering af kemisk nedbrydning af både OSC enheder og OSC materialer. Det sekundære fokus har været på karakterisering generelt af OSC enheder og OSC materialer. Karakteriseringen blev gennemført af time-of-flight sekundær ion mikroskopi (TOF-SIMS) og atomic force mikroskopi (AFM).

En stor inter-laboratorium undersøgelse, med seks forskellige sæt af OSC enheder, blev udført. Enhederne blev nedbrudt under identiske forhold hvorefter de blev analyseret på forskellige laboratorier af forskellige analyseteknikker. Denne afhandling indeholder nedbrydnings resultaterne fra TOF-SIMS analysen.

Nedbrydnings analyse af det aktive OSC lag bestående af polymer og polymerblanding blev også udført. Prøverne blev nedbrudt som en funktion af eksponeret lysdosis og bagefter analyseret ved TOF-SIMS og røntgen fotoelektron spektroskopi (XPS). Nogle af resultaterne blev analyseret ved anvendelse af multivariat analyse for at få yderligere indblik i kemien af nedbrydningen af det aktive lag.

I den sidste del af afhandlingen er mindre TOF-SIMS og AFM undersøgelser opsamlet, bestående af analyse studier af både OSC enheder og OSC, gennemført i ph.d. perioden.

Contents

<i>Preface</i>	<i>i</i>
<i>Abstract</i>	<i>iii</i>
<i>Resumé</i>	<i>v</i>
<i>Contents</i>	<i>vii</i>
Chapter 1	1
<i>Introduction</i>	1
1.1 Introduction	2
1.2 Basic principles	3
1.3 Organic photovoltaics (OPVs)	3
1.3.1 Device architecture	3
1.3.2 Working principles of OPVs	5
1.3.3 Solar cell performance	6
1.3.4 Status and challenges	8
1.4 Stability and degradation	8
1.5 Chemical and physical characterization of OPV devices and materials	10
1.6 Time-of-flight secondary ion mass spectrometry (TOF-SIMS)	11
1.6.1 Basic principles	11
1.6.2 Operational modes	11
1.6.3 The use of TOF-SIMS in OPV research	12
1.7 Multivariate Analysis (MVA)	13
1.7.4 Principal Component Analysis (PCA)	13
1.7.5 Multivariate Curve Resolution (MCR)	13
1.8 Atomic Force Microscopy (AFM)	13
1.8.1 Contact and tapping mode	13
1.9 Aim and overview of this thesis	14
1.10 List of publications and contributions	14
Chapter 2	17
<i>TOF-SIMS investigation of degradation pathways occurring in a variety of organic photovoltaic devices</i>	17
2.1 Introduction	18
2.2 Experimental	20
2.2.1 TOF-SIMS analysis	22
2.2.2 XPS analysis	24
2.3 Results and discussion	24
2.3.1 Quantification of TOF-SIMS depth profiling data	24
2.3.2 Oxygen incorporation and its effect on device degradation	29

2.3.3 Full sun, fluorescent, and dark degradation conditions.	31
2.3.4 Correlating LBIC and TOF-SIMS data	38
2.3.5 Correlating loss of performance with various TOF-SIMS information	40
2.4 Conclusions	48
2.5 Acknowledgements	50
Chapter 3	51
<i>Fast and efficient acquisition of organic material degradation data using concentrated light</i>	51
3.1 Introduction	52
3.2 Experimental	53
3.2.1 Sample preparation	53
3.2.2 Accelerated degradation – concentrated light	53
3.2.3 Analytical Techniques	54
3.3 Results and Discussion	56
3.3.1 AFM profilometry	56
3.3.2 Macro imaging	57
3.3.3 Surface images/spectra:	64
3.3.4 Depth profiles	68
3.4 Conclusions	70
Chapter 4	73
<i>Examples of Characterization and analysis of OPV devices and OPV materials</i>	73
4.1 Introduction	74
4.2 Characterising nanoparticles utilised in OPVs	74
4.2.1 Abstract:	74
4.2.2 AFM results and discussion	74
4.2.3 Conclusion	77
4.3 Polymer cross-linking and its effect observed in the active layer	77
4.3.4 Abstract:	77
4.3.5 Optical microscopy and AFM	77
4.3.6 Conclusions	79
4.4 Characterization of a double slot-die coated layer by TOF-SIMS depth profiling	79
4.4.7 Abstract	79
4.4.8 TOF-SIMS Experimental	80
4.4.9 Result and discussion of the bilayer TOF-SIMS characterization	80
4.4.10 Conclusion	81
4.5 TOF-SIMS depth profiling of polymer tandem solar cells prepared by R2R	81
4.5.11 Abstract	81
4.5.12 TOF-SIMS experimental	82
4.5.13 TOF-SIMS depth profiling results and discussion:	83
4.5.14 Conclusion:	83
4.6 Overall conclusion:	84
Chapter 5	85

<i>Conclusion and outlook</i>	85
Bibliography	87
Appendix A	93
<i>Supporting information to Chapter 3</i>	93
Appendix B	99
<i>The thesis is based on the following publications</i>	99

Chapter 1

Introduction

1.1 Introduction

Energy consumption is a significant part of everyone's lives in today's world, one might not think of it as such or it might not be as apparent to people. Electricity, lighting, transportation, clothing etc. in fact almost everything around you has consumed energy in some form at some point in order to have taken the shape it has and to be just there, right next to you.

The world energy consumption has increased over the last decades and predictions reported in the International Energy Outlook 2013 by The U.S. Energy Information Administration state that the world energy consumption will grow by 56% between 2010 and 2040 reaching a staggering 27.4TW by 2040.^a This and environmental factors have led to an increased interest in renewable energy and green energy, both in research, the private sector, and the public sector with policies written for a greener future.

There are many types of renewable energy sources such as wind, hydro, geothermal, sun etc. these energy sources can be harvested and converted in different ways into consumable energy. Out of the renewable energy sources it is hard to argue with the fact that the sun is by far the largest energy source we have. 96000 TW of solar energy hits the earth in a year, of this a feasible solar energy supply is 67 TW based on solar cells covering 2% of land area and an average power conversion efficiency (PCE) of 12%.¹ In theory this means that solar cells could substitute the global primary energy demand. However, the favourable and perhaps more realistic approach would be a mix of renewable energy sources because of the intermittent nature and lack of adequate energy storage of solar energy.¹

Today, there are different types of solar cell technologies, as the research and development has changed through the years going through so called generations of photovoltaic (PV) technologies.

1st generation (1G) solar cells are single junction devices, which are mainly based on crystalline silicon based, and consist of today's majority installed PV and most wide spread. Commercial modules typically have an efficiency of about 20%. Even though the 1G solar cells have a high efficiency there are some significant drawbacks that have to be considered, such as the cost of every energy unit produced is still higher than the same energy unit produced using fossil fuels. This high cost is among others due to the expensive material use (silicon wafers) and high production cost (high temperature, slow production). The cost per produced energy unit of 1G solar cells is decreasing, however, it will be difficult to compete with the already established fossil fuels energy market.

2nd generation (2G) solar cells are trying to address some of these issues by using cheaper materials (e.g. amorphous silicon and CuIn(Ga)Se₂ (CIGS)), and by producing thin film solar cells the production cost is further reduced. Although 2G solar cells have an efficiency of up to 16%, the cost per produced energy unit is still higher than the same energy unit produced by conventional fossil fuel energy sources.²

3rd generation (3G) solar cells address the cost and processability issues by making use of cheap unconventional materials such as plastic - or polymer solar cells, however, at the same time 3G which can be broadly divided into dye-sensitized and organic solar cells

^a [http://www.eia.gov/forecasts/ieo/pdf/0484\(2013\).pdf](http://www.eia.gov/forecasts/ieo/pdf/0484(2013).pdf) (20-Jan-2015)

(organic solar cells can be further divided into small molecule -, polymer -, and hybrid - solar cells) also covers expensive experimental and high efficient multi-junction solar cells. This thesis will focus on the 3G organic solar cells, in particular those based on polymers. The active material in polymer solar cells is based on soluble conjugate polymers that offer many advantages, such as simple solution processing, fast and cheap large scale production, which can be achieved by printing the solar cells using already existing roll-to-roll (R2R) technologies and temperature $<140\text{ }^{\circ}\text{C}$. Even though the efficiency and stability of polymer solar cells still is inferior when compared to the inorganic 1G and 2G solar cells at 10.7% for record lab scale devices and 2% for large scale modules, they house great potential.³ This potential is evident by the increased research interests and the high expectations that organic solar cell technology will be a competitive, sustainable, and environmentally friendly energy source of the future.

1.2 Basic principles

The basic principle behind both the organic and the other types of solar cells is the same, namely the conversion of electromagnetic radiation (sunlight) into electric energy, a phenomenon called the photovoltaic (PV) effect. The PV effect is made possible by the special properties that so-called semiconductors hold. Semiconductors are defined by their unique electric conductive behaviour which lies between that of a conductor and an insulator.

The device architecture of an organic solar cell or organic photovoltaic (OPV) can in the simplest form be described as a 3 layered sandwich sitting on a substrate in which a photoactive layer or simply active layer (where the light is absorbed) sits between two electrodes (where the charges are collected), see Figure 1.1. This layered structure can then be optimized by introducing more layers, so-called buffer layers with positive effects on the OPV performance.

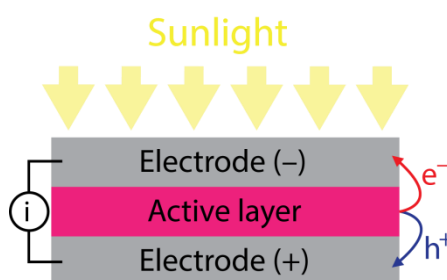


Figure 1.1 The simplest device architecture of an OPV.

1.3 Organic photovoltaics (OPVs)

1.3.1 Device architecture

Two main device geometries exist: the normal (or traditional) and the inverted. The normal geometry layers are usually built on top of a semi-transparent indium tin oxide (ITO) electrode followed by a hole transport layer (HTL) poly(3,4-

ethylenedioxythiophene):poly(styrene sulfonate) (PEDOT:PSS), the active layer, an electron transport layer (ETL) (e.g., LiF) and finally a low work function metal electrode (the cathode), see Figure 1.2a. In the inverted type geometry the order of the layers is reversed with the top metal electrode now being the hole collecting anode, see Figure 1.2b. The different order of the layers in the two geometries creates interfaces with different chemistries which may affect the stability. It is also very important that different types of metal electrodes can be used in the two cases. Low work function metals such as aluminium and/or calcium are typically used as back electrodes in the normal geometry while higher work function metals such as silver are used in the inverted geometry. As a consequence the inverted geometry devices tend to be much more stable, while the normal geometry devices may still have an edge in PCE.⁴

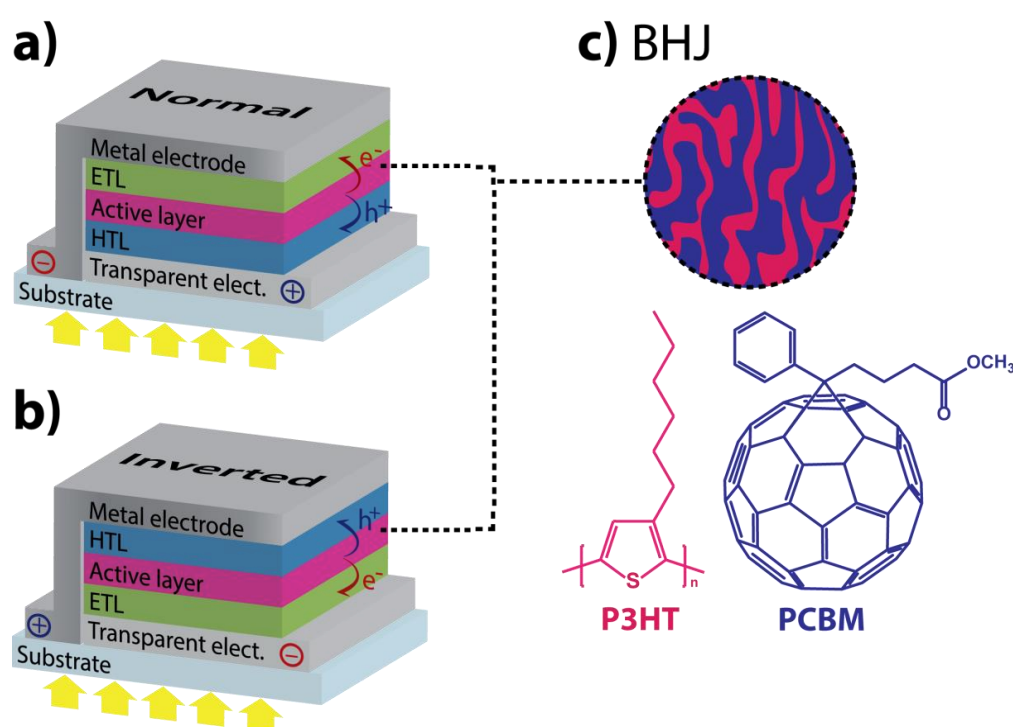


Figure 1.2 The normal and inverted device geometries are depicted in (a) and (b) respectively, with light entering from the bottom. (c) depicts the BHJ of the donor and acceptor materials of the active layer which in this case is P3HT and PCBM respectively.

Today, almost all organic photovoltaic (OPV) active layers are based on the concept of a so-called bulk-heterojunction (BHJ), see Figure 1.2c, whereby an electron donor and electron acceptor component are intimately mixed and processed simultaneously into the active layer. There are many different types of donor and acceptor materials used e.g. small molecule, conjugated polymers, and fullerenes. The most common and most studied BHJ is the polymer:fullerene more specifically poly(3-hexylthiophene):phenyl-C61-butyric acid methyl ester (P3HT:PCBM).

1.3.2 Working principles of OPVs

The principles behind the working mechanisms of an OPV device, in which light is converted into electric energy, are as follows (Figure 1.3):

- Light absorption in the active layer
- Exciton diffusion towards the interface
- Exciton dissociation and charge separation
- Charge transport towards the electrodes

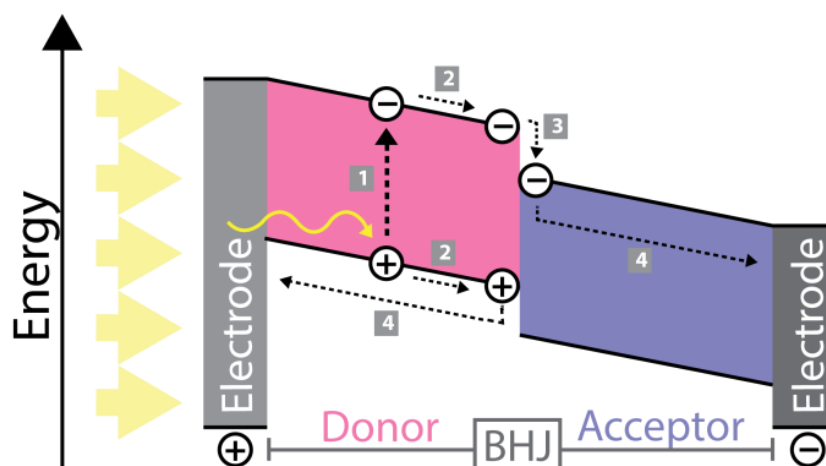


Figure 1.3 Diagram of the working principles of a BHJ solar cell: (1) absorption of light and exciton generation, (2) exciton diffusion towards the donor-acceptor interface, (3) exciton dissociation and separation, and (4) charge transport towards the electrodes.

Light absorption

Light passes through the transparent electrodes and can be absorbed in the active layer. The band gap between the HOMO and LUMO levels of the absorbing material determines the minimum wavelength of the absorbed light. Therefore, a good overlap between the spectrum of the absorbing material (the donor or the acceptor material) and the solar emission spectrum is necessary to achieve optimal absorption. When a photon is absorbed in the active layer an electron (e^-) is excited from the HOMO to the LUMO level leaving a hole (h^+) in its place in the HOMO level. This Coulombically bound electron-hole pair is called an exciton.

Exciton diffusion

Because excitons in organic material are characterized by a relative high binding energy, exciton dissociation and thus the formation of charge carriers does not occur spontaneously in the pure materials, but rather takes place at the interface between the donor and acceptor materials. Hence, the excitons created by the absorption of photons have to diffuse towards the donor-acceptor interface to contribute to the electrical power of the cell. If the exciton diffusion does not occur, the electron-hole pair will recombine and the photon energy is lost. Due to the excitons short lifetime and low diffusion constant the resulting diffusion length is typically 4-20 nm. Hence, excitons created further away than their diffusion length from a donor-acceptor interface are lost to recombination. Therefore there is a demand for an

intimate, nanoscale mixing of the donor and acceptor materials and hence the morphology of the before mentioned BHJ plays a central role in the active layer performance.⁵

Exciton dissociation

When the exciton has reached the donor-acceptor interface the generation of free electron and hole charge carriers can occur as long as it is energetically favourable. A prerequisite for an energetic driving force for exciton dissociation is given by the LUMO-LUMO and HOMO-HOMO energy level difference of the donor and acceptor materials. A minimum energy difference of 0.3 – 0.4 eV is generally considered sufficient for charge formation, e.g. when energetically favourable the electron of the exciton is transferred from the LUMO of the donor to the LUMO of the acceptor material and thus generating a free electron and a free hole.

Charge transport

After exciton dissociation the free electron and hole are transported towards the electrodes to contribute to the device photocurrent. The charge transport is driven by two phenomena: firstly, charge-carrier gradient through the device created as soon as excitons are generated, and secondly, the internal electric field which is the energy gradient due to the difference in work functions of the two electrodes. After charge separation the main loss in the OPV device is by bimolecular recombination. To prevent charge recombination electrons and holes have to be extracted at the electrode at sufficiently high rates. Which means that a high charge mobility and also a phase-separated morphology that provides uninterrupted pathways to the electrodes are needed in order to reduce the probability of recombination.

So these internal gradients coupled with the presence of free electrons and holes are the underlying reasons for the production of current in OPV devices.

1.3.3 Solar cell performance

The performance of OPVs is evaluated by electrical characterization. The measurement is conducted as a voltage sweep across the OPV while the current is measured, JV curve measurements. This means that all the components of an OPV, layers, interfaces etc. are probed to provide an overall device performance.

The JV curve can be measured in the dark (dark curve) when the device acts as a simple diode, see Figure 1.4. JV curve measured during illumination (light curve) are approximately parallel shifted with respect to the dark curve due to the current generation in the OPV. However, as the light curve in Figure 1.4 shows, this parallel-shift is not at all perfect and is this due to different types of losses within the device which are modelled as the series resistance (r_s) e.g. contacting to the electrodes, introduction of barrier layers etc. and shunt the resistances (r_{sh}) e.g. leakage of current through shunts due to defects in the layers. The current density at zero applied bias is referred to as the short circuit current density (J_{sc}). The J_{sc} critically depends on the charge separation and transport towards the electrodes in the active layer.⁵ The maximum voltage generated in the device, corresponding to the voltage for which the photocurrent is zero, is referred to as the open circuit voltage (V_{oc}). The V_{oc} depends on the difference between the electrode work functions and the difference between the HOMO and LUMO levels of the donor and acceptor materials, respectively.

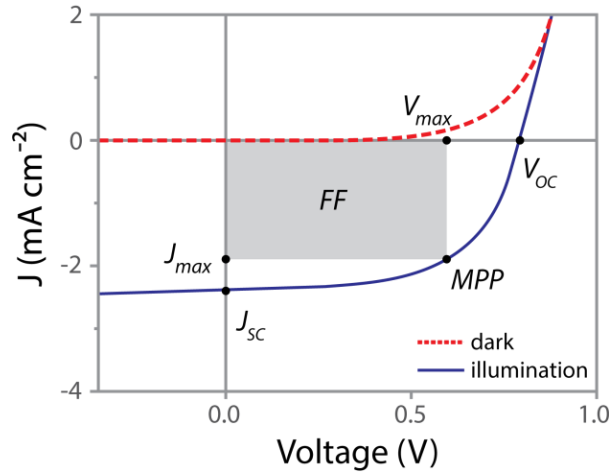


Figure 1.4 Schematic plot of the JV characterization curves of an OPV measured during illumination and in the dark, key cell parameters are indicated in the plot.

The power of an OPV under operation is described by equation (5).

$$P = J \times V \quad (1)$$

where the P , J and V are power, current and voltage respectively.

The OPV thus has a maximum power output at some point on the JV curve, this point is referred to as the maximum power point (MPP) and is defined by equation (2).

$$MPP = J_{max} \times V_{max} \quad (2)$$

where the J_{max} and the V_{max} are the current and voltage respectively at the MPP .

The fill factor (FF) is used to quantify the ratio between the MPP power output and the maximum theoretical power output and can be expressed in equation 3.

$$FF = \frac{MPP}{J_{sc} \times V_{oc}} = \frac{J_{max} \times V_{max}}{J_{sc} \times V_{oc}} \quad (3)$$

The FF thus describes the losses relative to an ideal diode and is affected by the before mentioned r_s and r_{sh} .

The power conversion efficiency (PCE or η) relates the power output (P_{out}) to the power input (P_{in} - the incident light power) and can be described by equation 4.

$$\eta = \frac{P_{out}}{P_{in}} = \frac{J_{max} \times V_{max}}{P_{in}} = \frac{J_{sc} \times V_{oc} \times FF}{P_{in}} \quad (4)$$

1.3.4 Status and challenges

There has been an increased research interest in the general OPV field, covering a large number of focus areas such as efficiency, processing techniques, new materials and material optimization, device configuration, and lifetime and stability. Impressive progress has been made in many of the focus areas.⁶

Although OPVs can offer many advantages as already mentioned, with cheaper materials, faster processing and so on there are some severe drawbacks in the existing OPV technology that inhibits the commercialisation of the technology. For OPVs to reach commercialisation there are three factors that need to be unified, efficiency, stability and processing, together this is called the unification challenge.⁷ This means that that an OPV needs to combine a high performance in all three areas to be a viable alternative to already existing energy conversion technologies. The focus should therefore be on the development of OPV devices that fulfil all three criteria.

Efficiency

The PCE for OPV is generally significantly lower than that of inorganic PVs.^{2,3} That is one of the reasons for why PCE optimization still receives the largest research interest in the field of OPV, the current record is 10.7% small scale laboratory devices and around 3.5% for large-scale R2R devices. The PCE optimization of small scale laboratory devices has no direct practical applicability when transferred to large-scale processing; the PCE optimization is often lost and has to be started again.

Processing

The transfer from small scale laboratory devices to large scale processed devices is necessary in order obtain a lower unit cost and for the commercialisation realization of OPVs. The progress in processing of OPV has been rapid in the last years with the use of already existing R2R printing technologies which allows fast large area production with minimum manual handling. However, as this is still a relatively new field there is still a lot of research and development needed to fully realize satisfactory properties of the printed OPVs.

Stability

The area of stability and lifetime has perhaps received the least research interest; however, this is changing now with more and more research papers addressing polymer and OPV device stabilities. Also here, there has been impressive progress made with device lifetime optimization where the lifetime has increased from minutes to a few years in outdoor conditions.^{4,8}

The focus of the thesis has been to characterize the stability and lifetime and thus the degradation of OPVs, therefore this area has been introduced in more detail below.

1.4 Stability and degradation

Ideally a solar cell technology should have a constant performance over time when subjected to illumination and should also show little dependence on inevitable operational

environmental changes such as temperature, humidity and light intensity. This is however not the case. Out of the before mentioned generations of PV technology, it is the OPVs that present the greatest and most complex collection of degradation phenomena, one of the reasons is simply that the architecture has become more elaborate with a large choice of layer components and in turn the pathway for failure has significantly increased.

Lifetime and stability are determined by the magnitude and multitude of degradation mechanisms that occur throughout the whole device not only under operation but also during storage. A detailed understanding of the degradation mechanisms is of utmost importance if acceptable lifetimes are to be achieved, which is a prerequisite for large-scale application and thus commercialization. OPV degradation is highly complex and constitutes an analytical challenge due to the multitude of materials, interfaces, and device architectures that are constantly being modified and optimized.

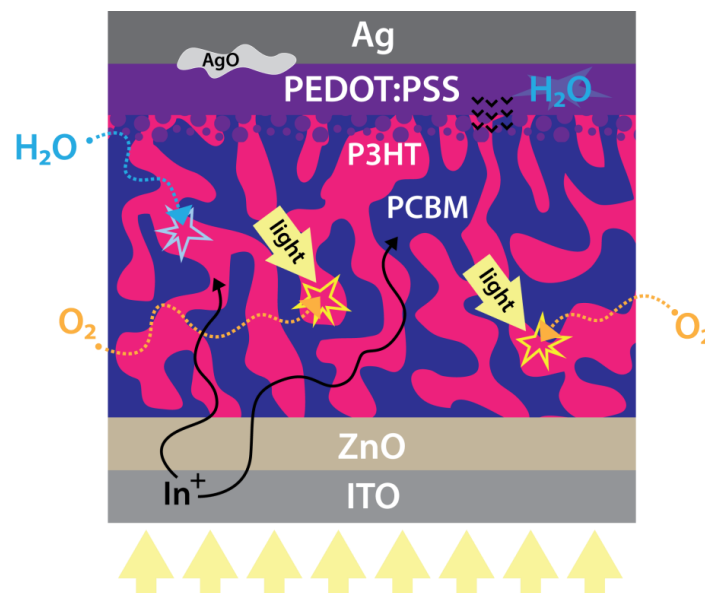


Figure 1.5 cross section view of a typical BHJ OPV device illustrating some of the many degradation pathways that can occur within an OPV device. Adapted with permission from Elsevier⁷

Some of the degradation mechanism at play can be seen Figure 1.5. Photo-oxidation, thermal oxidation, indium migration, diffusion of water and oxygen into the cell, hole and electron transport degradation, morphology and phase changes in the active layer, indium migration, and the list could go on and on. As mentioned, there are a multitude of degradation pathways possible in an OPV device, influenced both by internal and external factors. To get a better overview of the stability of OPVs the reader is referred to a review that was co-authored during the PhD, attached in Appendix B.⁴ Other reviews include.^{7,9-11}

1.5 Chemical and physical characterization of OPV devices and materials

There are many different techniques that can be used and some are already established in the OPV research field such as, electrical characterization, infrared spectroscopy (IR), UV-visible spectroscopy (UV-vis), optical microscopy, fluorescence microscopy, atomic force microscopy (AFM), scanning electron microscopy (SEM), transmission electron microscopy (TEM), light-beam-induced-current microscopy (LBIC), X-ray techniques, time-of-flight secondary ion mass spectrometry (TOF-SIMS) only to mention a few. There are different ways that OPVs can be characterized from the individual materials or building block e.g. the polymer in the active layer to individual layers e.g. the electrodes, the active layer etc. and finally as multi-layered completed OPV devices.¹²

The thesis will focus on the use of TOF-SIMS and AFM as characterization techniques of OPV materials, individual layers and whole devices. Herein, TOF-SIMS has been the main technique used for chemical OPV degradation pathway characterization.

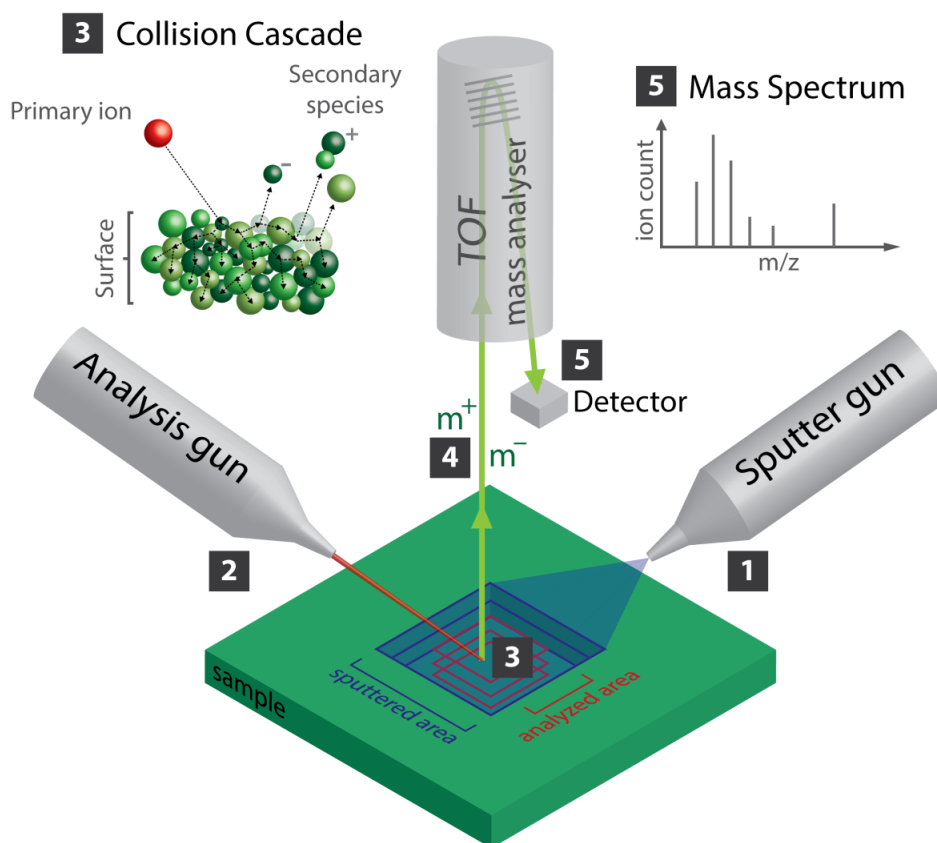


Figure 1.6. Schematic of the basic working principles of TOF-SIMS, (1) an ion gun is used for sputtering (removing of materials) (2) ion analysis gun is used for analysis, these ions are often called primary ions (3) when the primary ions hit the surface a collision cascade occurs repelling secondary species (molecules, fragments, atoms) from the top surface, less than 1% of the secondary species are ionized and can be further analysed (4) the secondary ions generated (m^+ and m^-) are extracted from the surface and mass analysed in a TOF mass analyser (5) the secondary ions' flight time are then detected at the detector and thus a mass spectrum of the analysed area can be generated.

1.6 Time-of-flight secondary ion mass spectrometry (TOF-SIMS)

The main analytical technique used during this PhD has been time-of-flight secondary ion mass spectrometry (TOF-SIMS), a technique producing direct chemical information. TOF-SIMS is a widely used technique for surface chemical analysis for biological, organic and inorganic samples.¹³ TOF-SIMS is useful for identification of trace elements, organic molecules and polymers on surfaces, with better than 1 ppm sensitivity for some molecules and down to ppb sensitivity for some elements.

1.6.1 Basic principles

A simplified schematic of the working principles of TOF-SIMS can be found in Figure 1.6.

Sputtering

The sample surface is bombarded by a high energy (usually 5 – 40 keV) primary ion beam in an ultra-high-vacuum (UHV) environment. The high-energy impact results in cascades of collisions between atoms and molecules in the solid, some of which return to the surface region resulting in sputtering (removal from the surface) of molecules, molecular fragments and atoms. While the technique is apparently destructive, the essence of the static mode is to use an extremely low dose of primary ions (never more than 10^{13} ions cm^{-2}) so that within the time frame of the experiment less than 1% of the top surface layer receive an ion impact. This ensures that no point on the surface receives more than one hit and that the ions detected are from the virgin surface.

Secondary ion generation

A small portion (<0.1 %) of the sputtered species are ionized as they leave the surface and it is these secondary ions that can be analysed by mass spectrometry. In TOF-SIMS the secondary ion species are extracted from the surface by a time-of-flight mass analyser and convert their flight time from the surface to the detector into m/z (mass over charge) to provide the mass spectrum which thus reflects the surface chemistry of a given sample.

The mass spectrum

The mass spectral data, i.e. the mass spectrum, constitutes the raw data of a TOF-SIMS analysis. The spectrum contains information on the molecular structure (in particular for organic molecules and polymers). Element identification is straight forward. Some structural information is stored in the systematic series of peaks; other information can be extracted from single peaks. Peak identification is based mainly on a combination of accurate mass (from calibration) and isotope distribution.

1.6.2 Operational modes

Spectrometry

Data is acquired from comparatively large areas directly at the surface. Element identification and structural molecular information can be obtained (mass).

Imaging

Data is acquired as a function of the position of a localized analysis beam at the surface. Information on the lateral distribution of the surface chemistry is obtained (x, y, mass).

Depth profiling

Data is acquired as a function of depth. The deeper layers are normally accessed by sputter erosion. Information on the lateral and vertical distribution of chemistry in the material is obtained (x, y, z, mass).

A schematic cross-section of an OPV device at various stages of depth profiling along with the resulting depth profile are shown in Figure 1.7a and b, respectively. It is to be noted that the depth profile shown in Figure 1.7b is an ideal case, in reality it is often the case that interfaces and depth resolution are not so defined as they are effected by numerous parameters such as sputter rate and sample thickness to only mention a few. Figure 1.7c shows the sputter erosion through the top layers of an OPV device at various sputter times of a depth profile experiment.

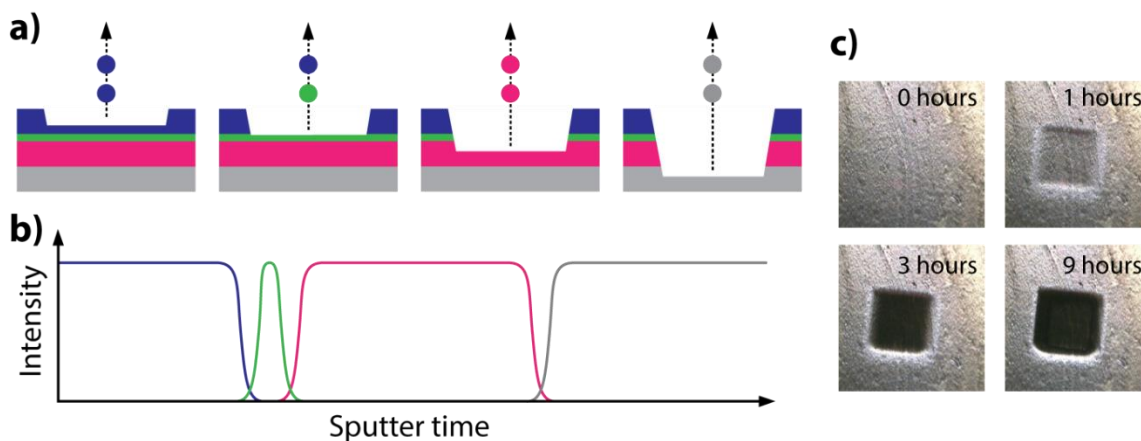


Figure 1.7 a) schematic cross-section of an OPV device at various stages of depth profiling, b) schematic depth profile showing the intensity of the various materials as a function of sputter time (i.e. depth). c) optical images of a sample surface at different sputter times as indicated.

1.6.3 The use of TOF-SIMS in OPV research

Although TOF-SIMS is a fairly specialized and not so wide spread technique there are some examples where TOF-SIMS has been used as a characterization tool of OPV materials and OPV devices. Most of the examples are of characterization in general often focusing on the active layer material BHJ.^{14–21} Whereas publications on specifically OPV degradation characterization the majority originates from the research group led by Frederik C. Krebs at DTU Risø campus, which is the group that I have been conducting my PhD research for the past since October 2010.^{8,22–26}

1.7 Multivariate Analysis (MVA)

Multivariate analysis (MVA) involves the use of simultaneous statistical procedure of two or more variables in a data set. An essential aspect of MVA is the statistical study of the dependence (covariance) between variables. Using a small number of statistical variables to summarise the data, the interpretation of complex data sets including a large number of dependant variables can quickly be simplified.²⁷

A typical TOF-SIMS spectrum can contain hundreds of peaks, the intensity of which can vary due to the composition, structure, order, and orientation of the surface species. TOF-SIMS data are inherently multivariate since the relative intensities of many of the peaks within a given spectrum are related, due to the fact that they often originate from the same surface species.²⁸ The use of MVA on TOF-SIMS data has increased in recent years, as is seen by an increase in publications.^{27,28} There are many different MVA methods that are applicable to TOF-SIMS data, however herein only a brief introduction to principle component analysis (PCA) and multivariate curve resolution (MCR) are given. For further details on these methods and other, see references.²⁷⁻³⁰

1.7.4 Principal Component Analysis (PCA)

PCA is a MVA technique for reducing matrices of data to their lowest dimensionality by describing them using a small number of orthogonal components. The aim of the PCA is to extract principal components (PCs), that capture the largest amount of variance within the multi-dimensional data set.²⁷

1.7.5 Multivariate Curve Resolution (MCR)

MCR is designed for recovery of pure components from multi-component mixtures, when little or no prior information is available. MCR uses an iterative least-squares algorithm to extract solutions to the component analysis, while applying suitable constraints.²⁷ MCR is often used for TOF-SIMS ion image analysis.³¹⁻³⁵

1.8 Atomic Force Microscopy (AFM)

Atomic Force microscopy (AFM) is a well-established imaging technique most commonly used to visualize surface topography. AFM provides Ångström range resolution in both the lateral and vertical planes under ideal conditions. A clear disadvantage is the limited analysis area and a very slow acquisition time.

1.8.1 Contact and tapping mode

In contact mode the tip is in contact with the surface while acquisitioning an image, surface damage by the tip can be very common as the two are in constant contact. Contact mode is preferred on hard sample surfaces

In tapping mode (sometimes referred to as intermittent contact mode) the tip resonates over the surface at its own resonance frequency. This means that the tip only comes close to the

Chapter 1

surface a fraction of the time, therefore intermittent contact mode is a much "softer" image acquisition, which often results in a higher resolution and, more importantly, less surface damage by the tip

1.9 Aim and overview of this thesis

The primary aim of the PhD project was to characterize possible degradation occurring in OPV devices and OPV materials. The ultimate goal was thus to increase the stability and life time of OPVs. The secondary aim was to generally characterize OPV devices and OPV materials. The characterization was conducted using TOF-SIMS and AFM as analysis techniques.

The research section of the thesis has been divided into 3 chapters.

Chapter 2

Is based on a large inter-laboratory study where different types of OPV devices were systematically degraded and analysed

Chapter 3

Looks at the active layer degradation pathways, degraded by concentrated light and analysed by TOF-SIMS and XPS. The mass spectra were then analysed by multivariate methods.

Chapter 4

The last research chapter is a collection of smaller TOF-SIMS and AFM analysis/characterization work conducted during the PhD period that have been published. This chapter then provides different OPV analysis examples.

1.10 List of publications and contributions

During the PhD study a long list of publications has been produced, whereby this thesis focuses on a selection of these that have been highlighted in blue.

- T.R. Andersen, H.F. Dam, **B. Andreasen**, M. Hösel, M. V. Madsen, S. a. Gevorgyan, R.R. Søndergaard, M. Jørgensen, F.C. Krebs, Sol. Energy Mater. Sol. Cells 120 (2014) 735.
- M. Jørgensen, J.E. Carlé, R.R. Søndergaard, M. Lauritzen, N.A. Dagnæs-Hansen, S.L. Byskov, T.R. Andersen, T.T. Larsen-Olsen, A.P.L. Böttiger, **B. Andreasen**, L. Fu, L. Zuo, Y. Liu, E. Bundgaard, X. Zhan, H. Chen, F.C. Krebs, Sol. Energy Mater. Sol. Cells 119 (2013) 84.
- Y. Liu, T.T. Larsen-Olsen, X. Zhao, **B. Andreasen**, R.R. Søndergaard, M. Helgesen, K. Norrman, M. Jørgensen, F.C. Krebs, X. Zhan, Sol. Energy Mater. Sol. Cells 112 (2013) 157.

- H. Pan, L. Zuo, W. Fu, C. Fan, **B. Andreasen**, X. Jiang, K. Norrman, F.C. Krebs, H. Chen, *Org. Electron.* 14 (2013) 797.
- J.E. Carlé, **B. Andreasen**, T. Tromholt, M. V. Madsen, K. Norrman, M. Jørgensen, F.C. Krebs, *J. Mater. Chem.* 22 (2012) 24417.
- **B. Andreasen**, D.M. Tanenbaum, M. Hermenau, E. Voroshazi, M.T. Lloyd, Y. Galagan, B. Zimmermann, S. Kudret, W. Maes, L. Lutsen, D. Vanderzande, U. Würfel, R. Andriessen, R. Rösch, H. Hoppe, G. Teran-Escobar, M. Lira-Cantu, A. Rivaton, G.Y. Uzunoğlu, D.S. Germack, M. Hösel, H.F. Dam, M. Jørgensen, S. a. Gevorgyan, M. V Madsen, E. Bundgaard, F.C. Krebs, K. Norrman, *Phys. Chem. Chem. Phys.* 14 (2012) 11780.
- G. Teran-Escobar, D.M. Tanenbaum, E. Voroshazi, M. Hermenau, K. Norrman, M.T. Lloyd, Y. Galagan, B. Zimmermann, M. Hösel, H.F. Dam, M. Jørgensen, S.A. Gevorgyan, S. Kudret, W. Maes, L. Lutsen, D. Vanderzande, U. Würfel, R. Andriessen, R. Rösch, H. Hoppe, A. Rivaton, G.Y. Uzunoğlu, D. Germack, **B. Andreasen**, M. V Madsen, E. Bundgaard, F.C. Krebs, M. Lira-Cantu, *Phys. Chem. Chem. Phys.* 14 (2012) 11824.
- T.R. Andersen, Q. Yan, T.T. Larsen-Olsen, R. Søndergaard, Q. Li, **B. Andreasen**, K. Norrman, M. Jørgensen, W. Yue, D. Yu, F.C. Krebs, H. Chen, E. Bundgaard, *Polymers (Basel)*. 4 (2012) 1242.
- M. Helgesen, J.E. Carlé, **B. Andreasen**, M. Hösel, K. Norrman, R. Søndergaard, F.C. Krebs, *Polym. Chem.* 3 (2012) 2649.
- E. Bundgaard, O. Hagemann, M. Bjerring, N.C. Nielsen, J.W. Andreasen, **B. Andreasen**, F.C. Krebs, *Macromolecules* 45 (2012) 3644.
- M. Jørgensen, K. Norrman, S.A. Gevorgyan, T. Tromholt, **B. Andreasen**, F.C. Krebs, *Adv. Mater.* 24 (2012) 580.
- Rösch, D.M. Tanenbaum, M. Jørgensen, M. Seeland, M. Bärenklau, M. Hermenau, E. Voroshazi, M.T. Lloyd, Y. Galagan, B. Zimmermann, U. Würfel, M. Hösel, H.F. Dam, S. a. Gevorgyan, S. Kudret, W. Maes, L. Lutsen, D. Vanderzande, R. Andriessen, G. Teran-Escobar, M. Lira-Cantu, A. Rivaton, G.Y. Uzunoğlu, D. Germack, **B. Andreasen**, M. V. Madsen, K. Norrman, H. Hoppe, F.C. Krebs, *Energy Environ. Sci.* 5 (2012) 6521.
- D.M. Tanenbaum, M. Hermenau, E. Voroshazi, M.T. Lloyd, Y. Galagan, B. Zimmermann, M. Hösel, H.F. Dam, M. Jørgensen, S. a. Gevorgyan, S. Kudret, W. Maes, L. Lutsen, D. Vanderzande, U. Würfel, R. Andriessen, R. Rösch, H. Hoppe, G. Teran-Escobar, M. Lira-Cantu, A. Rivaton, G.Y. Uzunoğlu, D. Germack, **B. Andreasen**, M. V. Madsen, K. Norrman, F.C. Krebs, *RSC Adv.* 2 (2012) 882.
- T.T. Larsen-Olsen, **B. Andreasen**, T.R. Andersen, A.P.L. Böttiger, E. Bundgaard, K. Norrman, J.W. Andreasen, M. Jørgensen, F.C. Krebs, *Sol. Energy Mater. Sol. Cells* 97 (2012) 22.

Chapter 1

- T.T. Larsen-Olsen, T.R. Andersen, **B. Andreasen**, A.P.L. Böttiger, E. Bundgaard, K. Norrman, J.W. Andreasen, M. Jørgensen, F.C. Krebs, *Sol. Energy Mater. Sol. Cells* 97 (2012) 43.
- M. Helgesen, M. V. Madsen, **B. Andreasen**, T. Tromholt, J.W. Andreasen, F.C. Krebs, *Polym. Chem.* 2 (2011) 2536.
- Y.-X. Nan, X.-L. Hu, T.T. Larsen-Olsen, **B. Andreasen**, T. Tromholt, J.W. Andreasen, D.M. Tanenbaum, H.-Z. Chen, F.C. Krebs, *Nanotechnology* 22 (2011) 475301.
- T.R. Andersen, T.T. Larsen-Olsen, **B. Andreasen**, A.P.L. Böttiger, J.E. Carlé, M. Helgesen, E. Bundgaard, K. Norrman, J.W. Andreasen, M. Jørgensen, F.C. Krebs, *ACS Nano* 5 (2011) 4188.
- **B. Andreasen**, K. Norrman, in: F.C. Krebs (Ed.), *Stab. Degrad. Org. Polym. Sol. Cells*, 1st ed., John Wiley & Sons, Ltd., Chichester, West Sussex, 2012, pp. 17–38.
- T.T. Larsen-Olsen, H.F. Dam, **B. Andreasen**, T. Tromholt, F.C. Krebs, in: *Kemiåret* 2011, 2012.

Chapter 2

TOF-SIMS investigation of degradation pathways occurring in a variety of organic photovoltaic devices²

² This chapter is based in its entirety on the 4th and final published article of the article series which were the outcome of the ISOS-3 collaboration.²⁶

2.1 Introduction

The presented work was part of a large inter-laboratory study that resulted from the 3rd International Summit on Organic Stability (ISOS-3) held at the DTU Risø campus in Roskilde, Denmark in October of 2010.³⁶ The collaboration involved six laboratories (Table 2.1) capable of manufacturing OPV devices, which produced seven distinct sets of OPV devices. The devices were all shipped to DTU Risø where they were degraded under identical well-defined conditions. Three different degradation conditions were used in accordance with the ISOS-3 protocols: accelerated full sun simulation; low level indoor fluorescent lighting; dark storage with daily monitoring of the photovoltaic parameters.³⁶ These conditions will be referred to as “full sun”, “fluorescent” and “dark”, respectively. The devices were analysed and characterized at different points of their lifetime by a large number of non-destructive and destructive techniques at different laboratories in the ISOS-3 collaborations. The terminology used for a lifetime of a device extracted from the degradation experiment is “TXX”, where XX denotes the percentage which the PCE has declined to from the initially measured PCE, i.e. T100 is the initial measurement, T80 is when PCE has declined to 80% of its initial value etc. The original goal was to extract the devices from the degradation experiment at T100, T80, T50, and T10, which more or less was achieved (some devices never reached T10 within the timeframe of the project). Once a device was extracted it was not reused, and since some of the characterization methods are destructive, it was necessary to manufacture a large number of devices. The degradation experiments lasted up to 1830 hours and involved more than 100 devices with more than 300 cells (a device can contain several cells).

The extent of the laboratories involved in the ISOS-3 collaboration can be seen on the map in Figure 2.1 where the OPV manufacturing labs and analysis labs are highlighted. The different OPV devices investigated in the collaboration are illustrated in Figure 2.1a-f.

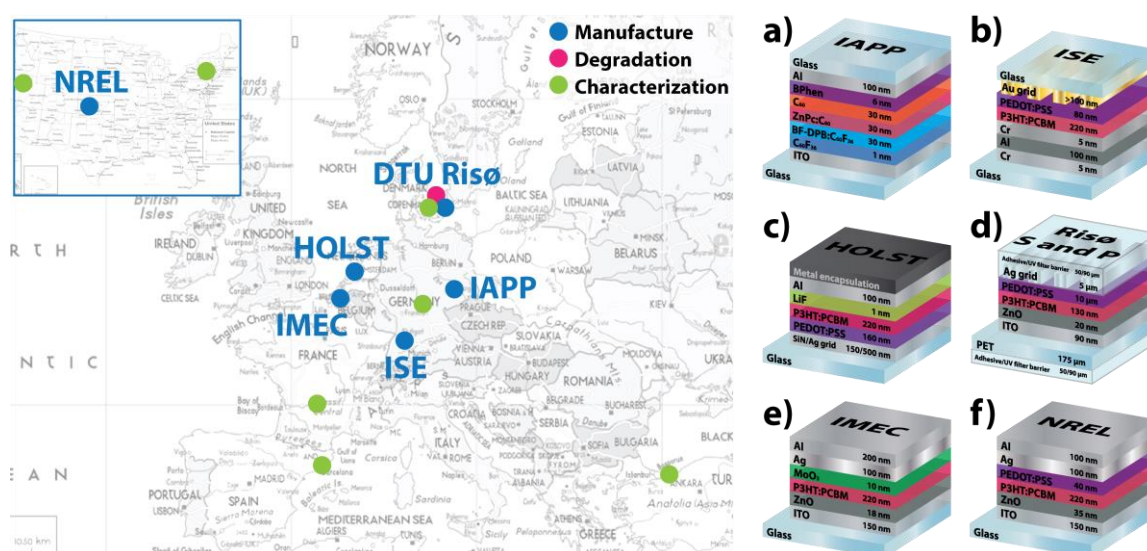


Figure 2.1 A map of all the participating laboratories is depicted on the right hand side showing different colour dots for manufacture, degradation and characterization laboratories. The left hand side (a – f) illustrates the seven different OPV devices that were part of the ISOS-3 study.

The ISOS-3 inter-laboratory study has produced a vast amount of results, resulting in four articles, hereafter termed ISOS-3 reports.³⁷⁻³⁹ The different device manufacturing methods along with the degradation procedures and electrical characterization have been presented in the first ISOS-3 report.³⁷ The second ISOS-3 report describes work using a suite of imaging techniques to map specific degradation mechanisms.³⁸ The following imaging techniques were employed: laser-beam induced current (LBIC), photoluminescence imaging (PLI), electroluminescence imaging (ELI) and lock-in thermography (LIT). In addition to analysing the ISOS-3 devices at specified T-values (in this case corresponding to different devices and thus cells), selected devices were cycled in order to monitor the evolution of spatial defects on the same cell. In the ISOS-3 third report incident photon-to-electron conversion efficiency (IPCE) and in situ IPCE were employed to describe various degradation mechanisms.³⁹ The fourth ISOS-3 report is the basis of this chapter. The most important conclusions regarding degradation mechanisms based on the previous ISOS-3 reports are summarized in the following.

The combination of the imaging techniques LBIC, PLI, ELI and LIT suggested that the main degradation mechanisms were the following:³⁸

- Formation of aluminium oxide (at the aluminium electrode).
- Formation of blocking contacts due to silver oxide formation or ZnO dedoping.
- Electro-migration of silver (especially at the edges due to enhanced electric fields).
- Water and oxygen ingress through pinholes and from the edges of the cells.
- Water release from highly conductive PEDOT:PSS.

The overall conclusion based on the imaging results is that OPV device stability is mostly controlled by the instability of the charge collecting electrodes. It should be emphasized that these imaging analyses alone do not directly reveal degradation mechanisms, complementary information is often necessary to come to plausible conclusions. Ideally, it would make sense to combine the analyses with techniques that produce direct chemical information. Because the IPCE and in situ IPCE analyses were conducted in both ambient and N₂ atmospheres it was possible to identify the materials more susceptible to degradation caused by molecular oxygen and water. The result of the IPCE and in situ IPCE analyses resulted in the following major conclusions/ comments regarding degradation:³⁹

- For some of the encapsulated devices the degradation could possibly be initiated at the Ag or Au/PEDOT:PSS interface by the formation of a chemical bond between the Ag (or Au) and the PEDOT:PSS, which can occur in the absence of oxygen and water.
- The devices without encapsulation were highly dependent on atmospheric conditions and water uptake was a major problem attributed to the hygroscopic nature of PEDOT:PSS and semiconductor oxides.
- For the devices without encapsulation the water uptake was observed to be random and reversible.
- For the devices without encapsulation water will primarily degrade the electrodes of the cell.

Chapter 2

- The cells within a device (a device can contain several cells) degraded differently depending on the position of the cell in the device.

The present work constitutes the fourth and final report in the series of reports that resulted from the ISOS-3 inter-laboratory study. The main analytical technique used in this work is time-of-flight secondary ion mass spectrometry (TOF-SIMS), a technique producing direct chemical information. The secondary technique is X-ray photoelectron spectroscopy (XPS), which also produces direct (but complementary) chemical information. The basic information of TOF-SIMS is mass spectral information, i.e. chemical information. TOF-SIMS imaging has an exceptional low probe depth of 1–2 nm and is able to obtain surface images based on the mass spectral information. Furthermore, material can be sputtered away from the surface during the TOF-SIMS imaging analysis, i.e. a microscopic hole can be made that when combined with the imaging capability produces a depth profile, i.e. mass spectral-based images as a function of depth. The principle of TOF-SIMS depth profiling was discussed in Chapter 1 see Figure 1.7 for further details. The fact that TOF-SIMS produces direct chemical information from any given point in the cell makes it, in principle, an ideal technique to either directly identify a degradation mechanism, or complement the analysis results described in the previous ISOS-3 reports.^{37–39} However, there are certain limitations such as a poor depth resolution, which makes it challenging to detect interface phenomena. Furthermore, the depth profiling properties used are such that all molecular information is destroyed leaving only atomic ions and small fragment ions to be monitored. Finally, the data interpretation can be very challenging due to the enormous amount of mass spectral peaks generated during a TOF-SIMS analysis, which is problematic if one does not know specifically what one is looking for, i.e. “looking for a needle in a haystack situation”.

The main focus of the work presented herein is to study the degradation of the active bulk material monitored by the oxygen incorporation that will be correlated with loss in performance for the various ISOS-3 devices. Furthermore, the oxygen incorporation will be quantified by correlating the TOF-SIMS results with results obtained by the quantitative XPS technique. Furthermore, degradation mechanisms suggested in the previous ISOS-3 reports will be correlated with information extracted from the TOF-SIMS depth profiling analyses. Finally, trends between loss in cell performance and information extracted from the TOF-SIMS depth profiling data will be described and discussed.

2.2 Experimental

Experimental details concerning the manufacture of the ISOS-3 devices, the degradation experiments, and characterization of the photovoltaic parameters can be found in the first ISOS-3 report.³⁷ Relevant information regarding the present work is that seven distinct device types (Table 2.1) were degraded under three different conditions: full sun, fluorescent, and dark (as mentioned previously in the text). The devices were extracted from the degradation tests at different lifetimes corresponding to (more or less) T100, T80, T50 and T10, and subsequently shipped to the participating laboratories around the world for analysis. The destructive analyses were obviously performed last and when Risø DTU (that initially

performed the degradation experiments) received the devices for the destructive TOF-SIMS analysis, they were placed in a glove box in a dry nitrogen atmosphere. Devices that were encapsulated had the encapsulation removed. A TOF-SIMS depth profiling analysis cannot penetrate the thick encapsulation. The Risø DTU cells were laminated and when delaminated the layers detached at the PEDOT:PSS/P3HT:PCBM interface, which turned out to be fortunate (will be evident later in the text). The devices and partial devices were placed on a TOF-SIMS sample holder in the glove box that was then placed in a specially designed transfer vessel that can sustain a controlled atmosphere long enough for the transfer vessel to be inserted into the vacuum chamber of the TOF-SIMS instrument. The encapsulated devices were thus never exposed to ambient air between the degradation experiments and the TOF-SIMS analysis. After the TOF-SIMS analysis the devices were transferred back to the glove box and stored until possible reanalysis.

Table 2.1 Device configurations used in the ISOS-3 study

Laboratory	Device configurations	Encapsulation and/or substrate (back - front)
IAPP	Al/BPhen/C ₆₀ /ZnPc:C ₆₀ /BF-DPB:C ₆₀ F ₃₆ /C ₆₀ F ₃₆ /ITO ^a	Glass - glass
ISE Holst	Au/PEDOT:PSS/P3HT:PCBM/Cr/Al/Cr ^b Al/LiF/P3HT:PCBM/PEDOT:PSS/SiN, Ag	Glass - glass Stainless steel - glass
Risø DTU S	Ag/PEDOT:PSS/P3HT:PCBM/ZnO/ITO	UV filter barrier - PET, UV filter barrier ^c
Risø DTU P	Ag/PEDOT:PSS/P3HT-co-P3AcET:PCBM/ZnO/ITO ^d	UV filter barrier - PET, UV filter barrier
IMEC	Al/Ag/MoO ₃ /P3HT:PCBM/ZnO/ITO	None - glass
NREL	Al/Ag/PEDOT:PSS/P3HT:PCBM/ZnO/ITO	None - glass

^a BPhen is 4,7-diphenyl-1,10-phenanthroline, C₆₀ is Buckminsterfullerene, ZnPc is zinc-phthalocyanine, BF-DPB is N,N'-((diphenyl-N,N'-bis)9,9-dimethyl-fluorene-2-yl)-benzidine. ^b PEDOT is poly(3,4-ethylenedioxythiophene), PSS is poly(styrenesulfonate), P3HT is poly(3-hexylthiophene), PCBM is phenyl-C₆₁-butyric acid methyl ester. ^c UV filter barrier is a 90 µm thick multi-laminate with a UV-filter with a pressure sensitive adhesive, PET is a 130 µm thick poly(ethylene terephthalate) substrate. ^d P3HT-co-P3AcET is poly(3-hexylthiophene-co-3-(2-acetoxyethyl)thiophene).

TOF-SIMS analyses were performed on six out of the seven distinct devices. The IAPP device was omitted since the main objective in this study was to compare the oxygen incorporation in the active material as a function of loss in performance.

The IAPP device is the only device not using P3HT:PCBM as the active material. The intensity of a mass spectral marker can only be compared for the same material when different cells are compared due to the response factors that are material dependent in a TOF-SIMS analysis. Another problem with the IAPP device was the long lifetime that by far exceeded the 1830 hours that the degradation experiments lasted. However, the IAPP device has previously been extensively studied at Risø DTU.²⁴ In that particular study the device was exposed to controlled atmospheres without encapsulation and illuminated (AM1.5G, 330 W m⁻², 49 °C). T50 was found to be ~2700 hours in a N₂ atmosphere, 74 hours in an O₂ : N₂ atmosphere, and 11 hours in a H₂O : N₂ atmosphere. It was found that water significantly causes the device to

degrade. The two most significant water-induced degradation mechanisms were found to be: (i) diffusion of water through the aluminium electrode in between the grains, resulting in formation of aluminium oxide at the BPhen/Al interface, and (ii) diffusion of water into the active layer (ZnPc : C₆₀), where ZnPc, but not C₆₀, becomes oxidized. Figure 2.2 shows schematics of the devices that were studied in this work, and associated layer thicknesses.

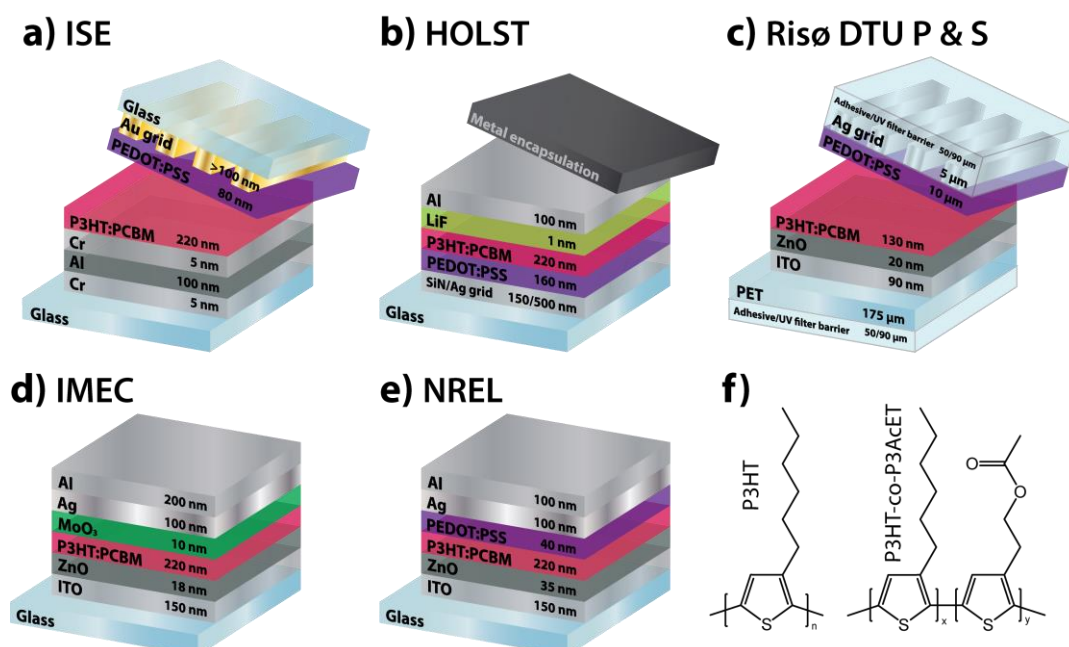


Figure 2.2 (a–e) illustrate the different device layer structures (materials and thicknesses) investigated in this work. The tilted sections on devices (a–c) indicate where the devices were opened/delaminated, thus making the TOF-SIMS analysis possible. The active layers of all the devices consisted of P3HT:PCBM except the Risø DTU S device that had the slightly modified P3HT polymer P3HT-co-P3AcET. The molecular structures of P3HT and P3HT-co-P3AcET are shown in (f).

2.2.1 TOF-SIMS analysis

The TOF-SIMS analyses were performed using a TOF-SIMS IV (ION-TOF GmbH, Munster, Germany). 25 ns pulses of 25 keV Bi⁺ (primary ions) were bunched to form ion packets with a nominal temporal extent of 0.9 ns at a repetition rate of 10 kHz, yielding a target current of 0.7 pA. These primary ion conditions were used to obtain mass spectra, ion images, and depth profiles. Depth profiling was performed using an analysis area of 200 × 200 nm² centred in a sputter area of 300 × 300 nm². 30 nA of 3 keV Xe⁺ was used as sputter ions.

An encapsulated IMEC device was analysed in a slightly different way: the encapsulation was removed and the Al–Ag–MoO₃ stack was partly removed. 11 × 8 mm² surface areas were then imaged, each covering four cells on the device. These images were cropped to sizes corresponding to the individual cells (5.2 × 2.7 mm²). Depth profiling was performed on the encapsulated IMEC device at various surface locations using an analysis area of 500 × 500 nm² centred in a sputter area of 750 × 750 nm². For all analyses electron bombardment (20 eV) was used to minimize charge built-up at the surface. Desorbed secondary ions were accelerated to 2 keV, mass analysed in the flight tube, and post-accelerated to 10 keV before detection. The

relative degree of oxygen incorporation (i.e. degradation) in the bulk active material is extracted from the depth profiling data by evaluating the depth profiles in order to pinpoint the sputter time window that corresponds only to the bulk P3HT:PCBM material. This is exemplified by the NREL device that exhibits illustrative depth profiles (Figure 2.3) that demonstrate the principle.

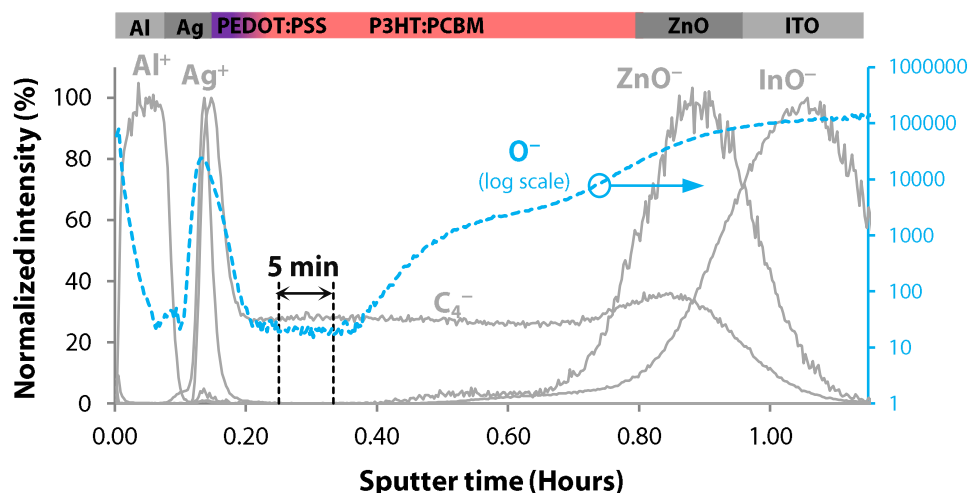


Figure 2.3 TOF-SIMS depth profiles of a T100 NREL device (the layer structure is indicated at the top of the figure). Various carefully selected mass spectral markers identify the different layers (grey lines). The oxygen profile (dashed blue line) and the indicated sputter time window corresponding to the bulk of the P3HT:PCBM material show from where the information is extracted. The thin PEDOT:PSS layer is defined by the Na^+ profile (not shown) and does not overlap with the 5 minute sputter time window in question.

Careful selection of more or less specific mass spectral markers enables distinction between the individual layers. Within the sputter time window for the P3HT:PCBM material the goal was to pinpoint where all the signal intensities are constant/parallel, i.e. without interference from other species. The oxygen depth profile (O^-) in Figure 2.3 shows that in that particular case there is only a limited sputter time window available due to interference from ZnO and ITO that contributes to the oxygen depth profile (O^-). In this case the interference is probably caused by a small degree of interlayer mixing, which is not caused by the sputter process that acts in the opposite direction. Furthermore, a depth profile only makes physical sense if the lateral plane of the probed volume is homogeneous, so to ensure lateral homogeneity the ion images were carefully analysed and any abnormalities such as spatially localized contaminants (e.g. particles) were bypassed in the dataset, which ensured that only the photo-oxidation was probed. The depth profiles in Figure 2.3 also demonstrate the unfortunate poor depth resolution that worsens for longer sputter times. It should be emphasized that different materials have different sputter rates, so there is no correlation between relative sputter time windows and relative layer thicknesses. To ensure that the extracted information could be compared within and across the different devices some simple measures had to be taken during the data interpretation. It is not a problem to maintain the experimental analysis conditions over short periods of time, however, due to the large amount of devices that were analysed over a very long time it was impossible to reproduce the experimental conditions accurately. The signal intensity is sensitive towards some instrumental parameters, so in order

to eliminate the instrument effects and maintain the comparability the following procedure was adapted: in each case equally sized sputter time windows corresponding to 30 scans were chosen. More importantly, the oxygen signal intensity was normalized against the sum of most of the abundant signals within the same sputter time window, which constituted (for the sputter conditions in question) the following signals: C_n ($n = 2-4; 6-10$). The peak C_{5-} was omitted due to significant peak overlap and C_{1-} was omitted because it, for unknown reasons, worsened the reproducibility. It was thus $\text{Int}(\text{O}^-)/\text{Int}(C_n, n = 2-4; 6-10)$ that was extracted from each depth profile (the ratio was multiplied by a factor of 1000 for practical reasons), which provides a semi-quantitative measure of the relative oxygen incorporation in the active layer for various devices at different lifetimes (T100, T80, T50, T10).

2.2.2 XPS analysis

XPS was employed to convert the semi-quantitative TOF-SIMS information into quantitative XPS information by correlating XPS data with TOF-SIMS data, i.e. creating a calibration curve. The XPS analyses were performed on a K-alpha (Thermo Electron Limited, Winsford, UK) using a monochromatic Al-Ka X-ray source and a take-off angle of 90° from the surface plane. Atomic concentrations were determined from surface spectra (100–600 eV, 200 eV detector pass energy, 5 scans) and were calculated by determining the relevant integral peak intensities using a Shirley type background. All XPS analyses were repeated at least three times on different surface locations.

2.3 Results and discussion

2.3.1 Quantification of TOF-SIMS depth profiling data

When studying oxygen incorporation/uptake in P3HT:PCBM (i.e. degradation) it is obviously interesting to attempt to quantify how much oxygen is incorporated. This turned out to be far from simple. The first approach was to create a series of calibration samples from which a calibration curve could be obtained. P3HT:PCBM was spin-coated onto ITO-coated glass substrates (ITO improved the quality of the mass spectral peak shapes) and illuminated for varying amounts of time. The idea was then to perform non-quantitative TOF-SIMS depth profiling on these calibration samples, extract the normalized oxygen intensities and then perform quantitative XPS depth profiling on the same samples, and subsequently correlate the data. This was, however, not possible because during the XPS depth profiling analysis the oxygen becomes underestimated due to a sputter phenomenon. The same phenomenon applies for the TOF-SIMS depth profiling but that is of less importance since TOF-SIMS is not quantitative to start out with, the only effect is a decrease in sensitivity towards oxygen during TOF-SIMS depth profiling. This problem was solved by performing XPS spectroscopy directly on the surfaces (i.e. not depth profiling) of the calibration samples and correlating these results with the TOF-SIMS depth profiling data. This is only justified because the surface chemistry appears to be equivalent with the bulk chemistry (often not the case), which is documented in Figure 2.4 for a spin-coated P3HT:PCBM sample. As is evident from Figure 2.4 all the profiles have a constant intensity from the first scan, which suggests that the surface chemistry in this

case is equivalent to the bulk chemistry. It is therefore justified to correlate surface obtained XPS data with bulk obtained TOF-SIMS data.

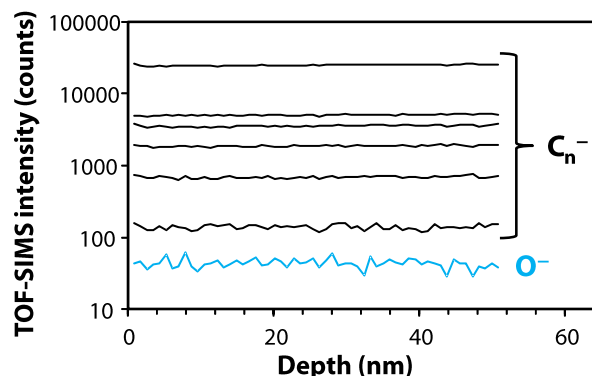
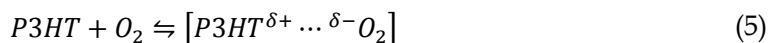


Figure 2.4 TOF-SIMS depth profiles of a spin-coated P3HT:PCBM sample. The sample was spun from dichlorobenzene (20 : 20 mg ml⁻¹) at 800 rpm for one minute producing a 208 ± 3 nm film thickness (measured by AFM profilometry). The sputter process is in increments of 10 s using 3 keV Xe⁺ (30 nA) over a 300 × 300 mm² surface area and the analysis covers the central 200 × 200 mm² part using 0.7 pA Bi⁺. The sputter time scale was converted to a depth scale from a measured sputter rate of 5.26 ± 0.08 nm min⁻¹ (only valid for P3HT:PCBM).

The second problem was caused by a well-described phenomenon. P3HT has the ability to interact with molecular oxygen resulting in the formation of a charge transfer complex (equation (5)).^{40–42}19–21 The process is reversible and is thus sometimes referred to as reversible degradation, see equation (5):



Abdou et al.⁴⁰ described the phenomenon for poly(3-alkylthiophenes) and found that ~1% of the p-conjugated segments and ~30% of the dissolved molecular oxygen form a charge transfer complex, which corresponds to a charge transfer complex concentration of ~1.3 × 10⁻³ M. They found that the complex is weakly bound (DHo = -10.6 kJ mol⁻¹) and possesses a distinct absorption band in the visible region. The electronic properties of the material are affected by the complex depending on the oxygen pressure. The authors found that the complex causes the carrier concentration to increase, the conductivity to increase, and the charge carrier mobility to be lowered, and the complex is a fluorescence quencher of mobile polaronic excitons.

In a recent publication Guerrero et al.⁴¹ studied the phenomenon in OPV devices with the configuration Ag-Ca-P3HT:PCBM-PEDOT:PSS-ITO. The authors showed that the complex is present in complete cells and that it is responsible for photocurrent reduction and loss in photo-voltage. Furthermore, it was found that irreversible degradation induced by molecular oxygen is attributed to calcium oxide formation.

Aguirre et al.⁴² demonstrated that illuminating P3HT in the presence of air induces persistent radical cations on the P3HT chains. They found that the photo-induced charges are stable at room temperature for several hours, but recombine quickly if the air is removed from the atmosphere. The authors postulate, that the persistency of the photo-induced charges is possible due to the existence of an energy barrier separating the excited charge transfer state

from the ground state charge transfer complex. The barrier is proposed to be a result of stabilization of the excited charge transfer state and possibly a result of chemical interaction between P3HT and molecular oxygen, resulting in a so-called relaxed charge transfer state. Finally, it was found that lowering the pressure of air in the chamber was sufficient to break up the charge pair.

In the present work the afore-mentioned calibration samples were spin-coated in ambient air and stored for ~20 hours in darkness in ambient air before being transferred to the vacuum chambers of the TOF-SIMS and XPS instrument. It became evident that the charge transfer complex had to be considered.

When extracting the normalized oxygen intensities from the calibration samples an effect of time was observed. This is demonstrated in Figure 2.5 for various spin-coated P3HT:PCBM samples exposed to various experimental conditions. All samples exhibit the same behaviour, which is a decrease in normalized oxygen intensity (oxygen content in the material, i.e. not in the gas phase) as a function of time. This phenomenon is not related to simple diffusion of solubilized molecular oxygen out of the material, which is a process that takes place within a few minutes at the most. It is presumably an effect of the reversible formation of the charge transfer complex (equation (5)). Once the samples are placed in a vacuum the equilibrium follows Le Chatelier's principle and shifts towards removal of molecular oxygen from the complex, i.e. depletion of the charge transfer complex.

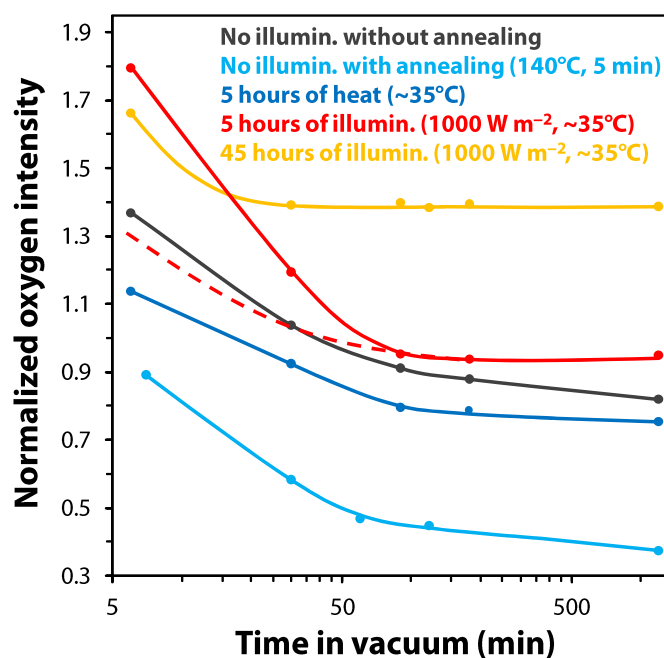


Figure 2.5 Normalized oxygen intensity of the film as a function of time in vacuum for spin-coated P3HT:PCBM films. The probe depth was ~25 nm. The samples were spun from dichlorobenzene (20 : 20 mg ml⁻¹) at 800 rpm for one minute. All illuminated samples were not annealed prior to illumination. The normalized oxygen intensity was extracted from TOF-SIMS depth profiles as described earlier in the text. All samples were introduced into the vacuum chamber approximately 20 hours after spin coating. It took 3 minutes to pump down and an additional 3 minutes to set up the analysis before data could be collected. The red dashed line indicates the sample that is illuminated for 5 hours and then reanalysed after storing in darkness in ambient air.

The plots in Figure 2.5 contain a lot of interesting information. If the result obtained for the non-annealed non-illuminated sample (black line) is compared with the annealed non-illuminated sample (light blue line), it is clear that a significant drop is observed in the normalized oxygen intensity. This has been confirmed by XPS that shows a 30% drop in oxygen content. Furthermore, it is consistent with the findings by Mattis et al. that concluded that an annealing temperature above 120 °C is required to promote oxygen desorption. The sample that was heated for five hours (dark blue line) was put under the simulated sun wrapped in aluminium foil so that it would receive the heat (~35 °C) but not the light. Five hours at ~35 °C must be considered as a very gentle annealing compared to five minutes at 140 °C (light blue line), which is consistent with the relative result observed in Figure 2.5. For the illuminated samples (red and orange lines) a significant increase in normalized oxygen intensity is observed. The illumination promotes the generation of the persistent radicals enabling the charge transfer complex to be formed, which partly explains the elevated normalized oxygen intensities. In addition, the harsh conditions will inevitably photo-oxidize the material forming covalently bound degradation products, i.e. an irreversible process. It appears that the more the photo-oxidation present the shorter the time to level out, i.e. faster depletion of the charge transfer complex. This is intuitively what one would expect based on the fact that photo-oxidation reduces the number of molecular sites available for charge transfer complex formation. The sample that had undergone the following procedure: stored in darkness for ~20 hours, illuminated for five hours, stored in darkness for ~20 hours, analysed, stored in darkness for ~20 hours, reanalysed, correspond to the solid red and dashed red lines, respectively (Figure 2.5). The reanalysed sample has an initial value that is significantly lower compared to the first time it was analysed, but levels out to the photo-oxidation level that was also observed during the first analysis. This observation suggests that once the material has been depleted for the charge transfer complex it requires light to restore it to the original charge transfer complex concentration. Assuming that the plots in Figure 2.5 were correctly interpreted, it means that the charge transfer complex is formed to some degree without illumination or, alternatively, because the samples unavoidably received some degree of low level illumination during handling. The findings presented in Figure 2.5 agree fairly well with what has been described in regard to the charge transfer complex using alternative techniques.⁴⁰⁻⁴² However, the time-scale for depletion of the charge transfer complex in a vacuum is somewhat surprising and unpractical.

A calibration curve could now be constructed based on samples that were stored in the XPS and TOF-SIMS vacuum chambers for at least 20 hours prior to analysis in order to remove/minimize the charge transfer complex to an acceptable degree (not shown). At this point the third problem revealed itself. The calibration curve (not shown) produced unrealistic results when applied to the ISOS-3 depth profiling results. After numerous systematic experiments it became clear that annealing had a crucial effect on the calibration curve, more precisely on the normalized oxygen intensities obtained by TOF-SIMS, which is presumably a matrix effect caused by the annealing that presumably changes the crystallinity. All the ISOS-3 devices were annealed during fabrication, which therefore requires calibration samples that are annealed under the same conditions. The TOF-SIMS depth profiling results are clearly very sensitive to experimental conditions, which raised some concern about whether the fact that the calibration samples were exposed to ambient air during illumination

could have an effect, i.e. the P3HT:PCBM material in the ISOS-3 devices was sandwiched between various barrier layers and electrodes. Due to the clearly complex nature of these calibration experiments an alternative (more safe) approach was chosen that was simpler but rougher. It was decided to use some of the ISOS-3 cells that were stored in darkness in a glove box after the degradation experiments and analyses. Since XPS depth profiling was not an option (discussed earlier in the text) the choice of cells was limited to those that were delaminated, i.e. with the P3HT:PCBM exposed (Figure 2.2). The ISE and the Risø DTU cells fulfilled this criterion.

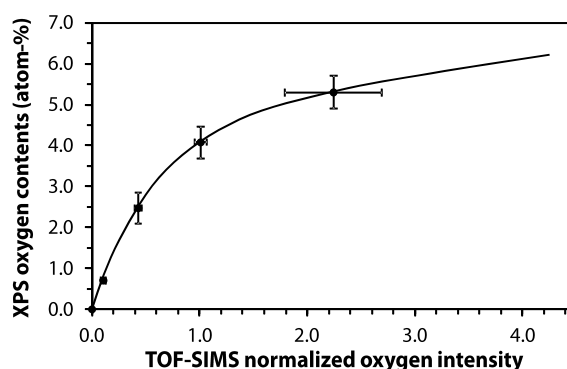


Figure 2.6 Calibration curve between TOF-SIMS depth profiling data and XPS data. The TOF-SIMS data were normalized from $\text{Int}(\text{O}^-) / \text{Int}(\text{C}_n, n = 2-4; 6-10)$ and multiplied by a factor of 1000 for practical reasons. Each point is an average of at least three points on different surface locations. All samples were placed in the vacuum chamber at least 20 hours prior to analysis in order to remove the weakly bound charge transfer complex between molecular oxygen and P3HT. The probe depth was ~ 25 nm.

The ISE was encapsulated with glass during the degradation experiments, so it is expected to have experienced a minimum of oxygen incorporation or none at all. The Risø DTU cells were encapsulated with a semi-impermeable organic barrier film, which previously was shown not to be 100% efficient.⁴³ Risø DTU T100 and T10 cells (full sun) were used for the calibration curve. The cells were stored at least 20 hours in the vacuum chambers of the TOF-SIMS and XPS instruments prior to analysis. The calibration curve is shown in Figure 2.6.

It is very fortunate that a modified version of P3HT (P3HT-co-P3AcET:PCBM) is used in the Risø DTU S device as it contains native oxygen in the form of an ester group (Figure 2.2f) that will help spread the points in the calibration curve. The lowest point is obviously (0.0) and the highest point is (2.2,5.3) that originates from the Risø DTU S T10 cell, so any measurements acquired above this value will be based on extrapolation.

The need for storing the samples for at least 20 hours in the TOF-SIMS vacuum chambers prior to analysis was realized after all the ISOS-3 devices were analysed, which obviously raised some concern. However, upon further reflection it turned out not to be a problem. All the glass/metal encapsulated cells were never exposed to ambient air at any point, so there is no concern about oxygen uptake. The Risø DTU cells were exposed to oxygen and water to some extent due to inferior encapsulation, and the non-encapsulated were obviously directly exposed to ambient air during the degradation experiments and during the non-destructive analysis in the various laboratories. After testing they were all sent back to Risø DTU and placed in a glove box. The devices were then prepared for analysis (removal of

encapsulation) and 13–18 samples were placed on the TOF-SIMS sample holder, a procedure that took most of a day. The sample holder was then typically transferred via a transfer vessel containing an inert atmosphere to the TOF-SIMS analysis chamber late in the day so that it would be ready for analysis the next morning. So by tracing back the working procedures it could be concluded that all the ISOS-3 devices were exposed to the nitrogen atmosphere in the glove box and the vacuum in the TOF-SIMS instrument for such a long time that it is safe to assume that the charge transfer complex had been depleted.

2.3.2 Oxygen incorporation and its effect on device degradation

It should be clear by now that oxygen incorporation in P3HT:PCBM is described by two processes: (i) formation of a charge transfer complex (reversible degradation), and (ii) photo-oxidation (irreversible degradation). Both processes are well-described in the literature and constitute an analytical challenge when present at the same time. However, due to the fortunate timescale of the analyses of the ISOS-3 devices we can assume that only irreversible photo-oxidation is probed. P3HT and P3HT:PCBM are well-described in terms of photo-oxidation both as materials but also as components in photovoltaic devices. In this study photo-oxidation of the active materials in the ISOS-3 devices was quantified using XPS calibrated TOF-SIMS depth profiling data, which has never been attempted before.

Photo-oxidation of the active material (P3HT:PCBM) was then compared to loss of photovoltaic performance, which is not necessarily an easy comparison since other degradation mechanisms are in play. The ultimate challenge in studying degradation phenomena in OPV devices is to quantify the contribution from each degradation mechanism to the overall degradation of the photovoltaic performance.

In terms of photo-oxidation it makes sense to group the six different devices (Table 2.1 and Figure 2.2) according to the encapsulation, well-knowing that we thereby do not consider possible internal photo-oxidation caused by metal oxides. The encapsulation used can be split up into three groups: (i) glass/ metal encapsulation (ISE and Holst), (ii) UV filter (flexible) encapsulation (Risø DTU S and P), and (iii) non-encapsulated (IMEC and NREL). The groups are listed here according to permeability with respect to molecular oxygen and water.

Comments on reproducibility for devices and TOF- SIMS analyses.

As described in the first ISOS-3 report devices were extracted from the degradation experiments at various degrees of performance, more or less corresponding to T100, T80, T50, and T10.15 Because some of the analyses were destructive it was not possible to follow loss of performance from the beginning to the end for one particular device, it had to be four devices that each represented T100, T80, T50, and T10, respectively. However, this will consequently result in strict requirements in terms of reproducibility when manufacturing the devices, which seems challenging considering the delicate device architectures requiring multiple processes to finally become a device. This was clearly seen in the third report that focused on IPCE analyses revealing significant differences in IPCE between equivalent devices and between cells in a device/module.³⁹

Oxygen incorporation in the active material is expected to be zero or close to zero in the impermeable encapsulated devices and modest in the others according to previous

experience.⁴⁴ Furthermore, the sputter process reduces the sensitivity profoundly, so detecting small changes with inferior sensitivity requires a good reproducibility with respect to device manufacturing since aberrations will result in chemical inhomogeneities that will consequently affect the relative results and thus the quality of the work.

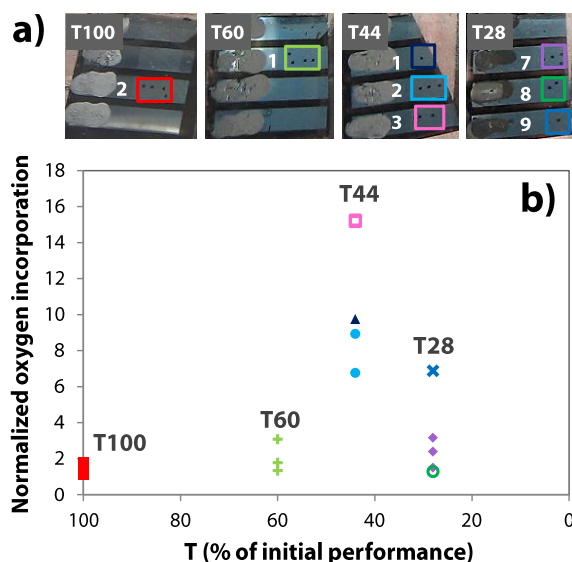


Figure 2.7 (a) Photographs of pieces of IMEC devices (full sun) showing the TOF-SIMS depth profiling holes. The devices were cut in pieces so that they could be analysed using various destructive methods. The coloured squares indicate which analyses were associated with this test. (b) Normalized oxygen incorporation corresponding to cell surface locations shown in (a) as a function of performance loss. The TOF-SIMS data were normalized from $\text{Int}(\text{O}^-)/\text{Int}(\text{Cn}, n = 2-4;6-10)$ and multiplied by a factor of 1000 for practical reasons.

In order to assess the reproducibility associated with the ISOS-3 cells a test was performed on four IMEC devices (full sun) corresponding to T100, T60, T44, and T28, respectively (Figure 2.7a). Multiple analyses were performed on one single cell, and multiple cells were analysed within the same device in order to measure the point-to-point variation within the same cell as well as the cell-to-cell variation. The result is shown in Figure 2.7.

Several interesting observations can be extracted from Figure 2.7. The reproducibility is observed to significantly deteriorate for lower T-values, which suggests that the oxygen incorporation becomes more inhomogeneous for increasing degree of photo-oxidation. In addition, the highest T44 and T28 values originate from the central parts of the devices (not obvious from Figure 2.7a), which, however, could be a coincidence considering the limited data. Finally, the result suggests that the cell-to-cell variation is significantly larger than the point-to-point variation on the same cell, which is surprising. No explanation was found for this observation. The magnitude of the relative (reverse) result of the T28 and T44 devices suggested that one of the devices was erroneous somehow. A comparison of the IV degradation characteristics revealed that the T28 IMEC device showed a clear inconsistency and was consequently omitted.

It is obvious from the reproducibility test that a certain degree of noise in the data is expected for especially the low T-value devices due to the fact that an apparent inhomogeneity

is introduced for an increased degree of degradation in the active material. Inhomogeneous degradation patterns were observed in the work described in the second ISOS-3 report.³⁸

2.3.3 Full sun, fluorescent, and dark degradation conditions.

After the TOF-SIMS depth profiling analyses were complete the effects in terms of oxygen incorporation were observed to be very subtle for the devices degraded under a full sun, i.e. the harshest condition compared to fluorescent and dark conditions. The results for the fluorescent and dark conditions were therefore, as expected, even more subtle, to a degree where the point-to-point variation caused by the material inhomogeneity is far greater. The following discussion will thus focus on devices degraded under full sun conditions.

Glass/metal encapsulation – ISE and Holst devices.

The ISE and Holst devices were encapsulated by glass–glass and glass–metal, respectively, and sealed with epoxy. These two devices thus had so-called impermeable encapsulation, which is expected to reflect in the analysis results. Figure 2.8a and b presents the measured oxygen contents as a function of loss of performance and illumination time for the ISE and Holst devices.

Because of the impermeable encapsulation no oxygen incorporation was expected during the degradation experiments, which is consistent with the fact that no detectable trend is observed in Figure 2.8a and b. However, the results are very scattered, which makes it impossible to detect possible subtle trends. The scattered nature of the points in the graphs suggests that the oxygen content to some extent is inhomogeneously distributed in the active material. How is this at all possible? The native oxygen comes exclusively from PCBM. A possible phase separation between P3HT and PCBM seems unlikely and would have to occur on a macroscopic scale, which is unlikely. An alternative explanation could be varying degree of internal oxidation caused by materials already present in the cells, e.g. water residues in the hygroscopic PEDOT:PSS, which then diffuses into the active material and causes oxidation. It is also possible that the excess PSS (always present in PEDOT:PSS) diffuses into the active material and contributes to the oxygen content (PSS contains $-\text{SO}_3\text{H}$ groups). The two suggested explanations could possibly explain why the measured average oxygen contents (~ 4 atom%) are elevated compared to the calculated values of 2.2 atom% (ISE) and 2.4 atom% (Holst). The calculated values are based on the theoretical element compositions and the P3HT:PCBM compositions, which are 1 : 0.7 for the ISE device and 1 : 1 for the Holst device. Since the T100 cells also have ~ 4 atom% oxygen, the phenomena (if the assumption is correct) must have happened in the time window between fabrication and analysis, which corresponded to months.

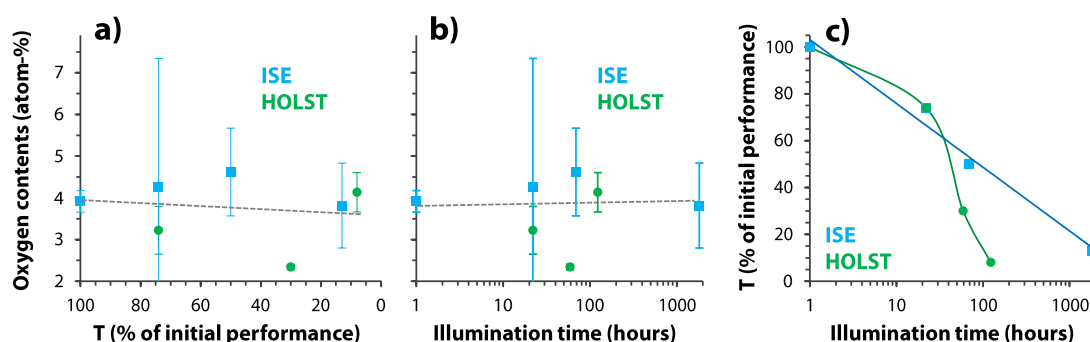


Figure 2.8 (a-b) Oxygen contents in the bulk of the active material extracted from the TOF-SIMS depth profiling analysis of the ISE and Holst devices under full sun degradation conditions. The dashed line is a straight guide line through all points in the graph. Each point is an average of three measurements on different surface locations. The T100 Holst sample was lost. (a) Oxygen contents as a function of loss in performance. (b) Oxygen contents as a function of illumination time (AM 1.5G, 1000 W m^{-2} , $85 \pm 5 \text{ }^\circ\text{C}$, metal halide lamp, KHS Solar Constant 1200). Zero was substituted with one on the logarithmic axis for practical purposes. (c) Loss of performance as a function of illumination time.

Figure 2.8c shows loss of performance as a function of time (logarithmic timescale). The ISE device exhibits an exponential decay (or close to within the accuracy) in performance with time, i.e. straight line behaviour on a logarithmic time-scale (Figure 2.8c). The Holst device has a non-linear behaviour that suddenly drops significantly after 21 hours, resulting in a relatively low lifetime (T8 after 122 hours). For comparison the ISE device reaches T13 after 1822 hours. It was suggested in one of the earlier ISOS-3 reports that the rapid degradation of the Holst device under full sun simulation is caused by a thermal instability at $75 \text{ }^\circ\text{C}$, which correlates well with the fact that under full sun conditions the temperature is $85 \pm 5 \text{ }^\circ\text{C}$ (AM1.5G, 1000 W m^2).³⁷ Furthermore, under dark conditions the temperature corresponds to room temperature, and under fluorescent conditions the temperature is $\sim 45 \text{ }^\circ\text{C}$ (100 W m^2), which further correlates well with the fact that the performance of these particular ISE and Holst devices did not deteriorate to any significant degree during more than 1830 hours of testing. The relative temporal behaviour in performance and the significant difference in lifetimes suggest a significant difference in degradation behaviour, which is not surprising, considering the different architectures (Figure 2.2a and b).

The degradation mechanisms that are in play in the ISE and Holst devices are not related to oxygen incorporation (i.e. photo-oxidation) in the active material, or at least not to any detectable degree. It should be emphasized that the interpretation is complicated by the scatter in the results. If photo-oxidation was not an important factor for the overall degradation, then other factors must have been in play for the ISE and Holst devices such as those suggested in the second and third ISOS-3 reports.^{38,39}

In the second ISOS-3 report it was suggested that for the Holst device elevated temperatures ($85 \pm 5 \text{ }^\circ\text{C}$) caused by the sun simulator and additional heating of the cell due to current collection within the PEDOT:PSS could result in water being released from the highly conductive PEDOT:PSS, which consequently would react with the Al electrode, forming aluminium oxide.³⁸ Furthermore, in the third ISOS-3 report an additional degradation mechanism was proposed for the Holst device. It was suggested that during the degradation experiment Ag reacts/interacts almost spontaneously with PEDOT:PSS, leading to

degradation of the device performance. In addition, it was suggested that Ag possibly also (or alternatively) reacts with P3HT, which induces a slow but steady degradation by migration of Ag into PEDOT:PSS and oxidation of the Ag electrode. It was furthermore proposed that oxidation of the LiF/Al electrode could be a possible degradation mechanism.³⁹ Additional TOF-SIMS analyses from this work (described later in the text) on the Holst and ISE devices did not reveal any chemical changes during the degradation experiments. However, that does not necessarily mean that the degradation phenomena in question are not occurring (discussed later in the chapter).

With respect to the ISE device the conclusion from the second ISOS-3 report states that one possible degradation mechanism is water being homogeneously released from PEDOT:PSS that consequently reacts with Cr-Al-Cr forming chromium and aluminium oxide.³⁸ The third ISOS-3 report has the same conclusion including possible degradation of the Au electrodes.³⁹ Lira-Cantu et al. propose these degradation mechanisms based on the fact that metals like Ag, Cu, and Au are known to interact with the S-atom of polymers like P3HT and PEDOT, and suggests that it is thus possible that the Cr/P3HT:PCBM interface reacts in a similar way as well as the Au/PEDOT:PSS interface.³⁹

In summary, due to the impermeable encapsulation no trends were expected. However, it was not possible to detect possible subtle trends due to significant point-to-point variation for both devices. The erratic nature of the measured oxygen contents suggests that oxygen to some extent is inhomogeneously distributed in the active material, which could be the result of (i) internal oxidation caused by water originating from PEDOT:PSS or (ii) diffusion of excess PSS from PEDOT:PSS. Both of these explanations could possibly explain the elevated (on average) oxygen content compared to the calculated contents. Water release from PEDOT:PSS was suggested in the previous ISOS-3 reports.^{38,39} The relative performance over time suggests significantly different degradation behaviour for the two devices, which is further supported by significantly different lifetimes. Photo-oxidation was most likely not an important factor for the overall device degradation, so other factors must have been in play for the ISE and Holst devices such as for example the degradation mechanisms proposed in the second and third ISOS-3 reports.^{38,39}

UV-filter encapsulation – Risø DTU P and Risø DTU S devices.

The flexible UV filter encapsulation used is to some extent permeable with respect to molecular oxygen and water (i.e. so-called semi-impermeable encapsulation), so some degree of photo-oxidation is expected. Figure 2.9 displays the measured oxygen contents as a function of loss of performance and illumination time for the Risø DTU P and Risø DTU S devices. The only difference between the Risø DTU P and Risø DTU S devices is that the Risø DTU S device uses a modified version of P3HT in the active material, i.e. P3HT-co-P3AcET instead of P3HT (see Figure 2.2f for the molecular structures). The results in Figure 2.9 are the most convincing, manifested in a relatively low degree of scatter.

Oxygen incorporation is observed for both devices for an increase in illumination time or for decreasing performance. The apparent linear relationship suggests that photo-oxidation could be the dominant degradation mechanism for these devices in particular. The increased level of oxygen contents in the Risø DTU S device compared to the Risø DTU P devices is due to fact that P3HT-co-P3AcET contains an ester group (Figure 2.2f). Figure 2.9c

reveals an exponential decay in performance over time, which was also observed for the ISE device. However, this relationship does not necessarily suggest equivalent degradation mechanisms.

The two Risø DTU devices seem to have similar degradation behaviour, but there are notable differences. The slope of the Risø DTU P device in terms of oxygen incorporation is steeper than for the Risø DTU S device, which is manifested in an oxygen increase of 3.0 atom% compared to 1.8 atom% during the degradation experiments. Furthermore, the Risø DTU S device exhibited a slightly better stability as it took more than 200 hours longer to degrade, which is consistent with a lower degree of oxygen incorporation (1.8 compared to 3.0 atom%) during testing. The results indicate that the use of P3HT-co-P3AcET instead of P3HT induces stability. The increased stability could in principle be because P3HT-co-P3AcET has a higher resistance towards molecular oxygen and/or water, but that seems unlikely since the molecular difference is only on the side chain, i.e. not the active part of the molecule. However, the side chain affects the morphology, so it is more likely that P3HT-co-P3AcET induces a morphological stability compared to P3HT.

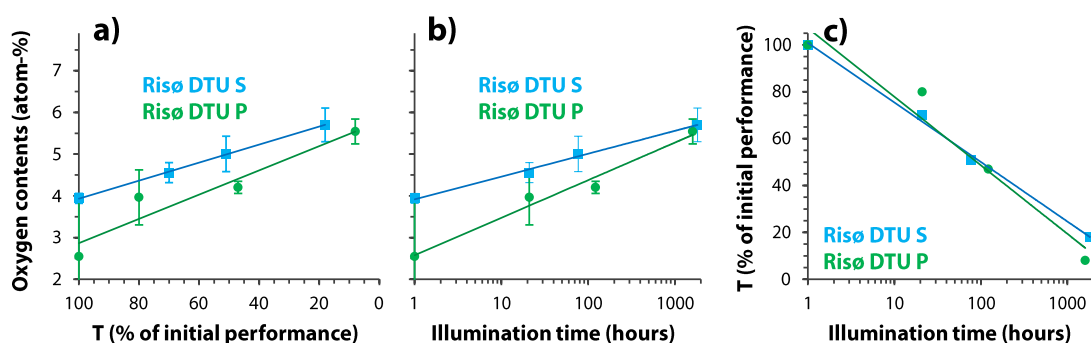


Figure 2.9 (a–b) Oxygen contents in the bulk of the active material extracted from the TOF-SIMS depth profiling analysis of the Risø DTU P and Risø DTU S devices under full sun degradation conditions. Each point is an average of three measurements on different surface locations. (a) Oxygen contents as a function of loss in performance. (b) Oxygen contents as a function of illumination time (AM 1.5G, 1000 W m^{-2} , $85 \pm 5 \text{ }^\circ\text{C}$, metal halide lamp, KHS Solar Constant 1200). Zero was substituted with one on the logarithmic axis for practical purposes. (c) Loss of performance as a function of illumination time.

In the work described in the second ISOS-3 report the population of shunts was observed to increase over time during the degradation experiments, which were suggested to be driven by electro-migration of Ag at places where the electric field was enhanced.³⁸ It was furthermore proposed that oxidation of Ag or ZnO de-doping results in subtle blocking contact features. In addition, during the degradation experiments an increase in the series resistance of the devices was observed that was assigned to morphological changes/degradation, whereas a current decrease was assigned to photo-oxidation of the active material. One notable difference was observed between the Risø DTU P and the Risø DTU S device. The latter exhibited practically no increase in series resistance, which was assigned to a more stable morphology in the active material. In the work described in the third ISOS-3 report it was found that under dark conditions both devices are susceptible to moisture.³⁹ However, consistent with the findings in the present work it was found that the Risø DTU S device has a higher resistance against moisture. The moisture effect was not observed under

full sun or fluorescent testing conditions, i.e. where light and heat are present. This is however inconsistent with the findings in the present work, where oxygen incorporation was detected under full sun conditions only, which suggests that the moisture under dark conditions is involved in degradation mechanisms other than photo-oxidation of the active material. This is consistent with the proposed mechanisms in the third ISOS-3 report that include oxidation of the Ag electrode and migration of Ag provoked by PEDOT due to well-documented Ag-S interactions.³⁹ It was proposed that the higher stability of the Risø DTU S device is caused by an impeding effect of having used P3HT- co-P3AcET in the reaction with Ag, which will inhibit degradation of the electrodes. Finally, it was suggested that it is the degradation of the electrodes that initially is responsible for the overall degradation of performance and not degradation of the active materials.

In summary, because a so-called semi-impermeable encapsulation was used some degree of photo-oxidation was expected for the Risø DTU P and Risø DTU S devices, which was indeed also observed. An apparent linear relationship is observed for oxygen incorporation as a function of loss in performance and an exponential increase of oxygen incorporation as a function of time, suggesting that photo-oxidation could be the dominant degradation mechanism. Using P3HT-co-P3AcET instead of P3HT induces stability, which is most likely morphological stability causing less oxygen to be incorporated resulting in a longer lifetime. Conclusions on the relative stability are supported by the findings in the previous ISOS-3 reports.^{38,39}

No encapsulation – NREL and IMEC devices.

The NREL and IMEC devices have no encapsulation and are thus expected to be significantly photo-oxidised during full sun testing conditions. The device architectures (Figure 2.2d and e) are very similar, the only significant difference is the hole transport layer that consists of PEDOT:PSS (NREL device) or MoO₃ (IMEC device). Any observed differences in degradation behaviour should therefore be directly related to the difference in the hole transport layer used.

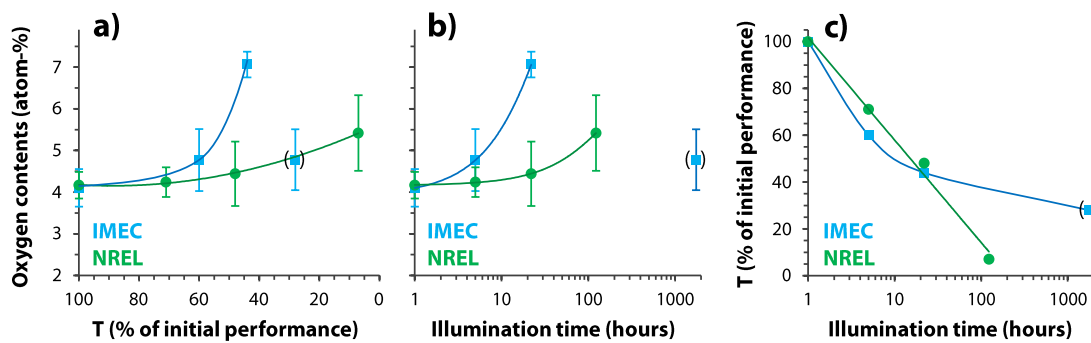


Figure 2.10 (a–b) Oxygen contents in the bulk of the active material extracted from the TOF-SIMS depth profiling analysis of the NREL and IMEC devices under full sun degradation conditions. Each point is an average of three measurements on different surface locations. (a) Oxygen contents as a function of loss in performance. (b) Oxygen contents as a function of illumination time (AM 1.5G, 1000 W m^{-2} , $85 \pm 5 \text{ }^\circ\text{C}$, metal halide lamp, KHS Solar Constant 1200). Zero was substituted with one on the logarithmic axis for practical purposes. (c) Loss of performance as a function of illumination time.

Figure 2.10 displays the measured oxygen contents as a function of loss of performance and illumination time for the NREL and IMEC devices. The oxygen incorporation is observed as expected to increase for a decrease in performance or increase in illumination time (Figure 2.10a and b). The T28 IMEC sample was erroneous, which was documented from a comparison of the IV degradation characteristics that showed a clear inconsistency for the T28 IMEC sample that consequently was omitted.

Considering that these devices had no encapsulation during the full sun illumination it is surprising that such a small amount of oxygen was incorporated. The oxygen content increased by 1.3 atom% for the NREL device and by 3.0 atom% for the IMEC device, the latter being equivalent to the Risø DTU P device that had a so-called semi-impermeable encapsulation. Both devices start out with a slow oxygen incorporation that later on accelerates, which is a completely different situation compared to the Risø DTU devices that exhibited a linear increase.

Figure 2.10c shows an exponential decay in performance over time for the NREL device, which was also observed for the ISE and Risø DTU devices. The NREL device reaches T7 within 122 hours, which is relatively fast and equivalent to the Holst device. However, in terms of performance loss over time the Holst device (Figure 2.10c) has a significantly different behaviour, suggesting that different degradation mechanisms are in play. The performance loss over time for the IMEC device (Figure 2.10c) is interesting since the behaviour is the opposite compared to the Holst device. Initially the performance for the IMEC device drastically decreases but levels out and stabilizes and surprisingly (since no encapsulation is used) ends up having a long lifetime (reaches T28 after 1751 hours). The IMEC device is the fastest to incorporate oxygen in the active material, but has a lifetime comparable with the encapsulated devices (except for the Holst device). It is tempting to assign the significantly different degradation behaviour of the IMEC device compared to the NREL device to the different hole transport layer (MoO_3 instead of PEDOT:PSS). However, another difference is the 200 nm thick Al electrode on the IMEC device compared to only 100 nm on the NREL device, which must be significant in terms of the barrier properties. Having said that, the MoO_3 layer must also have different barrier properties than PEDOT:PSS. MoO_3 is well-known to

induce better stability towards ambient atmosphere compared to PEDOT:PSS.⁴⁵ One thing is clear, the IMEC device has a complex degradation behaviour that calls for complementary analysis results.

The second ISOS-3 report offers a lot of discussion on possible degradation mechanisms in the IMEC device.³⁸ The degradation mechanisms are described as initially being two competing processes involving Ag penetration into MoO₃ and oxidation of Ag. The acting work function in direct vicinity to active layer becomes reduced at the place where Ag penetration is occurring. Later on blocking contact features start to occur. It was suggested that diffusion of molecular oxygen and/or water into the device could result in increasing barriers for charge injection and extraction by formation of Ag₂O or by dedoping at the ZnO layer.

The degradation behaviour of the NREL device is also described in the second ISOS-3 report.³⁸ It was found that a massive degree of shunting developed over large parts of the NREL device mainly at the places where injection remained possible after oxidation of Ag, i.e. around pinholes and at the edges of the metal electrode. It was concluded that electro-migration of Ag resulted in penetration of the PEDOT:PSS layer, which was proposed to be significantly less dense than the MoO₃ layer.⁴⁵

The third ISOS-3 report describes significant problems in characterizing the NREL device using IPCE.³⁸ It was not possible to detect possible trends due to an erratic response from the IPCE analysis. The erratic response was believed to be caused by a reversible uptake of water in the hygroscopic PEDOT:PSS that highly depended on the relative humidity at the time and place of analysis. It was nevertheless possible to detect an interaction between Ag and the sulphur in PEDOT:PSS, which together with the water uptake was taken as an indication that degradation takes place at the electrodes consequently reducing the flux of current throughout the cell over time. The combined degradation phenomenon affected the cells inhomogeneously, which was manifested in a significant variation in the IPCE results within the same cell on the device/substrate and between different cells on the same device/substrate. The erratic response was also observed in the present work for the NREL device (large error bars in Figure 2.10a and b), but that is not necessarily the same phenomenon since the erratic response is also observed for the impermeable encapsulated devices (Figure 2.8a and b) in the present work.

In an in situ IPCE analysis on the NREL device the charge transfer complex was identified and it was possible to monitor the release of molecular oxygen over time. The reversible formation of the charge transfer complex will unavoidably contribute to the erratic response when analysing devices without encapsulation. As described earlier in the text this phenomenon was not significant in the present work. From the in situ IPCE analysis it was furthermore possible to monitor release of oxygen from the ZnO crystalline structure. Finally, The IPCE analyses supported the findings from the second ISOS-3 report that electro-migration of Ag into the PEDOT:PSS layer occurs.³⁸

A lot of the features found in the NREL device were also found in the IMEC device including the charge transfer complex. However, one important observation was a significantly smaller degree of erratic response in the IMEC device that supported the conclusion that PEDOT:PSS was a significant contributor to the erratic response. However, at longer times in the degradation experiment a non-uniform effect of the cell position on the

device/substrate started to emerge. By comparing the IPCE results from an encapsulated IMEC device and one without encapsulation it was concluded that the ambient atmosphere is modifying the properties of MoO_3 and ZnO . When the IPCE analysis was performed in a nitrogen atmosphere on the IMEC and NREL devices, oxygen was observed to release from MoO_3 and ZnO , which is a well-known phenomenon for semiconductor oxides. The oxygen release from MoO_3 and ZnO will change the properties of the materials (including the photovoltaic properties) and provide a source of oxygen that can react with the organic materials such as the active layer (i.e. internal oxidation).

In summary, without encapsulation the NREL and IMEC devices were expected to be significantly photo-oxidated during full sun testing conditions, but surprisingly the level of photo-oxidation in the active material corresponded to the semi-encapsulated devices. A slow oxygen incorporation is observed initially that accelerates at longer times. The IMEC device has a surprisingly long lifetime compared to the NREL device, which is attributed to the only significant difference between the devices, which is the hole transport layer that consisted of PEDOT:PSS (NREL) and MoO_3 (IMEC). MoO_3 is well-known to induce better stability compared to PEDOT:PSS towards ambient atmosphere.⁴⁵

2.3.4 Correlating LBIC and TOF-SIMS data

LBIC visualizes the relative light-beam induced current typically over the entire solar cell area, which is useful for pinpointing where the current is low or zero in the lateral plane of the cell. However, the LBIC analysis contains no in-depth information that would otherwise reveal in which layer or interface the phenomenon causing the loss of current is located. In the second ISOS-3 report LBIC was employed and correlated with related techniques such as photoluminescence imaging (PLI), electroluminescence imaging (ELI), and lock-in thermography (LIT) that each provides useful complementary in-plane information based on different sensing characteristics.³⁸ The strength of this approach lies in the multitude of techniques (i.e. sensing characteristics) used to conclude on specific degradation mechanisms, which compensates for the indirect nature of the information (i.e. lack of in-depth information).

In this work an attempt was made to correlate LBIC data with TOF-SIMS data. TOF-SIMS provides three-dimensional chemical information, i.e. direct chemical information in-plane as well as in-depth. However, this comparison is not necessarily straightforward since the LBIC detected cell degradation could be caused by a missing contact, i.e. not a chemical phenomenon. Furthermore, if the degradation is caused by an interface phenomenon (often the case) the limited depth resolution of the in-depth analysis could be an issue. Diffusion of water and molecular oxygen into the device resulting in photo-oxidation is a degradation mechanism that has been described thoroughly in the past and is the focus of this present work.^{8,23–25,44,46,47} An available glass-encapsulated IMEC device was therefore chosen for the comparison, which should exclude this specific well-described degradation mechanism.

The grey images in Figure 2.11 represent the LBIC images for the IMEC device in question (see Fig. 2e for cell configuration). The device consists of 12 cells of which cells 1–3 were defective and 7 and 8 were apparently interconnected (equivalent LBIC images). After the LBIC analysis the device was transferred to a glove box where the glass encapsulation was removed. An attempt was made to peel off the Al-Ag- MoO_3 stack of the cells in order to

access the MoO₃/P3HT:PCBM interface. It is usually very easy to peel off the upper electrode on pristine cells, but illuminated/heated cells typically either do not peel off or only partly peel off depending on the cell configuration and the degree of illumination/heating. It is thus interesting that the peel off process was almost complete for the defective cells (1-3). The partially delaminated cells (4-12) were then transferred in an inert atmosphere to the TOF-SIMS instrument. A TOF-SIMS imaging analysis was performed on cells 4-12.

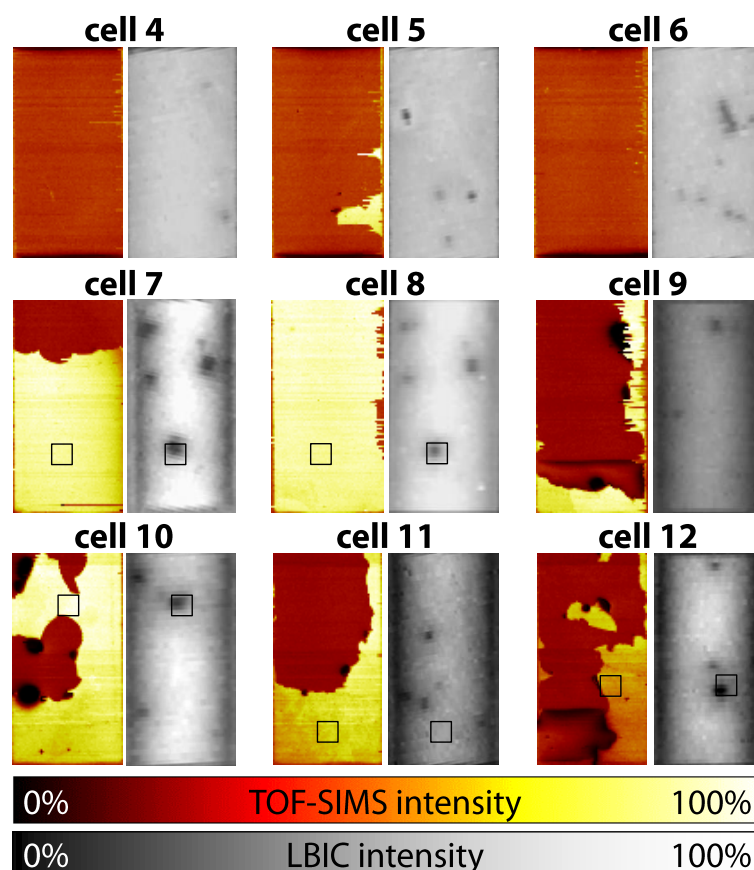


Figure 2.11 (a) Analytical results of cells 4-12 (1-3 were defective) from an encapsulated IMEC device. The grayscale images are LBIC images and the color images are the corresponding TOF-SIMS total ion images (5.2 x 2.7 mm²). The squares indicate areas (500 x 500 nm²) that were analyzed with TOF-SIMS depth profiling. The Al-Ag-MoO₃ layers were partly removed prior to TOF-SIMS analysis (the yellow/ white areas correspond to the Al surface).

The coloured images in Figure 2.11 represent the total ion images of the cell surfaces. The high intensity areas (yellow/ white) correspond to the Al surface and the dark red areas correspond to the exposed P3HT:PCBM surface (i.e. MoO₃/ P3HT:PCBM interface). The total ion signal is a convenient way to screen for chemical contrast on the surface. As is evident from Figure 2.11 there are no correlations between the LBIC images and the TOF-SIMS total ion images. The TOF-SIMS images are actually extremely homogeneous. The dark spots are instrument effects caused by flakes of upward-bended Al-Ag-MoO₃ causing loss of signal. It can now be concluded that localized loss of current in the cells (black spots in the LBIC images) is not related to a chemical phenomenon at the MoO₃/P3HT:PCBM interface. However, it is

not possible to conclude anything about a possible missing contact between MoO₃ and P3HT:PCBM from the TOF-SIMS ion images in Figure 2.11.

The next step was to study the remaining layers and inter- faces in the cells. TOF-SIMS depth profiling was performed on surface locations indicated by the squares in Figure 2.11. In a TOF-SIMS depth profiling analysis ion images are acquired as a function of depth. Ion images from 100 of the most abundant mass spectral markers were monitored as a function of depth in order to find a possible correlation between the LBIC image and the TOF-SIMS ion images. The depth profiling analyses were started at surface locations that partly covered (to get chemical contrast) the dark spots in the corresponding LBIC images with one exception (cell 11, reference location). All ion images were monitored through all layers and interfaces, i.e. from the Al surface to the bulk of the ITO. Unfortunately all ion images were extremely homogenous in all depths, which means that the degradation mechanism in question was not detectable by TOF-SIMS depth profiling.

2.3.5 Correlating loss of performance with various TOF-SIMS information

The primary objective of the TOF-SIMS investigation of the ISOS-devices was to correlate the photo-oxidation of the active layer with loss of cell performance. However, as documented in the previous ISOS-3 reports, photo-oxidation of the active material is not the only degradation mechanism in play during operation of the organic solar cells.^{38,39} The different cell architectures enable a variety of degradation mechanisms to contribute to the overall degradation of the cell. When the TOF-SIMS depth profiling analyses were performed relevant information was extracted from the raw data so that the photo-oxidation could be adequately described. The raw data consist of mass spectral data, which contain an overwhelming amount of information. This is one of the reasons that the TOF-SIMS technique is so attractive, but it is also the reason why it is often very complicated to interpret the results. It is tremendously less complicated if one knows what to look for. However, it should be emphasized that it is not possible to detect all degradation mechanisms. The raw data consist of mass spectral information, and mass spectral markers are typically chosen to represent a species that somehow is involved in the degradation mechanism or to support conclusions made on other mass spectral markers. The problem is that not all mass spectral markers are unique. One good example of a situation where it was not possible to extract direct information is the proposed mechanism involving migration of water from the PEDOT:PSS. Water produces mass spectral markers that are the same for all species containing oxygen, i.e. no unique markers. It is possible to detect the resulting oxidation, i.e. indirect information that requires assumption to be made. It is not impossible to study migration of water out of PEDOT:PSS, however, that would require a specially designed experiment where isotopically labelled water is used (H₂¹⁸O), which produces unique mass spectral markers. It has previously been shown that H₂¹⁸O is easily tracked in OPV devices from its reaction/degradation products.⁴⁶

The secondary goal of this study was to carefully study the raw data in detail in order to ascertain whether trends related to loss of performance could be extracted and possibly related to specific degradation mechanisms such as those suggested in the previous ISOS-3 reports.^{38,39} This was partially achieved and the result is presented and discussed in the following.

The IMEC device.

The IMEC device is by far the most complex system to analyse in terms of degradation mechanisms. The cell configuration is Al-Ag-MoO₃-P3HT:PCBM-ZnO-ITO and mass spectral information is obtained throughout the entire device starting from the outer aluminium surface and ending somewhere in the bulk of the ITO layer. Due to the poor depth resolution that gets worse for longer sputter times it is difficult to extract certain types of information from deeper layers, e.g. interface phenomena occurring at P3HT:PCBM/ZnO and ZnO/ITO that produces weak possible generic mass spectral markers. Since the active layer was thoroughly investigated in the primary work described herein, it made sense to focus on the upper layers (Al-Ag-MoO₃).

Upon close inspection of the raw data from the upper layers one surprising observation was made, which is presented in Figure 2.12. A layer of Al₂O₃ is present at the Ag/MoO₃ interface. Figure 2.12 shows a narrow sputter time window around that interface. The dashed line representing Al₂O₃ is located exactly between the Ag and MoO₃ layers and is presumably very thin. The reason that the MoO₃ layer (10 nm) appears so thick compared to the Ag layer (100 nm) is the poor depth resolution and a large detector response from MoO₃. This is a more plausible explanation rather than possible differences in sputter rates. The profiles in Figure 2.12 are extracted from a T100 device, so the phenomenon must have occurred during fabrication or in the time between fabrication and analysis. The Al₂O₃ at the Ag/MoO₃ interface could be the result of aluminium migration from the Al electrode through the Ag layer and subsequent oxidation somehow. Alternatively, it could be Al₂O₃ migration from MoO₃ that (like ZnO) contains trace amounts of various metal oxides. Al₂O₃ is not observed at the MoO₃/P3HT:PCBM interface, so if the latter explanation is correct the phenomenon must be catalyzed by the adjacent Ag layer.

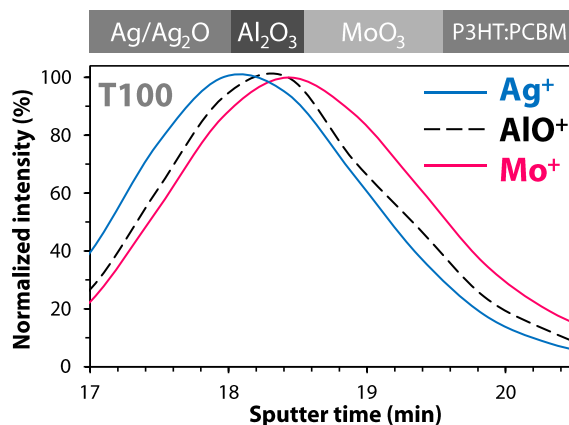


Figure 2.12 TOF-SIMS depth profiles for a T100 IMEC cell that was exposed to full sun conditions without encapsulation. The sputter time window is chosen to emphasize the existence of a thin Al₂O₃ layer at the Ag/MoO₃ interface, which is present in all the IMEC devices. The indicated ions are mass spectral markers chosen to represent the individual layers. The schematic on top of the plot illustrates the part of the layer stack the data were extracted from.

Figure 2.13 displays the profiles for the mass spectral marker AlO⁻ representing Al₂O₃ over a sputter time window covering Al-Ag-MoO₃. As is evident Figure 2.13 Al₂O₃ is present in the T100 cell through the entire Al electrode and is accumulated at the air/Al interface and at the

Al/Ag interface (and in the unintentional Al_2O_3 layer). The intensity of AlO^- clearly increases for decreasing cell performance consistent with Al_2O_3 formation as a result of molecular oxygen and water diffusing into the cell (i.e. no encapsulation) that consequently reacts with Al. This is one of the proposed degradation mechanisms presented in the second and third ISOS-3 reports.^{38,39}

It should be noted that one other phenomenon can affect the intensity of a mass spectral marker. If the physical properties of the material change it could affect the detector response, e.g. crystallinity, electric conductivity, etc. However, these possible effects are small compared to the intense signal boost you get for an increase in Al_2O_3 concentration.

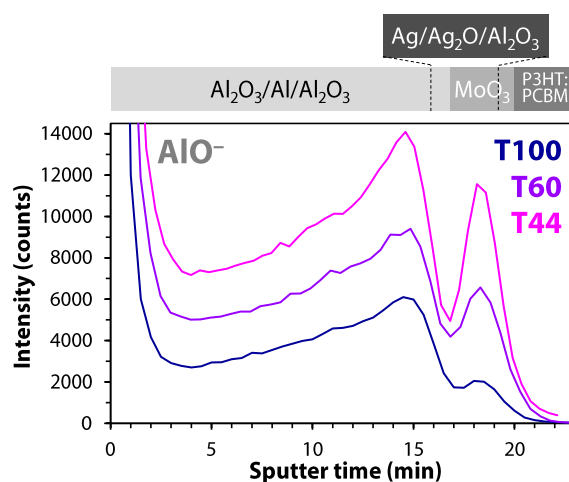


Figure 2.13 TOF-SIMS depth profiles for IMEC cells exposed to full sun conditions without encapsulation. The profiles show a massive build-up of aluminum oxide in the Al–Ag– MoO_3 region of the cells for decreasing cell performance. AlO^- is the mass spectral marker chosen to represent aluminum oxide. The schematic on top of the plot illustrates the part of the layer stack the data were extracted from.

The clear correlation between accumulation of Al_2O_3 and loss of cell performance suggests that this phenomenon is at least partly responsible for the degradation of the photovoltaic response. Unfortunately it is not possible to quantify how much this degradation mechanism is contributing to the over- all degradation of the photovoltaic response. Furthermore, it is not possible to determine how much the Al_2O_3 at the Ag/ MoO_3 interface contributes compared to the Al_2O_3 at the Al/Ag interface, but it is possible to conclude that Al_2O_3 accumulation at the Ag/ MoO_3 interface is faster than at the Al/Ag interface.

The comparison between LBIC images and TOF-SIMS data involved an encapsulated IMEC device. The availability of an encapsulated IMEC device makes it obvious to compare the TOF-SIMS depth profiling data with and without encapsulation. Figure 2.14 sums the results of that comparison. The T44 device without encapsulation was illuminated in ambient air for 21 hours, and the T50 device with encapsulation (glass) was illuminated for 2600 hours, which demonstrates the strength of glass encapsulation.

The first interesting observation is the lack of Al_2O_3 at the Al/Ag interface for the device with encapsulation. Half way through the Al electrode the AlO^- profiles are practically the same, but then the concentration of Al_2O_3 decreases to zero. Unfortunately it was not possible to obtain a T100 device with encapsulation, which would have been an interesting

comparison. It appears that the encapsulated device was fabricated with no Al_2O_3 at all at the Al/Ag interface, which is impressive from a technical point of view.

The second interesting observation is the intensity of the Al_2O_3 at the Ag/ MoO_3 interface, which is significantly elevated for the encapsulated device compared to the device without encapsulation. This is somewhat difficult to speculate on considering the lack of ambient air for the encapsulated device. It is still possible that Al_2O_3 originates from migration from the MoO_3 layer (as an impurity). A more farfetched explanation could be that Al_2O_3 migrates from the Al/Ag interface, which could explain why no Al_2O_3 is present at the Al/Ag interface (i.e. depletion). Since the encapsulated device has only reached T50 after 2600 hours it would seem that the presence of Al_2O_3 at the Ag/ MoO_3 interface is not deteriorating the photovoltaic performance, which is surprising. The Al^{2+} profile (T100 device without encapsulation) was included in Figure 2.14 to define the exact sputter time window for the Al electrode. The shape of the Al^{2+} profile did not change as a function of loss of cell performance.

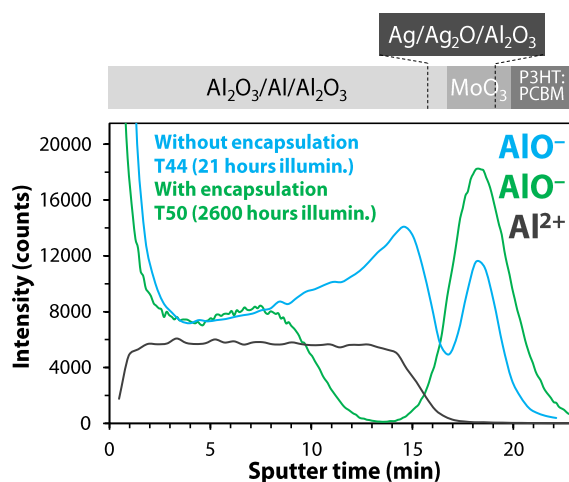


Figure 2.14 TOF-SIMS depth profiles for IMEC cells exposed to full sun conditions with and without encapsulation (glass). The device without encapsulation was illuminated for 21 hours (T44), and the encapsulated device was illuminated for 2600 hours (T50). The profiles show the relative build-up of aluminium oxide in the Al-Ag- MoO_3 region of the cells. AlO^- is the mass spectral marker chosen to represent aluminium oxide. The Al^{2+} profile (T100 device without encapsulation) was included to define the exact sputter time window for the Al electrode. Different sputter properties were used for the encapsulated device, so the sputter time was corrected such that the AlO^- peak at the Ag/ MoO_3 interface was aligned. The schematic on top of the plot illustrates the part of the layer stack the data were extracted from.

The encapsulated IMEC device revealed another difference when compared to the corresponding device without encapsulation (Figure 2.15). The mass spectral marker OH^- is typically formed (during the ionization part of the analysis) in metal oxides with limited intensity compared to O^- . However, on metal oxide surfaces exposed to an atmosphere the M-OH groups will typically be abundant resulting in a very intense OH^- signal intensity. The mass spectral marker OH^- is detected at the Ag/ MoO_3 interface (Figure 2.15) for both devices, which is not as interesting as the fact that it is also detected at the Al_2O_3 /Ag interface, but only for the encapsulated device. The OH^- profile for the encapsulated device appears to be wider than the corresponding profiles for the device without encapsulation, which could be due to the fact that other sputter properties were used for the encapsulated device (the sputter time axis was corrected to allow comparison). It is difficult to speculate on what type of chemistry

would explain the additional OH^- signal (arrow in Figure 2.15) at the $\text{Al}_2\text{O}_3/\text{Ag}$ interface. Since the phenomenon is observed on the stable device (T50 after 2600 hours) it is unlikely that it is related to degradation of the photovoltaic performance.

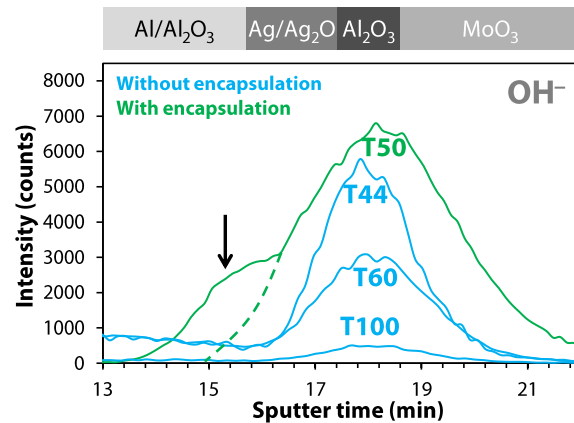


Figure 2.15 TOF-SIMS depth profiles for IMEC cells exposed to full sun conditions with (green) and without (blue) encapsulation (glass). The device without encapsulation was illuminated for 21 hours (T44), and the encapsulated device was illuminated for 2600 hours (T50). The intensity of the mass spectral marker OH^- increases (like AlO^- and O^-) in the unintentional aluminum oxide layer for decreasing cell performance. An additional OH^- peak indicated by the arrow is observed for the device without encapsulation at the $\text{Al}_2\text{O}_3/\text{Ag}$ interface. The dashed line is drawn to clarify that the additional OH^- profile peak (arrow) for the encapsulated device overlaps with the other OH^- profile peak and takes the form of a “shoulder”. Different sputter properties were used for the encapsulated device, so the sputter time was corrected such that the AlO^- peak at the Ag/MoO_3 interface was aligned. The schematic on top of the plot illustrates the part of the layer stack the data were extracted from.

In the second and third ISOS-3 reports silver migration and silver oxidation were suggested to be involved in degradation mechanisms.^{38,39} The mass spectral marker AgO^- representing silver oxide was detected on all the IMEC devices at the $\text{Ag}/\text{Al}_2\text{O}_3$ interface (Figure 2.16). As is evident from Figure 2.16 the AgO^- intensity is observed to increase for decreasing cell performance. However, it should be noted that the intensity is extremely weak (barely detectable). The apparent trace amount of Ag_2O is observed starting from all surface locations. It was not possible to detect silver migration. However, it should be emphasized that the TOF-SIMS depth profiling analyses are performed on random surface locations, i.e. not necessarily at lateral surface positions where degradation is more pronounced as described in the second ISOS-3 report where various imaging techniques were employed to visualize the lateral degradation patterns.³⁸

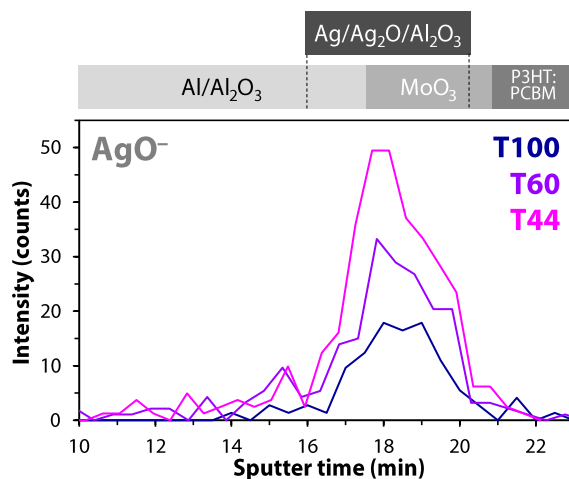


Figure 2.16 TOF-SIMS depth profiles for IMEC cells exposed to full sun conditions. The profiles show a very subtle increase in the intensity of the mass spectral marker AgO^- for decreasing cell performance, which most likely corresponds to a small degree of silver oxide formation. The schematic on top of the plot illustrates the part of the layer stack the data were extracted from.

The NREL device.

The NREL device has the architecture Al–Ag–PEDOT:PSS–P3HT:PCBM–ZnO–ITO. As mentioned earlier in the text, the device differs only by the hole transport layer compared to the IMEC device, i.e. PEDOT:PSS instead of MoO_3 . At first one would thus expect the degradation mechanisms to be similar. It turns out that besides similarities there are also surprising differences.

The first observation is the same as that for the IMEC device (with no encapsulation), that Al_2O_3 is observed to accumulate for decreasing cell performance (not shown), which was expected based on the fact that no encapsulation was employed. Formation of Al_2O_3 is consistent with conclusions drawn in the previous ISOS-3 reports.^{38,39} The second observation is the lack of the additional (unintentional) Al_2O_3 layer (see Figure 2.12), which suggests that its existence in the IMEC device is related to MoO_3 one way or the other.

Figure 2.17 reveals another interesting phenomenon not observed in the IMEC device. The profiles representing the Ag, Al_2O_3 , and PEDOT:PSS layers are observed to systematically widen for decreasing cell performance. In addition, Al_2O_3 and Ag have exactly the same sputter times (not shown), so it looks like the Al_2O_3 from the Al/Ag interface is dissolving in the Ag layer that consequently thickens the Ag layer (Figure 2.17a). When Al_2O_3 expands into the Ag layer the result will be a widening of the AlO^- profile as shown in Figure 2.17b.

The Al_2^+ T100 profile shown Figure 2.17d is consistent with the IMEC device, i.e. the expected depth profile for a normal Al electrode. However, unlike the IMEC device, this profile changes drastically for decreasing cell performance. The Al_2^+ signal is systematically lost at the Al/Ag interface for decreasing cell performance. This supports the proposed phenomenon of Al_2O_3 and apparently also Al dissolving in the Ag layer. This is not observed for the IMEC device,

suggesting that PEDOT:PSS is involved in the phenomenon, possibly from migration of water or acid from PEDOT:PSS to the Al/Ag interface.

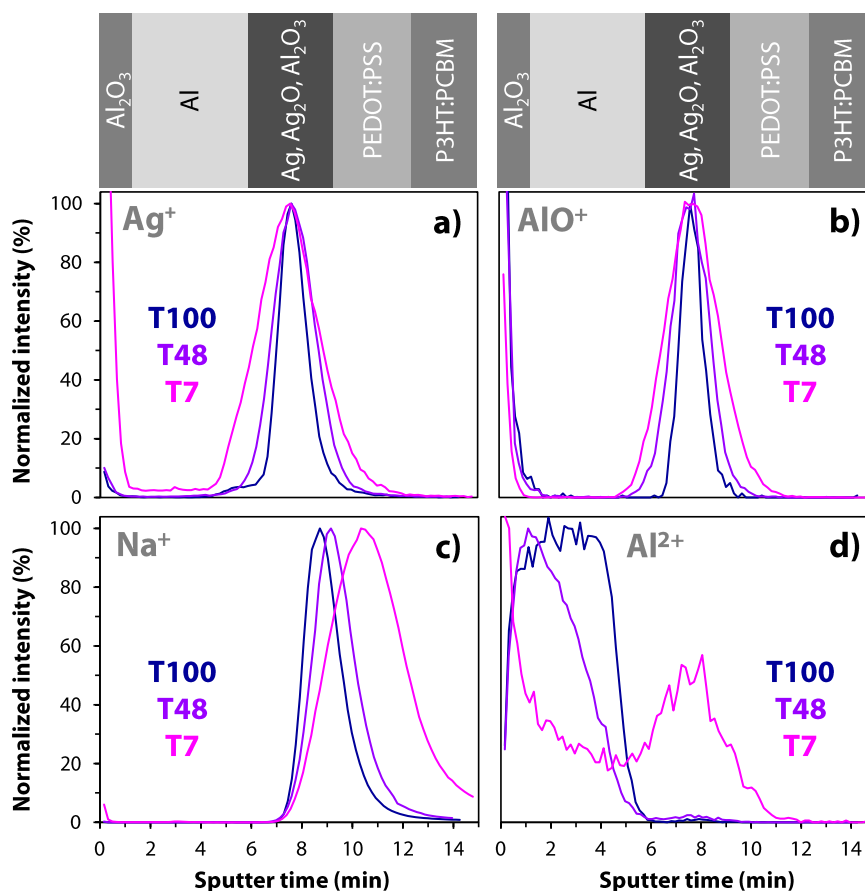


Figure 2.17 (a)–(d) TOF-SIMS depth profiles for NREL cells exposed to full sun conditions. (a)–(c) The profiles of the mass spectral markers Ag^+ , AlO^+ , Na^+ exhibit a widening in the sputter time window for decreasing cell performance. (b) The AlO^+ intensities increase (not shown) for decreasing cell performance, i.e. accumulation of aluminium oxide. (c) Na^+ is a native component in PEDOT:PSS, and is thus used as a marker for PEDOT:PSS. (d) Al^{2+} defines the non-oxide form of the aluminium electrode, which is observed to become oxidised and to dissolve in the silver layer for decreasing cell performance. The schematics on top of the plots illustrate the part of the layer stack the data were extracted from.

Figure 2.17c displays the Na^+ profiles that also widen for decreasing cell performance. Na^+ is a native component in PEDOT:PSS and is thus representative for PEDOT:PSS. The same trend is observed for the SO_x^- profiles, which are also representative of PEDOT:PSS (less pronounced trend though, not shown). The Na^+ profile is not just widening but also shifting to higher sputter times, suggesting that PEDOT:PSS is partly dissolving in P3HT:PCBM, a phenomenon that was not observed for MoO_3 in the IMEC device.

The Risø DTU devices.

The layer composition of the Risø DTU P device is Ag–PEDOT:PSS–P3HT:PCBM–ZnO–ITO and the Risø DTU S device differs only by using P3HT-co- P3AcET instead of P3HT. Due to the thick plastic encapsulation it was necessary to delaminate the device prior to analysis. The device delaminated at the PEDOT:PSS/P3HT:PCBM interface, which left the device without

the upper electrode. It was not possible to analyse the peeled off encapsulation-Ag-PEDOT:PSS layer stack because of the thickness of the Ag layer (5 μm) and the PEDOT:PSS layer (10 μm), which is too thick to be analysed with the sputter properties in question. That leaves the P3HT:PCBM(P3HT-co-P3AcET)-ZnO-ITO layer stack to be analysed. No trends were observed for any of the mass spectral markers with respect to cell performance for the Risø DTU P device. However, for the Risø DTU S device one trend was observed, which is shown in Figure 2.18 for a sputter time window corresponding to the P3HT-co-P3AcET-ZnO layer stack.

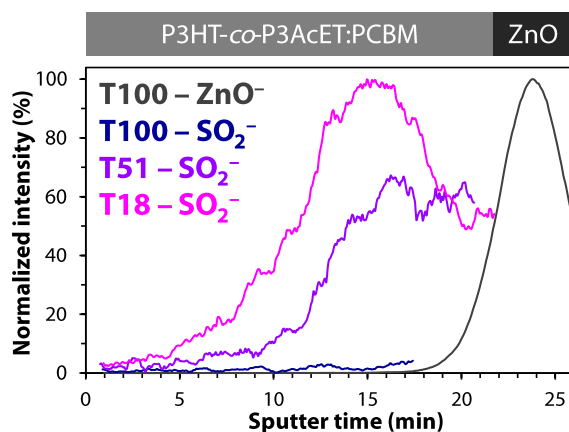


Figure 2.18 TOF-SIMS depth profiles for Risø DTU S cells exposed to full sun conditions. SO_2^- is a mass spectral marker for an unknown R- SO_x species that is increasing in intensity and evolving at the P3HT-co-P3AcET:PCBM/ZnO interface. ZnO^- is a mass spectral marker for ZnO and is included to define the ZnO layer for clarity. The schematic on top of the plot illustrates the part of the layer stack the data were extracted from.

The mass spectral marker SO_2^- for the Risø DTU S device is observed to increase systematically with decreasing cell performance. The shape of the profiles suggests that the phenomenon originates from within the ZnO layer. The species responsible for the mass spectral marker SO_2^- must be a R- SO_x species (R = H, organic, or metal). The ZnO layer contains trace amounts of a variety of inorganic and organic impurities.

However, it makes little sense that migration of that species into the active material should be affected by whether P3HT-co-P3AcET or P3HT is used in the active material. A less likely explanation could be oxidation of the thiophene sulphur by something very reactive originating from within the ZnO layer (e.g. O_2H^-), but it makes little sense that P3HT is not equally affected by it. The Risø DTU S device turned out to be more stable than Risø DTU P, i.e. it took 200 hours longer to degrade. It is difficult to conclude on how much the phenomenon described in Figure 2.18 affects the cell performance, or whether it affects it at all.

The Holst and ISE devices.

The cell configuration of the Holst cell is Al-LiF-P3HT:PCBM-PEDOT:PSS-SiN, Ag and the ISE cell configuration is Au-PEDOT:PSS-P3HT:PCBM-Cr-Al-Cr. The ISE device was unavoidably delaminated leaving the P3HT:PCBM-Cr-Al-Cr part of the layer stack for analysis. The raw depth profiling data were carefully investigated for both devices in order to

extract possible trends between mass spectral marker intensities and cell performance. No trends were found in any of the layers and interfaces.

As stated earlier in the text no oxygen incorporation could be detected in the active materials, and no other chemical changes are observed in the devices for decreasing cell performance. No electrode oxidation was observed, no layer thickening was observed, and no interlayer mixing was observed. Apparently it is not possible to detect the cause of degradation, suggesting that the phenomenon or phenomena are not chemical in nature (e.g. delamination at interfaces) or simply too subtle to detect using this analytical technique.

2.4 Conclusions

The work presented in this article is part of a large inter-laboratory study that resulted from the 3rd International Summit on Organic Photovoltaic Stability (ISOS-3). The collaboration involved six laboratories that produced seven distinct sets of OPV devices that were degraded under identical conditions in accordance with the ISOS protocols. The degradation experiments lasted 1830 hours and involved more than 300 cells on more than 100 devices. The devices were analysed and characterized at different points of their lifetime by a large number of non-destructive and destructive techniques in order to describe specific degradation mechanisms responsible for the deterioration of the photovoltaic activity that lead to insufficient lifetimes.

The present work is a systematic study of the ISOS-3 devices using TOF-SIMS in order to identify specific degradation mechanisms responsible for the deterioration of the photovoltaic activity. It was only possible to detect degradation in cells that were exposed to the harshest conditions (AM1.5G, 1000 W m⁻², 85 ± 5 °C). Two devices had impermeable encapsulations and it was not even possible under the harshest conditions to detect any form of chemical degradation as a function of cell performance, which suggests that degradation is not chemical in nature or too subtle to detect using the technique in question.

Photo-oxidation of the active layer (P3HT:PCBM) used in six of the seven devices was quantitatively monitored as a function of cell performance by correlating surface obtained XPS data with bulk obtained TOF-SIMS data. This calibration was complicated by various factors such as being sensitive towards experimental conditions, and the occurrence of a charge transfer complex between molecular oxygen and P3HT. No photo-oxidation could be detected in the two devices with impermeable encapsulations consistent with expectations. Two devices had so-called semi-impermeable encapsulations and both exhibited an apparent linear relationship in oxygen incorporation for decreasing cell performance, which suggests that photo-oxidation of the active material could be the dominant degradation mechanism. Using P3HT-co-P3AcET instead of P3HT in the devices with semi-permeable encapsulation induces stability, which is believed to be morphological stability causing less oxygen to be incorporated resulting in a longer lifetime. Two devices had no encapsulation and exhibited, at first, slow photo-oxidation of the active material that accelerated later in the degradation tests. Photo-oxidation behaviour with respect to the active layer was different for the two types of encapsulation, but the degree of photo-oxidation was surprisingly on the same order of magnitude.

Attempts were made to correlate degradation patterns in LBIC images and TOF-SIMS total ion images for an encapsulated IMEC device with the architecture Al-Ag-MoO₃-P3HT:PCBM-ZnO-ITO. It was concluded that localized loss of current in the cells as described by the LBIC images is not related to a chemical phenomenon at the MoO₃/P3HT:PCBM interface. No correlations could be found in any of the other layers and interfaces, which suggests that the degradation mechanism in question is not detectable by the technique used.

The raw depth profiling data were screened in order to extract possible correlations between the mass spectral data and loss in cell performance that could assist in identifying specific degradation mechanisms and possibly support conclusions drawn in the first three ISOS-3 reports. Several trends were discovered that could be contributing to the overall degradation of the photovoltaic performance.

The trends for the IMEC device were observed to be:

- Increased migration of Al₂O₃ from either the Al/Ag interface or from the bulk MoO₃ layer to the Ag/MoO₃ interface for decreasing cell performance.
- The additional Al₂O₃ layer and the Al₂O₃ from the Al interfaces accumulate for increasing illumination time and thus for decreasing cell performance.
- When the IMEC device is encapsulated no Al₂O₃ is found at the Al/Ag interface, but the additional Al₂O₃ layer is still present.
- Trace amounts of Al₂O were detected that exhibited a very weak increase for decreasing cell performance.

The trends for the NREL device were found to be:

- Accumulation of Al₂O₃ for decreasing cell performance.
- Dissolution of Al and Al₂O₃ in the Ag electrode for decreasing cell performance possibly catalyzed by water or acid from PEDOT:PSS.
- Thickening of the Ag electrode for decreasing cell performance due to the addition of Al₂O₃.
- Partly dissolution of PEDOT:PSS in the active layer (P3HT:PCBM) for decreasing cell performance.

One trend was found for the Risø DTU S device:

- The concentration of an unknown R-SO_x species migrating out from within the ZnO layer increases for decreasing cell performance, but it is uncertain whether it contributes to the overall degradation.

The present study and the previous studies in this inter-laboratory collaboration clearly demonstrate the strength of combining complementary analysis techniques on systematically prepared OPV devices in order to gain improved knowledge of the dominant degradation mechanisms responsible for loss of photovoltaic response. The extensive investigation on OPV stability presented in the series of ISOS-3 reports has significantly improved the understanding of degradation behaviour in OPV devices, which is a vital step towards large scale application of organic solar cells.

2.5 Acknowledgements

This work has been supported by the Danish Strategic Research Council (2104-07-0022), EUDP (j.no. 64009-0050, 64009-0051) and the Danish National Research Foundation. Partial financial support was also received from the European Commission as part of the Framework 7 ICT 2009 collaborative project HIFLEX (grant no. 248678), partial financial support from the EUIndian framework of the "Largecells" project that received funding from the European Commission's Seventh Framework Programme (FP7/2007-2013. grant no. 261936), partial financial support was also received from the European Commission as part of the Framework 7 ICT 2009 collaborative project ROTROT (grant no. 288565) and from PVERA-NET (project acronym POLYSTAR). are due to CONACYT (Mexico) for the PhD scholarship awarded to G. T.-E; to the Spanish Ministry of Science and Innovation, MICINN-FEDER project ENE2008-04373; to the Consolider NANOSELECT project CSD2007-00041; to the Xarxa de Referencia en Materials Avancats per a l'Energia, XaRMAE of the Catalonia Government (Spain). RR and HH are grateful for financial support from the Thuringian Ministry of Culture and the German Federal Ministry of Education and Research in the frameworks of FIPV II and PPP (contract number 13N9843), respectively. DMT acknowledges generous support from the Inger and Jens Bruun Foundation through The American-Scandinavian Foundation.

Chapter 3

Fast and efficient acquisition of organic material degradation data using concentrated light ³

³ This chapter is based on unpublished data, a manuscript is being prepared.

3.1 Introduction

In contrast to Chapter 2 that focused on degradation of functioning OPV devices as a whole, this chapter will only describe degradation of the active layer, the polymer and the polymer blend P3HT and P3HT:PCBM. As previously mentioned, degradation of OPVs and the active layer therein is not exactly straight forward, there are many different degradation processes simultaneously at play and the effect these have on the active layer depends of course on the environment that it resides in. There have been several studies published that focus on degradation P3HT and P3HT blends.^{23,48-55} Photochemical stability is usually studied by monitoring the UV/Vis photo bleaching as a function of degradation time. The photochemical stability of the active layer is known to be dependent on different parameter, e.g. atmosphere composition, humidity, temperature, light intensity, UV content, polymer molecular weight, film thickness etc.⁵⁵ The study of active layer degradation as a function of exposed light is a time consuming process that usually require illumination times in the excess of several hours, and when the monitored property cannot be measured in situ, the sample has to be moved back and forth between the degradation setup and the analysis chamber, this while keeping all of the aforementioned external parameters constant. This is further complicated if the analysis technique used is destructive, making the sample less ideal for continuous degradation. This can of course be solved by using several samples at the starting point and then extracting them intermittently as a function of time with subsequent transfer to the analysis chamber. This is not an ideal situation as new external parameters can affect the samples e.g. from the sample preparations method, as the preparation of absolutely uniform samples can be challenging.

In this study the degradation of P3HT and P3HT:PCBM was monitored chemically by TOF-SIMS (surface analysis and depth profiling) and XPS analysis as a function of exposed light dose. As TOF-SIMS depth profiling is a destructive technique the multiple samples conundrum was solved by using a set up that utilised concentrated light and a moving sample stage, which meant that only one sample was necessary for each film studied. The concentrated light meant that the illumination time could be accelerated, and the automated movement of the stage meant that a gradient of light dose could be created across the film. Effectively this created a degradation data bank on one single sample substrate.

As mentioned in the Chapter 1 the TOF-SIMS data interpretation can be very challenging due to the enormous amount of mass spectral peaks generated, which is especially problematic when one does not know exactly what one is looking for thus generating the “looking for a needle in the haystack situation”. Even though there are suggested mechanism for the degradation of P3HT published.⁴⁸ It is difficult to predict which ions will be detected in TOF-SIMS and which ions carry the relevant information. In an attempt to simplify the mass spectral data analysis MVA was utilised.

3.2 Experimental

3.2.1 Sample preparation

Regio-regular P3HT was purchased from Rieke Metals and PCBM was purchased from Solenne. Chlorobenzene solutions (20 mg mL^{-1}) of P3HT and a 1:1 blend of P3HT:PCBM were spin-coated (700 rpm) onto $2.5 \times 5.0 \text{ cm}^2$ microscopy glass slides obtained from Menzel. Attempts to spin coat PCBM was unsuccessful. The two samples (P3HT and P3HT:PCBM) were used without annealing, see Figure 3.1 for further details.

3.2.2 Accelerated degradation – concentrated light

For the accelerated ageing experiments a setup was used that utilizes an Osram 1200 W metal halide arc lamp powered by a Schiederwerk 12-12 AC SL power supply providing an approximate AM1.5G spectrum with an intensity of 1000 W m^{-2} . The light was concentrated by a rhodium coated elliptical reflector made by Optiforms (focal length 509 mm, diameter 260 mm, height 206 mm) that focuses the light from the light bulb into at the second focal point of the ellipse. At this focal point a fused silica kaleidoscope ($10 \times 10 \times 75 \text{ mm}^3$) obtained from Quartz Plus is positioned, homogenizing the spatial light distribution of the outgoing light, providing an $1 \times 1 \text{ cm}^2$ illuminated area. A shielding plate was used to avoid direct light from the bulb to reach the kaleidoscope and induce poor light distribution. Light intensity is controllable by a custom-made, thermally resistant automated two blade iris, optimized to provide a high spatial conservation of the light intensity distribution on the illumination area at different light intensities. The light intensity was calibrated with a S314C thermopile from Thorlabs. The two samples were placed under the square light spot and moved such that the light spot is scanned along the sample surfaces with a systematically decreased velocity such that a gradient of light dose is created along the sample surfaces. The setup is further documented in references.^{55,56}

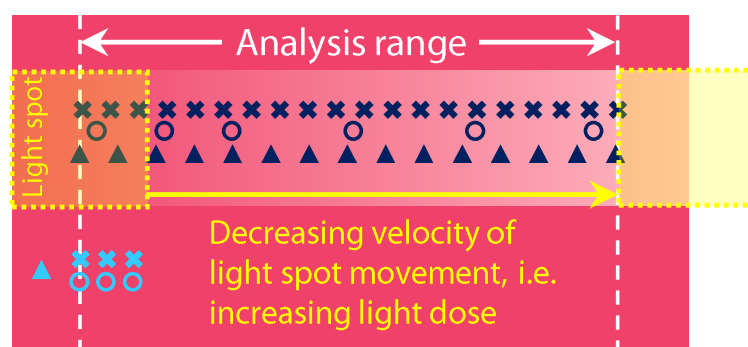


Figure 3.1 Schematic of a spin-coated (P3HT or P3HT:PCBM) $2.5 \times 5.0 \text{ cm}^2$ glass slide showing from where to where (yellow arrow) the samples were exposed to concentrated light (100 suns , 10 W cm^{-2}) in ambient air with a $1 \times 1 \text{ cm}^2$ light spot (yellow open squares). The analysed range (between the dashed lines) represents the well-defined illuminated surface area. The symbols show on which surface locations the samples P3HT and P3HT:PCBM were analysed on the exposed (dark blue/black) and non-exposed (light blue) areas. Cross: XPS analysis, Circle: TOF-SIMS analysis, and Triangle: AFM profilometry analysis.

3.2.3 Analytical Techniques

Prior to the XPS and TOF-SIMS analyses the samples were stored in the vacuum chamber of the instrument in question for approximately 24 hours. This was done to ensure removal of the charge transfer complex that is known to exist between molecular oxygen and P3HT as previously reported in Chapter 2.^{40,42,57}

AFM

A scratch was applied exposing the substrate in each film along the sample, which was subsequently analysed with AFM profilometry that was performed on an N8 Neos (Bruker Nano GmbH, Herzogenrath, Germany) operating in an intermittent contact mode using PPP-NCLR cantilevers (NANOSENSORS, Neuchatel, Switzerland). The obtained profiles were based on images that were recorded at a scan speed of $27 \mu\text{m s}^{-1}$. Profiles revealing the film thicknesses were acquired along the samples every 2.5 mm such that the film thickness could be plotted as a function of the dose of light.

TOF-SIMS

TOF-SIMS analyses were performed using a TOF-SIMS IV (ION-TOF GmbH, Münster, Germany). 25-ns pulses of 25 keV Bi^+ (and Bi_3^+ in the case of macro-imaging) primary ions were bunched to form ion packets with a nominal temporal extent of <0.9 ns at a repetition rate of 10 kHz, yielding a target current of 0.7 pA. These primary ion conditions were used to obtain mass spectra, ion images, and depth profiles. 30 nA of 3 keV Xe^+ was used as sputter ions. For all analyses electron bombardment (20 eV) was used to minimize charge built-up at the surface. Desorbed secondary ions were accelerated to 2 keV, mass analysed in the flight tube, and post-accelerated to 10 keV before detection.

Surface images were acquired in negative ion mode over a period of 10 scans on a $200 \times 200 \mu\text{m}^2$ area, from which the data was subsequently added together.

Macro-imaging ($>500 \times 500 \mu\text{m}^2$) was conducted using both Bi^+ and Bi_3^+ as primary ions and only consist of one full scan.

Depth profiling was performed in negative mode using an analysis area of $200 \times 200 \mu\text{m}^2$ centred in a sputter area of $300 \times 300 \mu\text{m}^2$.

Surface images and depth profiles were acquired from 3 different positions of the non-exposed sample i.e. the reference points, and 6 different positions along the illuminated sample. This was done for both the P3HT and the P3HT:PCBM samples, see Figure 3.1 for further details. Macro images were acquired of both sample slides using Bi^+ and Bi_3^+ as primary ions resulting in 4 images onwards identified as P3HT Bi^+ , P3HT Bi_3^+ , P3HT:PCBM Bi^+ , and P3HT:PCBM Bi_3^+ .

XPS

The XPS analyses were performed on a K-alpha (Thermo Electron Limited, Winsford, UK) using a monochromatic Al-K α X-ray source and a take-off angle of 90° from the surface plane. Atomic concentrations were determined from surface spectra (100–600 eV, 200 eV detector pass energy, 5 scans) and were calculated by determining the relevant integral peak intensities using a Smart type background. High-resolution S_{2p} and C_{1s} XPS spectra were obtained using 50 eV detector pass energy and 10 scans. The C_{1s} peak deconvolution (Figure 3.2) was based on binding energies acquired from Reference R1. The peak positions used were relative to the main peak, which is assumed to be the C-H peak (285.0 eV). Peak fitting was based on the following peak positions: C=C (284.5 eV), C-H (285.0 eV), C-OR (286.4 eV), C=O (287.8 eV), COOR (289.4 eV). The following constraints were used in the peak deconvolution: full width at half maximum (FWHM) was fixed at 1.50 eV, and the relative peak positions were fixed relative to the C-H peak (285.0 eV).⁵⁸

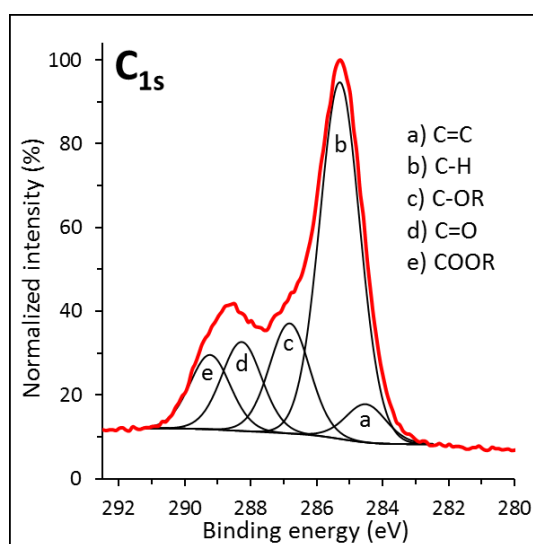


Figure 3.2 Peak deconvolution of a high resolution C_{1s} peak obtained from the P3HT sample after exposure to a 7.0 kJ cm⁻² dose of light in ambient air.

MVA

The raw mass spectral data was first analysed using the IonSpec 4.1 and IonImage 3.1 software (Ion-ToF GmbH, Münster, Germany). All mass spectra were mass calibrated. Peak selection was done by first using the software automated peak selection option with a signal threshold of 100 counts at mass unit interval of 10–800 u. Thereafter the generated peak list was manually adjusted to fit the data series in question, adding and deleting peaks and making sure, the overlapping peaks were binned together for image analysis (image-peaklist) and carefully separated for surface analysis and depth profiling (mass spect-peaklist). Mass spectra were batch processed in Ion Spec (Ion-ToF GmbH) using the generated “mass spect-peaklist” and saved as txt files with samples in rows and ions in columns making sure that the total ion count of each sample was included. The macro images were analysed one by one using the “image-peaklist” to generate ion images in IonImage (Ion-ToF GmbH), all of the ion

Chapter 3

images including the total ion and the sum of rest images were then exported as one binary image file (BIF) file.

The generated txt and BIF files were imported into Matlab R2012a (The MathWorks, Inc., Natwick, MA, USA) using the Cameca Ion-ToF BIF/BIF6 Image importer routine provided by the MIA toolbox v2.8.5 (Eigenvector Research, Inc., Wnatchee, WA, USA). The PCA and MCR analysis was conducted using the PLS Toolbox v7.5.2 (Eigenvector Research) with the MIA Toolbox add-on for multivariate image analysis.

The macro images of each sample (P3HT Bi⁺, P3HT Bi₃⁺, P3HT:PCBM Bi⁺, and P3HT:PCBM Bi₃⁺) were cropped to 245×66 pixels from the original 256×256 pixels prior to MVA analysis. This was done to focus the analysis on the illuminated portion of the sample and as far as possible to exclude instrumental artefact as the PCA and MCR models often try to model these as significant chemical components. Data pre-processing consisted of Poisson scaling.^{59,60,34,61} To estimate the number of components to use in the MCR models, PCA models were calculated and their scree plots (eigenvalue plots) were evaluated albeit this was not used to determine the final number of components to use for the MCR model but rather as a good starting point or range. The number of components to use in the MCR model is further complicated by the fact that the study is a degradation study in which the degradation products are somewhat unknown or in how many components they can be grouped is unknown.

The surface images were analysed as spectra, the spectra were all normalized to a range of C_n⁻ (n=1-4,6-9) peaks (n=5 was left out due to significant peak overlap) so that comparison across spectra was possible without intensity differences caused by instrumental effects.²⁶ As mentioned above, there were 9 data points (spectra) analysed for each sample, 3 reference spectra and 6 spectra along the exposed sample (Figure 3.1). The spectra were each set as a sample and the ion peaks were set as variables for the PCA analysis. The dataset for both samples (P3HT and P3HT:PCBM) were augmented so that the final dataset contained 18 samples (spectra) and 535 variables (ions). Prior to PCA analysis the data was mean centred and Poisson scaled.^{59,60,34,61}

In each of the depth profiles, the profiles in a specific sputter time window were extracted such that a level profile could be obtained, thus eliminating ions from the glass substrate that can obscure the results. All the profiles in the selected sputter window were then normalized to the C_n⁻ (n=1-4, 6-9) peaks. There after an average of each profile was calculated along with the standard deviation. These averages were then further examined using PCA analysis. The data was mean centred and Poisson scaled.^{59,60,34,61}

3.3 Results and Discussion

3.3.1 AFM profilometry

The measure film thicknesses of samples P3HT and P3HT:PCBM are plotted as a function of exposed light dose, see Figure 3.3. The film thickness decreases as the light dose increases.

This is due to loss of material and is in the case the P3HT sample supported by the presence of Si- in the TOF-SIMS surface spectra (not shown here).⁵¹

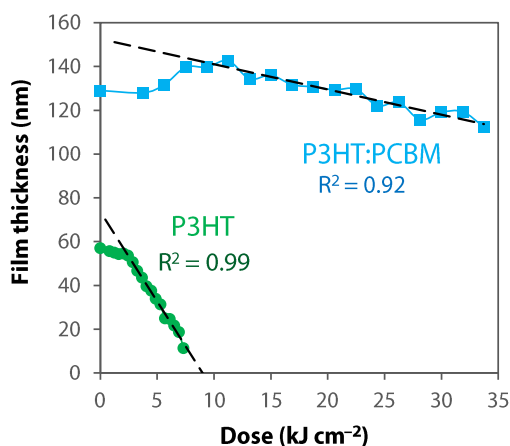


Figure 3.3 Film thickness measured by AFM profilometry as a function of exposed light dose. Each point is an average of three line profiles. The error bars are omitted for clarity. The error bar range is 1–3 nm for P3HT and 2–8 nm for P3HT:PCBM. The slopes are $-8.2 \text{ nm cm}^2 \text{ kJ}^{-1}$ (P3HT) and $-1.2 \text{ nm cm}^2 \text{ kJ}^{-1}$ (P3HT:PCBM).

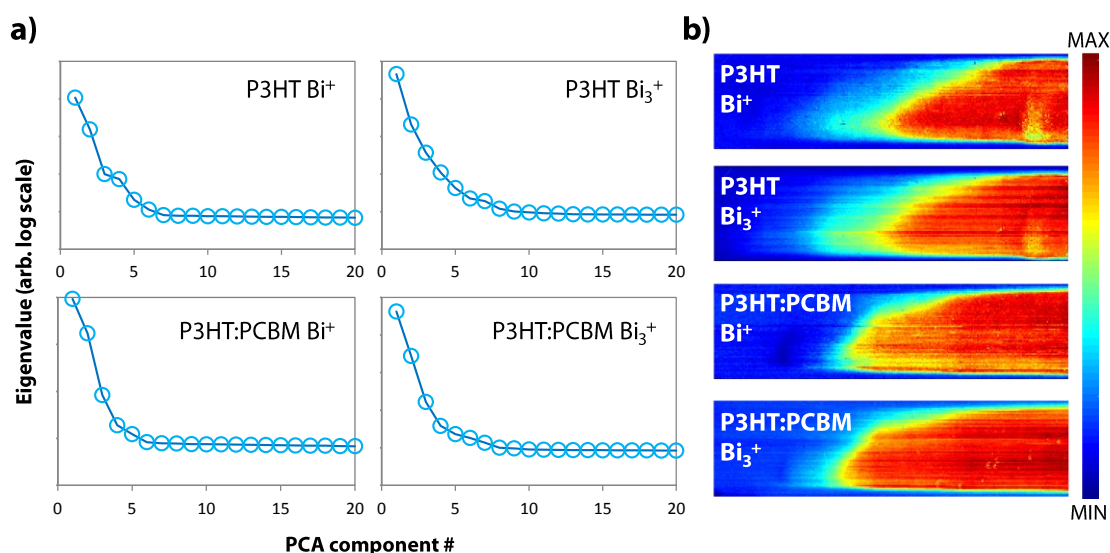


Figure 3.4 (a) The scree plots of the eigenvalues of the first 20 components from PCA calculations of the P3HT and P3HT:PCBM macro images analysed using Bi^+ and Bi_3^+ primary ions as indicated on the different graphs. The total ion images cropped to 66×245 pixels on which the MVA calculations were conducted are depicted in (b).

3.3.2 Macro imaging

The scree plots from the PCA calculated models, of the 4 macro ion sample images are depicted in Figure 3.4a. The cropped total ion images of all the samples are shown in Figure 3.4b, the samples exposure time was increased from left to right which is also indicated in the total ion images by the increase in measured ion intensity from left to right. The ion intensity is increased to the right due to the fact that degradation has occurred revealing different

molecular fragments and the incorporation of oxygen which can yield intense oxygen incorporated ion fragments, this will be discussed in further detail later in this section.

The scree plots in Figure 3.4a suggest that the number of components to use is between 2 and 7 for all the images. MCR models were then calculated using components 2 through to 7 and the belonging loadings and score plots were then evaluated and compared, the calculated score plots for each of the MCR models of sample P3HT Bi⁺ are illustrated in Figure 3.5 along with the scores overlay for each model.

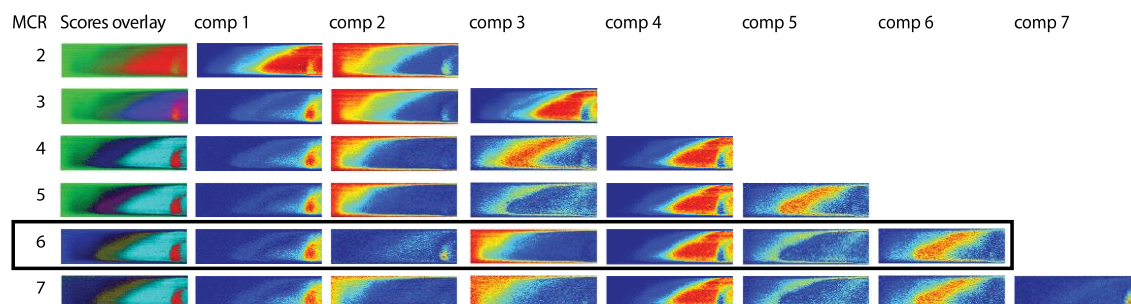


Figure 3.5 The calculated scores plots from the different compound no. MCR models are illustrated for sample P3HT Bi⁺. The no. of components used for each model is indicated in the left hand side MCR column. The scores overlay is an overlay of each of the component score plots for that particular model (the overlays are falsely coloured). The comp no. columns are the score plots for that particular component in that particular MCR model (the colour bar used is the same as in Figure 3.4b). The black box indicates what component no. was chosen in the onwards analysis.

From Figure 3.5 the MCR model using 6 components was selected for the onwards analysis of sample P3HT Bi⁺, as this model contains well separated components with not too much overlap, with the exception of comp. 1 and comp. 2, however, the loadings spectrum (not shown here) on comp. 1 in the MCR 5 model and the loadings spectra on comp. 1 and comp. 2 in the chosen MCR 6 model (Figure 3.6a) suggests that the spectra has been separated in regards to the intense peaks, however some of the less intense peaks do appear in both components. In fact this is the case for most of the components, which suggest that these are not pure component spectra but rather mixtures which was to be expected. These sort of evaluations are made when selecting the number of significant components to include in a model, and this does sometimes mean that less significant components are included in order to include a more significant component appearing in a higher order MCR model.³⁰ This process was then repeated on the other three sample and are attached in Appendix A (Figure A. 1, Figure A. 2 and Figure A. 3)

The MCR 6 model information and variance captured on sample P3HT Bi⁺ can be seen in Table 3.1. The MCR 6 model thus explains 91% of the data, which is relatively good for an MCR model of TOF-SIMS image data. The MCR model information of the other three samples are attached in Appendix A (Table A. 1, Table A. 2, and Table A. 3).

Fast and efficient acquisition of organic material degradation data using concentrated light

Table 3.1 Percent variance captured by the MCR 6 component model calculated using the P3HT Bi⁺ stripe.

MCR component #	Fit (% Model)	Fit (% X)	Cumulative Fit (% X)
1	9.25	8.42	8.42
2	1.27	1.15	9.57
3	27.42	24.95	34.52
4	51.16	46.56	81.08
5	2.88	2.62	83.70
6	8.02	7.30	91.00

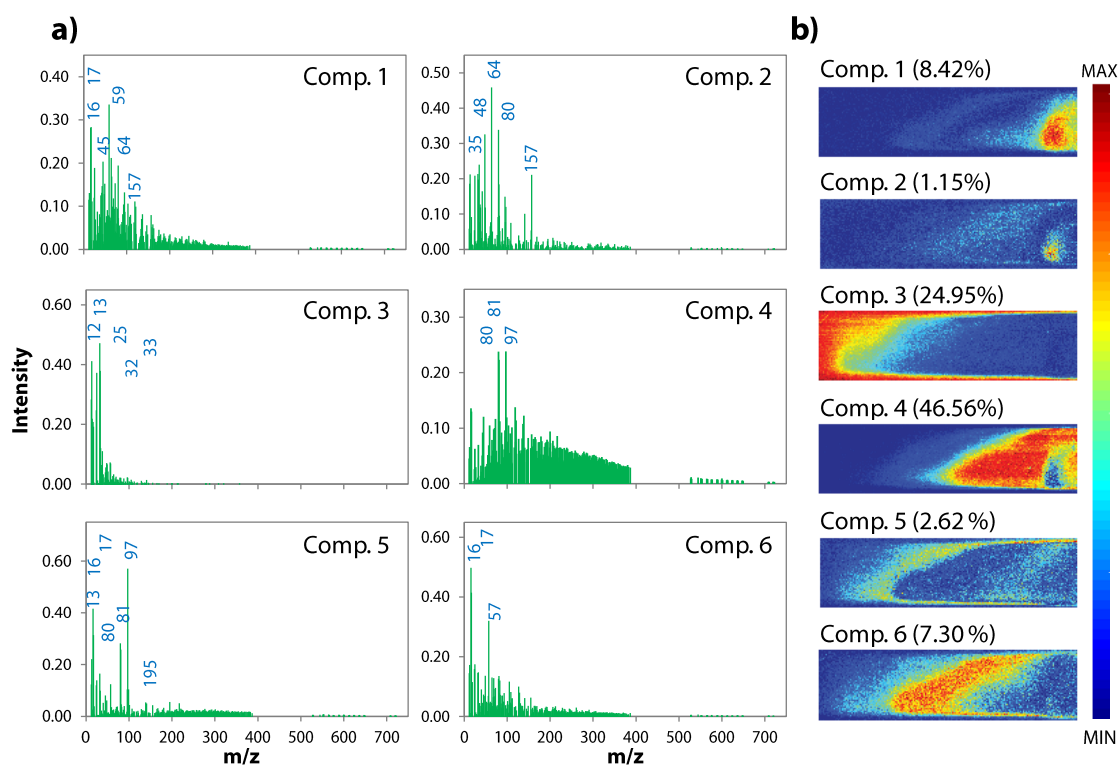


Figure 3.6 The loadings plots (a) and scores plots (b) on the indicated component of the MCR 6 model of sample P3HT Bi⁺. The percentages listed next to the component no. in (b) are the % fit of the data to that particular component.

The loadings on the different components in the MCR 6 model of P3HT Bi⁺ are illustrated in Figure 3.6a along with the scores plots in Figure 3.6b. The loadings spectra can be read a bit like mass spectra with the intense peaks carrying the most weight in that particular component. The most intense peaks in each of the loadings spectra have been highlighted, note that the numbers have been rounded for visual convenience. It can be seen that some of the peaks appear in several of the loading spectra, e.g. the peaks at 16 and 17, O and OH respectively appear in comp. 1, 5 and 6 which means that the compounds aren't purely separated as previously mentioned.

The most intense peaks from Figure 3.6a are highlighted in blue, these are listed in Table 3.2 column 1. The specificity of the peaks will be discussed below. The scores plots in Figure 3.6b

can be ordered such that the intensity moves from left to right comp. 3 → comp. 5 → comp. 6 → comp. 4 → comp. 1 → comp. 2, which corresponds to the total ion image. Further investigation of the loadings plot should give an indication if this is also true for the level of degradation of the polymer.

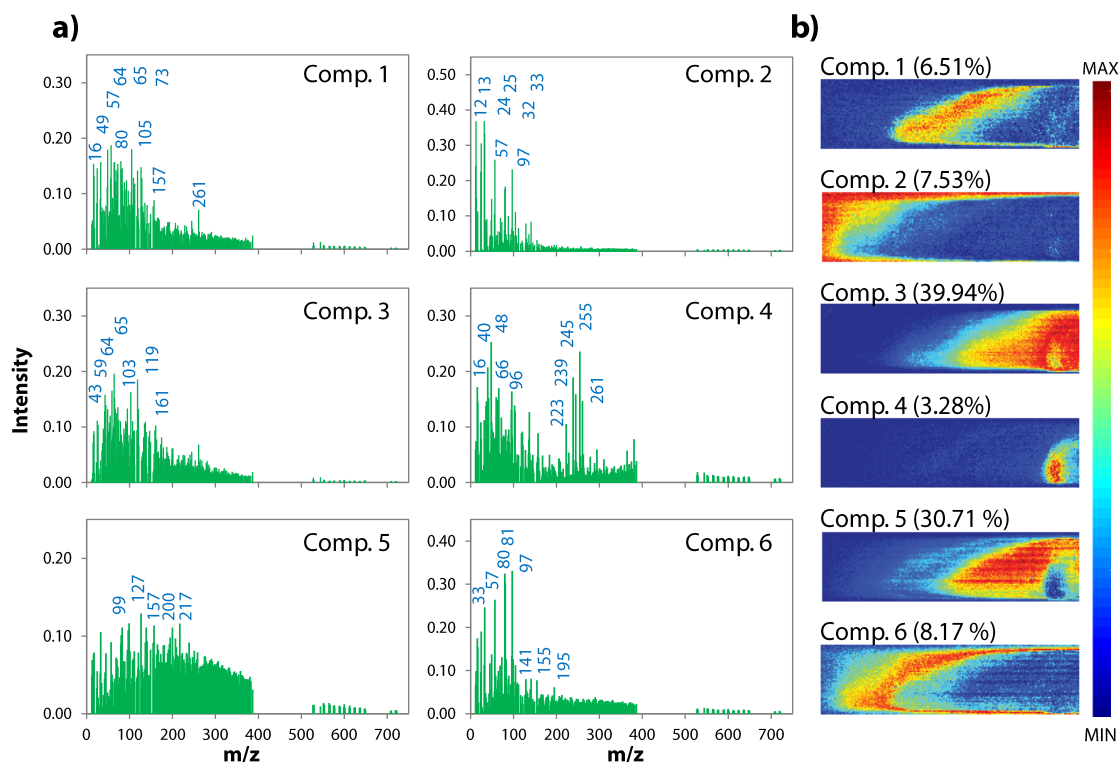


Figure 3.7 The loadings plots (a) and scores plots (b) on the indicated component of the MCR 6 model of sample P3HT Bi₃⁺. The percentages listed next to the component no. in (b) are the % fit of the data to that particular component.

The loadings and scores plots on the different components from the MCR 6 model data of the P3HT Bi₃⁺ sample are illustrated in Figure 3.7a and b respectively. The only difference between samples P3HT Bi⁺ and P3HT Bi₃⁺ is the primary ion used. When using Bi₃⁺ primary ions opposed to Bi⁺ primary ions the secondary ion yield is higher meaning more ion species are detected.^{62,63} This is also the case here and can be seen in the loadings plots Figure 3.7a compared to the loadings plots in Figure 3.6a, however, the question is, if this will reveal useful information.

The MCR 3 models loadings and scores plots on samples P3HT:PCBM Bi⁺ and P3HT:PCBM Bi₃⁺ are illustrated in Figure 3.8 and Figure 3.9 respectively. In both cases it was estimated that 3 components can be used to explain the data sets, as a higher number of components did not separate the scores plots very well and did not produce any new information on specific ion peaks, the data might have started to become over fitted, see Figure A. 2 and Figure A. 3.

Fast and efficient acquisition of organic material degradation data using concentrated light

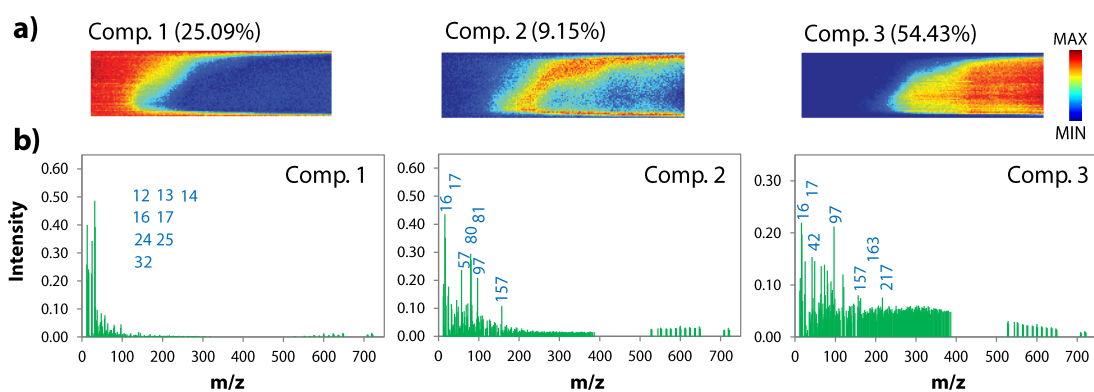


Figure 3.8 The scores (a) and loading plots (b) on the indicated component of the MCR 3 model of sample P3HT:PCBM Bi⁺. The percentages listed next to the component no. in (a) are the % fit of the data to that particular component

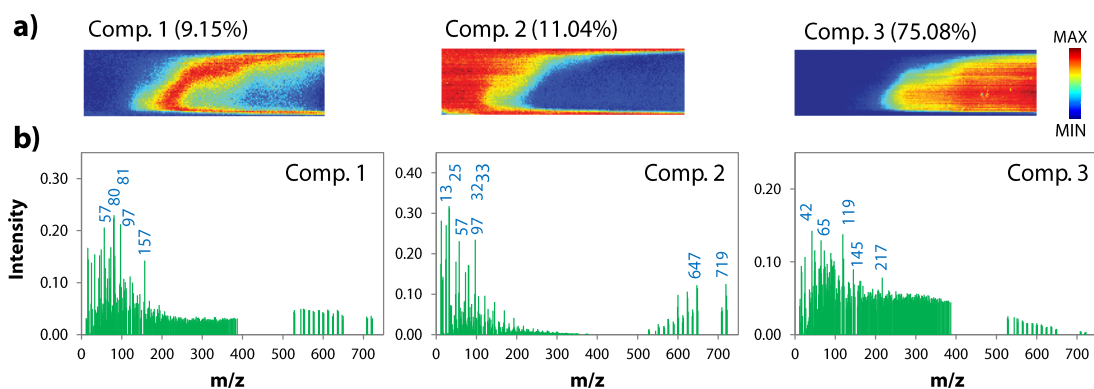


Figure 3.9 The scores (a) and loading plots (b) on the indicated component of the MCR 3 model of sample P3HT:PCBM Bi₃⁺. The percentages listed next to the component no. in (a) are the % fit of the data to that particular component

The most intense peaks in all of the MCR model calculated loadings plots from the 4 macro images have been listed in Table 3.2 along with the possible ion identification and comments on that particular ion peak.

Table 3.2 The most intense peaks from the MCR models on the macro images of the four samples, P3HT Bi⁺, P3HT Bi₃⁺, P3HT:PCBM Bi⁺ and P3HT:PCBM Bi₃⁺, are listed in the four first columns. The Ion column contains the possible ion identification and comments on that particular peak are given in the last column

P3HT Bi ⁺ m/z	P3HT Bi ₃ ⁺ m/z	P3HT:PCBM Bi ⁺ m/z	P3HT:PCBM Bi ₃ ⁺ m/z	Possible ion	Comment
11.97	11.97	11.97		C ⁻	
12.98	12.98	12.98	12.98	CH ⁻	
		13.99		CH ₂ ⁻	
15.97	15.97	15.97	15.97	O ⁻	
16.98		16.98		OH ⁻	
	23.95	23.95		C ₂ ⁻	

Chapter 3

24.98	24.98	24.98	24.98	C ₂ H ⁻	
31.93	31.93	31.93	31.93	S ⁻	P3HT peak
32.93	32.93	32.93	32.93	SH ⁻	P3HT peak
34.93				Cl ⁻	Impurity
	39.96			C ₂ O ⁻	
	41.97	41.97	41.97	C ₂ H ₂ O ⁻	
	42.97			C ₂ H ₃ O ⁻	
44.95			44.95	CHO ₂ ⁻	
47.93	47.93			SO ⁻ , C ₄ ⁻	Peak overlap
	48.94	48.94	48.94	SOH ⁻ , C ₄ H ⁻	Peak overlap
56.91	56.91	56.91	56.91	C ₂ HO ₂ ⁻ C ₂ HS ⁻	P3HT peak
58.94	58.94			C ₂ H ₃ O ₂ ⁻	
	59.92			CSO ⁻ , SiO ₂ ⁻ , C ₅ ⁻	Peak overlap
63.89	63.89			SO ₂ ⁻	Complete oxidation of sulphur atom in thiophene ring
	64.91	64.91	64.91	C ₄ HO ⁻	Peak overlap
	65.90			H ₂ S ₂ ⁻ , C ₄ H ₂ O ⁻	Peak overlap
	72.93	72.93	72.93	C ₂ HSO, C ₆ H ⁻	Peak overlap
79.90	79.90	79.90	79.90	SO ₃ ⁻ , C ₄ S ⁻	P3HT peak Thiophene ring
80.90	80.90	80.90	80.90	SO ₃ H ⁻ , C ₄ SH ⁻	P3HT peak Thiophene ring
			82.92		
			88.93		
	95.87			C ₈ ⁻ , SO ₄ ⁻ , C ₄ SO ⁻	P3HT peak
96.86	96.86	96.86	96.86	SO ₄ H ⁻ , C ₄ HSO ⁻	Oxidation of sulphur atom in thiophene ring
	98.88				Peak overlap
	102.87				
	104.87			C ₆ HS ⁻	
	118.84		118.84		
	126.89			C ₅ H ₃ SO ₂ ⁻	P3HT peak Oxidation of the thiophene sidechain

	140.89			Peak overlap
			144.89	
	154.88			
156.92	156.92	156.92	156.92	
	160.90			Peak overlap
		162.89		
194.83	194.83			P3HT peak
	199.80			P3HT peak
	216.81	216.81	216.81	Peak overlap
	222.80			P3HT peak
	238.76			P3HT peak
	244.74			P3HT peak
	254.77			P3HT peak
	260.75			P3HT peak
			647.15	C ₅₄ ⁻ PCBM peak
			719.05	C ₆₀ ⁻ PCBM peak

From Table 3.2 it is evident that more variance is captured at high masses when using Bi₃⁺ as a primary ion as opposed to Bi⁺, this is in particular true for in the case of the P3HT sample. The interpretation of the overwhelming amount of peaks detected is entirely a different matter.

By looking at the calculated scores plots on all the components from all the samples categorically with the intensity moving from left to right, then perhaps a degradation process could be highlighted.

- Starting at the left, comp.3, comp. 2, comp. 1 and comp. 2 of samples P3HT Bi⁺, P3HT Bi₃⁺, P3HT:PCBM Bi⁺, and P3HT:PCBM Bi₃⁺ respectively. These are dominated by low mass carbon peaks (C⁻, CH⁻, C₂⁻, C₂H⁻ etc.) and sulfur S⁻. In the cases where Bi₃⁺ was used as the primary ion, peaks at 57 and 97 (C₂HO₂⁻ and C₄HSO⁻ respectively) are also present the latter being a step in the in oxidation mechanism of the thiophene sulfur atom.⁴⁸
- Moving to the right of the sample, i.e. the light dose increases, comp. 5 and 6, comp. 1 and 6, comp. 2, and comp. 1 of samples P3HT Bi⁺, P3HT Bi₃⁺, P3HT:PCBM Bi⁺, and P3HT:PCBM Bi₃⁺ respectively. Here O⁻ and OH⁻ have high loadings in the samples where Bi⁺ was used as primary ion. The ions C₄S⁻ and C₄SH⁻ (80 and 81 respectively) are present in all the samples, these ions are from the thiophene ring, if these are just fragments originating from the ion bombardment or a product of the degradation is questionable; however, since the concentration of these ions is on the illuminated area and not on the reference these ions are most likely present due to degradation of P3HT. As before the presence of C₂HO₂⁻ and C₄HSO⁻ is detected. A peak at 157 is also detected, but the ion hasn't been identified.

- Then from about the middle and onwards to the right, comp. 4, comp. 3 and 5, comp. 3 and comp. 3 of samples P3HT Bi⁺, P3HT Bi₃⁺, P3HT:PCBM Bi⁺, and P3HT:PCBM Bi₃⁺ respectively. Most of the variance in each model is captured in these components, which is not odd since this is where most of the detected secondary ion originate. The C₄HSO⁻ is detected again this time only in Bi⁺ analysed samples. Peaks 64 and 65 (SO₂⁻ and C₄HO⁻ respectively), SO₂⁻ could be the fully oxidised sulfur atom in the thiophene ring and C₄HO⁻ a product of the side chain oxidation. Some carbon oxygen peaks are also present C₂H₂O⁻, C₂H₃O⁻, and C₂H₃O₂⁻ (42,43, and 59 respectively). Some unknown ions at higher masses are also present *e.g.* 99, 103, 126, 200 are only present in the P3HT Bi₃⁺ sample while the ion at 217 is present in the P3HT Bi₃⁺ and both the P3HT:PCBM samples.
- In the P3HT sample using both Bi⁺ and Bi₃⁺ primary ions the right hand side is separated further into comp. 1 and 2, and comp. 4 for P3HT Bi⁺ and P3HT Bi₃⁺ respectively. The ions at mass 40, 45, 48, 59, 64, 66, 80 and 96 (C₂O⁻, CHO₂⁻, SO⁻, C₂O⁻, C₂H₃O₂⁻, SO₂⁻, C₄H₂O⁻, C₄H₂O⁻ and C₄SO⁻) all oxygen species from either the side chain oxidation or the thiophene sulfur atom oxidation. There were also unknown ions at higher masses present 223, 239, 245, 225, and 261, these were only present in the P3HT Bi₃⁺ sample which makes it likely that the presence of these ions is due to the degradation of P3HT. This was further established by investigating these ions in the surface spectra (which are discussed later in this chapter) of the two samples and they did indeed increase in intensity ratio as a function of exposed light (the data is not shown).

3.3.3 Surface images/spectra:

XPS

The elemental compositions of the P3HT and P3HT:PCBM samples measured on the reference locations i.e. the non-exposed surface by XPS, are given in Table 3.3, with the calculated theoretical atom-% listed in the brackets. It shows that the measured atom-% of oxygen on the reference points is elevated compared to the theoretical atom-% in all the samples. This phenomenon has been observed before and it was suggested that some oxygen is already incorporated in the sample during processing,^{23,26} in Chapter 2 this oxygen elevation was seen even in the encapsulated OPV samples. The sulphur contents on the P3HT:PCBM surface is 6.5 atom-% higher than the theoretical value and could this suggest that there is an accumulation of P3HT on the surface of the P3HT:PCBM sample, this P3HT enrichment of a vertical gradient has been previously documented where the P3HT enrichment occurred either at the top or the bottom of the P3HT:PCBM layer,^{23,64-66} suggesting that there is a strong dependence on deposition and processing methods.

Fast and efficient acquisition of organic material degradation data using concentrated light

Table 3.3 Element compositions of the P3HT and the P3HT:PCBM samples, from surface locations that were not exposed to light (yellow and red symbols in Figure 3.1). Each value is an average of three different surface locations. Values in brackets are calculated theoretical values.

Films measured on reference locations	Oxygen (atom-%)	Sulfur (atom-%)	Carbon (atom-%)
P3HT	3.8 ±0.4 (0)	9.8 ±0.1 (9.1)	86.4 ±0.4 (90.9)
PCBM	8.1 ±1.6 (2.7)	0 (0)	91.9 ±1.6 (97.3)
P3HT:PCBM	6.0 ±0.1 (2.4)	7.7 ±0.1 (1.2)	86.3 ±0.1 (96.5)

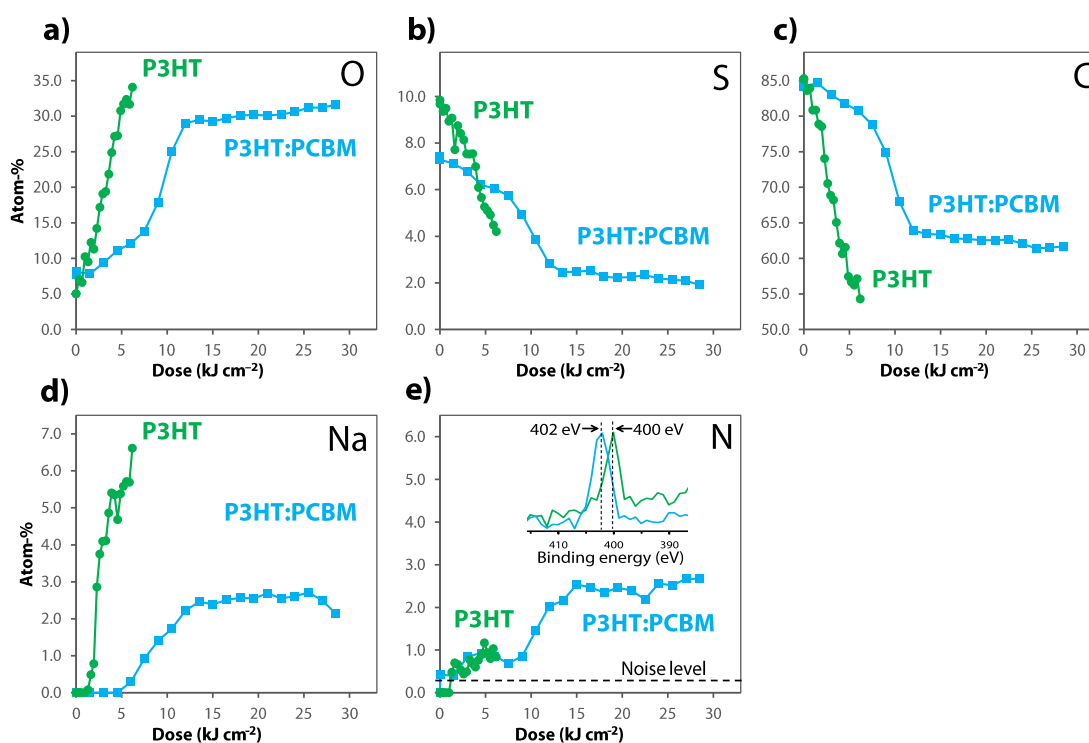


Figure 3.10 (a-e) XPS measured element compositions for P3HT and P3HT:PCBM as a function of exposed light dose. The quantifications are based on the following peaks: O_{1s} , S_{2p} , C_{1s} , Na_{KL1} , and N_{1s} . Each point is a single measurement. (e) The inset shows the N_{1s} peak positions for P3HT (400 eV) and P3HT:PCBM (402 eV).

The XPS results are seen in Figure 3.10 and Figure 3.11 where the elemental composition and the deconvoluted peak ratios are plotted, respectively. There are a few things that are notable for all of the XPS results, in the case of the P3HT:PCBM sample the gradient is small at lower light doses, then there is a sudden increase until about 15 kJ cm^{-2} when there is a plateau until the end of the measurements (these observations are inverted for the elemental compositions of S and C (Figure 3.10b,c)). This last feature of a plateau at higher light doses has been previously observed by Tournebize et al in the study of the photodegradation/stabilization of poly(3-hexyl- d_{13} -thiophene (P3HdT):PCBM.⁵⁴ Where it was attributed to a morphological reorganization/optimization after x amount of hours of illumination due to increased temperature exposure from the illumination, which stabilized the P3HdT:PCBM with regards to photo-oxidation. However the initial small gradient observed herein was not seen in the photo degradation of P3HdT:PCBM.

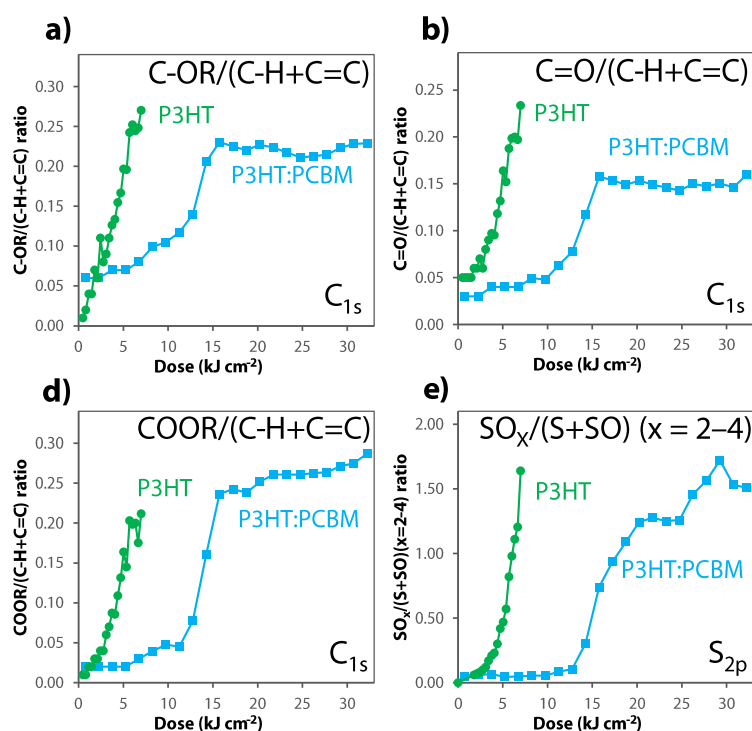


Figure 3.11 (a-c) Deconvoluted C_{1s} peaks (Figure 3.2) relative to the sum of the deconvoluted C-H and C=C peaks as a function of exposed light dose. (d) The ratio between the SO_x ($x = 2-4$) peak and the (S+SO) peak (S_{2p}) as a function of exposed light dose. Each point is a single measurement.

Tof-sims

The PCA model based on two components is represented in Figure 3.12 with scores and loadings appearing in (a-b) and (c-d) respectively. The scores and loadings plots in PCA can in simple turns be interpreted as such: a sample that has high scores on e.g. PC1 implies that it has a lot of the phenomenon represented in loadings 1, i.e. it has variation where the positive variables in loadings 1 are high and the negative variables in loadings 1 are low at the same time (relatively). Furthermore, the variables that have low loadings close to zero do not follow this trend. Hence the loadings tells us about what the trend is and which variables are part of that trend and which variables are not part of that trend.³⁰ So, the scores on PC1 in Figure 3.12a are low for the lower doses and high for the higher doses in each of the samples P3HT and P3HT:PCBM. As peaks 25, 32 and 33 (C_2H^- , S^- , and SH^- respectively) decrease and peaks 16, 17, 80 and 81 (O^- , OH^- , SO_3^- or C_4S^- , and SO_3H^- or C_4SH^- respectively) increase, the higher the scores become. Thus an increase in exposure time i.e. higher dose implies an increase in O^- and OH^- ions and a decrease in S^- and SH^- at the surface, this is what is expected when the light dose increases so should the photo oxidation of the polymer. The scores on PC2 effectively separates P3HT from P3HT:PCBM at higher light doses with the exception of one point in P3HT at 3 kJ cm^{-2} (this is most likely due to an error in that particular mass spectrum, which was also evident from the Q residuals vs T^2 hotelling plot (not shown here), however only the addition of more spectra at that specific exposure time could conclude this). The loadings on PC2 (Figure 3.12e) indicate that P3HT has variations when 80 and 81 peaks are

high combined with low 16, 19 and 26 peaks, the opposite is true for P3HT:PCBM added by the negative loadings on peaks with m/z above 340 of which many can be ascribed to PCBM. Furthermore, in the P3HT:PCBM sample there seems to be a small gradient at smaller light doses and then there is an increase from $\sim 10\text{--}14\text{ kJ cm}^{-2}$ where the variation levels off. This was also observed in the XPS results (Figure 3.10 and Figure 3.11).

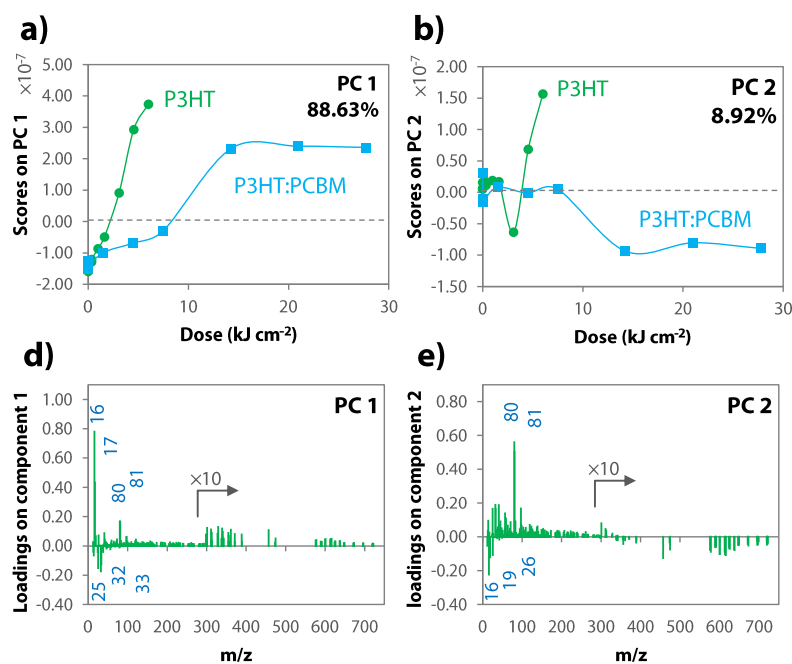


Figure 3.12 The PCA 2 component model scores (a - b) and loading plots (d-e) of the surface spectra on the P3HT and P3HT:PCBM samples. The percentages listed next to scores plots (a and b) are the % fit of the data to that particular component

From the PCA analysis of the surface spectra it is possible to go back and look at the raw data, now with some indication of where to look for the needle in the haystack so to speak. The ions from the surface spectra with the highest loadings from the PCA analysis (16, 19, 25, 26, 32 and 80) were plotted as a function of exposed light dose, see Figure 3.13a-f. As expected, the variation in ion intensities of O^- , C_2H^- and S^- measured by TOF-SIMS (Figure 3.13a-c) is comparable to the elemental composition measured of O, C and S measured by XPS (Figure 3.11a-c). PC2 from the PCA analysis also suggested peak 26 to be of significance in describing variance across the samples. At 26 u the ion is usually considered to be C_2H_2^- ; however, in this case the peak seemed to be broadened and shifted slightly thus could also be the CN^- ion, or more likely an overlap between the two. This combined with the fact that the XPS analysis revealed an increase in N atom-% in the P3HT:PCBM sample, strongly indicated that the peak indeed was dominated by CN^- . The trend in the NH^- peak (Figure 3.14) further supported this observation that there is an increase in the nitrogen contents of the P3HT:PCBM sample as a function of exposed light dose. One explanation for the presence of nitrogen on the surface is because of the harsh illumination condition of the experiment, atmospheric nitrogen can react with the surface via a radical mechanism.⁶⁷⁻⁷⁰

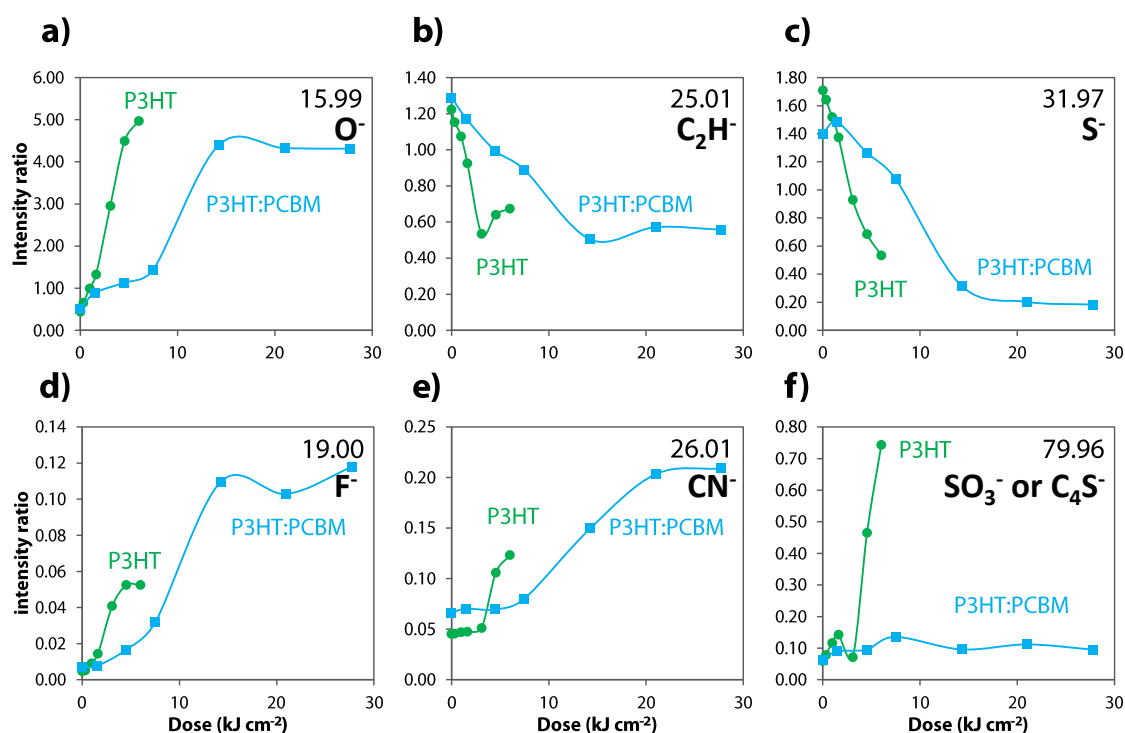


Figure 3.13 (a-f) Selected ions from the surface spectra of P3HT and P3HT:PCBM are plotted as a function of exposed light dose. The m/z of the ions plotted is given in the upper right hand corner of each plot. The intensity of each spectra was normalized against the sum of carbons (C_{n^-} , $n = 1-4, 6-9$).

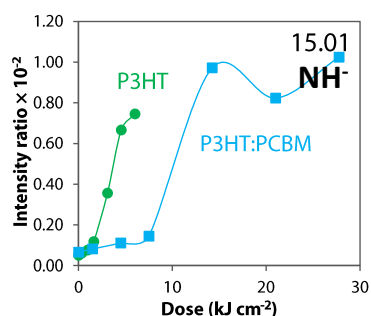


Figure 3.14 The NH^- ion from the surface spectra as a function of exposed light dose. The intensity of each spectra was normalized against the sum of carbons (C_{n^-} , $n = 1-4, 6-9$).

3.3.4 Depth profiles

The depth profiles were examined to explore the bulk of the samples, as appose to the surface spectra and imaging that effectively only has a probe depth of 1-2 nm, and XPS that has a probe depth of 5-10 nm.

From the P3HT and P3HT:PCBM extracted depth profiles, A 3 component PCA model was calculated, the resulting scores and loadings are depicted in Figure 3.15a-c and d-f respectively. The variation in the three scores are quite similar to the variation explained by

the PCA analysis of the surface spectra, which suggest there are similarities between the surface and the bulk of the samples. Closer inspection of the three loadings plots Figure 3.13a-c, indicates that the variance is captured by almost the same ions 16, 17, 25, 26, 32 (O^- , OH^- , C_2H^- , CN^- , and S^- respectively) with the addition of 60, 76, 104, and 136 (CSO^- , CSO_2^- , unknown, and unknown respectively). The loadings of the CN^- ion on PC2 in particular (Figure 3.13e) are higher than that observed in the surface spectra. It should also be noted that the P3HT depth profile at the highest light dose behaves oddly in the modelled PC2 and PC3, this could be because this point is in fact that much different from the other data points on the sample or due to an actual error in the depth profile measurement, it is most likely that it is a combination of the two, as the thickness of the P3HT film decreases as a function of exposed light dose (Figure 3.3). Thus rendering the extracted shallow profiles more susceptible to erroneous measurements possibly aided by unwanted detection of ions from the glass substrate.

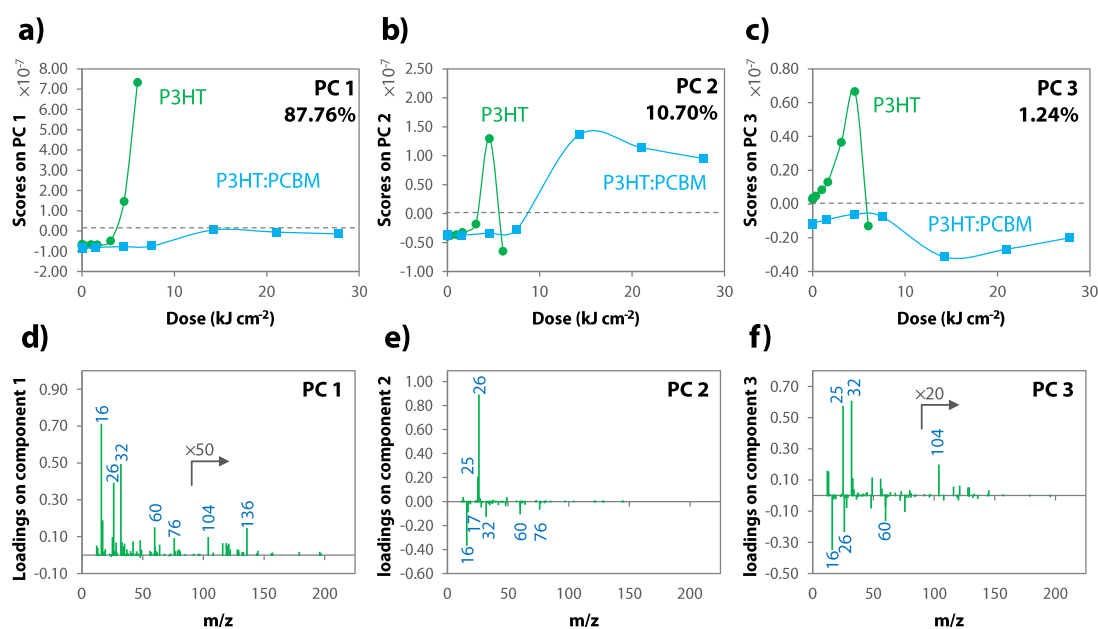


Figure 3.15 The PCA 3 component model scores (a-c) and loading plots (d-f) of the depth profiles on the P3HT and P3HT:PCBM samples. The percentages listed next scores plots (a and b) are the % fit of the data to that particular component

The ions O^- , CN^- , S^- , and 104 from the extracted depth profiles are plotted in Figure 3.16. The oxygen incorporation into the bulk of the two samples (Figure 3.16a) follows the same trend as the oxygen incorporation at the surface. The bulk oxygen incorporation into the P3HT sample is a bit smaller than the oxygen incorporation on to the P3HT surface; however, P3HT bulk oxygen incorporation is 3 orders of magnitude larger than the incorporation into the P3HT:PCBM sample bulk. This indicates that in the P3HT:PCBM blend the PCBM stabilises the P3HT with regards to photo-oxidation as previously mentioned, one of the reasons for the higher oxygen incorporation at the P3HT:PCBM surface compared to the bulk is the P3HT enrichment at the surface,⁵⁴ meaning the surface will be more like P3HT and thus more prone to photo-oxidation.

The S⁻ ion intensity ratio in the bulk increases as a function of exposed light dose, which is the opposite to that observed at the surface of the samples. One explanation for this could be the harsh sputtering conditions that fragments the molecules further thus detecting S⁻ at artificial high levels. Another explanation is that in the bulk of the material sulphur isn't oxidised to the same extent as it is at the surface and rather the source of oxygen in the bulk is from photo-oxidation at a different site, e.g. the hexyl side chain.

The CN⁻ ion which had a high loading in component PC2 in particular (Figure 3.15b) also increases as a function of exposed light dose and is present at a higher content in the bulk compared to the surface especially in the P3HT sample.

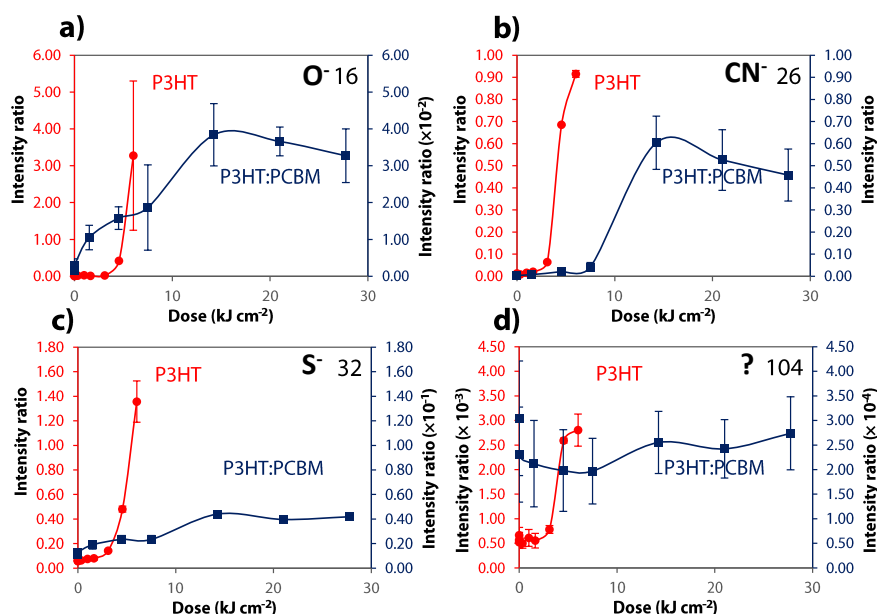


Figure 3.16 Selected ions from the extracted depth profiles of the P3HT and P3HT:PCBM samples are plotted as a function of exposed light dose. Note that the samples are plotted on different intensity ratios axis with the scale stated in the axis title. Each point is the average of that particular ion for the sputter time window extracted depth profile and the error bars are the standard deviations for that ion in the sputter time window.

3.4 Conclusions

The fact that all this data came from on sample substrate for each material is quite something. The MVA analysis of the TOF-SIMS macro images revealed that photo oxidation had occurred, this was seen by the detected oxygen containing ions, however it was difficult to conclude much else as both carbon oxygen species and sulfur oxygen species started to appear at the same time when moving from left to right on the sample, so that it was not possible to say which photo oxidation process occurred first, side chain oxidation or thiophene sulfur atom oxidation. One conclusion from the macro images is that more information on higher mass ions is gained by using Bi₃⁺ as the primary ion.

Surface spectra and depth profiles revealed small difference between the surface and the bulk of the material, although there were some significant differences detected. The oxygen content in P3HT:PCBM is significantly less in the bulk than at the surface, this could

be due to the P3HT enrichment at the surface or that the PCBM stabilizes the P3HT because the fullerene to act as a radical scavenger.

The presence of nitrogen was detected both on the surface and in the bulk, and could be explained by reaction with atmospheric nitrogen via a radical mechanism which is only possible due to the harsh illumination conditions that the samples were subjected to. The nitrogen contents increases as a function of increased light dose indicating that its presence is affected by the light dose.

For future work it is necessary to address the difference in film thickness of the samples to begin with and due to the loss of material, i.e. the film thickness decreased, this problem should be addressed as it is known that the film thickness of a polymer or polymer blend highly affects the photochemical stability. There is also a necessity for more replica data points, which will improve PCA the model and make it easier to detect real outliers. This experiment setup is easily repeated, making it trivial to investigate the degradation behaviour of other materials.

Chapter 4

Examples of Characterization and analysis of OPV devices and OPV materials⁴

⁴ This chapter is based on a selection of publications

4.1 Introduction

This chapter contains an assortment of the already published TOF-SIMS and AFM characterization work conducted during the PhD. Each example gives a short introduction to the article using their abstract, however, the focus will only be on the TOF-SIMS and/or the AFM characterization work conducted by me. For further details such as material synthesis, device manufacture, J-C characterization etc. the reader is referred to Appendix B which includes the full copies of the articles discussed herein.

4.2 Characterising nanoparticles utilised in OPVs

From the publication:

*Aqueous Processing of Low-Band-Gap Polymer Solar Cells Using Roll-to-Roll Methods*⁷¹

4.2.1 Abstract:

Aqueous nanoparticle dispersions of a series of three low-band-gap polymers (P1, P2, and P3) were prepared using ultrasonic treatment of a chloroform solution of the polymer and PCBM mixed with an aqueous solution of sodiumdodecylsulphate (SDS).

- P1: poly[4,8-bis(2-ethylhexyloxy)benzo(1,2-b:4,5-b')dithiophene-alt-5,6-bis(octyloxy)-4,7-di(thiophen-2-yl)(2,1,3-benzothiadiazole)-5,50-diyl]
- P2: poly[(4,4'-bis(2-ethylhexyl)dithieno[3,2-b:2',3'-d]sil-ole)-2,6-diyl-alt-(2,1,3-benzothiadiazole)-4,7-diyl]
- P3: poly[2,3-bis-(3-octyloxyphenyl)qui-noxaline-5,8-diyl-alt-thiophene-2,5-diyl]

The size of the nanoparticles was established using small-angle X-ray scattering (SAXS) of the aqueous dispersions and by both AFM and grazing incidence SAXS (GISAXS) in the solid state as coated films. The aqueous dispersions were dialyzed to remove excess detergent and concentrated to a solid content of approximately 60 mg mL⁻¹. The formation of films for solar cells using the aqueous dispersion required the addition of the nonionic detergent FSO-100 at a concentration of 5 mg mL⁻¹. This enabled slot-die coating of high quality films with a dry thickness of 126 ± 19, 500 ± 25, and 612 ± 22 nm P1, P2, and P3, respectively for polymer solar cells. Large area inverted polymer solar cells were thus prepared based on the aqueous inks. The PCE reached for each of the materials was 0.07, 0.55, and 0.15% for P1, P2, and P3, respectively. The devices were prepared using coating and printing of all layers including the metal back electrodes. All steps were carried out using R2R slot-die and screen printing methods on flexible substrates. All five layers were processed using environmentally friendly methods and solvents. Two of the layers were processed entirely from water (the electron transport layer and the active layer).

4.2.2 AFM results and discussion

AFM imaging was performed on an N8 NEOS (Bruker Nano GmbH, Herzogenrath, Germany) operating in an intermittent contact mode using PPP-NCLR cantilevers (NANOSENSORS, Neuchatel, Switzerland). Images were recorded at a scan speed of 0.8 lines s⁻¹. The images

were analysed using the image processing software package SPIP 5.1.5 (Image Metrology A/S, Hørsholm, Denmark).

Particle size

The polymers were spin-coated on glass substrates in order to measure the particle size. It is wellknown that AFM can at times overestimate particle sizes in the lateral plane and therefore the height z is often used as a measure for the diameter of spherical particles.⁷²⁻⁷⁴ However, since the particles in the samples at hand are closely packed the height measurements of individual particles would be too time-consuming and inaccurate.⁷⁵ Therefore the best estimate to determine the particle size was to employ the Particle & Pore Analysis module included in the SPIP 5.1.5 software. The size was analysed on at least two different positions of the sample analysing a minimum of 2000 particles on each sample. The measured polymer particle sizes and distributions can be seen in Figure 4.1 and Table 4.1.

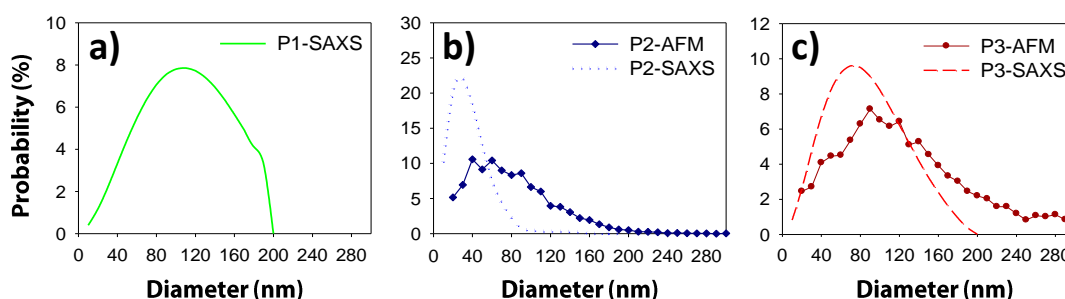


Figure 4.1 The size distributions of the particles P1 (a), P2 (b), and P3 (c) measured by AFM and SAX. The SAX measurements were performed with the particles in a water suspension, and AFM was measured from spin-coated films. The distribution for P1 could not be determined by AFM due to aggregation of the particles, see Figure 4.3a.

Table 4.1 The average particle diameter of P1, P2, and P3 as determined by SAXS and AFM. The standard deviation is given in the brackets.

Polymer	SAXS (dispersion)	AFM (films)	GISAXS (films)
	nm	nm	nm
P1	130(38)	<i>a</i>	<i>a</i>
P2	32(10)	69(47)	32(22)
P3	87(21)	120(82)nm	107(72)

^a not possible to determine due to aggregation in the sample

Film thickness

The polymer solar cells were first delaminated by ripping the plastic laminate off in a swift motion the open cell was thereafter placed on a glass slide using double sided tape. The thicknesses of the dry films were measured by AFM profilometry, see Figure 4.2. The thickness was measured at a minimum of three different positions on each film, with each position consisting of at least three individual measurements. The measured dry active layer film thickness was 126 ± 19 , 500 ± 25 , and 612 ± 22 nm for P1, P2, and P3 respectively.

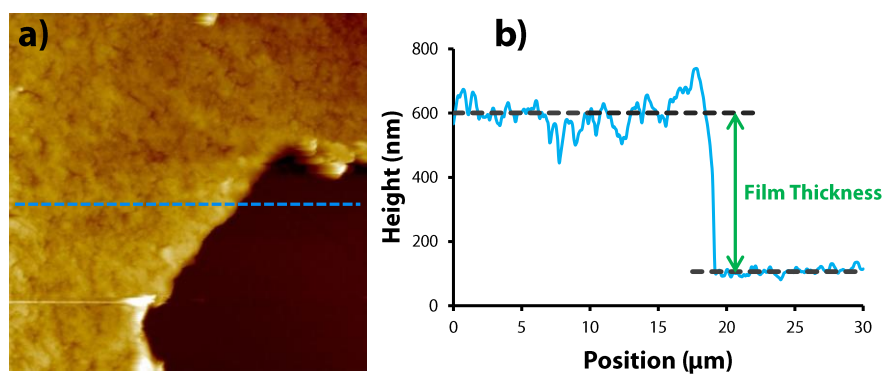


Figure 4.2 (a) $30 \times 30 \mu\text{m}^2$ AFM topography, the dashed blue line indicates where the thickness was measured. (b) the extracted line profile from the AFM image.

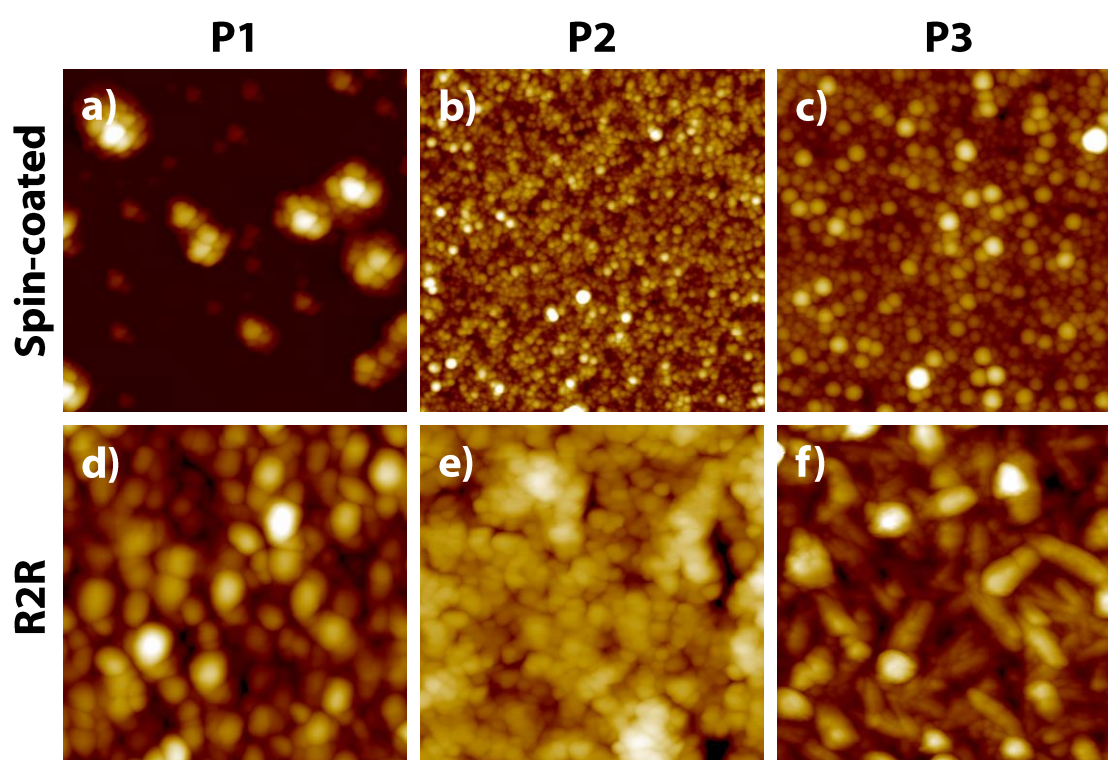


Figure 4.3 AFM topography images of the spin-coated samples (a – c) and R2R (d – f) prepared samples of P1, P2, and P3. All the images are $5 \times 5 \mu\text{m}^2$.

Morphology

The morphology differences between spin-coated and R2R prepared samples and between the different sample materials can clearly be observed in the AFM images in Figure 4.3. On the spin-coated samples the individual nanoparticle shapes can be observed (with exception of P1, which looks like agglomerates made up of smaller particles). In the R2R samples the nanoparticles can no longer be clearly distinguished; instead it looks like the nanoparticles have merged in places. The different morphologies observed across the R2R samples could be caused by the “harsh” process conditions, where annealing at high temperatures is involved,

and due to the different thermal properties of the polymers. When the R2R coated samples in Figure 6 panels d, e, and f are compared, it looks like the particles are increasingly merged ($d < f < e$). This could be because these samples were prepared at slightly different conditions with the annealing time increasing ($d < f < e$). Each roll-to-roll experiment (a roll of foil) comprises six coated stripes as described earlier.⁷⁶ The first coated stripe will thus pass the oven a total of eight times, whereas that last coated stripe will pass the oven a total of three times (including the two passages when coating PEDOT:PSS and printing the silver back electrode).

4.2.3 Conclusion

The aqueous nanoparticle dispersions were successfully prepared of three low-band-gap polymers and formulated inks for roll-to-roll processing into polymer solar cells on a flexible substrate which resulted in PCEs of 0.55, 0.15, and 0.07% for P2, P3, and P1 respectively. The nanoparticles were analysed in aqueous dispersion using SAXS and in solid film using GISAXS, GIWAXS, and AFM. The ink formulation and roll-to-roll processing was found to be challenging, however a reproducible method giving homogeneous films that adhered well to the surface of the zinc oxide based electron transport layer was obtained. The relatively poor device performance is ascribed to shunting and non-optimum morphology. Further work should be directed at improving coating condition and ink formulation as this has been successful in the case of organic solvent systems.

4.3 Polymer cross-linking and its effect observed in the active layer

From the publication:

*Comparative studies of photochemical cross-linking methods for stabilizing the bulk hetero-junction morphology in polymer solar cells.*⁷⁷

4.3.4 Abstract:

A comparative study between four different types of functionalities for cross-linking were presented. With relatively simple means bromine, azide, vinyl and oxetane could be incorporated into the side chains of the low band-gap polymer TQ1. Cross-linking of the polymers was achieved by UV-light illumination to give solvent resistant films and reduced phase separation and growth of PCBM crystallites in polymer:PCBM films. The stability of solar cells based on the cross-linked polymers was tested under various conditions. This study showed that cross-linking can improve morphological stability but that it has little influence on the photochemical stability which is also decisive for stable device operation under constant illumination conditions.

4.3.5 Optical microscopy and AFM

AFM imaging was performed on an N8 NEOS (Bruker Nano GmbH, Herzogenrath, Germany) operating in an intermittent contact mode using PPP-NCLR cantilevers (NANOSENSORS, Neuchatel, Switzerland). Images were recorded at a scan speed of 1 lines s^{-1} . The images were

analysed using the image processing software package SPIP 6.0.2 (Image Metrology A/S, Hørsholm, Denmark).

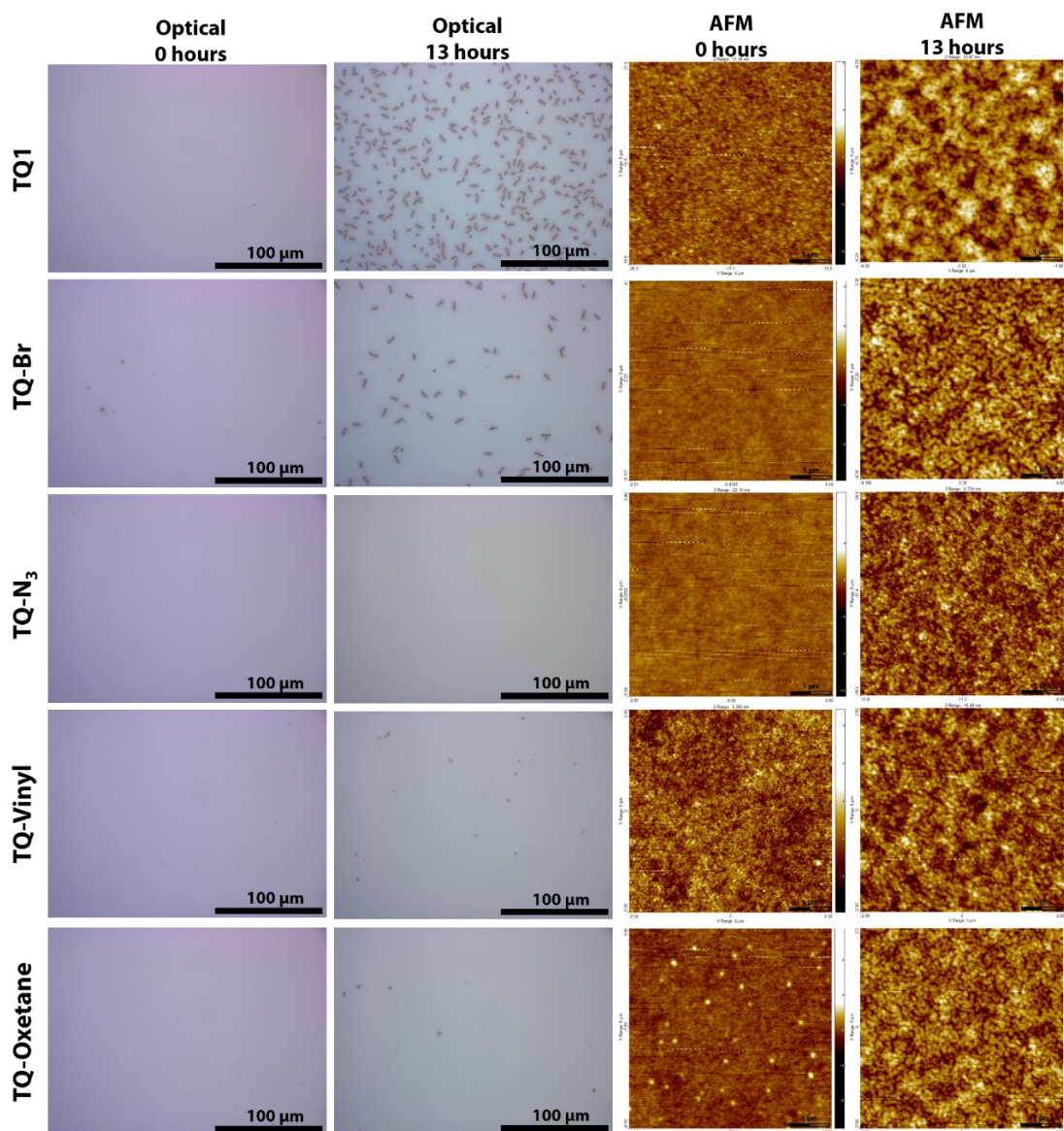


Figure 4.4 Optical images and AFM topography images ($5 \times 5 \mu\text{m}^2$) of the five polymer:PCBM blends (1:1 wt) before (0 hours) and after (13 hours) annealing at 150°C . All the samples were exposed to UV light at 254 nm for 10 minutes prior to the image were recorded.

The active layer blends (1 : 1 by weight) of the polymers and PCBM in chlorobenzene (20 mg ml^{-1}) were spin-coated on glass slides at 700 rpm. The samples were then treated with UV-irradiation (254 nm) for 10 minutes in a glove box using a hand held lamp. The samples were then annealed in ambient air for 13 hours at 150°C . Optical images along with AFM topography images of the samples were acquired before and after the annealing procedure, see Figure 4.3. As expected, large PCBM crystallites formed in the TQ1:PCBM film similar to what has been observed for annealing of P3HT:PCBM.^{78,79} Blends containing TQ-Vinyl, TQ-N3 and TQ-Oxetane showed either none or only very little phase segregation while the blend containing TQ-Br showed some phase segregation but not to the extent seen for TQ1:PCBM.

This confirms that the cross-linking has taken place for all the polymers with incorporated functional groups and that the cross-linking stabilizes the morphology of the BHJ layer towards thermal annealing as has been reported earlier.⁷⁸⁻⁸⁵

4.3.6 Conclusions

This study has shown that different types of cross-linking moieties can be incorporated into the side chains of the low band gap TQ1 type polymer by relatively simple means. The cross-linking reaction could be achieved by UV-irradiation of the pure polymer films to give insoluble products. When PCBM was included the cross-linking was less efficient presumably due to the optical absorption band of PCBM. Some solvent resistance was however observed in this case indicating some degree of cross-linking.

Cross-linking was shown to inhibit excessive phase separation and growth of PCBM crystallites in polymer:PCBM films during dark thermal annealing as shown by optical microscopy. This resulted in improved solar cell device stability under the conditions in question. It did; however, not improve the device stability under constant illumination in an ambient atmosphere, which is probably dominated by photochemical degradation rather than by thermal mechanisms. When oxygen-water was excluded by employing an inert atmosphere the stability increased somewhat and more importantly, some differences in stability became apparent between the polymers with TQ-Br and TQ-N3 giving the most stable devices. At present no explanation is provided for this observed difference, but it could be ascribed to different cross-linking mechanisms and also to different reaction rates.

This study thus showed that cross-linking can improve morphological stability, but that other factors such as photochemical degradation might be more important for device stability under constant illumination conditions.

4.4 Characterization of a double slot-die coated layer by TOF-SIMS depth profiling

From the publication:

*Simultaneous multilayer formation of the polymer solar cell stack using roll-to-roll double slot-die coating from water.*¹⁸

4.4.7 Abstract

Double slot-die coating using aqueous inks was employed for the simultaneous coating of the active layer and the HTL in fully R2R processed polymer solar cells. The double layer film was coated directly onto an ETL comprising doped zinc oxide that was processed by single slot-die coating from water. The active layer comprised P3HT:PCBM as a dispersion of nanoparticles with a radius of 46 nm in water characterized using SAXS, transmission electron microscopy (TEM), and AFM. The HTL was a dispersion of PEDOT:PSS in water. The films were analysed using TOF-SIMS as a chemical probe and X-ray reflectometry as physical probe, confirming the identity of the layered structure. The devices were completed with a back electrode of either Cu tape or evaporated Ag. Under standard solar spectrum irradiation (AM1.5G), current-voltage characterization (J-V) yielded a V_{OC} , J_{SC} , FF, and PCE of 0.24 V, 0.5

mA cm^{-2} , 25%, and 0.03%, respectively, for the best double slot-die coated cell. A single slot-die coated cell using the same aqueous inks and device architecture yielded a V_{OC} , J_{SC} , FF, and PCE of 0.45 V, 1.95 mA cm^{-2} , 33.1%, and 0.29%, respectively.

4.4.8 TOF-SIMS Experimental

TOF-SIMS Depth profiling analysis was performed using a TOF-SIMS IV (ION-TOF GmbH, Münster, Germany). 25-ns pulses of 25-keV Bi^+ (primary ions) were bunched to form ion packets with a nominal temporal extent of 0.9 ns at a repetition rate of 10 kHz yielding a target current of 1 pA. Depth profiling was performed using an analysis area of $100 \times 100 \text{ mm}^2$ and a sputter area of $300 \times 300 \text{ mm}^2$. 30 nA of 3-keV Xe^+ was used as sputter ions. Electron bombardment (20 eV) was used to minimize charge build-up at the surface. Desorbed secondary ions were accelerated to 2 keV, mass analysed in the flight tube, and post-accelerated to 10 keV before detection.

4.4.9 Result and discussion of the bilayer TOF-SIMS characterization

The obvious concern when performing double slot-die coating is whether the expected bilayer is formed, or whether complete mixing of the layers had occurred. An experiment was designed to resolve this issue. A piece of double slot-die coated sample was submerged in a sodium hydroxide solution in order to facilitate delamination (Figure 4.5a). After a while a discrete PEDOT:PSS film simply floated off the top of the surface leaving a P3HT:PCBM film on the substrate surface (Figure 4.5a). This is clear visual evidence that the double slot-die coating experiment yields a discrete bilayer film. The observations were confirmed by chemical analysis using TOF-SIMS. TOF-SIMS depth profiling was in addition employed to support the observation and to further document that a bilayer had indeed formed during the double slot-die coating process. Figure 4.5a–b shows the surface location where the depth profiling analysis was carried out. Several factors complicate the depth profiling analysis: (i) the sputter depth resolution (under the conditions in question) in soft materials is very poor (compared to hard materials, e.g. metals), and (ii) depth profiles are typically based on unique mass spectral markers that consist of molecular fragment ions or atomic ions, but no unique mass spectral markers are formed under the given experimental conditions. However, due to the fact that equivalent mass spectral markers originating from different molecular environments will produce a different signal response, the different materials may still be uniquely resolved. It turns out that the signal intensities for the S^- and SO_x^- fragment ions (formed in both layers) are extremely dependent on their origin. S^- is intense in PEDOT:PSS and relatively weak in P3HT:PCBM whereas SO_x^- exhibits the opposite behaviour. Figure 4.5(1) shows the depth profiles using S^- and SO_x^- as mass spectral markers. In spite of the complicated experimental conditions it was still possible to confirm that a bilayer was formed during the double slot-die coating process. In addition, a depth profile was acquired at a surface location where delamination (removal of PEDOT:PSS) had occurred, i.e. one layer (excluding ZnO/ITO/PET). In spite of noisy data it is evident that the S^- and the SO_x^- profiles have the same shape, which confirms the presence of a single layer (excluding ZnO/ITO/PET). The elevated signal intensities at ~40 minutes sputter time for S^- and SO_x^- are matrix effects caused by the close vicinity of metal oxides (ZnO and ITO). The extent of the matrix effect varies with experimental conditions (see Figure 4.5(2)).

Due to the aforementioned factors affecting the analysis it is not possible to conclude anything about the extent of interlayer mixing that was a consequence of the coating process. From the delamination experiment shown in Fig. 4 we however assume that the interface is discrete when viewed on the scale of the film thickness and probably resembles the roughness that an individual film of the P3HT:PCBM nanoparticles would.

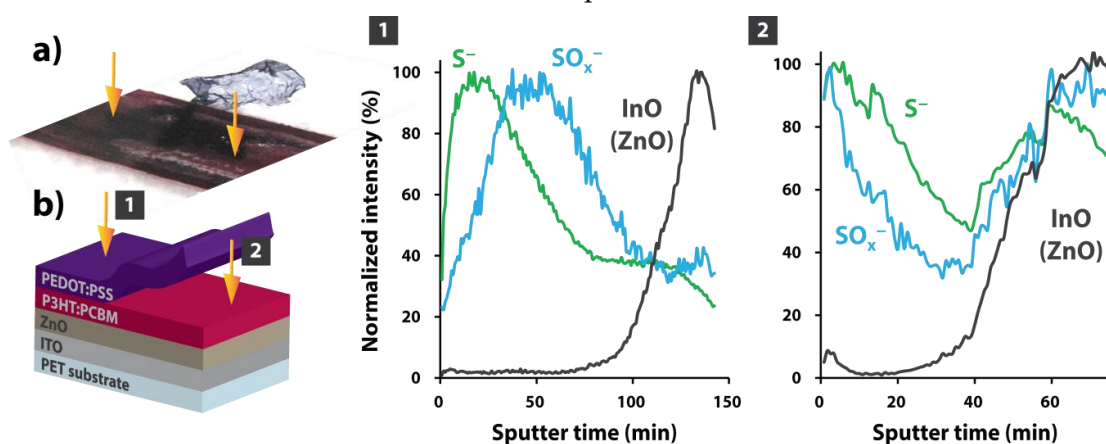


Figure 4.5 (a) Photography showing a section of the device where a section of the film has delaminated from the double slot-die coated film in NaOH (aq.). (b) Schematic of the sample shown in (a) including the surface locations (orange arrows) where the TOF-SIMS depth profiling analysis was conducted. TOF-SIMS depth profiles in negative mode confirmed that the double slot-die coated film has formed a bilayer (1) and further it was confirmed that at the surface location where the film delamination had occurred (2) only a single layer was present (beyond ZnO/ITO/PET). The ZnO layer was very thin resulting in a noisy profile and due to the thin nature of the film the ZnO⁻ profile is superimposed on the InO⁻ profile and was thus left out for clarity.

4.4.10 Conclusion

Double slot-die coated polymer solar cells processed roll-to-roll were successfully demonstrated, using two aqueous inks for the simultaneous formation of both the active layer (P3HT:PCBM) and hole transporting layer (PEDOT:PSS). The devices performed relatively poor compared to similar devices processed by single slot-die coating. This is ascribed to far from perfect layer separation due to the complex nature of the bilayer formation process; resulting in shunts and low current extraction efficiencies. This convincingly demonstrates a possible route for lowering the energy payback time of polymer solar cells, which is an important factor in a possible future scenario of large scale energy production.

4.5 TOF-SIMS depth profiling of polymer tandem solar cells prepared by R2R

From the publication:

*Roll-to-roll processed polymer tandem solar cells partially processed from water.*¹⁹

4.5.11 Abstract

Large area polymer tandem solar cells completely processed using R2R coating and printing techniques are demonstrated. A stable tandem structure was achieved by the use of orthogonal ink solvents for the coating of all layers, including both active layers. Processing

solvents included water, alcohols and chlorobenzene. Open-circuit voltages close to the expected sum of sub cell voltages were achieved, while the overall efficiency of the tandem cells was found to be limited by the low yielding back cell, which was processed from water based ink. Many of the challenges associated with upscaling the multilayer tandem cells were identified giving valuable information for future experiments and development.

4.5.12 TOF-SIMS experimental

TOF-SIMS depth profiling analysis Time-of-flight secondary ion mass spectrometry (TOF-SIMS) was employed to perform a depth profiling analysis. The experiments were conducted using a TOF-SIMS IV (ION-TOF GmbH, Münster, Germany). 25-ns pulses of 25-keV Bi⁺ (primary ions) were bunched to form ion packets with a nominal temporal extent of 0.9 ns at a repetition rate of 10 kHz yielding a target current of 1 pA. These primary ion conditions were used to obtain depth profiles in both negative and positive ion mode. Depth profiling was performed using an analysis area of 100×100 mm² and a sputter area of 300×300 mm². 30 nA of 3-keV Xe⁺ were used as sputter ions. Electron bombardment (20 eV) was used to minimize charge build-up at the surface. Desorbed secondary ions were accelerated to 2 keV, mass analysed in the flight tube, and post-accelerated to 10 keV before detection.

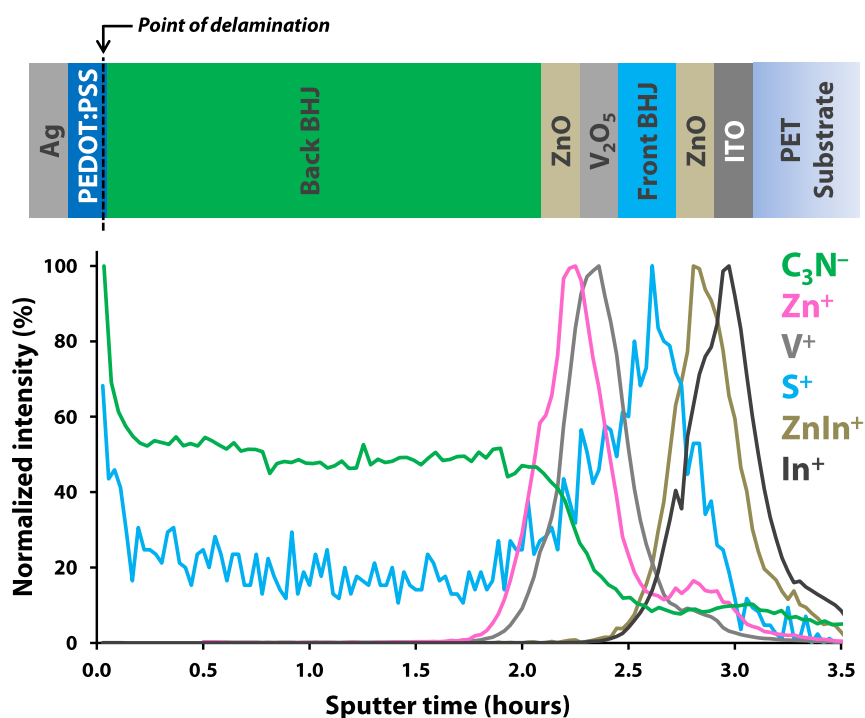


Figure 4.6 TOF-SIMS depth profiles through the delaminated tandem solar cell. C₃N⁻ is a marker for the back BHJ obtained from a depth profile run in negative mode, Zn⁺ is a marker for the ZnO, V⁺ is a marker V₂O₅, S⁺ is a marker for both front and back BHJ, and ZnIn⁺ (formed during the ionization step of the analysis) is a marker for the front ZnO and In⁺ is a marker for ITO.

4.5.13 TOF-SIMS depth profiling results and discussion:

TOF-SIMS depth profiling analysis was employed in both negative and positive ion mode in order to document the layer stack order. The encapsulation film is too thick for a depth profiling analysis, so it was necessary to delaminate the tandem solar cell. TOF-SIMS mass spectra of the exposed surfaces revealed that delamination took place at the PEDOT:PSS/back BHJ interface.

Figure 4.6 shows the results of the depth profile analysis. Various factors complicated the analysis, such as interface roughness, which is well known phenomenon in R2R processing (e.g. compared to spin coating). Furthermore, depth profiling in soft materials is associated with an inferior depth resolution (under the given sputter conditions), compared to hard materials (e.g. metals). These conditions constitute a challenge especially when it comes to performing depth profiling on very thin layers such as the ZnO (~25 nm) and V₂O₅ (~15 nm) layers present in this device. However, as is evident from Figure 4.6 it was quite possible, in spite of the conditions, to document the multilayer stack composition in the tandem solar cell device. Residual PEDOT:PSS was present in the PEDOT:PSS/back BHJ interface after the delamination process presumably due to a small degree of interlayer mixing that resulted in presumably a matrix effect, which is observed as initially elevated signals from the back BHJ material (i.e. at the beginning of the sputter time window). During the ionization process the Zn⁺ signal is discriminated due to the formation of the ZnIn⁺ cluster ion caused by the close vicinity of the ITO (i.e. an ionization phenomenon). Finally, a significantly long sputter time window is observed for the back BHJ compared to the front BHJ, which suggests that the back BHJ is significantly thicker (assuming similar sputter rates) than the front BHJ consistent with an expected layer thickness of ~600 nm for the back BHJ as compared to the thickness of the front BHJ ~200 nm.⁷¹

4.5.14 Conclusion:

Large area flexible polymer tandem solar cells with all layers processed entirely from solution, and partially from water, were successfully demonstrated. The multilayer stack on flexible PET substrate comprised a cathode of ITO/ZnO, a recombination layer of V₂O₅/ZnO, and a PEDOT:PSS/Ag (printed) anode. The two serially connected BHJs was comprised of a P3HT:PCBM front cell processed from chlorobenzene and a back cell processed from an aqueous dispersion of poly[2,3-bis-(3-octyloxyphenyl)-qui-noxaline-5,8-diyl-alt-thiophene-2,5-diyl]:PCBM nanoparticles. The composition and integrity of the multilayer stack was confirmed by TOF-SIMS depth profiling. The V_{OC} of the best tandem device was 0.9 V, while both the corresponding single junction reference devices had a V_{OC} around 0.5 V. This confirms a serial connection of the sub cells while the observed voltage losses are ascribed to visible defects in the recombination layer and a non-ohmic connection of the two sub cells.

4.6 Overall conclusion:

Chapter 4 has demonstrated 4 examples where TOF-SIMS and/or AFM was successfully utilised in the characterization of OPV devices and OPV materials. These two characterization techniques proved to be useful on many occasion, both as primary investigative techniques and as techniques to confirm what was already established. As previously mention the examples mentioned here are only a selection of the published characterization work that was conducted during the PhD, more examples can be found in the publications list in Chapter 1. It is also worth to mentioned, that not every characterization study conducted during the PhD resulted in a publication, there were of course instances where some exploratory study did in deed not bear fruit.

Chapter 5

Conclusion and outlook

Chapter 5

The focus of this PhD was on OPV material and OPV device characterisation and degradation characterisation using TOF-SIMS and AFM as primary techniques which was reflected in the thesis as well.

A large inter-laboratory study in which seven distinct OPV devices were studied by TOF-SIMS as a function lifetime (degradation) in order to identify specific degradation mechanisms responsible for the decline of the photovoltaic effect. The degradation experiment lasted over 1830 hours and included more than 300 cells and over 100 devices. Large amounts of data were generated and analysed which lead to many different observation. One of which was the photo-oxidation of the active layer (P3HT:PCBM) which was quantitatively monitored as a function of cell performance by correlating the bulk obtained TOF-SIMS data with surface obtained XPS data. No photo-oxidation was observed in the encapsulated devices, an apparent linear relationship in oxygen incorporation for decreasing cell performance was seen for the so-called semi-impermeable encapsulated devices. The non-encapsulated devices had a slow initial oxygen incorporation that accelerated later in the degradation tests. Although the non-encapsulated and semi-impermeable encapsulated devices had different photo-oxidation behaviours they did surprisingly exhibit a degree of photo-oxidation in the same order of magnitude.

In hindsight MVA analysis could have been very beneficial for the TOF-SIMS data analysis from the ISOS-3 collaboration data, not necessarily revealing more information but at least it would have sped up the analysis work.

The degradation study of P3HT and P3HT:PCBM that utilised concentrated light and a mechanical sample stage effectively generated a data bank of degradation data on a single substrate. Although not much substantial could be deduced about the degradation mechanisms of the material, there were however small differences found between the surface degradation and the degradation of the bulk e.g. the level of oxygen incorporation was much larger on the P3HT:PCBM surface than it was in its bulk. The use of MCR on the macro images revealed much more information and was much faster compared to manual analysis. PCA analysis of the surface and depth profile mass spectral data proved to be useful as an explorative tool.

Future work should include repeated measurements at each data point, which will improve PCA the model and make it easier to detect real outliers. The experimental setup can be easily repeated, making it trivial to investigate the degradation behaviour of other materials.

The smaller characterization work by TOF-SIMS and AFM of OPV materials and OPV devices demonstrated the usefulness of these two techniques in this field.

The many degradation behaviours observed through the characterisation of functioning OPV devices and the building block materials have significantly improved the understanding of the degradation behaviours in OPVs. These observation can ultimately assist in the pursuit of OPVs with higher stability which is a vital step towards large scale commercial application of OPVs.

Bibliography

1. Darling, S. B. & You, F. The case for organic photovoltaics. *RSC Adv.* **3**, 17633–17648 (2013).
2. Green, Martin, A., Emery, K., Hishikawa, Y., Warta, W. & Dunlop, E. D. Solar cell efficiency tables (version 44). *Prog. Photovoltaics Res. Appl.* **22**, 701–710 (2014).
3. Carlé, J. E. & Krebs, F. C. Technological status of organic photovoltaics (OPV). *Sol. Energy Mater. Sol. Cells* **119**, 309–310 (2013).
4. Jørgensen, M. *et al.* Stability of Polymer Solar Cells. *Adv. Mater.* **24**, 580–612 (2012).
5. *Polymer Photovoltaics: A Practical Approach*. 336 (SPIE - International Society for Optical engineering, 2008). at <<http://spie.org/Publications/Book/737854>>
6. Jørgensen, M. *et al.* The state of organic solar cells—A meta analysis. *Sol. Energy Mater. Sol. Cells* **119**, 84–93 (2013).
7. Jørgensen, M., Norrman, K. & Krebs, F. C. Stability/degradation of polymer solar cells. *Sol. Energy Mater. Sol. Cells* **92**, 686–714 (2008).
8. Krebs, F. C. & Norrman, K. Analysis of the Failure Mechanism for a Stable Organic Photovoltaic During 10 000 h of Testing. *Prog. Photovoltaics Res. Appl.* **15**, 697–712 (2007).
9. Rivaton, A. *et al.* Photostability of organic materials used in polymer solar cells. *Polym. Int.* **63**, 1335–1345 (2014).
10. Zimmermann, Y.-S. *et al.* Organic photovoltaics: Potential fate and effects in the environment. *Environ. Int.* **49**, 128–40 (2012).
11. Grossiord, N., Kroon, J. M., Andriessen, R. & Blom, P. W. M. Degradation mechanisms in organic photovoltaic devices. *Org. Electron.* **13**, 432–456 (2012).
12. Andreasen, B. & Norrman, K. in *Stability and Degradation of Organic and Polymer Solar Cells* (ed. Krebs, F. C.) 17–38 (John Wiley & Sons, Ltd., 2012).
13. Benninghoven, A. & Wiley, J. The development of SIMS and international SIMS conferences : a personal retrospective view. 2–11 (2011). doi:10.1002/sia.3688
14. Heinemann, M. D., Thummalakunta, L. N. S. A., Yong, C. H. & Luther, J. Formation and Characterisation of Solution Processed “ Pseudo-Bilayer ” Organic Solar Cells. **1**, 291–298 (2011).
15. Yu, B. *et al.* Effect of Fabrication Parameters on Three-Dimensional Nanostructures of Resolution Scanning ToF-SIMS. *ACS Nano* **4**, 833–840 (2010).
16. Vedraïne, S. *et al.* <title>Surface plasmon effect on metallic nanoparticles integrated in organic solar cells</title>. **8172**, 81720G–81720G–6 (2011).
17. Franquet, a. *et al.* Characterization of organic solar cell materials by G-SIMS. *Surf. Interface Anal.* **45**, 430–433 (2013).

Bibliography

18. Larsen-Olsen, T. T. *et al.* Simultaneous multilayer formation of the polymer solar cell stack using roll-to-roll double slot-die coating from water. *Sol. Energy Mater. Sol. Cells* **97**, 22–27 (2012).
19. Larsen-Olsen, T. T. *et al.* Roll-to-roll processed polymer tandem solar cells partially processed from water. *Sol. Energy Mater. Sol. Cells* **97**, 43–49 (2012).
20. Bulle-lieuwma, C. W. T., Gennip, W. J. H. Van & Duren, J. K. J. Van. Characterization of polymer solar cells by TOF-SIMS depth pro @ ling. **204**, 547–550 (2003).
21. Smentkowski, V. S. *et al.* ToF-SIMS depth profiling of organic solar cell layers using an Ar cluster ion source. *J. Vac. Sci. Technol. A Vacuum, Surfaces, Film.* **31**, 030601 (2013).
22. Norrman, K. & Krebs, F. C. Oxygen and water induced degradation of polymer solar cells – normal versus inverted geometry. *Energy*
23. Norrman, K., Madsen, M. V, Gevorgyan, S. a & Krebs, F. C. Degradation patterns in water and oxygen of an inverted polymer solar cell. *J. Am. Chem. Soc.* **132**, 16883–92 (2010).
24. Hermenau, M. *et al.* Solar Energy Materials & Solar Cells Water and oxygen induced degradation of small molecule organic solar cells. *Sol. Energy Mater. Sol. Cells* 1–10 (2011). doi:10.1016/j.solmat.2011.01.001
25. Norrman, K., Larsen, N. & Krebs, F. Lifetimes of organic photovoltaics: Combining chemical and physical characterisation techniques to study degradation mechanisms. *Sol. Energy Mater. Sol. Cells* **90**, 2793–2814 (2006).
26. Andreasen, B. *et al.* TOF-SIMS investigation of degradation pathways occurring in a variety of organic photovoltaic devices--the ISOS-3 inter-laboratory collaboration. *Phys. Chem. Chem. Phys.* **14**, 11780–11799 (2012).
27. Lee, J. L. S. & Gilmore, I. S. in *Surface Analysis - The Principal Techniques* (eds. Vickerman, J. C. & Gilmore, I. S.) 563–612 (John Wiley & Sons, Ltd., 2009).
28. Graham, D. J. & Castner, D. G. Multivariate Analysis of ToF-SIMS Data from Multicomponent Systems : The Why , When , and How. (2012). doi:10.1007/s13758-012-0049-3
29. Rasmus Bro. Multi-way Analysis in the Food Industry. 1–311 (Royal Veterinary and Agricultural University of Denmark, 1998).
30. Bro, R. & Smilde, A. K. Principal component analysis. *Anal. Methods* **6**, 2812 (2014).
31. Scurr, D. J. *et al.* Strategies for MCR image analysis of large hyperspectral data-sets. *Surf. Interface Anal.* **45**, 466–470 (2013).
32. Aoyagi, S. *et al.* Evaluation of white radish sprouts growth influenced by magnetic fields using TOF-SIMS and MCR. *Surf. Interface Anal.* **45**, 264–267 (2013).
33. Gallagher, N. B. *et al.* Curve resolution for multivariate images with applications to TOF-SIMS and Raman. *Chemom. Intell. Lab. Syst.* **73**, 105–117 (2004).
34. Smentkowski, V. S., Ostrowski, S. G. & Keenan, M. R. A comparison of multivariate statistical analysis protocols for ToF-SIMS spectral images. *Surf. Interface Anal.* **41**, 88–96 (2009).

35. Lee, J. L. S., Gilmore, I. S., Fletcher, I. W. & Seah, M. P. Multivariate image analysis strategies for ToF-SIMS images with topography. *Surf. Interface Anal.* **41**, 653–665 (2009).
36. Reese, M. O. *et al.* Solar Energy Materials & Solar Cells Consensus stability testing protocols for organic photovoltaic materials and devices. **95**, 1253–1267 (2011).
37. Tanenbaum, D. M. *et al.* The ISOS-3 inter-laboratory collaboration focused on the stability of a variety of organic photovoltaic devices. *RSC Adv.* (2012). doi:10.1039/c1ra00686j
38. Rösch, R. *et al.* Investigation of the degradation mechanisms of a variety of organic photovoltaic devices by combination of imaging techniques—the ISOS-3 inter-laboratory collaboration. *Energy Environ. Sci.* **5**, 6521 (2012).
39. Teran-Escobar, G. *et al.* On the stability of a variety of organic photovoltaic devices by IPCE and in situ IPCE analyses - the ISOS-3 inter-laboratory collaboration. *Phys. Chem. Chem. Phys.* **14**, 11824–11845 (2012).
40. Abdou, M. S. A. *et al.* Interaction of Oxygen with Conjugated Polymers: Charge Transfer Complex Formation with Poly(3-alkylthiophenes). **7863**, 4518–4524 (1997).
41. Marchesi, F., Ripolles-sanchis, T., Pereira, E. C., Guerrero, A. & Boix, P. P. Solar Energy Materials & Solar Cells Oxygen doping-induced photogeneration loss in P3HT : PCBM solar cells. **100**, 185–191 (2012).
42. Aguirre, a., Meskers, S. C. J., Janssen, R. a. J. & Egelhaaf, H.-J. Formation of metastable charges as a first step in photoinduced degradation in π -conjugated polymer:fullerene blends for photovoltaic applications. *Org. Electron.* **12**, 1657–1662 (2011).
43. Madsen, M. V., Norrman, K. & Krebs, F. C. Oxygen- and water-induced degradation of an inverted polymer solar cell: the barrier effect. *J. Photonics Energy* **1**, 011104 (2011).
44. Madsen, M. V *et al.* Ellipsometry as a Nondestructive Depth Profiling Tool for Roll-to-Roll Manufactured Flexible Solar Cells. 10817–10822 (2011).
45. Voroshazi, E. *et al.* Influence of cathode oxidation via the hole extraction layer in polymer : fullerene solar cells. *Org. Electron.* **12**, 736–744 (2011).
46. Krebs, F. C. & Norrman, K. Using light-induced thermocleavage in a roll-to-roll process for polymer solar cells. *ACS Appl. Mater. Interfaces* **2**, 877–87 (2010).
47. Lira-Cantu, M., Norrman, K., Andreasen, J. W. & Krebs, F. C. Oxygen Release and Exchange in Niobium Oxide MEHPPV Hybrid Solar Cells. *Chem. Mater.* **18**, 5684–5690 (2006).
48. Manceau, M., Rivaton, A. & Gardette, J. The mechanism of photo-and thermooxidation of poly (3-hexylthiophene)(P3HT) reconsidered. *Polym. Degrad.* **94**, 898–907 (2009).
49. Manceau, M., Rivaton, A., Gardette, J.-L., Guillerez, S. & Lemaître, N. Light-induced degradation of the P3HT-based solar cells active layer. *Sol. Energy Mater. Sol. Cells* **95**, 1315–1325 (2011).
50. Tromholt, T., Manceau, M., Helgesen, M., Carlé, J. E. & Krebs, F. C. Degradation of semiconducting polymers by concentrated sunlight. *Sol. Energy Mater. Sol. Cells* **95**, 1308–1314 (2011).

Bibliography

51. Hintz, H., Egelhaaf, H.-J., Peisert, H. & Chassé, T. Photo-oxidation and ozonization of poly(3-hexylthiophene) thin films as studied by UV/VIS and photoelectron spectroscopy. *Polym. Degrad. Stab.* **95**, 818–825 (2010).
52. Abad, J., Urbina, a. & Colchero, J. Kelvin probe microscopy and current images of the degradation process of layered poly-3-octyl-thiophene structures. *Eur. Polym. J.* (2013). doi:10.1016/j.eurpolymj.2013.04.031
53. Sai, N., Leung, K., Zádor, J. & Henkelman, G. First principles study of photo-oxidation degradation mechanisms in P3HT for organic solar cells. *Phys. Chem. Chem. Phys.* **16**, 8092–9 (2014).
54. Tournebize, A. *et al.* New Insights into the Mechanisms of Photodegradation/Stabilization of P3HT:PCBM Active Layers Using Poly(3-hexyl - d 13 -Thiophene). *Chem. Mater.* **25**, 4522–4528 (2013).
55. Tromholt, T., Madsen, M. V., Carlé, J. E., Helgesen, M. & Krebs, F. C. Photochemical stability of conjugated polymers, electron acceptors and blends for polymer solar cells resolved in terms of film thickness and absorbance. *Journal of Materials Chemistry* **22**, 7592 (2012).
56. Madsen, M. V. *et al.* Influence of processing and intrinsic polymer parameters on photochemical stability of polythiophene thin films. *Polym. Degrad. Stab.* **97**, 2412–2417 (2012).
57. Guerrero, A. *et al.* Oxygen doping-induced photogeneration loss in P3HT:PCBM solar cells. *Sol. Energy Mater. Sol. Cells* **100**, 185–191 (2012).
58. Moulder, J. F., Stickle, P. E. & Bomben, K. *Handbook of X-ray Photoelectron Spectroscopy*. (Physical Electronics Inc., 1992).
59. Keenan, M. R. & Kotula, P. G. Accounting for Poisson noise in the multivariate analysis of ToF-SIMS spectrum images †. 203–212 (2004). doi:10.1002/sia.1657
60. Keenan, M. Optimal scaling of TOF-SIMS spectrum-images prior to multivariate statistical analysis. *Appl. Surf. Sci.* **231-232**, 240–244 (2004).
61. Lee, J. Time-of-Flight Secondary Ion Mass Spectrometry – Fundamental Issues for Quantitative Measurements and Multivariate Data Analysis Time-of-Flight Secondary Ion Mass Spectrometry – Fundamental Issues for. (2011).
62. Seah, M. P., Green, F. M. & Gilmore, I. S. Cluster Primary Ion Sputtering : Secondary Ion Intensities in Static SIMS of Organic. 5351–5359 (2010).
63. Seah, M. P. & Gilmore, I. S. Cluster primary ion sputtering: correlations in secondary ion intensities in TOF SIMS. *Surf. Interface Anal.* **43**, 228–235 (2011).
64. van-Bavel, S. S., Sourty, E., de With, G. & Loos, J. Three-dimensional nanoscale organization of bulk heterojunction polymer solar cells. *Nano Lett.* **9**, 507–13 (2009).
65. Van Bavel, S., Sourty, E., de With, G., Veenstra, S. & Loos, J. Three-dimensional nanoscale organization of polymer solar cells. *J. Mater. Chem.* **19**, 5388 (2009).
66. Oh, J. Y., Jang, W. S., Lee, T. Il, Myoung, J.-M. & Baik, H. K. Driving vertical phase separation in a bulk-heterojunction by inserting a poly(3-hexylthiophene) layer for highly efficient organic solar cells. *Appl. Phys. Lett.* **98**, 023303 (2011).

67. Petrat, F. M., Wolany, D., Schwede, B. C., Wiedmann, L. & Benninghoven, a. In situ ToF-SIMS/XPS investigation of nitrogen plasma-modified polystyrene surfaces. *Surf. Interface Anal.* **21**, 274–282 (1994).
68. Benninghoven, a. Chemical Analysis of Inorganic and Organic Surfaces and Thin Films by Static Time-of-Flight Secondary Ion Mass Spectrometry (TOF-SIMS). *Angew. Chem. Int. Ed. Engl.* **33**, 1023–1043 (1994).
69. Truica-Marasescu, F. & Wertheimer, M. R. Vacuum Ultraviolet-Induced Photochemical Nitriding of Polyolefin Surfaces. *J. Appl. Polym. Sci.* **91**, 3886 (2004).
70. Romero-Sánchez, M. D., Mercedes Pastor-Blas, M., Martín-Martínez, J. M. & Walzak, M. J. Addition of ozone in the UV radiation treatment of a synthetic styrene-butadiene-styrene (SBS) rubber. *Int. J. Adhes. Adhes.* **25**, 358–370 (2005).
71. Andersen, T. R. *et al.* Aqueous processing of low-band-gap polymer solar cells using roll-to-roll methods. *ACS Nano* **5**, 4188–4196 (2011).
72. Villarrubia, J. S. Algorithms for Scanned Probe Microscope Image Simulation, Surface Reconstruction, and Tip Estimation. **102**, (1997).
73. Hoo, C. M., Starostin, N., West, P. & Mecartney, M. L. A comparison of atomic force microscopy (AFM) and dynamic light scattering (DLS) methods to characterize nanoparticle size distributions. *J. Nanoparticle Res.* **10**, 89–96 (2008).
74. Boyd, R. D. & Cuenat, A. New analysis procedure for fast and reliable size measurement of nanoparticles from atomic force microscopy images. (2010). doi:10.1007/s11051-010-0007-2
75. Dias, A., BUONO, V. T. L., VILELA, J. M. C., Andrade, M. & Lima, T. Particle size and morphology of hydrothermally processed MnZn ferrites observed by atomic force microscopy. *J. Mater. Sci.* **32**, 4715–4718 (1997).
76. Alstrup, J., Jørgensen, M., Medford, A. J. & Krebs, F. C. Ultra Fast and Parsimonious Materials Screening for Polymer Solar Cells Using Differentially Pumped Slot-Die Coating. *ACS Appl. Mater. Interfaces* **2**, 100929091656071 (2010).
77. Carlé, J. E. *et al.* Comparative studies of photochemical cross-linking methods for stabilizing the bulk hetero-junction morphology in polymer solar cells. *J. Mater. Chem.* **22**, 24417–24423 (2012).
78. Bertho, S. *et al.* Effect of temperature on the morphological and photovoltaic stability of bulk heterojunction polymer:fullerene solar cells. *Sol. Energy Mater. Sol. Cells* **92**, 753–760 (2008).
79. Drees, M. *et al.* Stabilization of the nanomorphology of polymer–fullerene “bulk heterojunction” blends using a novel polymerizable fullerene derivative. *J. Mater. Chem.* **15**, 5158 (2005).
80. Kim, B. J., Miyamoto, Y., Ma, B. & Fréchet, J. M. J. Photocrosslinkable polythiophenes for efficient, thermally stable, organic photovoltaics. *Adv. Funct. Mater.* **19**, 2273–2281 (2009).
81. Griffini, G. *et al.* Long-term thermal stability of high-efficiency polymer solar cells based on photocrosslinkable donor-acceptor conjugated polymers. *Adv. Mater.* **23**, 1660–1664 (2011).
82. Gholamkhash, B. & Holdcroft, S. Toward stabilization of domains in polymer bulk heterojunction films. *Chem. Mater.* **22**, 5371–5376 (2010).

Bibliography

83. Kim, H. J. *et al.* Solvent-resistant organic transistors and thermally stable organic photovoltaics based on cross-linkable conjugated polymers. *Chem. Mater.* **24**, 215–221 (2012).
84. Hsieh, C. H. *et al.* Highly efficient and stable inverted polymer solar cells integrated with a cross-linked fullerene material as an interlayer. *J. Am. Chem. Soc.* **132**, 4887–4893 (2010).
85. Nam, C. *et al.* Supporting Information : Photocrosslinkable azide-functionalized polythiophene for thermally stable bulk heterojunction solar cells. 3–5 (2012).

Appendix A

Supporting information to Chapter 3

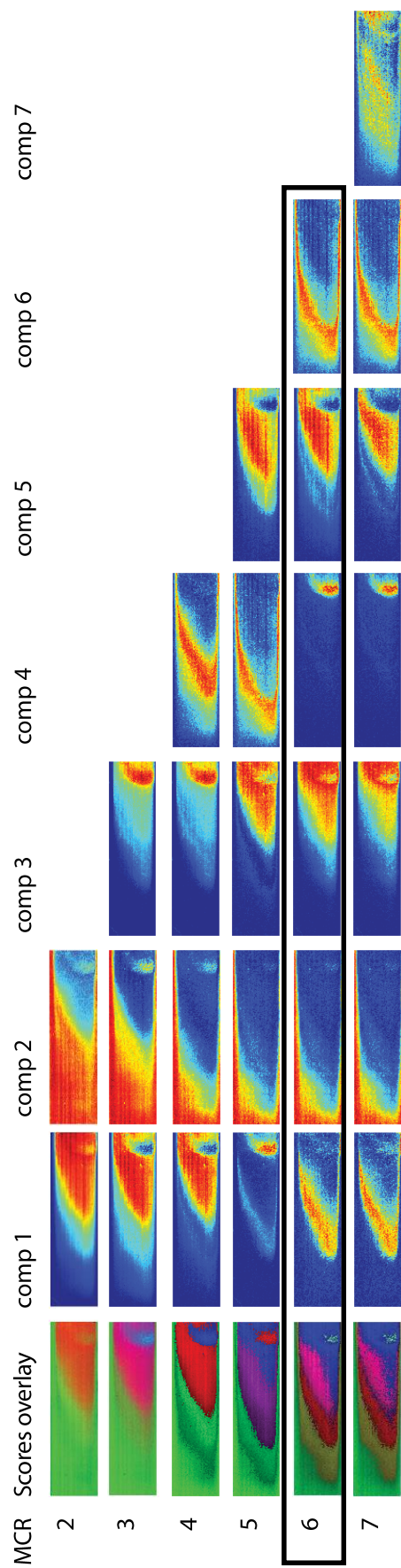


Figure A. 1 The calculated scores plots from the different compound no. MCR models are illustrated for sample P3HT Bi3+. The no. of components used for each model is indicated in the left hand side MCR column. The scores overlay is an overlay of each of the component score plots for that particular model (the overlays are falsely coloured). The comp no. columns are the score plots for that particular component in that particular MCR model (the colour bar used is the same as in Figure 3.4b). The black box indicates what component no. was chosen in the onwards analysis.

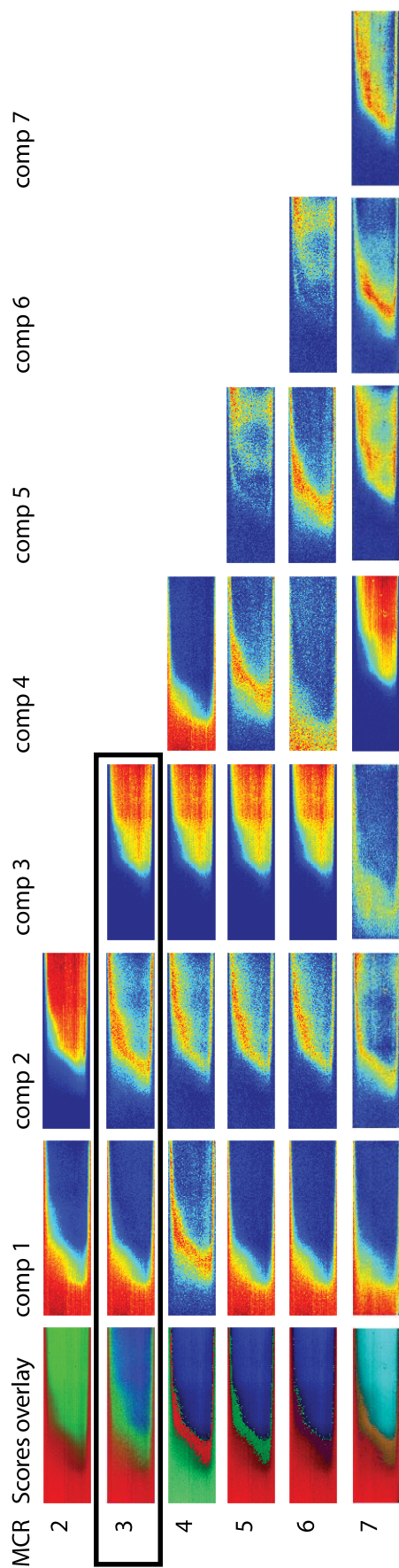


Figure A. 2 The calculated scores plots from the different compound no. MCR models are illustrated for sample P3HT:PCBM Bi+. The no. of components used for each model is indicated in the left hand side MCR column. The scores overlay is an overlay of each of the component score plots for that particular model (the overlays are falsely coloured). The comp no. columns are the score plots for that particular component in that particular MCR model (the colour bar used is the same as in Figure 3.4b). The black box indicates what component no. was chosen in the onwards analysis.

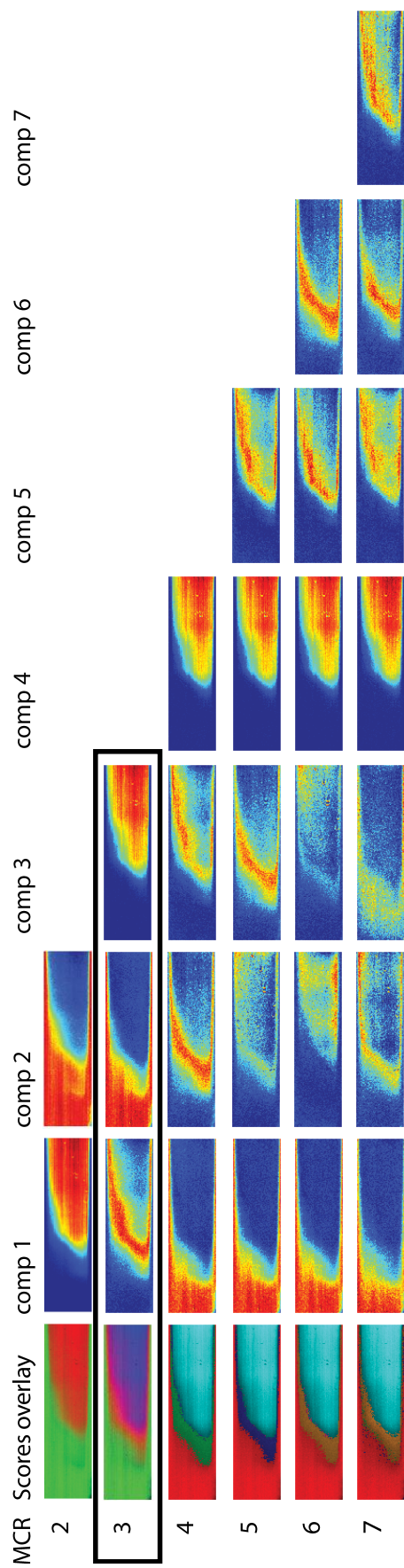


Figure A. 3 The calculated scores plots from the different compound no. MCR models are illustrated for sample P3HT:PCBM Bi_3^+ . The no. of components used for each model is indicated in the left hand side MCR column. The scores overlay is an overlay of each of the component score plots for that particular model (the overlays are falsely coloured). The comp no. columns are the score plots for that particular component in that particular MCR model (the colour bar used is the same as in Figure 3.4b). The black box indicates what component no. was chosen in the onwards analysis.

Table A. 1 Percent variance captured by the MCR 6 component model calculated using the P3HT Bi₃⁺ stripe.

MCR component #	Fit (% Model)	Fit (% X)	Cumulative Fit (% X)
1	6.77	6.51	6.51
2	7.83	7.53	14.03
3	41.55	39.94	53.97
4	3.41	3.28	57.25
5	31.94	30.71	87.96
6	8.50	8.17	96.13

Table A. 2 Percent variance captures by the MCR 3 component model calculates using the P3HT:PCBM Bi⁺ stripe.

MCR component #	Fit (% Model)	Fit (% X)	Cumulative Fit (% X)
1	28.30	25.09	25.09
2	10.32	9.15	34.24
3	61.38	54.43	88.67

Table A. 3 Percent variance captures by the MCR 3 component model calculates using the P3HT:PCBM Bi₃⁺ stripe.

MCR component #	Fit (% Model)	Fit (% X)	Cumulative Fit (% X)
1	9.66	9.21	9.21
2	11.58	11.04	20.25
3	78.76	75.08	95.33

Appendix B

The thesis is based on the following publications

- Jørgensen, M. *et al.* Stability of Polymer Solar Cells. *Adv. Mater.* **24**, 580–612 (2012).
- Andreasen, B. *et al.* TOF-SIMS investigation of degradation pathways occurring in a variety of organic photovoltaic devices--the ISOS-3 inter-laboratory collaboration. *Phys. Chem. Chem. Phys.* **14**, 11780–11799 (2012). Reproduced by permission of the PCCP Owner Societies
- Andersen, T. R. *et al.* Aqueous processing of low-band-gap polymer solar cells using roll-to-roll methods. *ACS Nano* **5**, 4188–4196 (2011). Reprinted with permission from ACS Nano. Copyright 2011 American Chemical Society.
- Carlé, J. E. *et al.* Comparative studies of photochemical cross-linking methods for stabilizing the bulk hetero-junction morphology in polymer solar cells. *J. Mater. Chem.* **22**, 24417–24423 (2012). Reproduced by permission of The Royal Society of Chemistry
- Larsen-Olsen, T. T. *et al.* Simultaneous multilayer formation of the polymer solar cell stack using roll-to roll double slot-die coating from water. *Sol. Energy Mater. Sol. Cells* **97**, 22–27 (2012). Reprinted with permission from Elsevier
- Larsen-Olsen, T. T. *et al.* Roll-to-roll processed polymer tandem solar cells partially processed from water. *Sol. Energy Mater. Sol. Cells* **97**, 43–49 (2012). Reprinted with permission from Elsevier

Stability of Polymer Solar Cells

Mikkel Jørgensen, Kion Norrman, Suren A. Gevorgyan, Thomas Tromholt, Birgitta Andreasen, and Frederik C. Krebs*

Organic photovoltaics (OPVs) evolve in an exponential manner in the two key areas of efficiency and stability. The power conversion efficiency (PCE) has in the last decade been increased by almost a factor of ten approaching 10%. A main concern has been the stability that was previously measured in minutes, but can now, in favorable circumstances, exceed many thousands of hours. This astonishing achievement is the subject of this article, which reviews the developments in stability/degradation of OPVs in the last five years. This progress has been gained by several developments, such as inverted device structures of the bulk heterojunction geometry device, which allows for more stable metal electrodes, the choice of more photostable active materials, the introduction of interfacial layers, and roll-to-roll fabrication, which promises fast and cheap production methods while creating its own challenges in terms of stability.

1. Introduction

1.1. The Solar Cells and Their Instabilities

The ideal photovoltaic device or solar cell should present constant performance over time when illuminated and also show little dependence on being subject to cyclic changes in the environment light/dark, hot/cold, dry/humid. Historically this is observed to have become increasingly incorrect as new solar cell technologies have evolved. The very first solar cell that qualifies as a technology is the monocrystalline silicon solar cell developed at Bell Laboratories in the 1950s by Chapin, Fuller, and Pearson.^[1] The monocrystalline silicon exhibited little degradation in performance that could be linked to a failure in the internal components and mechanism of operation but presented a reversible loss in performance with increasing temperature that was well explained by semiconductor theory. From the birth of the solar cell as a technology it was thus not an integral part of the understanding that such a device could exhibit instability, unpredictable or dynamic performance. One drawback of the monocrystalline silicon solar cell

was the significant loss in material when sawing the ingots into wafers (known as kerf loss) and also the appreciable thickness of the wafers (~0.25–1 mm). In an effort to decrease the manufacturing cost of the technology massive research efforts were dedicated towards realizing the thin film solar cell with the idea of lowering the thermal budget and the materials usage. This quickly bore fruit and impressively early the amorphous silicon solar cell was described by Carlson and Wronski in 1976 as a thin film solar cell prepared using vacuum techniques at relatively lower temperatures.^[2] The immediate reaction from the community was that the costly crystalline technology had come to an end. However, this rapidly changed when Staebler and Wronski reported a phenomenon that

was unprecedented within the established field of solar cells. This phenomenon became known as the Staebler–Wronski effect^[3] and is the observation of a rapid decrease in performance when the solar cell is illuminated. Clearly an unpleasant surprise at the time and while Staebler and Wronski reported that the effect was reversible when subjected to a high temperature treatment it was a show stopper. At this point one of two things could happen; the invention could be left as a scientific curiosity with no practical implications (and perhaps forgotten) or scientists could pick up the challenge and figure out what the reasons were and from there perhaps find a cure for the problem. Fortunately the latter happened and while this meant that it took a relatively long time before the amorphous silicon solar cell became commercially available for electrical energy production, it also meant that the scientific and technological community became accustomed to the fact that a solar cell may present a degradative behavior and while best avoided that this might not be a complete show stopper or a challenge for which no solution exists even if it is not a complete cure. Since amorphous silicon was described several thin film technologies have evolved each with their Achilles heel and each with a solution to the problems. At the very end of this relatively long list of technologies we find the polymer and organic solar cells that present the greatest potential in terms of cost, scalability and environmental impact. They however also present the most complex selection of degradation phenomena. When viewed from above one could say that the first incarnations of “the solar cell” had a simple constitution/process and therefore the possibilities for failure were limited. The more elaborate the solar cell has become the larger the choice of constitution and

Dr. M. Jørgensen, Dr. K. Norrman, Dr. S. A. Gevorgyan, T. Tromholt, B. Andreasen, Prof. F. C. Krebs
Risø National Laboratory for Sustainable Energy
Technical University of Denmark
Frederiksborgvej 399, DK-4000 Roskilde, Denmark
E-mail: frkr@risoe.dtu.dk



DOI: 10.1002/adma.201104187

process and in turn the room for unforeseen failure modes increases. The polymer solar cell is currently the ultimate in terms of complexity and presents enormous variability in all aspects. It is therefore not unexpected that the polymer solar cell (and to some extent the small molecule organic solar cell) presents the most uncontrollable situation in terms of stability. This is also supported by the observation of the number of scientific reports on stability/degradation of solar cells by category. For the crystalline silicon solar cells this is a very limited body of information where the focus has been on extrinsic failure paths such as yellowing of the encapsulation materials or corrosion of the electrical connections.^[4–10] For the thin film devices such as amorphous silicon (a-Si), cadmium telluride (CdTe) or copper indium gallium diselenide (CIGS) there is more literature dedicated to degradation phenomena. Both detailed mechanistic studies, modeling and technological solutions have been reported for a-Si^[11–21] and more phenomenological studies and elucidation of degradation mechanisms for CdTe^[22–28] and CIGS^[29–41] linked to back electrode diffusion and water ingress. For the polymer and organic solar cells the existing body of literature on degradation far exceed all the other technologies taken as a whole and this significant point has to be considered while remembering that the polymer and organic solar cells are only about to enter the market.

1.2. When Organic Matter is Illuminated

The heart of the matter is that organic materials subjected to illumination (i.e., by sunlight) react via photolytic and photochemical reactions. This is an undisputable fact that has many implications when one wishes to apply organic materials either as a structural or a functional element with some degree of illumination. The list of possible photolytic and photochemical reactions is large and while some of them may be benign in a particular context some of those reactions inevitably lead to degradation of the performance when taking any given parameter as a metric (i.e., photovoltaic performance). It should at this point be added that the yield and rate of photochemical reactions span an enormous range with quantum yields ranging from the exceptionally low to nearly unity and rates that range from exceptionally low to very high. To complicate matters these photolytic and photochemical reactions are not only limited to the absorption of light but also to the presence of components from the atmosphere such as water and oxygen and the interfaces and components that constitute the device.

1.3. An Overview of the Field

An overview of the degradation of polymer and organic solar cells was presented by us in 2008^[42] and from the point of view of categorizing degradation phenomena in polymer and organic solar cells this earlier review still fully accounts for the understanding available today. There have however, been many developments since then in terms of processing, device structure, materials and scale that present new examples of degradation phenomena which warrant the detailed review that we present here. The earlier review covered the state-of-the-art



Frederik C. Krebs received his PhD from the Technical University of Denmark (2000) and has since then worked in the field of polymer solar cells at Risø National Laboratory for Sustainable Energy. He is currently professor at Risø DTU within areas of research that include new materials with low band gap and novel processing capability, large area processing and manufacture of polymer solar cells, all aspects of roll-to-roll printing-coating-processing and testing, life cycle analysis, stability and lifetime testing, degradation mechanism studies, outside testing and demonstration.



Mikkel Jørgensen received his Ph.D. in organic chemistry from the University of Copenhagen (1990). He worked as an industrial chemist at NycoMed during his Ph.D. studies and later at PNA Diagnostics before becoming employed as a senior Scientist at Risø National Laboratory for Sustainable Energy at the technical university of Denmark. Scientific interests include synthetic chemistry, nuclear Magnetic resonance, chemistry of materials, solar cells, polymers, and supramolecular chemistry.

from the first descriptions of polymer and organic solar cells until the end of 2007 where the next generation of materials started to appear with lower band gap and a larger degree of intrinsic stability. There has also been an increased general interest in device stability and degradation as a consequence of the increased interest from industry. Among the first questions a technological representative from industry asks is: how efficient is it, how stable is it, what is the cost and what is the required investment in infrastructure. The attempt to answer these questions has thus transcended into the research laboratories active within the field of OPV and has resulted in reports on stability with this industrial view in mind. We will in this review focus on the new additions to the field that have brought new understanding of degradation phenomena. When looking broadly at the field of OPV there have been numerous reviews and an exhaustive list would constitute a review in itself. To give the reader an overview; the field has been reviewed initially in attempts to encompass the entire field and later by specific reviews of the field with a view to a particular topic such as stability, materials, low band gap materials, device structures, physics, processing

and analysis methods. The most recent developments that have had a direct impact on the performance of polymer solar cells with respect to stability and degradation are listed in Figure 1:

General reviews;^[43–55] low band gap materials;^[56–59] materials;^[60–63] morphology;^[64–66] tandem structures;^[67–70] processing;^[71–73] hybrid materials;^[74–76] interfaces;^[77–79] physics;^[80–82] inverted and oxides materials.^[83–85]

When searching Thompson Reuters ISI web of knowledge for polymer/organic solar cells one finds that more than 12000 peer reviewed scientific articles in the form of original research articles, proceedings, and reviews. There are several hundred reviews, which is clearly too much to survey here. What it does show is that the field has grown exponentially from being a small research field to now being a relatively large research field

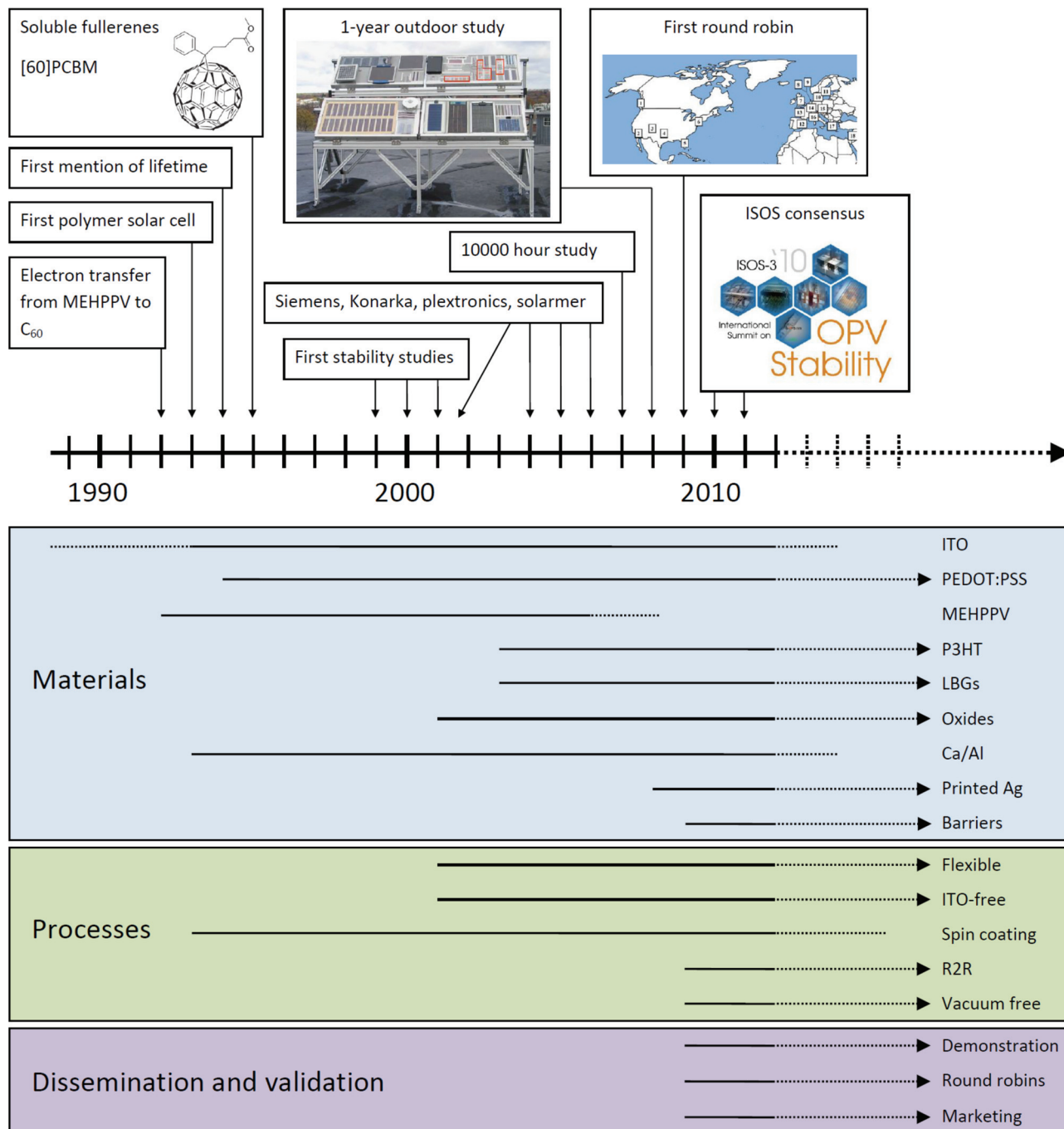


Figure 1. A schematic view of the timeline for polymer solar cell stability. Some important events have been highlighted above the timeline and some projections on the use of materials, processes and methods are shown below. The lines with arrow heads indicate timelines that the authors believe will continue into the future. Reproduced with permission: 1 year outdoor study,^[248] first round robin,^[221] ISOS consensus.^[223] Copyright 2008, 2009, and 2011, respectively, Elsevier.

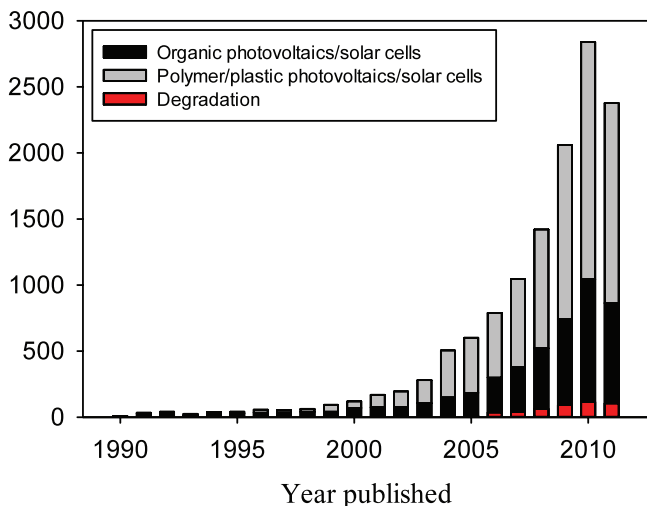


Figure 2. The number of peer reviewed scientific reports (on the y-axis) as a function of the year (on the x-axis) within the field of OPV covering broadly organic/polymer/plastic solar cells/photovoltaics. The time of search was September 2011 and for this reason not all of the scientific production in 2011 is accounted for. The number of publications from the same set that is related to degradation is also shown and accounts for less than 5% of the published work.

as shown in **Figure 2**. The field as a whole has received around 250,000 citations. When analyzing the field with respect to stability and degradation it is difficult to search the massive body using the search term “stability” as this descriptor has been used in many contexts not directly related to the operational stability of the solar cell (i.e., morphological stability, thermal stability, structural stability).

The use of the search term “degradation” has a more unique meaning and around 500 articles can be identified. As shown in **Figure 2** it is only recently that this area has attracted interest. It should at this point be stressed that there are several views that one can have on what stability or degradation means in the context of polymer or organic solar cells. The view we take here is with respect to the solar cell in operation albeit extended to the reasons for particularly stable operation or the causes of failure and mechanisms of degradation.

1.4. The Research

The research field of organic solar cells has diversified into at least three overlapping fractions, see **Figure 3**. The main topic is still on improving the power conversion efficiency (PCE) were the ever changing record value is >10% presented by Mitsubishi on their web page (www.mitsubishi.com). This represents an order of magnitude improvement since the first small organic molecule two-layer device described by C. W. Tang in 1986.^[86] Early reports on stability began to appear around 1990 with the advent of polymer (PPV) based solar cells^[87] and has slowly gained acceptance as an important branch of research in

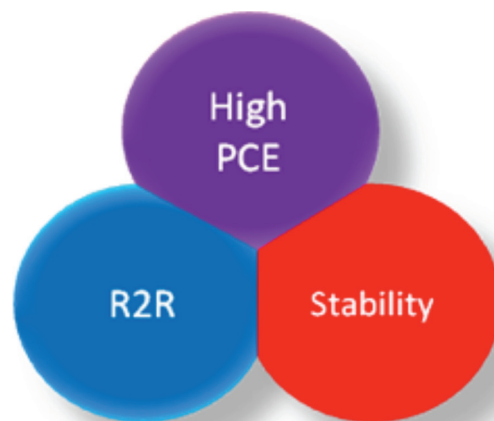


Figure 3. The three major organic solar cell research fields.

itself and has yielded impressive results. While the first polymer devices may have lasted only a few minutes when exposed to ambient conditions and full sun (AM1.5G) lifetimes of the order of many thousands of hours are now possible. The last topic that has appeared is research on roll-to-roll (R2R) fabricated devices and the appearance of several companies with products based on this technology. The R2R fabricated devices are as yet quite different from those prepared with the aim of obtaining a high PCE and do therefore present their own stability issues.

Two main device geometries exist: the normal (or traditional) and the inverted^[88,89] schematically represented in **Figure 4**. In the normal geometry the layer stack is usually built on top of a semitransparent indium tin oxide (ITO) electrode followed by a hole transport layer poly(3,4-ethylenedioxythiophene):poly(styrene sulfonate) (PEDOT:PSS), the active layer, an electron transport layer (e.g., LiF) and finally a low workfunction metal electrode (the cathode). In the inverted type geometry the order of the layers are reversed with the top metal electrode now being the hole collecting anode. The different order of the layers in the two geometries creates interfaces with different chemistries which may affect the stability. It is also very important

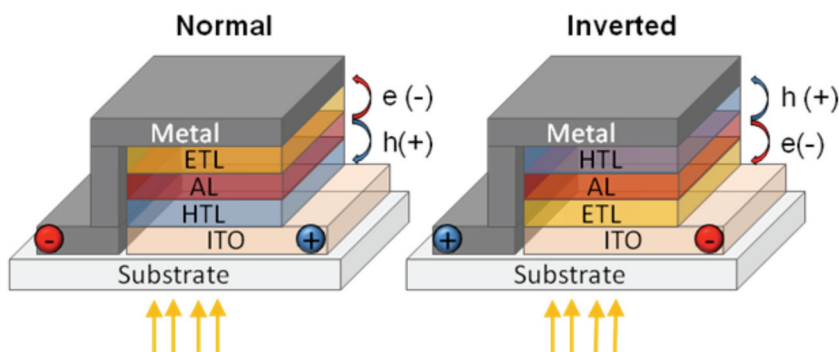


Figure 4. The normal (left) and inverted (right) device geometries with light entering from the bottom. ETL: electron transport layer; AL: active layer; HTL: hole transport layer; ITO: indium tin oxide electrode.

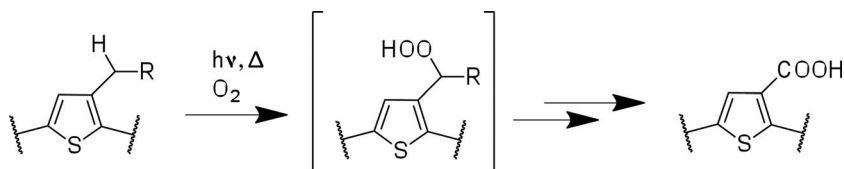
that different types of metal electrodes can be used in the two cases. Low workfunction metals such as aluminum and/or calcium are typically used as back electrodes in the normal geometry while higher work function metals such as silver are used in the inverted geometry. As a consequence the inverted geometry devices tend to be much more stable, while the normal geometry devices may still have an edge in power conversion efficiency.

The organization of this review reflects the developments in organic solar cell research. Great strides have been taken mainly in the area of materials stability that has enabled taking the devices out of the inert atmosphere glovebox environment. This has resulted in sharing devices between research groups validating results and contemplating their future use in actual products. The materials stability have been subdivided according to each of the typical layers that usually constitutes an OPV-device: active layer, electrodes, electron transport layer and hole transport layer, each contributing their own degradation mechanisms. The physical stability is also touched upon although less improvement seems to have been gained, presumably because this is an even more complex issue. Most devices rely on the bulk heterojunction concept although knowledge on what actually constitutes the optimal structure is still not clear and progress is gained by empirical trial-and-error methods. Enough workers have studied stability issues so that more rigorous standards on how to test organic solar cells have appeared, presently in the form of the ISOS-3 recommendations described later. Finally, R2R fabricated devices have been granted their own section.

2. Materials Stability

2.1. The Active Layer

The active layer component in the organic solar cell is the part of the device that is very prone to degradation and since it is integral to the device functionality this translates directly into a degradation of the power conversion efficiency. One of the most important reactions is photo-degradation with or without oxygen. It is also a research area where some large gains in terms of stability have been obtained so that device operation can now be measured in years rather than minutes. Many organic molecules and polymers are by nature set up to undergo photo oxidation and this was very evident with the poly-phenylenevinylene (PPV) type polymers used in the early days of OPV research. The photochemical decomposition of the PPV type polymer has been shown to involve both side chain degradation, but also attack at the vinylene moieties.^[90] Previously, the reactive species singlet oxygen was thought to be involved, but at recent investigation concluded that photoinduced electronic transfer leads to formation of the superoxide oxygen anion.^[91–93] Fortuitously, the next “work horse” material;

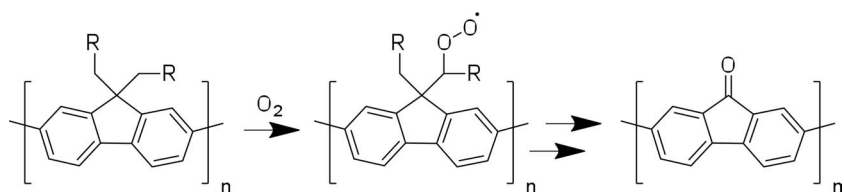


Scheme 1. Photo-oxidation mechanism according to Manceau et al. Reproduced with permission.^[94] Copyright 2010, Elsevier.

poly(3-hexyl-thiophene) (P3HT) was found to be orders of magnitude more stable^[94,95] allowing the development of e.g. R2R processing. Previously it was believed that the chemical reaction responsible for its degradation was direct attack on the thiophene ring by singlet oxygen, but instead it has been shown to be a side chain oxidation starting with a hydroperoxide formation at the benzylic position as shown in **Scheme 1**.^[96,97]

Films of P3HT are photo-oxidized fairly rapidly with complete bleaching after 700 hours depending on thickness. Adding PCBM slows this process considerably, presumably by sub nanosecond quenching the reactive excited state on P3HT^[98] forming a lower energy charge transfer complex. A study by Reese et al.^[99] concluded that oxidation of PCBM, creating species with up to eight oxygen atoms, formed traps for the electron transport decreasing the electron mobility. Schafferhans et al.^[100] similarly investigated the effect of oxygen doping of P3HT:PCBM blends and concluded that exposure to O₂ in the dark resulted in a loss of *J*_{sc} while all solar cell parameters were affected in light, all due to increased number of oxygen generated trap states. This is also in line with a previous study by Seemann et al. on the influence of oxygen on organic solar cells with gas permeable electrodes.^[101] The reaction between P3HT and oxygen may be initiated with an initial reversible formation of one or more meta-stable charge transfer states.^[102,103] ESR studies showed that charges were formed when P3HT:PCBM were illuminated and exposed to oxygen. This charge build-up could be reversed in vacuum indicating a weak P3HT⁺-O₂⁻ complex. Recent studies carried out with the analogous polymer poly-(3-octyl-thiophene) (P3OT) by Abad et al. concludes that the degradation mechanism involves UV-initiated ozone formation and that ozone is the reactive species responsible for the P3OT degradation.^[104,105]

Since then a large number of new polymers have been synthesized with the aim of covering more of the solar spectrum and hence improve the power conversion efficiency. In the majority of the publications on these new polymers has been focused solely on high efficiency while neglecting stability. The result is that although interesting many of the active materials based on these compounds may not be useful for real world applications. One example (**Scheme 2**) is the polyfluorenes that are used



Scheme 2. Proposed general degradation mechanism for fluorene containing polymers. Reproduced with permission.^[106] Copyright 2011, American Chemical Society.

as blue emitters in OLEDs, they have been shown to be prone to oxidation giving rise to an unwanted green emission (the so-called g-band). It has long been known that the end-product of the oxidation at the 9-position of fluorene is to produce fluorenone units. The mechanism has now been studied in more detail by Grisorio et al.^[106] who proposed a stepwise process starting with the side chain oxidation adjacent to the 9-position in the substituted fluorene. It seems that the fluorenone formation is so energetically favored that no matter what kind of substitution is chosen this degradation route will predominate for fluorene containing polymers, their conclusion was thus to seek other alternatives.

The photo stability of a large number of polymers has been investigated, most notably by Manceau et al.^[107] In their method the accumulated number of absorbed photons is calculated by taking UV-vis spectra at intervals during a time study where samples are exposed to light (1000 W m⁻², AM1.5G). The normalized number of absorbed photons are plotted versus time and compared for different polymers with a limited number of monomers. With this set of data the relative effect on the rate of photo degradation from each type of monomer could be established. With these results Manceau et al. created a ranking of some of the most commonly used monomers for creating polymers for OPV which could be set up as a crude guide for predicting photostability, see Figure 5.

Several inferences can be learned from these studies. Donor groups with side chains are the most susceptible to degradation; especially the fluorene and cyclopentadithiophene units impart low stability. The most stable donor monomers are clearly those without side chains. Though only one example is shown, it is interesting to note that substituting a carbon for silicon as the atom for attachment of the side groups increase the stability significantly.

This methodology clearly has a potential for rapid evaluation of a significant stability parameter and has already been used for selecting low band gap polymers for R2R coating.^[108] A smaller study by Kim et al. on three different polymers where actual devices were fabricated and the device efficiencies were followed as a function of time for a low band gap polymer (PININE-DTBT) with similar stability to P3HT was identified,^[109] see Figure 6. Another set of donor-acceptor polymers similar to the PININE-DTBT, but with different thieno[3,4-*b*]pyrazine acceptors were compared by the relative photo-chemical stability by Xia et al.^[110] who found that aryl side chains imparted higher stability relative to alkyl side chains. Finally, a study by Carlé et al. investigated the photostability of a series of three low band gap polymers with a common 2,3-bis(3-octyloxy)phenyl quinoxaline acceptor group and either thiophene, benzo-dithiophene or dithieno-thiophene donors.^[111] All showed superior stability compared to P3HT.

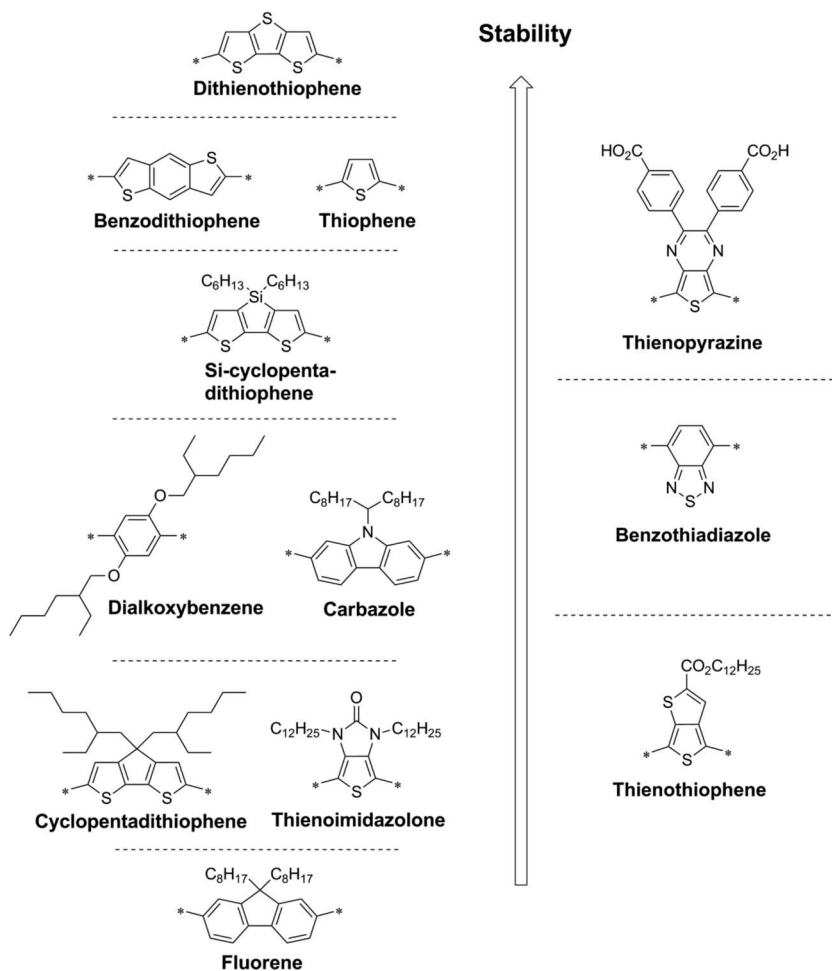


Figure 5. Rule-of-thumb photostability ranking of donor and acceptor monomers for OPV polymers. Adapted with permission.^[107] Copyright 2011, Royal Society of Chemistry.

The side chains are obviously the Achilles heel of these polymers in terms of photochemical stability and a possible solution is to remove them after film formation. One option is to incorporate heat labile groups that allow thermo-cleavage of the side groups. In a separate study Manceau et al. substituted simple alkyl side chains for tertiary alkyl ester groups that have previously been shown to cleave off completely at temperatures above 240 °C leaving the native backbone polymer.^[112] Examples of polymers where these thermo-cleavable groups were placed on either the donor or the acceptor moieties were investigated and shown to have much improved photo stability after the thermo-cleavage step.

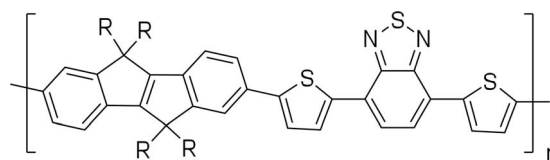


Figure 6. PININE-DTBT polymer with similar photo stability as P3HT.^[109]

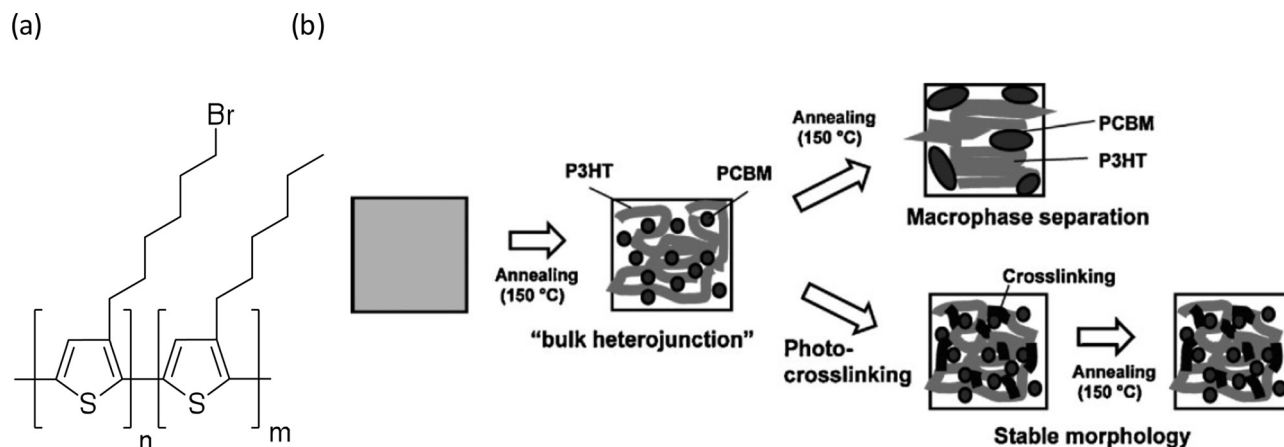


Figure 7. Bromo alkyl derivatives of P3HT for UV cross-linking (a) and the proposed stabilization route of the morphology (b). Reproduced with permission.^[134]

Another important problem with the bulk hetero-junction active layer is that it is a meta-stable structure that will evolve further with time even at ambient temperature. This affects the function of the delicate nano-structure that should be optimized for minimum exciton diffusion length and a maximum inner surface between the polymer hole transport and small molecule acceptor domains. The usual acceptors like PCBM forms nano crystalline domains that tend to grow in size.^[113,114] It has been studied by non-invasive methods such as energy dispersive X-ray reflectivity (EDXR) by Paci et al.^[115] The crystallization process is limited by the high viscosity of the polymer/acceptor mixture. Unfortunately, the side chains giving solubility to the polymer also lowers the T_g so that physical mobility of the polymer chains increases. When the solar cell devices are illuminated they heat up and may reach 80 °C in full sun (1000 W m⁻²) exacerbating the process. The activation energy for the phase segregation of MDMO-PPV and PCBM blends have been modeled from the short circuit current decay of devices based on this active material and found to be rather low (0.85 eV) corresponding to the rapid degradation observed.^[116] Ray and Alam developed a mathematical model for the short circuit current degradation as a function of how the domain sizes evolve with time at different temperatures.^[117] The influence of different processing parameters on the morphological stability have been studied by Kumar et al. who found that P3HT:PCBM films spin-coated with added 1,8-octanedithiol degraded much faster than films made from other solvents.^[118] The temperature used to dry the active layer film may also affect both efficiency and stability as shown by Lin et al.^[119] If the active layer film is dried at -5 °C compared to RT the efficiency increased from 3.23 to 4.70% and a storage half-life increased from 143 h to 1250 h. Also the regio-regularity of the P3HT seems to have a large effect. In a study with two regio-regularities of 94% and 98% Ebadian et al. showed that the devices based on the high regio-regular P3HT lost efficiency much faster than those based on the low regio-regular material.^[120] Most studies focus on the polymer part of the active material, but Johnson et al. have shown that variations in the acceptor material may also have a marked influence on

stability.^[121] Comparing the standard C₆₁-butyric acid methyl ester (PCBM) with the longer chain analogue C₆₁ butyric acid octadecyl ester (PCBOD) they found a slower initial decay of the efficiency with the latter acceptor compound.

One of the first solutions to be suggested was to chemically engineer a stable morphology by connecting the donor and acceptor parts by bonds to create block copolymers that would form stable bicontinuous networks for the hole and electron charge carriers by supra-molecular forces.^[122–125] For recent reviews see Topham et al.^[126] and Sommer et al.^[127] This strategy has not succeeded widely, perhaps due to overwhelming synthetic obstacles.

A few examples of devices with block copolymer materials exceeding 1% PCE have been reported.^[128,129] Instead alternating donor acceptor copolymers have become a main research theme in the form of low-band-gap polymers.^[156–159] A second strategy is to freeze the optimal nano-structure once it has been established in the film. Several options exist. Ryu et al.^[130] added a photocurable cross linking agent in the amount of 1–5% and obtained a slight increase in the power conversion efficiency, but no information about the effect on the stability was given. Sahu et al. explored polymers incorporating hydrogen a donor and acceptor group to form the cross links.^[131] A number of studies have incorporated cross-linkable groups in the side-chains. Farinhas et al. used the polymer F8T2Ox1 with reactive oxetane groups.^[132] Drees et al. introduced cross-linkable fullerenes with glycidol esters of PCBM.^[133] Kim et al.^[134] and Griffini et al.^[135] used UV cross-linkable bromo-alkyl side chains (**Figure 7**) and showed an increased thermal stability in the power conversion efficiency ascribed to stabilization of the morphology.

A somewhat similar approach has been studied by Gholamkhash and Holdcroft with an azide-functionalized graft copolymer of P3HT and polystyrene (**Figure 8**).^[136] After completing the polymer:PCBM devices they were heat treated at 140 °C with the intent of chemically linking the two components via the intermediate nitrene. Although the efficiency of the devices prepared were lower (1.73% PCE) they degraded substantially slower than similar standard P3HT:PCBM devices.

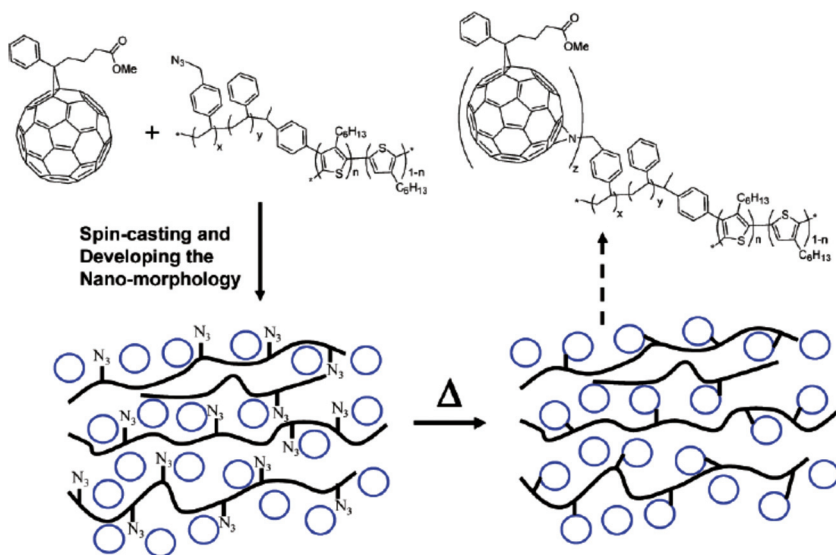
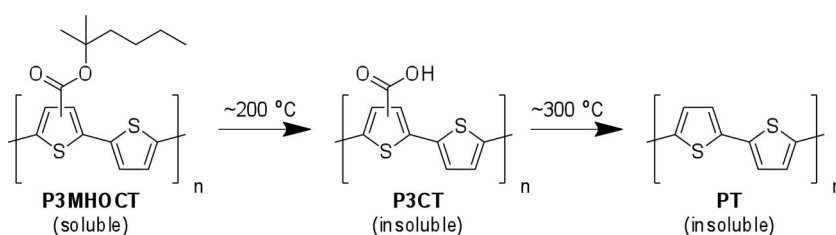


Figure 8. Cross-linking polymer and PCBM domain chemically. Reproduced with permission.^[136] Copyright 2010, American Chemical Society.



Scheme 3. Thermo-cleavage reaction of P3MHOCT to P3CT and PT.

The last and perhaps most successful option have been to remove the side chains altogether leaving the electro-optically active main chain polymer. Thermo-cleavable side groups in polythiophene type polymers intended for OPV were introduced by Liu et al. in 2004.^[137] To every second thiophene moiety a carboxylic ester of 2-methyl-2-hexanol was attached at the 3-position. Heating a film of this material to 200 °C for 60 minutes cleaved the ester function leaving the carboxylic acid function. The original purpose with this polymer was to create an interface layer between P3HT and a titanium oxide (TiO_x) layer improving the PCE. It was later realized that the thermo-cleavage reaction presented an opportunity for creating a rigid and thermally stable nano-morphology in the bulk heterojunction.^[138] The tertiary ester derivative of Liu et al., now called P3MHOCT (for poly-(3-(2-methylhexan-2-yl)-oxy-carbonyldithiophene) was found to cleave of the side chains in two distinct chemical steps (see **Scheme 3**). At about 200 °C the alkyl group is shed as a volatile alkene leaving the insoluble poly-3-carboxydithiophene (P3CT) and above 300 °C even the carboxylic acid group is lost leaving the native poly-thiophene (PT). Thermogravimetric analysis and solid state NMR were used to corroborate this sequence of reactions.^[139]

Solar cells based of P3MHOCT:PCBM were shown to decay rapidly, but when thermo-cleaved to P3CT:PCBM the power conversion efficiency remained stable for at least 4000 h of full sun (AM1.5 , 1000 W m^{-2}) albeit with low current density.^[140]

A detailed analysis of the failure mechanisms for this type of device during 10 000 h full sun concluded that oxidation of the metal electrode (Al) rather than of the active layer materials caused the slow degradation observed.^[141] In a later study, solar cells heat treated at different temperature between RT and 310 °C representing all three stages (P3MHOCT, P3CT and PT) with either [60]PCBM or [70]PCBM were prepared.^[138] The thermo-cleaved devices (P3CT and PT) were significantly more stable, but it was also observed that the power conversion efficiency went through a minimum for devices annealed at about 200 °C representing the P3CT. The best performing devices with an efficiency of 1.5% were those heated to 310 °C containing native polythiophene (PT), see **Figure 9**.

These studies were extended to R2R fabricated devices on heat stable Kapton substrates using a powerful light source to thermo-cleave the polymer.^[142] Thermo-cleavable side groups were also extended to a series of low band gap polymers based on diphenyldithienylthienopyrazine (**Figure 10**).^[143] This paper contains a careful analysis of different types of thermo-cleavable side groups and their synthesis. Solar cell devices based on these polymers were shown to possess remarkable stability towards oxygen, but show fairly rapid degradation in a humid environment. The work was extended to solar cells based on other types of low band gap polymers.^[144,145]

Thermo-cleavable polymers change from soluble to insoluble upon heat treatment and this can be exploited during device preparation. Tandem cell devices of polymer solar cells have been difficult to prepare because this would usually involve printing several organic soluble layers on top of each other. The solvent from the later layers will then tend to dissolve the underlying materials destroying the ordered geometry. With thermo-cleavable materials this can be avoided by including a heat treatment step between each layer deposition.^[146,147] Further modifications have yielded thermo-cleavable polymers with water soluble/miscible side chains^[148] and water based emulsion for processing the back cell in roll-to-roll coated tandem solar cells with significant differences in the lifetime performance of the two subcells.^[149]

2.2. The Metal Electrode

Aluminum and calcium metal films are highly reactive, but as long as they are kept in an oxygen and water free atmosphere in a glovebox environment or encased rigidly, this does not present a problem. In a real world application water and oxygen will always be present and will eventually lead to degradation. The rate of influx or transmission can to a certain extent be controlled by encapsulating the device as will be discussed later.

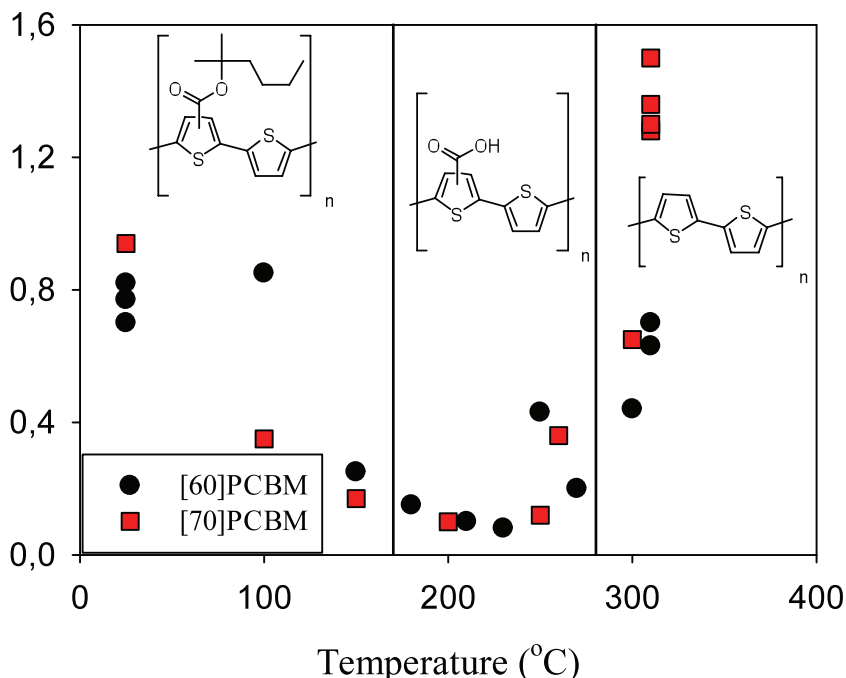


Figure 9. Thermo-cleavage study of P3MHOCT:PCBM devices showing a distinct minimum for the efficiency versus heat treatment temperature. Reproduced with permission.^[138] Copyright 2009, American Chemical Society.

Because of the low work function these metals can act as potent reducing agents especially if hydrogen donating reagents like water or alcohols are present. This mode of degradation has not been described yet and the dominant reaction seems instead to be diffusion of water through pores in the metal and reaction to form metal oxides at the interface between the metal and the rest of the device. This metal oxide layer is electrically insulating and creates a transport barrier eventually degrading the performance of the device as seen in the diode characteristics. Glatthaar et al. showed in a series of papers that this layer of Al₂O₃ gives rise to a capacitance that can be estimated from the layer thickness and that the IV curve changes shape from a standard exponential diode curve to one with an inflection point. This may erode the fill factor to a point where the device no longer produces power creating an S-shaped IV-curve.^[150,151]

A very similar S-shaped IV-curve also occurs for inverted structure devices with a photo-activated ZnO layer (vide supra). Many of the problems with the low work function metal electrodes have been described in an earlier review^[42] and will also be dealt with in a later section on oxygen/water degradation in this review.

The metal electrode in inverted devices can be selected from a wider range and is typically made of silver. Due to its less reactive nature it is not prone to degradation by oxygen or water. It is also attractive because it does not need to be evaporated onto the device in vacuum. Instead it is possible to print/coat emulsions with a high content of silver particles using industrially relevant techniques such as screen printing. This is one of the enabling technologies for roll-to-roll printing of organic solar cells. A number of commercial silver emulsions/pastes exist and they were of course not invented for use in organic solar cells and are therefore not equally suited for the task. Most have an organic binder that may be heat curable and some are even photo curable. An investigation of ten different silver emulsions showed a great variation in efficiency.^[152] Later a more detailed analysis showed that the organic binder used may partly destroy the underlying layers.^[153]

2.3. The Transparent Electrode

The ITO/organic interface has been implicated in the degradation of mainly small molecule organic solar cells. Sullivan and Jones^[154] have shown that devices with the structure: ITO/pentacene/C₆₀/BCP/Al deteriorates rapidly over a 70 min study in air. A kink in the J-V-characteristic increased progressively and eroded the PCE. They ascribed this to photo-oxidation of the pentacene at the ITO interface that could be retarded by an UV-filter. Another study by Schäfer et al.^[155] concluded that the work function of ozone treated ITO changed upon UV irradiation and caused a drop in the open-circuit voltage (V_{oc}) responsible for the observed degradation. Kanai et al.^[156] also studying small molecule organic solar cells observed a similar degradation and found that it could be prevented by inserting a 20 nm thick molybdenum oxide (MoO₃) layer between the ITO electrode and the organic part of the device. Cesium carbonate (Cs₂CO₃) has been used as an interfacial layer to lower the work function of the ITO.^[157,158]

2.4. The Electron Transport Layer

Several n-type materials have been explored as electron transport layer (ETL) in organic solar cells. One of the first was lithium fluoride (LiF)^[159,160] used for energy alignment and stability of the cathode interface. Recently, a mixture of C₆₀ and

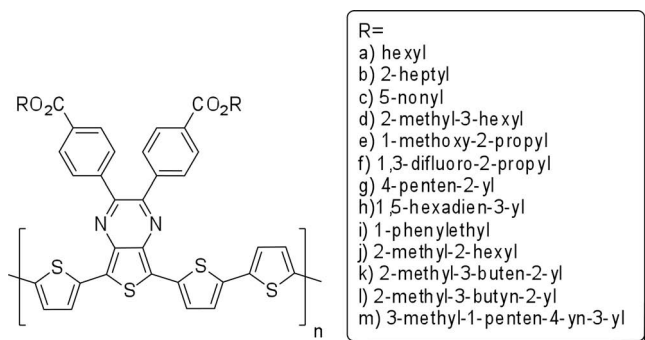


Figure 10. Examples of diphenyldithienylthienopyrazine with various thermocleavable side groups.

LiF has been explored for this purpose in bulk heterojunction solar cells.^[161,162] In addition to the enhanced current density the effect of this composite layer was to increase the device lifetime. A number of other types of buffer layers have been introduced for increasing the lifetime of devices with low work function metal electrodes. Sol-gel processed titanium suboxide (TiO_x)^[163,164] can be used, but is a relatively poor conductor in its amorphous form.^[165] A recent study by Li et al. concluded that TiO_x acts as a photochemically activated oxygen scavenger significantly enhancing the stability of P3HT:PCBM towards both UV exposure and oxygen.^[166] M. Wang et al. have applied thermally evaporated chromium oxide (CrO_x) between the active layer and the aluminum cathode to enhance stability.^[167] Later, M. Wang et al. showed a similar effect for copper oxide (CuO_x) as interface layer either alone or together with lithium fluoride.^[168] Y. Wang et al. found that a 1 nm thick layer of lithium benzoate improved both performance and stability.^[169] Similarly, the phosphine oxide 2,7-bis(diphenylphosphoryl)-9,9'-spirobifluorene has been used to improve the thermostability.^[170] An early example of using cesium carbonate as a cathode buffer layer was reported by Chen et al.^[171] A later comparative study between LiF and Cs_2CO_3 concluded that the latter is superior for enhancing both performance and stability of the devices.^[172] Jin et al. have shown that a thin (5 nm) cadmium selenide (CdSe) interface layer retards degradation.^[173] Zinc oxide (ZnO) has a high electron mobility and is therefore better suited as an ETL.^[174] It is used as an electron transport layer in inverted type devices e.g. ProcessOne roll-to-roll coated devices. It can be coated in the form of a precursor solution of zinc acetate or nanoparticles from water or alcohol solutions. The conductance of ZnO is variable and can be modulated by dopants, oxygen vacancies and Zn interstitial atoms.^[175,176] In addition it can be changed by exposure to UV-irradiation in the presence of oxygen. This has been exploited in diode devices with memory effects.^[177] In solar cell devices this variable conductance can have a dramatic effect where the device has to be pre-treated with exposure to UV-irradiation before full power

conversion efficiency is obtained. In such cases the IV-curve in the beginning exhibits a distinct S-shaped appearance that gradually changes into a normal IV-characteristic as ZnO is photo-oxidized. In the dark the process may revert with increased resistance. A chemical mechanism have been proposed by Verbakel et al.^[177] and further elaborated by Krebs et al.^[152] In the natural state the surface layer of the ZnO film is doped with bound oxygen radicals that can be removed either by UV-irradiation or electrochemically creating persistent charge carrier states. In the dark a reuptake of oxygen slowly occurs, see **Figure 11**.

A more detailed investigation of the effect of photo annealing of the ZnO layer was carried out by Lilliedal et al.^[178] The R2R fabricated devices with the structure: ITO/ZnO/P3HT:PCBM/PEDOT:PSS/Ag were encapsulated by lamination with a barrier foil. When illuminated in an ambient atmosphere the IV-characteristics changed drastically over ca. 10 min from zero current generation to maximum. A slow partial reversion was seen when the device was kept in the dark. They concluded that the photo-annealing process is accelerated by illumination intensity and temperature. A mechanism was proposed based on the redistribution of the oxygen in the device during the light/dark cycles. The ZnO nanoparticle layer absorbs light in the range of 360 to 395 nm^[179] giving rise to a photo chemical reaction as described earlier. The effect of ZnO electron transport layer in normal geometry devices on the shelf-life have been investigated by Ferreira et al.^[180] The lifetime of devices without any ETL stored in the dark (shelf-lifetime) was very short as opposed to devices with a ZnO nanoparticle HTL or mixed ZnO nanoparticle/ZnO sol-gel studied over 78 days. The mixed ETL device proved to be best and retained about 60% efficiency after this period. Transmission electron microscopy cross-sections of the devices showed that voids appeared at the aluminum/P3HT:PCBM interface when no ZnO layer was present. A modification in the form of indium doped zinc oxide nanoparticles (IZO) have been explored by Puetz et al. in both normal and inverted geometry devices.^[181] Sarenpää et al.

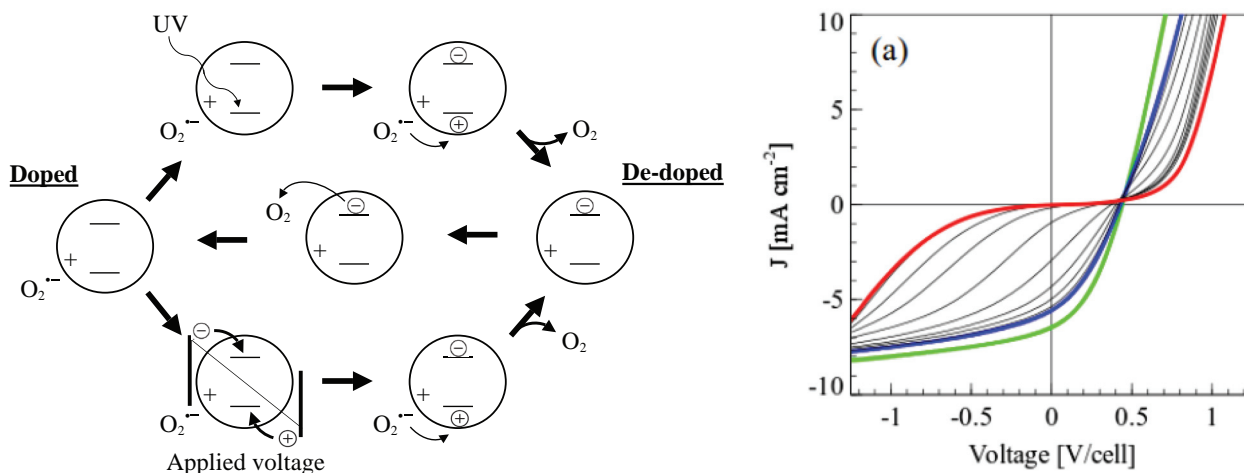


Figure 11. Left: Proposed mechanism and interaction of ZnO with oxygen and UV-irradiation. Charges in circles denote mobile carriers. Reproduced with permission.^[152] Copyright 2010, Royal Society of Chemistry. Right: The dynamic evolution of the IV-curves for a single solar cell module due to slow UV photoactivation of the ZnO layer. Reproduced with permission.^[178] Copyright 2010, Elsevier.

investigated aluminum doped zinc oxide (AZO) prepared by atomic layer deposition using diethyl zinc and trimethyl aluminum with water as oxygen source. Small molecule devices based on this material showed increased stability with no degradation observed after 40 days.^[182] In inverted type devices a thin evaporated layer of aluminum later oxidized to aluminum oxide between the ITO cathode and the PEDOT:PSS layer have been used to enhance electron extraction and in conjunction with a MoO₃ anode interface layer to increase stability.^[183] Zimmermann et al. investigated the use of thin evaporated chromium and titanium metal interfaces between the active layer and an aluminum anode.^[184] With the chromium interlayer superior long-term stability was achieved compared to devices with titanium. For small molecule organic solar cells the influence of various exciton blocking layers on the stability have been investigated.^[185] It was found that AlQ₃ was superior to In₂S₃, (Z)-5-(4-chlorobenzylidene)-3-(2-ethoxyphenyl)-2-thiothiazolidin-4-one (CBBTZ) or bathocuproine (BCP). Lo et al. found that doping the AlQ₃ buffer layer with metallic magnesium enhanced the stability even better than for AlQ₃ alone.^[186]

2.5. The Hole Transport Layer

PEDOT:PSS is the most widely used hole transport layer (HTL) with several commercial varieties available. This ionic polymer is mostly sold as a water solution/suspension that is applied as a layer in solar cell devices by either spin coating or slot die coating in an R2R process.^[187] Some formulations of PEDOT:PSS are highly acidic with a pH of 1-3 and together with residual water or moisture from the air this is a possible source of corrosion especially in conjunction with low work function metals such as aluminum or calcium used in normal type geometry devices, but may also be implicated in degradation of the ITO electrode.^[188] The pH of the PEDOT:PSS solution can be adjusted by addition of base as described by Kim et al. leading to a 25% improved lifetime at 0.2 molar ratio of NaOH.^[189] The PEDOT:PSS may degrade thermally as shown by Vitoratos et al. with an exponential degradation of the conductance with time. A half life of some 55 hrs at 120 °C was observed.^[190] Voroshazi et al. recently investigated the role of PEDOT:PSS in cathode oxidation for polymer solar cells with normal geometry^[191,192] and found that it greatly accelerates oxidation due to its hygroscopic nature. Substituting PEDOT:PSS with vacuum deposited MoO₃ as the hole conducting layer enhanced the stability. In a latter more comprehensive study it was found that even in a dry inert atmosphere PEDOT:PSS accelerates degradation presumably due to residual humidity that can diffuse through the device to the cathode interface where it will react.^[192] Sputtered nickel oxide (NiO) can also be used as an alternative to PEDOT:PSS with a marked increase in stability.^[193] Hancox et al. have found a similar enhanced lifetime of small molecule solar cells with a MoO_x hole-extraction layer.^[194] Chromium oxide–chromium nitride films prepared by sputtering have been used by Qin et al. as another alternative to PEDOT:PSS.^[195] Lloyd et al. studied inverted geometry devices with and without a PEDOT:PSS hole transport layer and found a great difference in degradation was seen in the solar cell parameters (V_{oc} , I_{sc} , FF and PCE). Both devices degraded slowly in the beginning, but at approximately 600 hours the point defects suddenly increased in

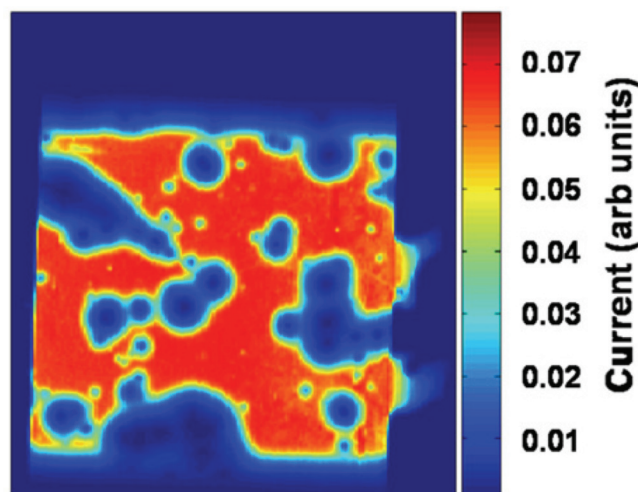


Figure 12. Light beam induced current (LBIC) image of an aged device with inverted geometry using a PEDOT:PSS HTL. Point defects have spread and begun to coalesce leading to catastrophic failure. Reproduced with permission.^[196] Copyright 2011, Elsevier.

size and ultimately coalesced in contrast to a uniform degradation in the non-PEDOT device.^[196] **Figure 12** shows the LBIC image for the PEDOT:PSS device.

Hains et al. studied the effect of various interface layers on solar cell performance.^[197] In a test for thermal stability PEDOT:PSS was evaluated as HTL versus 4,4'-bis[(*p*-trichlorosilylpropylphenyl)-phenylamino]biphenyl (TPDSi₂):poly[9,9-dioctylfluorene-*co*-N-[4-(3-methylpropyl)]-diphenylamine (TFB). Standard type devices (MDMO-PPV:PCBM) with either of the two different HTLs were heated on a hot-plate to 60 °C for 1 hour and then subjected to IV testing. The PEDOT:PSS devices no longer exhibited photovoltaic response while those containing TPDSi₂:TFB were unaltered. Norrman et al.^[198] studied the degradation of inverted geometry devices in different atmospheres using chemical surface analysis techniques (XPS and TOF-SIMS) and found a very dynamic chemical behavior at the PEDOT:PSS/active layer interface. They ascribe the major failure mechanisms for inverted devices to be related to PEDOT:PSS phase separation and to changes at the interface to the active layer. In small-molecule solar cells stability has been enhanced by using a polymerized fluorocarbon anode buffer layer between the ITO and the copper phthalocyanine/C₆₀ active layer.^[199] Gholamkhash and Holdcroft replaced part of the PEDOT:PSS with gold nano-dots to improve device stability in accelerated aging tests.^[200] While UV irradiation generally degrades polymer photovoltaic devices through photo oxidation reactions of the active layer it has been argued that UV treatment of the PEDOT:PSS layer actually increases the lifetime.^[201] Mixed oxides (WO₃-V₂O₅) have been used by Huang et al. to replace PEDOT:PSS creating air stable inverted devices.^[202]

2.6. Effect of the Atmosphere

There are numerous degradation mechanisms in play during operation of the organic solar cell and each contributes to the

overall deterioration of photovoltaic performance that consequently shortens the device lifetime. The most significant contributor is believed to be diffusion of atmosphere into the device of which molecular oxygen and water are known to cause photo-oxidation of the organic layers and interfaces (i.e., chemical degradation), which consequently will disrupt the delicate electrochemical processes that are vital for the photovoltaic performance. Water and molecular oxygen induced photo-oxidation is influenced by various factors that are not necessarily equivalent for both types of atmospheres. Important factors involve: i) whether or not encapsulation is employed, and if it is, the type/quality of the encapsulation (described in detail in a subsequent paragraph), ii) the barrier effect of the individual layers towards molecular oxygen and water, which, among other things, is linked to the individual layer thickness, iii) and finally the layer stack configuration is important since it will define the accumulated barrier effect at a given location in the device, which could be at an interface or in the bulk of an organic layer. The numerous parameters of which many are interrelated will determine how significant a degradation mechanism is at a specific location in the device.

2.6.1. Organic/Metal Electrode Interface

The organic/metal electrode interface is vulnerable towards molecular oxygen and water. Three photo-oxidative degradation mechanisms can take place: i) as mentioned earlier low work function electrodes such as aluminum and calcium can form metal oxides in the interface that consequently will act as a transport barrier causing deterioration of the photovoltaic performance, ii) photo-oxidation of the organic material that will degrade the electron/hole transport properties and thus the photovoltaic performance, and iii) the metal can form an adduct with the organic material (e.g., via vinylic bonds) that will react efficiently with molecular oxygen and water. However, the latter mechanism has so far not been documented. There are several examples in the literature that demonstrate how powerful it is to combine time-of-flight secondary ion mass spectrometry (TOF-SIMS) with isotopic labeling in order to study water and molecular oxygen induced photo-oxidation of organic solar cells.^[203–208] Hermenau et al.^[203] employed TOF-SIMS in combination with isotopically labeled atmospheres such as H_2^{18}O and $^{18}\text{O}_2$ to study photo-oxidation in specific device locations in a non-encapsulated small-molecule organic solar cell with the configuration ITO/MeO-TPD:C₆₀F₃₆/ZnPc:C₆₀/C₆₀/BPhen/Al. The authors performed TOF-SIMS depth profiling through the BPhen/Al interface and were able to semi-quantify the formation

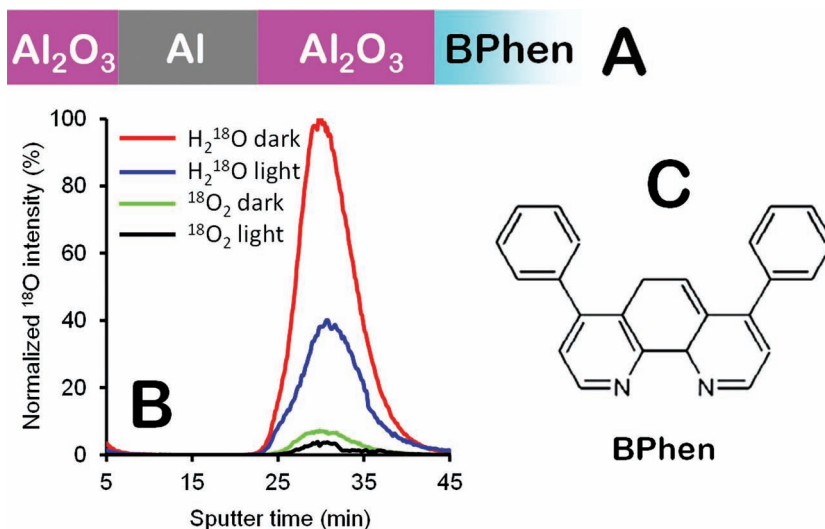


Figure 13. A) schematic organic solar cell with the configuration ITO/MeO-TPD:C₆₀F₃₆/ZnPc:C₆₀/C₆₀/BPhen/Al showing the BPhen/Al interface. B) The corresponding TOF-SIMS oxygen depth profiles for various experimental conditions. C) The chemical structure of 4,7-diphenyl-1,10-phenanthroline (BPhen). Reproduced with permission.^[203] Copyright 2011, Elsevier.

of aluminum oxide in the interface for various experimental conditions during the device lifetime (Figure 13). Hermenau et al.^[203] observed that water is significantly worse than molecular oxygen. However, the authors furthermore observed that illumination impedes the aluminum oxide formation at the BPhen/Al interface for both atmospheres, which was ascribed to a temperature effect, i.e., illumination heats up the outer aluminum surface resulting in a lower concentration of molecules from the atmosphere.

Photo-oxidation of the organic material in the organic/metal electrode interface has been described for different types of organic solar cells.^[203–208] For evaporated aluminum electrodes a distinct difference in diffusion dynamics is observed for water and molecular oxygen. The phenomenon is schematically described in Figure 14.

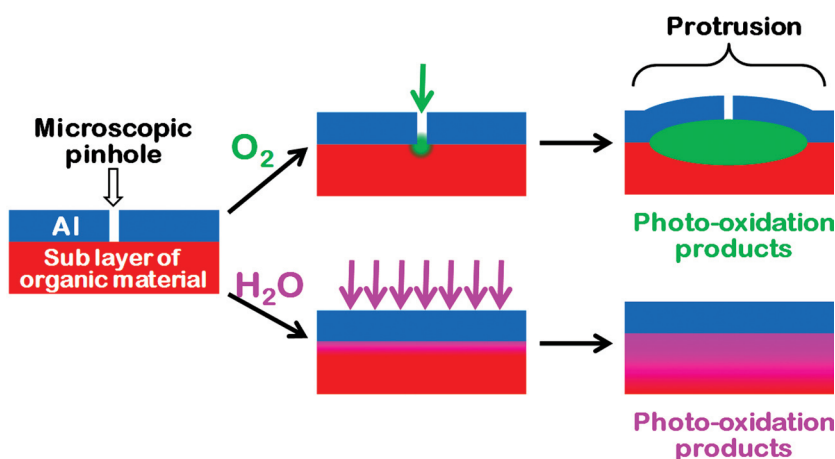


Figure 14. Schematic representation of the outer aluminum electrode showing the two different entrance channels for water and molecular oxygen. The molecular oxygen mainly diffuses through microscopic pinholes and water mainly diffuses in between the aluminum grains.

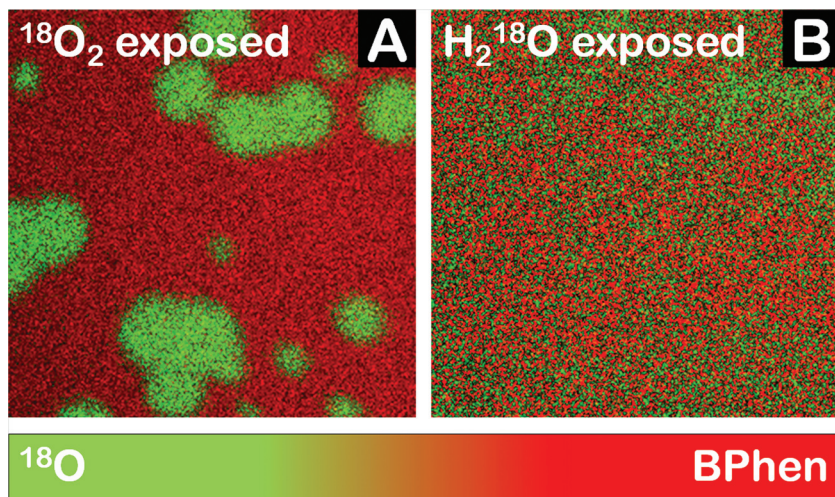


Figure 15. TOF-SIMS composite ion images (500 $\mu\text{m} \times 500 \mu\text{m}$) showing the relative distribution of ^{18}O and BPhen in the BPhen/Al interface for (A) an $^{18}\text{O}_2$ exposed device and (B) a H_2^{18}O exposed device with the configuration ITO/MeO-TPD:C₆₀F₃₆/ZnPc:C₆₀/C₆₀/BPhen/Al. Reproduced with permission.^[203] Copyright 2011, Elsevier.

Water reaches the organic/metal electrode interface by preferentially diffusing in between the aluminum grains, and molecular oxygen preferentially diffuses through microscopic pinholes.^[205] Water will thus result in homogeneous photo-oxidation of the organic material in the interface and molecular oxygen will result in inhomogeneous photo-oxidation in the lateral plane, i.e. photo-oxidation will be centered on the microscopic pinholes causing circular degradation in the lateral plane. As a consequence of the photo-oxidation the organic material will expand in all directions, which for molecular oxygen is manifested as electrode surface protrusions centered on the pinholes. Such protrusions have been measured using interference microscopy and AFM.^[204] In the study by Hermenau et al.^[203] TOF-SIMS imaging was utilized to visualize this phenomenon for the BPhen/Al interface (**Figure 15**).

The authors found the corresponding CN¹⁸O image for the $^{18}\text{O}_2$ exposed device to be equivalent with the ^{18}O image, which they took as evidence that it was (at least) the nitrogen part of the molecule (Figure 13) that was photo-oxidized. The phenomenon shown in Figure 15 has been mentioned by Norrman et al.^[203–206] in several of publications where TOF-SIMS was used in combination with isotopically labeled atmospheres. The circular oriented degradation pattern caused by molecular oxygen has (besides from TOF-SIMS imaging) been observed using techniques such as fluorescence microscopy,^[204] electroluminescence imaging (ELI),^[209] photoluminescence Imaging (PLI),^[209] and light beam induced current microscopy (LBIC).^[196] The obvious way to avoid or diminish this phenomenon is to use thicker electrodes and/or encapsulation. This phenomenon is not significant for R2R processed devices where the top electrode (e.g. Ag) usually is printed from solution that typically results in electrode thicknesses of 10–20 μm as opposed to $\sim 100 \text{ nm}$ for evaporated electrodes.

2.6.2. The Active Layer

The active layer in organic solar cells is by definition organic as opposed to certain barrier layers that can be inorganic (e.g., LiF,

ZnO, V₂O₅, MoO₃, etc.). The active layer is thus susceptible to photo-oxidation. However, the active layer is, regardless of the configuration, always somewhat protected by the other layers in the device, i.e. each material possesses barrier properties with respect to water and molecular oxygen, so photo-oxidation will always be impeded in the active layer compared to being directly exposed to the atmosphere. A recent study on photo-oxidation of a non-encapsulated device with the configuration ITO/ZnO/P3HT:PCBM/PEDOT/Ag revealed that P3HT:PCBM (measured at the P3HT:PCBM/PEDOT:PSS interface) is especially vulnerable towards molecular oxygen but only when illuminated.^[198] The authors quantified the oxygen uptake and found that during the lifetime of the device that was exposed to molecular oxygen, the oxygen increase was only 0.2 atom-%, which constituted an extremely small fraction of the oxygen uptake observed in a series of experiments with the active layer exposed directly to the atmosphere. The relative

degree of photo-oxidation of the active material for the two atmospheres was observed to be consistent with the relative lifetime of the devices (O_2 , 0.2 atom-%, $T_0 = 68 \text{ h}$ versus H_2O , 0.01 atom-%, $T_0 = 480 \text{ h}$), which suggests a direct relationship between photo-oxidation of the active material and the lifetime of the device.

In the study by Hermenau et al.^[203] the relative photo-oxidation was measured as relative oxygen uptake in the various bulk layers in their small-molecule organic solar cell ITO/MeO-TPD:C₆₀F₃₆/ZnPc:C₆₀/C₆₀/BPhen/Al. It was found that the largest degree of photo-oxidation occurs in the active layer ZnPc during illumination in a water atmosphere. Also in this case there was a good correlation between the device lifetime and the degree of photo-oxidation in the active layer (O_2 , 10%, $T_{50} = 74 \text{ h}$ versus H_2O , 100%, $T_{50} = 11 \text{ h}$) (normalized to the oxygen uptake for the water atmosphere), which is indicative of a direct relationship between photo-oxidation of the active material and the lifetime of the device.

Figure 16 presents the result of a study involving a R2R processed polymer solar cell with the composition encapsulation/PET/ITO/ZnO/P3HT:PCBM/PEDOT:PSS/Ag/encapsulation that was illuminated (AM1.5G, 1000 W m^{-2}) in ambient air. The goal was to measure the relative photo-oxidation (via the relative oxygen uptake) of the active material (P3HT:PCBM) as a function of performance loss.

As is evident a linear correlation was observed between TOF-SIMS obtained oxygen intensities and loss of photovoltaic performance, which suggests that loss of performance is directly related to photo-oxidation of the active material, and that this degradation mechanism is possibly the dominant one. Finally, the result unfortunately supports the fact that organic barrier films (i.e., encapsulation) are not 100% efficient with respect to preventing diffusion of water and molecular oxygen through the barrier (discussed in a subsequent section).

2.6.3. The Barrier Effect

As mentioned previously the likelihood of water or molecular oxygen reaching a particular location in the device is influenced

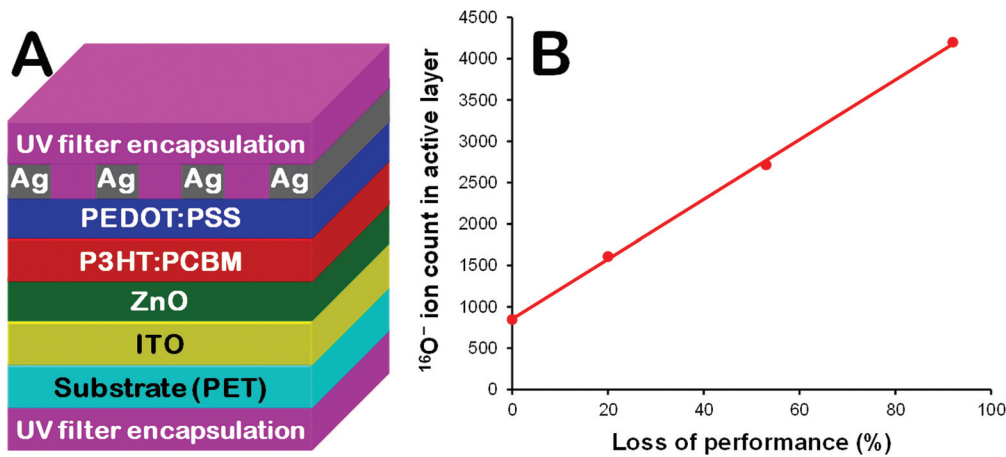


Figure 16. A) Schematic R2R fabricated polymer solar cell with an UV filter encapsulation. B) TOF-SIMS obtained oxygen intensities from the bulk active material (P3HT:PCBM) as a function of loss of photovoltaic performance.

by various factors. From the previous examples it is clear that different types of organic solar cells have different vulnerabilities towards water and molecular oxygen. One recent systematic study by Madsen et al.^[208] describes accumulated barrier effects with respect to water and molecular oxygen for a polymer solar cell (Figure 17).

The authors used TOF-SIMS in combination with isotopically labeled water and molecular oxygen on a device with the configuration glass/ITO/ZnO/P3HT:PCBM/PEDOT:PSS/Ag/encapsulation together with partial devices as shown in Figure 17. The authors were able to semi-quantify the incorporation of ^{18}O

on the ZnO surface after layer removal, which they used as a measure for the accumulated barrier effect of the layers situated on top of the ZnO layer. For a molecular oxygen atmosphere they observed a steady decrease in oxygen uptake on the ZnO surface for an increased number of layers (Figure 17). However, for the water atmosphere Madsen et al.^[208] observed a drastic decrease for just one layer (P3HT:PCBM) and an equally low level for the subsequent layers, which they ascribed to a bottleneck effect of the P3HT:PCBM layer, which thus must be a relatively good barrier for water. A slightly elevated increase of ^{18}O incorporation was observed for the complete device illuminated in an H_2^{18}O

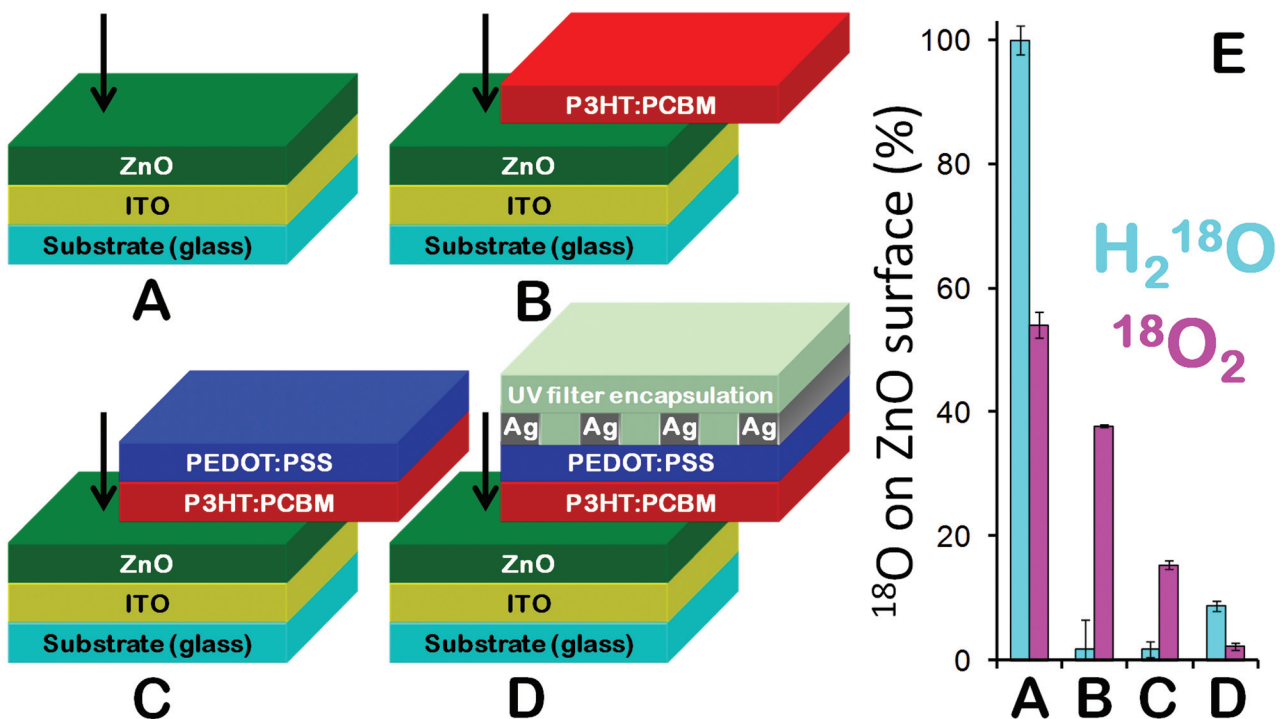


Figure 17. Schematic partial polymer solar cells (A–C) and a complete polymer solar cell with encapsulation (D). E) Normalized degree of oxygen incorporation on the ZnO surface. The vertical arrows indicate where TOF-SIMS obtained ^{18}O intensities were measured after illumination in H_2^{18}O or $^{18}\text{O}_2$ with subsequent layer removal.

atmosphere, which they suggested could be due to the binder being hygroscopic.

2.6.4. Inert Atmospheres

As is evident from the previous discussion there are several examples from the literature that demonstrate how water and molecular oxygen affect organic solar cells.^[203–208] However, in the absence of water and molecular oxygen the organic solar cell will still degrade during illumination, i.e. via other processes. If an inert atmosphere is used the typical outcome will be a significant increase in stability and thus device lifetime. Degradation will in this case be in the form of pure photo-chemical processes, and lifetime studies will reflect the photochemical stability. The most inert atmosphere one can utilize is not to have any atmosphere, i.e. a vacuum. In the study by Krebs and Norrman^[141] where a polymer solar cell with the composition ITO/P3CT/C₆₀/Al was illuminated (AM1.5G, 1000 W m⁻²) in a vacuum lasted for a bit more than 10 000 hours before the performance had reached zero. The previously mentioned study by Hermenau et al.^[203] included an experiment involving a nitrogen atmosphere, which provided a good comparison to the equivalent devices that were illuminated in water or in molecular oxygen: In a water atmosphere the lifetime (T_{50}) was 11 hours, in a molecular oxygen atmosphere the lifetime was 74 hours, but in the nitrogen atmosphere the lifetime was 2700 hours. This clearly demonstrates the devastating effect of water and molecular oxygen and the excellent photo-chemical stability.

3. Physical Stability

3.1. Encapsulation

Due to the organic solar cell sensitivity towards oxygen and water it has been natural to encapsulate them in various ways. This also increases the mechanical stability and scratch resistance. Finally, encapsulation can act as an UV filter removing the most harmful part of the solar spectrum. The most drastic (and impractical) example is perhaps devices sealed totally in glass with an inert atmosphere. Another more popular type of glass encapsulation involves encasing the device between a top sheet of glass and a substrate or other fixed base using a glue to seal the edges as shown in **Figure 18**.^[210] These methods sacrifice the possibility of having a flexible solar cell, but they ensure an almost zero transmission rate of oxygen and water.

The earliest encapsulation schemes simply involved PET foil as barrier but this was not enough.^[211] More practical solutions involve plastic barrier films that can be laminated on top of the devices. This approach is also much more suited towards R2R fabrication where lamination has been used for a long time. A drawback is that these barrier films still allow some oxygen and water to penetrate into the device albeit at a much reduced rate. An example is an undisclosed “ultrahigh gas barrier material” used by Konarka to encapsulate MDMO-PPV/PCBM devices.^[212] In a later publication the authors disclose the use of an encapsulation film

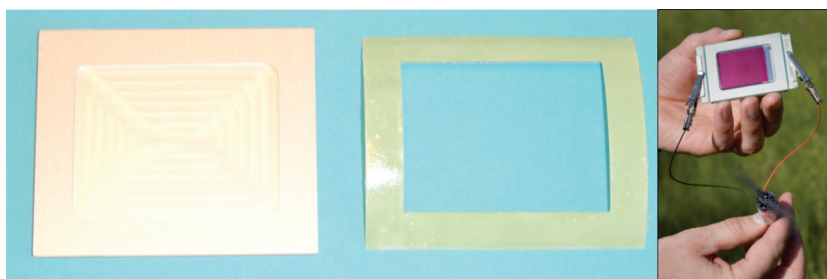


Figure 18. A rigid encapsulation using a glass front and a metal back. The metal backplate is shown from the inside (left) and the thermosetting glass fiber re-enforced epoxy is shown before being sandwiched between the metal back plate and the glass front carrying the solar cell stack (middle). The completed and functional device is shown driving a small electrical motor (right). Reproduced with permission.^[210] Copyright 2006, Elsevier.

on a PEN (poly(ethylenephthalene)) substrate with an ultra-high barrier deposited by plasma enhanced chemical vapor deposition (PECVD).^[213] Madakasira et al. investigated the use of multiple layers of parylene and aluminum oxide and concluded that they might hold promise for solar cells.^[214] Sarkar et al.^[215] investigated to use of atomic layer deposition (ALD) of ultrathin barrier layers of Al₂O₃ generated from trimethyl aluminum and ozone.

Cros et al.^[216] used identical conditions for barrier measurements of water uptake and for lifetime measurements of electrical parameters of both normal and inverted type organic solar cells. This allowed them to link the amount of water in contact with the devices and the decrease in performance. This could be used to assess different types of barrier materials such as simple PET or multi layer combinations PE/EVOH/PE or PP/PVA/In/PE. A main conclusion was that to obtain device lifetimes of several years a water transmission rate of 10⁻³ g m⁻² day⁻¹ was required which is favorable compared to the requirements for OLEDs (10⁻⁶ g m⁻² day⁻¹). The effect of encapsulation on degradation of PEDOT:PSS and poly(aniline):poly(styrene sulfonate) PANI:PSS was studied by Ecker et al.^[217] and showed that it reduced the amount of degradation.

R2R fabricated solar cells require an easily applicable barrier material of which several are offered as commercial barrier films for food packaging. Such a barrier film can be applied to the roll of solar cell devices in a separate R2R step with a barrier film carrying a pressure sensitive adhesive as shown in **Figure 19**. In one study with ProcessOne type devices fabricated at Risø DTU barrier films from either Fasson Roll Materials (25 μm PET) or Amcor Flexibles (100 μm PET) were used.^[218] A separate study looked at different barriers in the context of the OE-A demonstrator in 2011.^[219] The seal around the edges of the devices has also been explored and was found to impart significant stability even though the adaptability to product integration is lost.^[220] Larger series/parallel connected modules were constructed from these laminated panels and laminated for outdoor use in an industrial process used for silicon solar cell panels. The devices were laminated in a sandwich consisting of glass/EVA/encapsulated device/EVA/Tedlar/glass and baked in an oven at 130 °C, 0.1 mBar to melt the EVA.^[218] In other studies the barrier foil was obtained from Alcan Foil Products to demonstrate upscaling of polymer solar cell fabrication^[152] and to enable the first large round robin study between several different laboratories (**Figure 20**).^[221]



Figure 19. A simple roll-to-roll laminator using pressure sensitive adhesive. The unencapsulated solar cells are unwound on the left and rewound on the right. The barrier material (top right) carrying the adhesive and the liner is laminated onto the solar cell material. The liner is removed before lamination and is seen as the clear foil passing out of the right side of the photograph.

4. Measuring and Reporting Device Lifetime

There has been recorded a significant increase of lifetime reports for OPV devices in recent years. This has automatically generated a competitive environment among the groups for reporting the best lifetime. A competition however, requires fair rules for comparison of data or in other words, certain

guidelines on how to measure and report device lifetime in a comparative manner. As has been discussed in the previous review in 2008,^[42] OPVs lack certain standard procedures for device lifetime measurements, which can lead to incomparable results, as has been well shown in recent inter-laboratory stability studies.^[222]

This section of the review is devoted to recent developments in measuring and reporting device lifetimes. In particular, new designs of atmosphere chambers for measurements in controlled environments reported in recent years are discussed as well as a new approach of accelerated studies via concentrated light is presented. Additionally, inter-laboratory studies (ILS) carried out for the first time for OPV devices are presented together with the detailed discussion of the results, which have helped in establishing standard guidelines for OPV device lifetime measurements.^[223] The final part discusses the aforementioned protocols, which have been developed via discussions and consensus at international summits on OPV stability (ISOS 1,2 & 3).^[224–226]

4.1. Atmosphere Controlled Testing

Recently, the testing of OPV device stability in weathering or atmosphere chambers has become a rather common procedure. The reason is that such a controlled testing allows distinguishing the effects of different environmental factors, such as oxygen, humidity, temperature and light on the performance of devices, as well as providing accuracy and reproducibility of testing conditions. Examples of atmosphere chambers have already been discussed in the previous stability review from 2008,^[42] where the possibility of the control of atmosphere

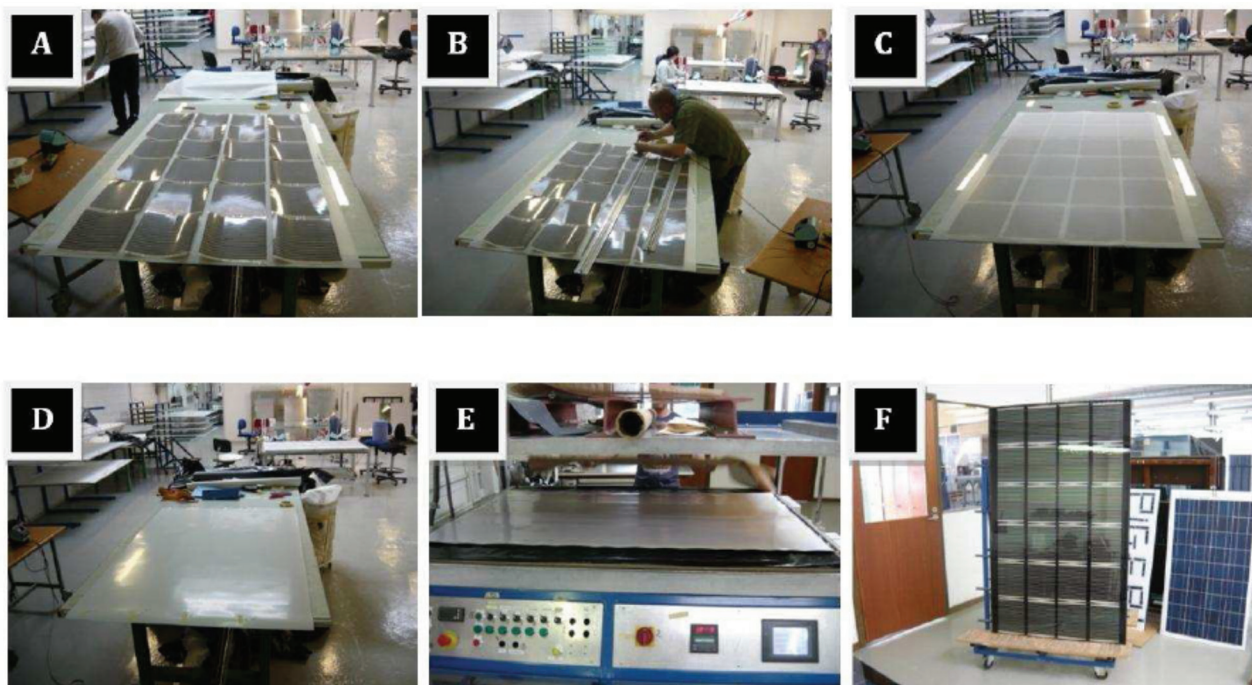


Figure 20. Rigid encapsulation of larger modules with glass/EVA/Tedlar for outdoor use. Reproduced with permission.^[218] Copyright 2010, Optical Society of America.

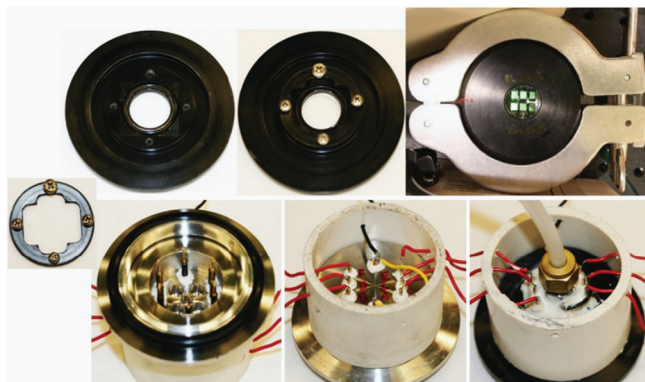


Figure 21. Images of components of the KF50 based atmosphere chambers in varying levels of assembly: retaining ring (far left), inside view of chamber top with o-ring seal and sample inset visible (top left), inside view of chamber top with retaining ring (top middle), fully assembled chamber with lit OLEDs (top right), inside view of chamber bottom with getter pockets visible (bottom left), outside view of chamber bottom with electrical feedthroughs only (bottom middle), outside view of chamber bottom with gas feedthrough (bottom right). Reproduced with permission.^[227] Copyright 2010, Elsevier.

during regular and accelerated lifetime testing of devices via custom made chamber was discussed.

Recently there have been a number of reports of new atmosphere chambers particularly designed for characterization of organic solar cell devices. In particular, Reese et al.^[227] reported a miniature chamber designed in a way suitable for optical and electrical characterization of 1 inch square size devices in controlled environment. The chamber was constructed on a KF50 flange as presented in **Figure 21**. Two versions of chambers were presented with one having a quartz window serving as a lid for the chamber for device illumination, while in the other version the sample substrate itself was used as the window sealed to the chamber cover via an o-ring. The second case eliminated any additional reflection effects from the window. For the electrical measurements the device terminals could be accessed through electrode pins mounted on the backside of the chamber. Additional gas port integrated in the chamber through the bottom allowed controlling atmosphere in the chamber. This allowed carrying out optical and electrical characterization of devices under controlled levels of oxygen.

Lira-Cantu et al.^[228] presented a similar custom-made chamber used for studying the influence of transparent conducting oxide layer and the polymer layer on stability of hybrid and organic solar cells in controlled environment. The chamber was based on a two-piece glass reactor equipped with a temperature and humidity sensors and a quartz window for irradiation of the samples. The setup is shown in **Figure 22**. The reactor had a cooling jacket for water cooling and inlet/outlet for flushing it with desired gases. The temperature and the humidity inside the chamber were measured using a digital thermo-hygrometer. Gevorgyan et al.^[229,230] presented a different design of atmosphere chamber, which consisted of four sectors with individual control of environment in each. **Figure 23** shows the images of the general setup (left) and the enlarged view of the chamber interior (right). Each chamber was equipped with thermocouple, gas inlet and outlet and a small fan for providing

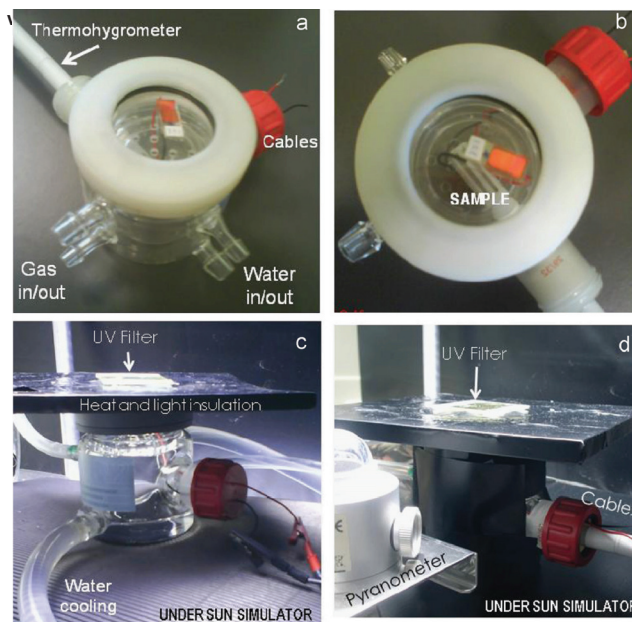


Figure 22. Home-made glass reactor with a cooling jacket used for solar cell testing under controlled atmosphere. Water cooling, thermo-hygrometer and UV-filter included: a) side view, b) top view, c), and d) different configurations mounted under the sun simulator. Reproduced with permission.^[228] Copyright 2011, Elsevier.

uniform distribution of the gases throughout the chamber. Electrode pins were integrated through the bottom for contacting the device terminals. Device substrate was used as a top window for illumination. The entire system was equipped with water cooling channels for controlling the setup temperature. Such a design allowed both easy transport of the chamber into a glove-box through a typical size load lock and usage of the chamber as a stage for various optical and electrical characterizations. Additionally, it was possible to perform simultaneous measurements of four samples in four different environments illuminated by one solar simulator. As an example the group demonstrated comparison of device degradation in four conditions, such as: nitrogen, humid nitrogen, dry oxygen and room atmosphere, presented elsewhere.^[230]

A more standard approach of controlled device stability testing is however based on utilizing commercially available so called aging or weather chambers. Such chambers are designed particularly for testing commercial products including polymer based products in a standardized manner. They can provide an accurate control of temperature and relative humidity level, as well as programmed periodic temperature and light cycling in accordance with ASTM and IEC standards. There are different types of aging chambers, such as: i) Weather chambers—provide a static control of temperature and relative humidity with simultaneous illumination of the samples (with light spectrum typically close to daylight). Light cycling can be programmed as well for day and night simulations. Additionally, the system has an option of periodic water spraying of the samples for simulation of natural precipitations. Typically there are two types of weather chambers: chambers with static flat stage for sample exposure and

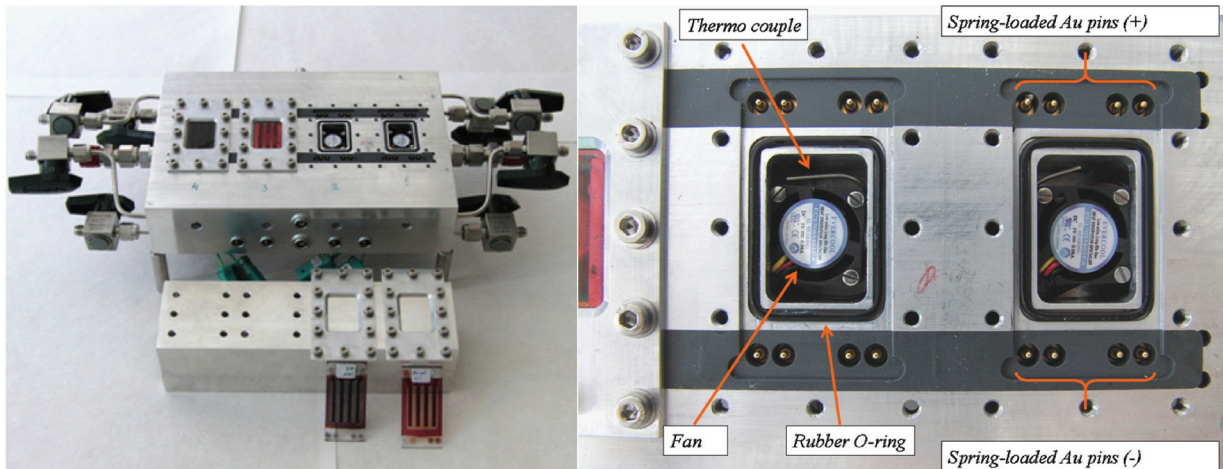


Figure 23. General view of the chamber with two sectors opened (left) and enlarged photo of the chamber interior (right). Reproduced with permission.^[230] Copyright 2011, Elsevier.

chambers with rotating racks onto which the tested samples are mounted. In the second case the rotation offers a better uniformity of sample irradiation and temperature. The first type is more suited for large size devices, while in the second case a larger number of device but with limited sizes (typically 7 cm × 13 cm) can be fitted. ii) Thermal cycling chambers—provide a static control of relative humidity and programmed periodic cycling of temperature in a wide range (for example, −65 °C to +18 °C). Such a cycling is used for simulation of seasonal variation of outdoor conditions.

Figure 24 shows an example of thermal cycling chambers (a) and weathering chambers (b). The insets in Figure 24 demonstrate the controlled aging of R2R printed OPV modules

produced in Risø DTU. Although such setups do not have a function of controlling the oxygen level as the previously discussed atmosphere chambers, the important advantage of using such standardized chambers lies in the accuracy of testing conditions, which can drastically improve the reproducibility and comparability of device testing results among different groups. The disadvantage is that such equipments are rather expensive and unaffordable for many scientific groups.

4.2. Accelerated Testing Conditions

The extended lifetime of organic solar cells have necessitated some form of accelerated testing in order to obtain data in a

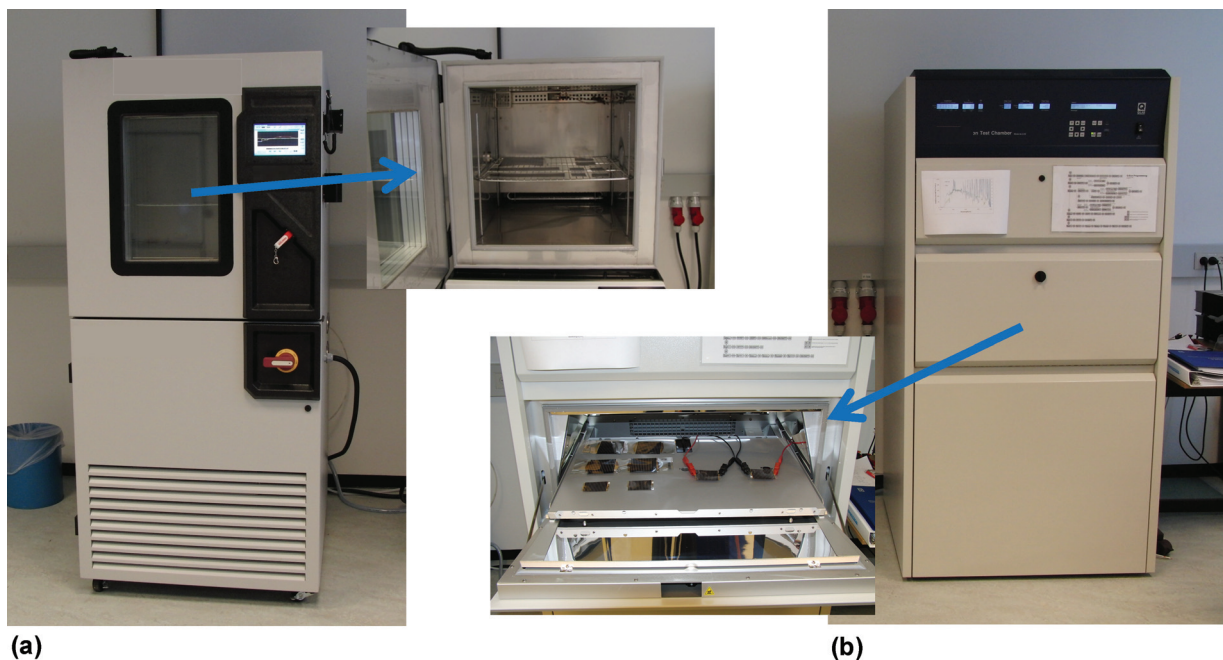


Figure 24. a) Thermal cycling chamber with temperature cycling range of −65 °C to +180 °C and control of relative humidity level, the inset shows OPV modules mounted on the stage. b) Weather chamber with Xe light source and flat stage for device exposure, the inset shows OPV modules mounted on the stage.

meaningful timeframe. This was already recognized when we wrote our last review in 2008, but was restricted to mean tests done at elevated temperature. A more general review of the concept of accelerated testing of organic solar cells has been described by Haillant including increased irradiation, temperature, increased humidity and time compression.^[231] In a later paper mathematical expressions were formulated to deal with acceleration due to a combination of both temperature and irradiation.^[232] In the simplest case the degradation only depends on the temperature and the rate of the reaction follows the Arrhenius equation:

$$k = A \exp\left(\frac{-E_a}{RT}\right)$$

Where E_a is the activation energy for the process and R the gas constant. The expression for the acceleration factor AF at two different temperatures (T_1 and T_2) is then given by:

$$AF = \exp\left[\frac{E_a}{R}\left(\frac{1}{T_1} - \frac{1}{T_2}\right)\right]$$

When illumination is also considered this equation was expanded to include two different irradiances (I_1 and I_2):

$$AF = \left(\frac{I_1}{I_2}\right) \cdot \exp\left[\frac{E_a}{R}\left(\frac{1}{T_1} - \frac{1}{T_2}\right)\right]$$

The authors list a number of assumptions and approximations to this simplistic model and describe the calculation of acceleration factors of an indoor artificial laboratory weathering test relative to two natural outdoor environments.

4.2.1. Temperature

Based on the assumption that the degradation processes studied followed an Arrhenius type model with a simple exponential rate equation an acceleration factor could then be obtained as the ratio between the rates of degradation at the two temperatures. In one case an acceleration factor of 4.5 was found going from 25 °C to 60 °C.^[233] Using the acceleration factor it is possible to estimate the lifetime at other temperatures. Usually there are many competing degradation processes for organic solar cells each with their own relationship between rate and temperature invalidating the exact prediction of a lifetime.

4.2.2. Illumination

The application of concentrated sunlight to OPV is a relatively novel approach, which has demonstrated a large potential in terms of both stability testing as well as to general solar cell characterization. Originally being developed for inorganic photovoltaics, sunlight concentration setups have primarily been developed for high performance multi junction solar cells on which sun light has been focused to increase the output power.^[234] By this the active area of the costly solar cell is effectively increased by a relatively cheap concentrator system. Conventional stability assessments of organic solar cells are performed by studying the decrease of PCE as a function of degradation time under 1 sun. However, a multitude of parameters different from the polymer affect the observed stability, e.g. the electron and hole transport layers, the electrodes, and the interfaces. As a result the interplay between many different parameters is probed while the stability of the polymer itself remains rather inconclusive. To focus on the actual stability of the polymer, degradations of the polymer deposited on glass substrates under 1 sun illumination have more clearly demonstrated the intrinsic stability of polymers. By monitoring the UV-visible absorption decrease as a function of ageing time in the ambient, stabilities of different polymers have been established.^[107] A novel approach to the assessment of polymer stability is concentrated sunlight. By exposing pure polymers to concentrated light the photonic flux as well as the temperature are increased significantly accelerating the material degradation. Tromholt et al. performed such accelerated degradations of MEH-PPV and P3HT by using a lens based solar concentrator to obtain solar intensities in the range of 1 to 200 suns (1 sun = 0.1 W cm⁻²).^[235] By UV-visible spectroscopy, the total absorption of the polymer within the UV visible range was recorded at different ageing times. By increasing the solar intensity from 1 to 200 suns a clear increase of the degradation rate was observed (Figure 25a). From the ratio between the degradation rate at high solar intensities and the rate at 1 sun standard degradation, acceleration factors for each solar intensity could be deduced. For both MEH-PPV and P3HT the acceleration factors were found to increase linearly with solar intensity (Figure 25b). At 200 suns a complete degradation of MEH-PPV took place within 80 seconds, which clearly demonstrates the highly decreased time frame of the stability assessment and the

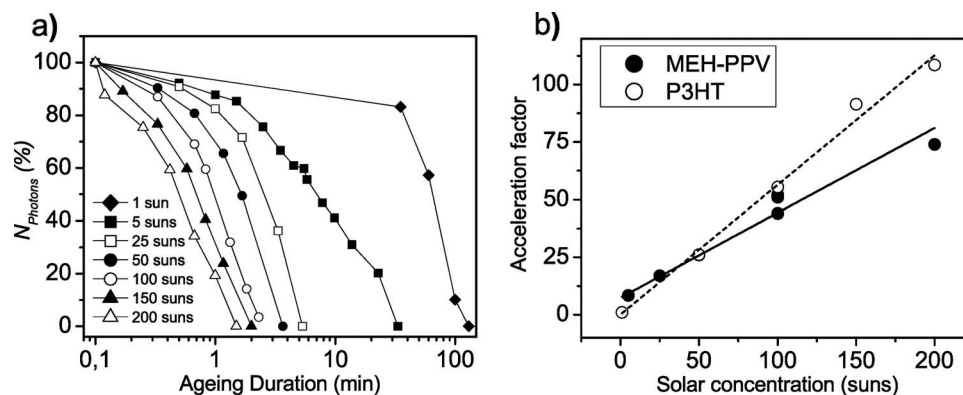


Figure 25. a) Degradation of MEH-PPV expressed as a decrease of the total absorption. b) Acceleration factors for MEH-PPV and P3HT at different solar intensities. Reproduced with permission.^[235] Copyright 2011, Elsevier.

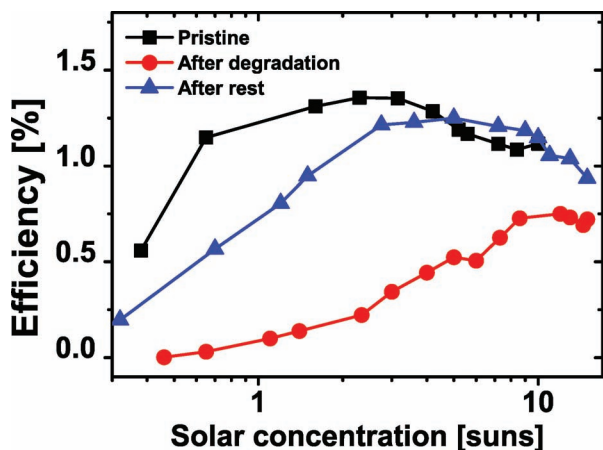


Figure 26. PCE as a function of solar intensity for a pristine inverted P3HT:PCBM cell, after 30 min illumination at 5 suns and after 30 min in the dark. Reproduced with permission.^[238] Copyright 2011, IOP Publishing.

potential of using concentrated light as an acceleration parameter for stability studies.

The response of complete solar cells to concentrated sunlight is more complex than that of a single polymer layer due to the several different materials and interfaces in the solar cell stack. Inverted P3HT:PCBM solar cells have been studied in terms of their key cell parameters from 1 to 20 suns.^[236–238] This demonstrated that unlike the case for inorganic PV, organic solar cells suffer from low mobilities in the layers impeding the exciton generation and charge extraction. The V_{oc} was found to increase logarithmically with the solar intensity, while the FF dropped strongly at high solar intensities due to resistive losses induced by the high current density. The overall effect is that the PCE increases until a peak position around 1 sun after which it steadily decreases (Figure 26 - black curve).

Normally, IV characterization is performed with flash illuminations of the cells to avoid excessive heating and thermally induced degradation. However, by exposing inverted P3HT:PCBM cells to 30 min exposure of 5 suns irradiation the cell performance was significantly changed.^[238] The PCE was found to decrease significantly right after degradation by which only 6% of the initial performance was conserved at 1 sun (Figure 26 - red curve). However, after 30 min in the dark the cells demonstrated an almost complete recovery of the performance (blue curve). This reversible effect was found to be introduced by the nanoparticulate ZnO electron transport layer, which by UV illumination became highly conductive by desorption of oxygen from the particle surfaces. The overall effect of this was a loss of the diode behavior severely decreasing the V_{oc} and therefore also the PCE. After UV illumination, oxygen re-adsorbs on the ZnO particles thus decreasing the shunting, which explains the reversibility of the effect. The proposed model for the oxygen doping of the ZnO suggested that a negative reverse bias could introduce the same shunting of the ZnO. This was indeed demonstrated recently where the shunting effects could quickly be turned on and off by high voltage forward and reverse biases, which confirms the validity of the proposed model.^[237]

Hermenau et al. used an LED based setup to study the effect of accelerated degradation of small molecule devices in air with

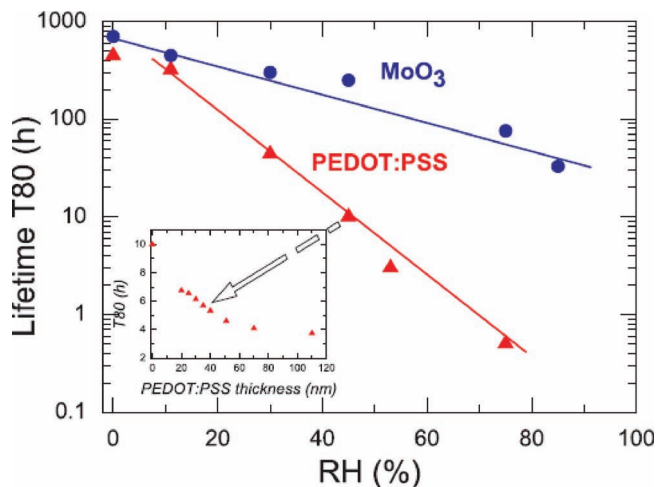


Figure 27. Accelerated testing as a function of humidity for normal geometry devices with either PEDOT:PSS or MoO₃ as HTL. Reproduced with permission.^[192] Copyright 2011, Elsevier.

either a red LED (617 nm) or a blue LED (470 nm) and found that devices aged much faster under blue light irradiation.^[239]

4.2.3. Humidity

Voroshazi et al.^[191,192] studied the degradation of normal geometry devices with either PEDOT:PSS or MoO₃ as HTL at a range of humidity values and found that the devices based on PEDOT:PSS degraded faster (Figure 27) and had a higher dependence on humidity than devices based on MoO₃ (vide supra).

A larger number of flexible devices were studied by Hauch et al. at 65% RH representing accelerated conditions.^[240] They found a limited influence of these damp heat conditions and inferred that humidity would not be a significant limiting factor on the lifetime of these devices.

4.3. Inter-Laboratory Studies of Device Lifetime

Round robin (RR) and inter-laboratory studies (ILS) have commonly been employed in the photovoltaic community as tools for calibration of testing equipments and reference specimens. The principle of these studies is based on sharing samples among a number of groups/laboratories and comparing the results of measurements. In the case of RR the same sample goes around among all the participating parties and returns to the original party, while in the case of ILS studies the sample can be shared in a number of ways. The second case often involves sending a number of identical samples to a few parties at the same time. There have been many reports of such studies in inorganic photovoltaics (see for example, some previous reports^[241–246]). The typical devices used for RR and ILS must be stable and durable during the entire testing process, since any intrinsic instabilities in the devices can largely affect the accuracy of the measurement process. Due to insufficient stability properties of OPVs RR and ILS have not been commonly used in the OPV field. The only type of sharing of organic solar cells

among labs is often reported when device efficiency is being certified by an accredited laboratory.

The first example of an ILS for OPV devices among a large number of groups was reported in 2009. Krebs et al.^[221] presented inter-laboratory measurements of roll-to-roll coated flexible organic solar cell devices preformed among 18 different laboratories across three continents. The studies involved production and *J*-*V*-characterization of a large number of identical modules at the hosting site (Risø DTU) and distribution of the modules to other participating parties for the second *J*-*V*-measurement followed by transportation of the modules back to the original site for the final measurement. The module architecture was based on typical P3HT:PCBM inverted structure with ITO/ZnO as the front electrode and printed silver paste as back electrode. The modules were encapsulated using commercially available standard barrier foil (detailed description of the device production has been published previously^[222]). The main purpose of the studies was to demonstrate that OPVs can provide sufficient stability and durability for such tests. **Table 1** shows the average of the photovoltaic parameters of the modules measured at all sites together with the standard deviations. The entire experiment lasted approximately 4 months and the modules did not show signs of degradation during this period (as can be seen from the average values in Table 1) proving the possibility of such studies. On the other hand, the experiment revealed a number of setbacks, such as: the handling of flexible substrates during transport and testing introduced mechanical stresses in the modules, the periodic contacting of the modules by applying alligator clips on the back (printed silver) electrode gradually damaged the terminals of the module, the light sources used by groups for measurements differed in terms of spectral distribution, intensity and homogeneity of illumination over the module area. All these factors resulted in significant fluctuations of the reported data especially pronounced in the short circuit current values at recipient labs (see Table 1).

In 2011, the same group reported a new set of ILS, which this time included testing of OPV device stability in different conditions.^[222] The process of these studies again involved a distribution of identical modules to a large number of groups for lifetime measurements both in indoor and outdoor conditions. The main purpose was to investigate the capabilities of different groups in accurately measuring and reporting OPV device lifetimes and to study the effect of different geographic locations on the device stability. The new studies additionally addressed some of the setbacks of the previous ILS. The structure of the samples was the same as in the previous ILS, yet the sizes of the modules were somewhat smaller in this case (12 cm × 8.5 cm) to ease the uniform illumination during measurements. Additionally,

Table 1. Average values of the module parameters. The data is presented as average values ± standard deviation. Numbers are taken from a previously published article.^[221]

Parameter	At Risø DTU	At Recipient	Back at Risø DTU
PCE (%)	1.09 ± 0.24	1.08 ± 0.29	1.16 ± 0.23
<i>I</i> _{sc} (mA)	99.97 ± 8.6	96.52 ± 27	97.51 ± 15
<i>V</i> _{oc} (V)	3.35 ± 0.3	3.56 ± 0.33	3.47 ± 0.28
FF (%)	38.5 ± 3.9	38.0 ± 3.7	40.0 ± 2.6

punch-buttons were applied on the module terminals to avoid fluctuations seen in previous studies. Despite the fact that the flexibility of the modules was a source of additional fluctuations, this property was kept in this study as well in order to further study the effect of mechanical stressing on the lifetime of the modules. Short basic guidelines for different procedures were distributed to the groups. The tests involved: i) Shelf life studies performed by leaving modules in the dark in either ambient conditions or in controlled temperature/humidity chambers. ii) Light soaking in indoor conditions performed by placing the modules under simulated sun light in laboratory conditions. The modules were either stored under illuminated conditions and measured continuously or were periodically taken out and measured under calibrated sun simulators. iii) Outdoor studies under real sun were performed either by storing and measuring modules under natural sun light, or by bringing the modules indoors (daily or weekly) and testing them under a calibrated light source. Due to a rather large amount of results obtained from these studies, we choose to present only the key points here, while the detailed description of all the results can be found in literature.^[222]

The shelf life studies, which were carried out by simply storing the modules in a dark room environment and periodically measuring the IV curves, showed some spread in the results with standard deviations of measured PCE reaching 13% after 1000 h of dark storage. **Figure 28** shows the plot of PCE decay of all the modules measured at different sites together with the error bars showing the standard deviations. The spread of the data could however, come from intrinsic fluctuations of performance of modules and therefore, it was hard to judge the reproducibility of the measurements at different sites. Additionally, some groups reported de-lamination or cracking in the layers induced by the periodic handling/mechanical stressing of the flexible modules, which could be another source of inconsistencies in the results.

As another procedure the groups were asked to store some of the modules in dark, but in an environment with controlled temperature and relative humidity. The purpose was to investigate the potential of the groups in performing controlled aging tests as well as the effect of environmental factors on device performance. **Figure 29** shows the plot of the degradation rates of PCE vs. temperature and relative humidity for modules measured by

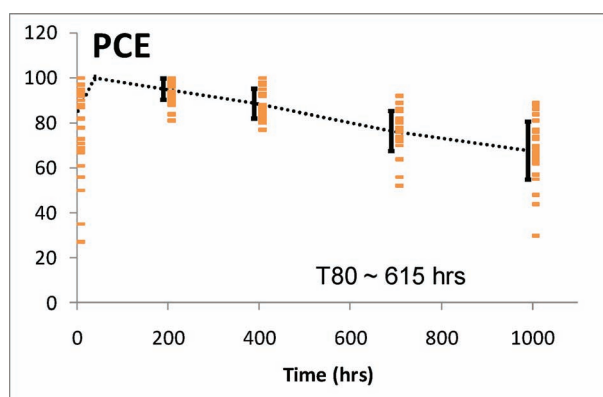


Figure 28. PCE vs. time for 29 modules (orange rectangles) for shelf life test. The dashed line intersects the average values for guiding the eye and the error bars represent standard deviations. Reproduced with permission.^[222] Copyright 2011, Elsevier.

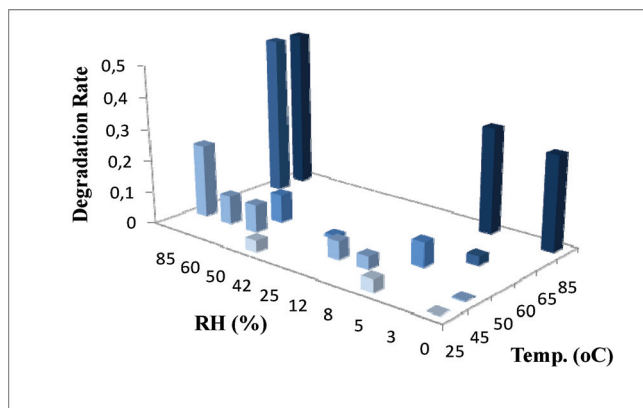


Figure 29. Degradation rate of the modules versus temperature and humidity (RH) for dark tests in controlled environments. Reproduced with permission.^[222] Copyright 2011, Elsevier.

different groups. From the plot it is obvious that the elevated levels of both temperature and relative humidity significantly accelerate the decay process. More importantly, the reports showed that the groups used completely random temperature and relative humidity combinations varying in the ranges of ambient temperature to 85 °C and 0 to 85% humidity, which made the comparison of data among the groups impractical. This stressed the need for certain standard guideline protocols for performing aging tests of OPV in a comparable manner.

Further sophistications were recorded during the indoor light soaking test under solar simulators. The modules in this case were exposed to simulated light in a room environment and IV curves were periodically recorded. The lamp types used by the groups were falling into different categories, such as: incandescent lamps (halogen lamps), high-intensity discharge lamps (metal halide lamps, Xe arc lamps) and sulfur plasma lamps. **Figure 30** shows the reported PCE curves with the colors distinguishing the different lamps used for measurements. Obviously, the light type significantly affects the decay rate, for example the typical sulfur plasma lamps with low UV caused a slower decay (red circles in Figure 30). Therefore, it was concluded that in order to be able to compare indoor stability testing among different groups, a special requirement on the lamp type (light spectrum) has to be applied. The results also showed a diversity of reported device temperature during the tests, which is another source of data scattering and points to the need of device temperature control during aging.

Outdoor testing of the modules under real sun irradiation included two types of procedures. In one test the modules were placed on outdoor platforms and continuously measured under real sun irradiation, while in the second test the modules were periodically taken inside and measured under calibrated sun simulators. **Figure 31** shows the PCE decay for firsts (a) and the second (b) cases measured by many groups. Obviously, in the case of measurements in outdoor conditions the deviations of degradation rates are significantly smaller compared to the other one. The reason was mostly ascribed to the fact that in the second case a periodic handling of the flexible modules was involved as well as different setups and procedures were used by different groups for periodic IV measurements, which seemed

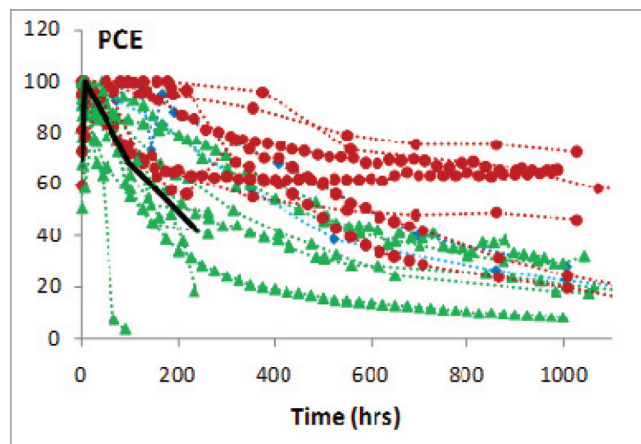


Figure 30. Decay of PV parameters for 14 modules measured in different labs. Red circles correspond to sulfur plasma lamps, green triangles to metal halide and xenon lamps and blue rhombs to halogen lamps, black solid line corresponds to outdoor measurement under real sun. The measured points are connected by dashed lines for guiding the eye. Reproduced with permission.^[222] Copyright 2011, Elsevier.

to be the main reason for fluctuations. In the mean time the disadvantage of the first experiment was that it requires instrumentation for IV testing of devices in outdoor conditions, which might be unaffordable for many groups. This was also seen by the ratio of the participating laboratories in the first and the second outdoor testing, which was 1:3 correspondingly.

The tests also revealed a number of setbacks in reporting insufficient data. Obviously, three measurements within 1000 hours of test cannot represent the complete dynamics of degradation, as is demonstrated in **Figure 32**, where the decay of two identical modules is presented with different frequency of measurements. Another example is too short measurements, which might record the initial (often fast) stage of the decay, but not the change of the decay rate at a later stage.

Thus, it is crucial that the frequency and duration of the measurements is always adjusted to accommodate the dynamics of the device behavior in order to accurately determine the lifetime of the tested sample.

4.4. ISOS Standard Procedures for Lifetime Measurements and Reporting

As already mentioned a number of times in this review, OPVs are in urgent need of standard procedures for lifetime measurements. One of the objectives of the ISOS 1,2 & 3 summits held in the past three years was to establish some protocols for lifetime testing of OPV.^[224–226] The first two summits established some guidelines using the experience gained mostly from the inorganic field. However, the complex architecture and dynamics of OPV required a slightly different approach. Thus, based on the lessons learned from the inter-laboratory studies and the discussions of the ISOS-3 summit a new set of ISOS standard procedures were established,^[223] which give detailed descriptions of how to perform lifetime measurements of OPVs both in indoor and outdoor conditions as well as how to report

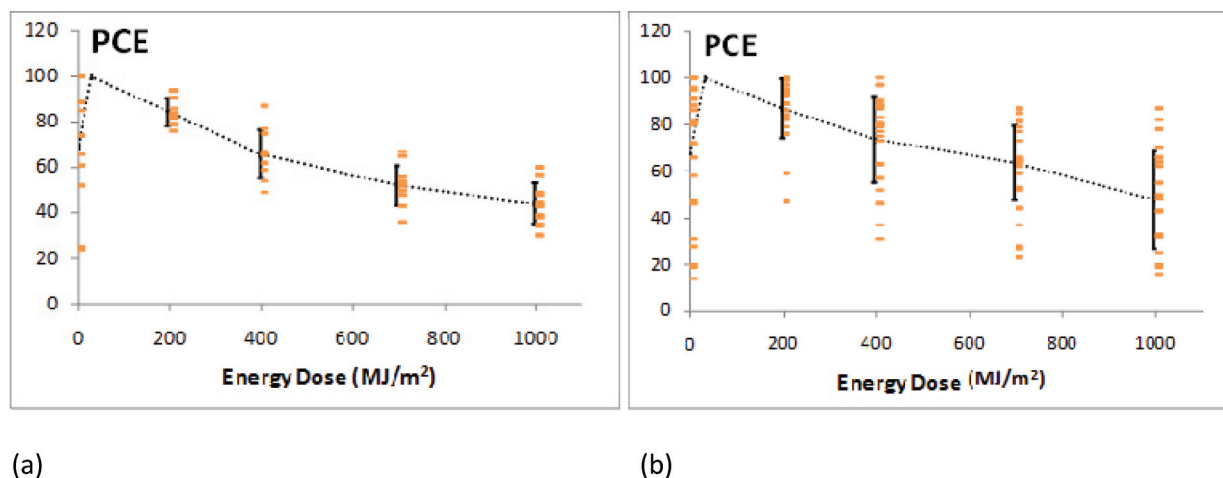


Figure 31. Variation of PCE (orange rectangles) versus energy dose for outdoor testing 1 (modules measured under real sun) (a) and outdoor testing 2 (modules measured under simulated light sources) (b). The dashed line intersects the average values for guiding the eye and the error bars represent the standard deviations. Reproduced with permission.^[222] Copyright 2011, Elsevier.

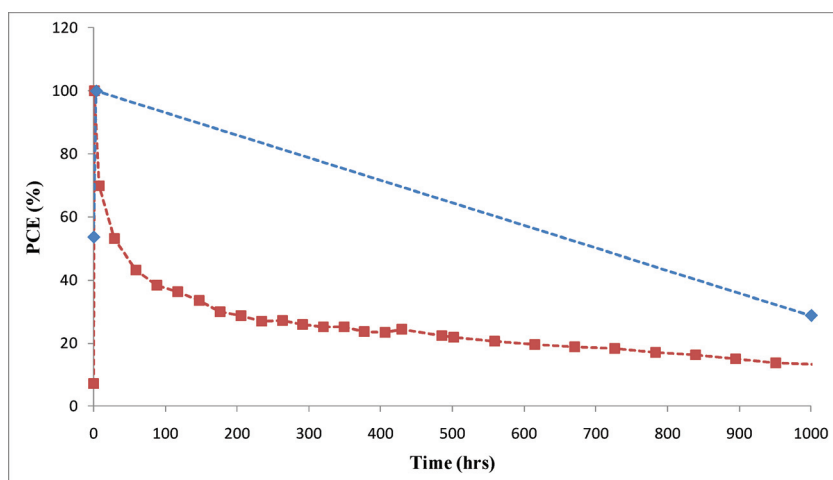


Figure 32. Decay curves of two identical modules aged under indoor conditions. Markers show the frequency of the measurements and the dashed lines are for guiding the eye.

the results of the measurements. The procedures include dark testing, outdoor testing, indoor simulations testing, thermal cycling tests, as well as low light testing. Each category has been split up in three different levels to meet the capabilities of a wider range of laboratories/groups: level 1 (basic) requires a basic set of tools and can provide limited, but useful information about tested specimens, level 2 (intermediate) targets most of the scientific laboratories/groups with slightly more advanced equipment for testing, while level 3 (advanced) is aimed for the advanced laboratories including the accredited certifying laboratories. **Table 2** presents the summary of all the procedures.

Shelf life measurements involve storing the specimen in the dark and periodically measuring the performance under calibrated sun simulators or real sun. The storage equipment can vary from simple shelf (basic–shelf life) to ovens (intermediate–high temperature storage) to weather chambers (advanced–damp heat). Obviously, the most reproducible results can be obtained by using

weather chambers for aging with an accurate control of temperature and humidity levels. In order to be able to compare the results among various groups, the recommended combinations of temperature–humidity were limited to only two: 65 °C–85% and 85 °C–85%.

The outdoor testing was split to two approaches. In the first one the specimen is stored on an outdoor platform for aging and periodically removed from the platform and measured under calibrated solar simulator in indoor conditions (basic level). In the second one the specimen is continuously stored and measured under sun irradiation in outdoor conditions (intermediate level). The advanced level requires storage and characterization in outdoor conditions, but also from time to time retesting of specimen under calibrated solar simulators in indoor conditions. The testing performed only in outdoor conditions mini-

mizes the periodic handling of the modules, which as was shown earlier to be problematic for device stability measurements. While outdoor monitoring is the most convenient and perhaps scalable, it can however raise several issues, including the effects due to temperature coefficients, cloud cover, non-linearity between performance and irradiance, wind, seasonal variation of energy dosage received by the specimen. Furthermore, the variations associated with different climates, latitudes, and altitudes should all be presented to allow ready comparison between different geographic locations. This often requires sophisticated instrumentation for outdoor characterization of solar cells as well as “weathering station” for recording outdoor conditions, such as sun irradiation, wind speed, temperature etc.

The indoor weathering testing employs solar simulators for aging of the specimen under irradiation in indoor conditions. As was discussed earlier the light spectrum of the irradiation significantly affects the rate of decay of OPV devices^[222] and UV light

Table 2. Overview of different types of test protocols.

Three levels						
Basic (Level 1):	"Hand held" measurements using the simplest equipment and few conditions.					
Intermediate (Level 2):	Fixed conditions and protocols suited for most labs.					
Advanced (Level 3):	Standardized tests applied in certified labs. Extended range of parameters to monitor etc.					
Test Type	Dark			Outdoor		
Test ID	ISOS-D-1 Shelf	ISOS-D-2 High temp. storage	ISOS-D-3 Damp heat	ISOS-O-1 Outdoor	ISOS-O-2 Outdoor	ISOS-O-3 Outdoor
Light Source	None	None	None	Sunlight	Sunlight	Sunlight
Temperature ^{a)}	Ambient	65 °C/85 °C	65 °C/85 °C	Ambient	Ambient	Ambient
Relative Humidity (R.H.) ^{a)}	Ambient	Ambient (low)	85%	Ambient	Ambient	Ambient
Environment ^{a)}	Ambient	Oven	Env. chamber	Outdoor	Outdoor	Outdoor
Characterization light source	Solar simulator or sunlight	Solar simulator	Solar simulator	Solar simulator	Sunlight	Sunlight & solar simulator
Load ^{b)}	Open Circuit	Open Circuit	Open Circuit	MPP or Open Circuit	MPP or Open Circuit	MPP
Test Type	Laboratory Weathering Testing			Thermal Cycling		
Test ID	ISOS-L-1 Laboratory weathering	ISOS-L-2 Laboratory weathering	ISOS-L-3 Laboratory weathering	ISOS-T-1 Thermal Cycling	ISOS-T-2 Thermal Cycling	ISOS-T-3 Thermal Cycling
Light Source	Simulator	Simulator	Simulator	None	None	None
Temperature ^{a)}	Ambient	65 °C/85 °C	65 °C/85 °C	Between room temp. and 65 °C/85 °C	Between room temp. and 65 °C/85 °C	-40 °C to +85 °C
Relative Humidity (R.H.) ^{a)}	Ambient	Ambient	Near 50%	Ambient	Ambient	Near 55%
Environment/setup	Light only	Light & Temp.	Light, Temp., R.H.	Hot plate/Oven	Oven/Env. Chamb.	Env. Chamb.
Characterization light source	Solar simulator	Solar simulator	Solar simulator	Solar simulator or sunlight	Solar simulator	Solar simulator
Load ^{b)}	MPP or Open Circuit	MPP or Open Circuit	MPP	Open Circuit	Open Circuit	Open Circuit
Test Type	Solar-Thermal-Humidity Cycling					
Test ID	ISOS-LT-1 Solar-Thermal Cycling		ISOS-LT-2 Solar-Thermal-Humidity Cycling		ISOS-LT-3 Solar-Thermal-Humidity-Freezing Cycling	
Light Source	Simulator		Simulator		Simulator	
Temperature	Linear or step ramping between room temp. and 65 °C		Linear ramping between 5 °C and 65 °C		Linear ramping between -25 °C and 65 °C	
Relative Humidity (R.H.)	Monitored, uncontrolled		Monitored, controlled at 50% beyond 40 °C		Monitored, controlled at 50% beyond 40 °C	
Environment/setup	Weathering chamber		Env. Chamb. with sun simulation		Env. Chamb. with sun simulation and freezing	
Characterization light source	Solar simulator		Solar simulator		Solar simulator	
Load ^{b)}	MPP or Open Circuit		MPP or Open Circuit		MPP or Open Circuit	

^{a)}The ambient conditions are defined as 23 °C/50% RH in general, and 27 °C/65% RH accepted in tropical countries according to ISO 291(2008): Plastics - Standard atmospheres for conditioning and testing; ^{b)}Open circuit refers to a simply disconnected device or device connected to a sourcemeter set to 0 current

especially is detrimental for device degradation. Therefore, a light source with close match to AM1.5G is required for accurate measurements. However, such a requirement can make the testing rather expensive and therefore, the basic level of indoor weathering test allows a freedom of choice of lamp type provided that the lamp spectrum is reported, while a close matching of the lamp spectrum to AM1.5G is required for the intermediate and advanced levels of measurements. Such a requirement can

be fulfilled by simulators based for example on Xe arc lamps, metal halide lamps, sulfur plasma lamps with broad spectrum (class A). **Figure 33** shows a plot of the spectra of these lamps together with the IEC specified AM1.5G spectrum.

Thermal cycling test is aimed for simulating the seasonal changes of the outdoor conditions. Basic category is an initial test in which a sample is cycled from a high temperature (65/85 °C) to room temperature using a hot plate set to the high

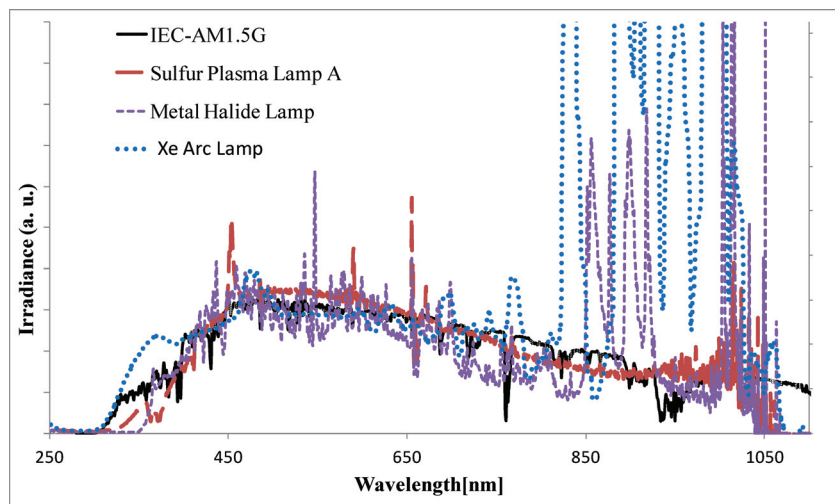


Figure 33. Typical spectral power distributions of xenon arc, metal halide lamps with daylight filters and A class sulfur plasma lamp. AM1.5G defined in IEC 60904-3 is also shown for comparison.

temperature and a clock-actuated switch to turn the hot plate on/off. Intermediate (ISOS-T-2) cycling is similar except that more advanced equipment such as an environmental chamber or a hot plate with the ability to automatically vary temperature over time is used to precisely cycle the temperature gradually over the course of the cycle period. Advanced (ISOS-T-3) category requires the most advanced equipment where the temperature can be cycled from 85 to 45 °C and controlled during the course of the cycle. Typical thermal cycling is carried out in dark, but a light test can be performed as well with solar thermal humidity cycling protocol presented in Table 2. The detailed graphical representations of the cycles can be found in literature.

sun irradiance spectrum.

The reporting of device lifetime is another important issue that was addressed in the protocols. The parameter that has commonly used for reporting device lifetime in the photovoltaic community is T_{80} – the time when the device performance has degraded to 80% of its initial performance. Due to the very dynamic behavior of OPV devices, the shapes of stability curves can take various forms, an example is presented in Figure 35. This makes it hard to correctly define T_{80} for different curves. Additionally, reporting only T_{80} does not give full information about device degradation kinetics, for example burn-in period, decay nature, possible catastrophic failures etc.

Table 3. Recommended test procedures for low light level or fluorescent lamp stability and IV testing.

		Basic (Level 1)	Advanced (Level 3)
Testing Protocol	Light source	Fluorescent lamp	Fluorescent lamp
	Illuminance	Measured (1000 lx suggested)	Measured (1000 lx, 500 lx, and 200 lx). Illuminance can be adjusted by distance lamp to solar cell.
	Spectrum	Light color 830 recommended. Report light color and manufacturer.	Light color 830 recommended. Report light color and manufacturer. Measure spectrum.
	IV measurement	Periodic measurement	Periodic measurement
	Temperature	Measure	Measure
Output	Measurement light source	Report type and irradiance level	Report type and irradiance level
	Performance parameters	Report I_{sc} and V_{oc} (FF & PCE and MPP (power density) and/or full $J-V$ s if possible)	Report I_{sc} , V_{oc} , FF, PCE and MPP (power density); (full IVs optional)
	Temperature	Report	Report
	IPCE	Optional	Report
	Description of measurement protocol and setup	Report	Report
Required Equipment	Light source	Fluorescent lamp (light color 830 suggested)	Fluorescent lamp (light color 830 suggested)
	Luxmeter	Required	Required
	Calibrated Spectrometer	Optional	Required
	$J-V$ Measuring Setup	Required	Required

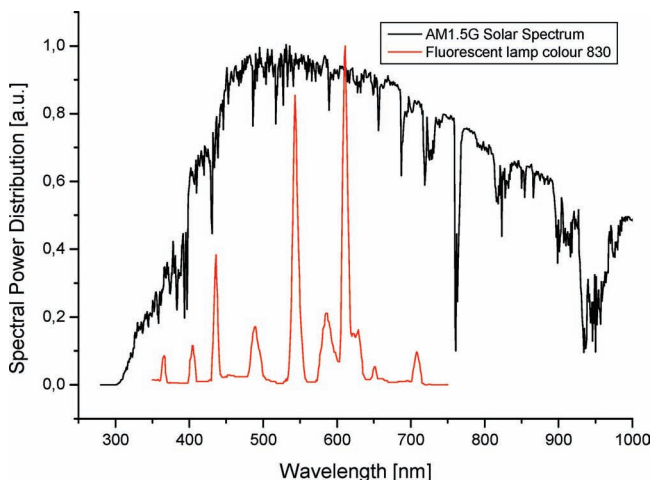


Figure 34. Comparison of the spectrum of a fluorescent lamp with the light color 830 and the AM1.5 spectrum of the sun. Reproduced with permission.^[223] Copyright 2011, Elsevier.

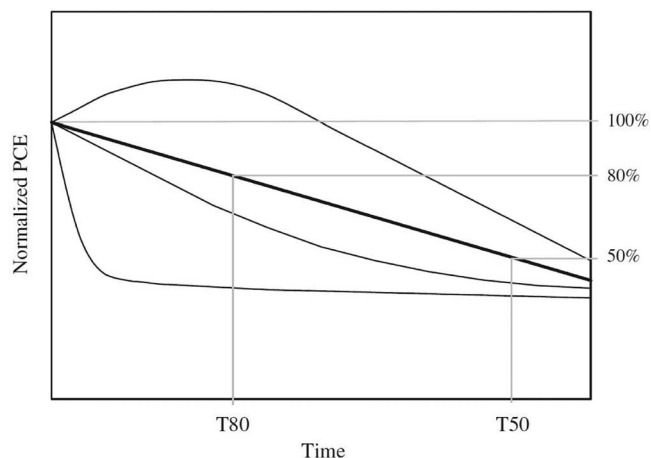


Figure 35. Example of various decay curves that have been commonly reported and the T80 and T50 values for the linear decay. Reproduced with permission.^[223] Copyright 2011, Elsevier.

This led to the creation of a new set of parameters for description of device lifetime, see **Table 4**. **Figure 36** shows the representation of these parameters on a decay curve for the device PCE. There are four pairs describing the decay pattern. The first measurement point E_0 is the initial testing measurement of an OPV device immediately after final fabrication of the device, at time $t = 0$, T_0 (E can stand for any PV parameter, such as I_{sc} , V_{oc} , FF etc.). This measurement should represent the pristine device most accurately. The second parameter, E_S , is the second testing measurement of the OPV device, defined arbitrarily by the user at some time, T_S , after the fabrication of a device. Defining the second parameter, E_S , allows the representation of cases where an OPV device is not immediately subjected to the stability testing conditions, or if a device is first ‘stabilized’ before subjecting it to further aging conditions. The third and fourth parameters, E_{80} and E_{S80} represent the performance of an OPV device after it has decayed 20% from

Table 4. Four pairs of parameters needed to define OPV device stability.

E_0, T_0	E_0 is the initial testing measurement of an OPV device immediately after final fabrication of the device, at time = 0, T_0 .
E_S, T_S	E_S is a second testing measurement of an OPV device, defined arbitrarily by the user as some time, T_S , after the fabrication of a device.
E_{80}, T_{80}	E_{80} is the testing measurement of an OPV device after the device has decayed 20% from the initial testing measurement, E_0 . T_{80} is the time it took to decay to E_{80} .
E_{S80}, T_{S80}	E_{S80} is the testing measurement of an OPV device after the device has decayed 20% from the second testing measurement, E_S . T_{S80} is the time it took to decay to E_{S80} .

its initial or second testing measurement, after some time, T_{80} or T_{S80} respectively. While the time evolution of a given parameter will capture the decay behavior of an OPV device, it is also necessary to report the IV curve for each of the four time points highlighted in the decay curve.

As far as catastrophic failures are concerned, when the device fails at some point accompanied by a fast decay of the performance (broken degradation curve), the experimenter is advised to study and report the reproducibility of such a failure.

While reporting device stability it is also recommended to report so called ‘device protection and handling history’ to improve the comparability of the results. This includes parameters, such as: device encapsulation, layer thicknesses of device electrodes and substrates, device layout and geometric sizes, technique for contacting device terminals, handling history of the device. The list can be more exhaustive and therefore, it is recommended that the experimenter determines and reports all the additional parameters that can possibly influence the device lifetime.

4.5. Raising the Stakes

The ISOS initiative is quite possibly the most powerful instrument developed within the field of OPV. The strength lies in

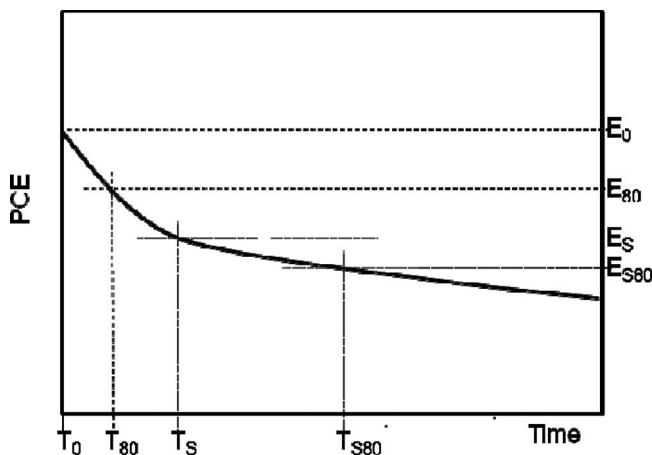


Figure 36. Representative figure defining the parameters to be included in the reporting of OPV stability data. The time evolution of a given parameter of an OPV device, illustrating the four pairs of necessary parameters to describe the decay pattern, including E_0 and T_0 , E_S and T_S , E_{80} and T_{80} , and E_{S80} and T_{S80} . Reproduced with permission.^[223] Copyright 2011, Elsevier.

bringing many different groups together with specific competencies thus ensuring a breadth of capacity and the combination of this with the consensus. i.e. the agreement by a large group on numbers and methods. If OPV is to survive the entire field will have to learn that the voice of one ambitious research group or company does not inspire credibility whereas the voice of many or ideally the entire field as a unit does just that. Within the ISOS community it was decided to instigate a large ILS experiment on device stability (possibly the largest in any PV field). The purpose was to prepare devices in many different laboratories, each laboratory thus contributed with a series of (ideally identical) devices that were then degraded in parallel under the same conditions according to the ISOS protocol. The multifold purpose being to validate the ISOS procedures, to provide the first true comparison between many of the different device types that are reported, and finally to compare the degradative phenomena as a function of time using many different techniques. The study was initiated in 2010 and completed in 2011. The first part of the study that simply charts the seven different device types spanning normal/inverted device geometries, small molecule/polymer devices, encapsulated/unencapsulated, ITO based/ITO free, rigid/flexible, evaporated electrodes/printed electrodes. All these devices were then subjected to dark, indoor light and AM1.5G accelerated studies. The study lasted for around ~1700 hours and was followed by many different imaging techniques, chemical and physical techniques. The first report has been published and remaining results from the study are due to appear shortly.^[247]

5. Stability Studies on R2R Fabricated Devices

One of the most exciting developments during the last 5 years has been the advent of roll-to-roll (R2R) fabricated solar cell devices. The first of these were the devices produced and sold by Konarka, later came devices produced at universities such as Risø DTU that have been disseminated widely. The nature of R2R devices are quite different from other organic solar cells reported in several distinct ways. First of all they usually have a much larger active area. Many devices with record PCE values (lab devices) are only on the order of 10^{-2} cm² while R2R devices are typically 10^1 – 10^3 cm² or even larger. Another point is the production methods that are also very different. The production methods used by Konarka^[248] have not been disclosed in any detail, but if we look to those presented by Risø DTU they require dedicated printing/coating machinery operating in an ambient atmosphere. This means that these devices are subjected to light, oxygen and humidity

during fabrication, which is in total contrast to standard lab devices that are usually produced in glove box environments with exclusion of strong light, oxygen and humidity. Yet another difference is that R2R devices usually pass through several oven stages to remove solvents for each layer put down exposing them to temperatures of about 140 °C in ambient atmosphere several times. These process conditions clearly limit the available materials greatly and may also affect the bulk heterojunction morphology. Vacuum deposition of electrodes such as aluminum may in theory be possible, but have been replaced by printable silver powder emulsions. All these factors taken together imply that the knowledge on degradation/stability we have gained from lab devices may not be directly applicable to R2R fabricated devices.

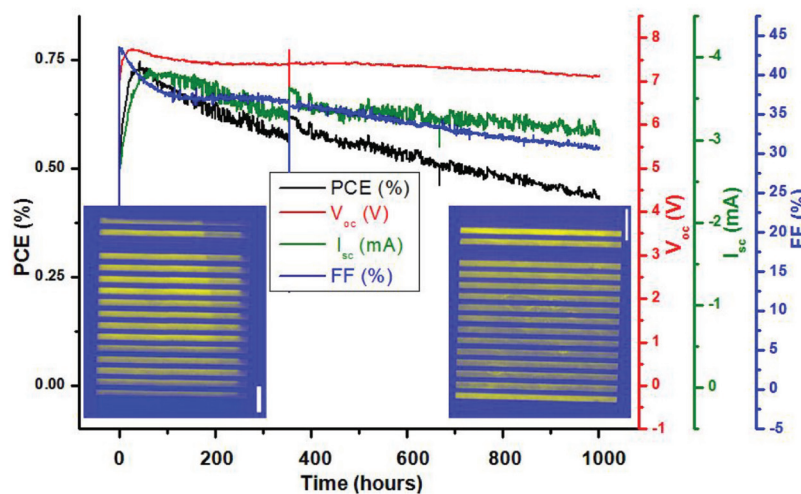


Figure 37. R2R processing of the active layer for credit card sized polymer solar cell modules for the OE-A demonstrator in year 2011 (above). The operational stability under accelerated conditions is shown below along with LBIC images. Reproduced with permission.^[220] Copyright 2011, Royal Society of Chemistry.

Most of the information available on the stability of R2R fabricated devices comes from a number of Risø DTU investigations. A first example was circular solar cell modules with five individual cells serially connected based on the thermo-cleavable P3MHOCT polymer. These devices (+2000) were produced using all screen printing at a company Mekoprint Electronics A/S and intended for use in hats worn at a music festival and powering a miniature radio.^[249] Some of these devices were unencapsulated and degraded relatively fast over a few tens of hours at AM1.5G conditions while others encapsulated with a 25 μm thick PET film and adhesive lasted an order of magnitude longer. The lifetime study also showed a burn-in time due to activation of the ZnO ELT layer. Since then a number of papers have dealt with the manufacturing and stability issues of R2R fabricated devices (Figure 37). In 2009 Krebs et al. compared R2R fabrication of both normal and inverted type devices.^[187] Stability studies in dry nitrogen, humid nitrogen, dry oxygen and ambient atmosphere showed that the main difference was that normal devices were mostly sensitive to water, while the inverted devices were sensitive to oxygen. The special problems associated with the ZnO electron transport layer used in the inverted devices have been thoroughly investigated by Lilliedal et al.^[178] that have already been discussed in section 2.4. Devices of this type have been the subject of a large inter-laboratory study on stability.^[222] Both indoor and outdoor measurements were carried out according to ISOS-3 protocols at 22 locations over the world.

Later a series of demonstrator projects from Risø-DTU have included solar power lamps for the "Lighting Africa" initiative^[250] and recently 10,000 credit-card sized solar cell-LED lamps for an OE-A conference.^[219] The solar cells in these devices were based on the ProcessOne technology^[187] which has an inverted geometry (PET/ITO/ZnO/P3HT:PCBM/PEDOT/Ag) and several have been used in inter-laboratory studies of degradation.

The devices operated quite well over around 1000 hours under accelerated conditions without edge sealing which is a requirement for the processing and integration of many units. This demonstrated that operational stability is not always a question of getting the ultimate stability but rather to find the best compromise between operational stability, process and integration. We can expect to see many more examples of these compromises in the future which present an extra layer of complexity with respect to reporting data and reporting stability. A separate issue that can be expected to receive increased attention in the years to come is a direct consequence of the flexible nature of OPV which is of course a requirement for roll-to-roll manufacture but that is rarely researched on rigid laboratory glass based devices. The thermo-mechanical properties of the multilayer structure is not necessarily optimal for stability when

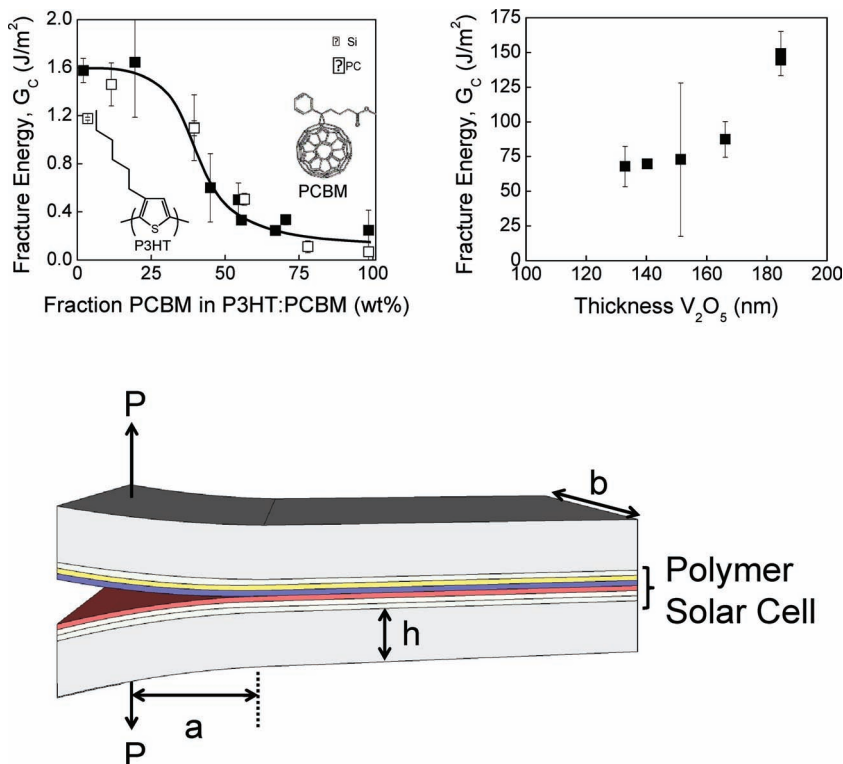


Figure 38. Fracture energy for roll-to-roll processed OPV as a function of fullerene content (top left) along with a significant improvement using a V_2O_5 interlayer (top right). A schematic of the process of delamination is shown below. Reproduced with permission.^[253] Copyright 2011, Elsevier.

bending the devices or over time. When working with flexible devices delamination^[251,252] may for instance be a result of low adhesion energy at a particular interface. For the lamps prepared for the "Lighting Africa" project^[249] the operation of the device implied that the devices was flexed and subjected to significant bending forces and this did result in device failure long before the operation of the solar cell ceased. The weak interface in that case was found to be the P3HT:PCBM-PEDOT:PSS interface. This led to a careful analysis of the fracture energy (Figure 38) as a function fullerene content by careful variation in increments of 1%^[253] using a fast roll-to-roll coating technique.^[254]

6. Conclusions and Outlook

The polymer and organic solar cells started out as the "enfant terrible" with respect to operational stability when compared to the established photovoltaic technologies but has improved tremendously with respect to stability but also in terms of power conversion efficiency and scalable processing. In this review we have covered the ground since the field was firstly reviewed and operational stability has improved pending severe efforts in encapsulation to today's significantly more stable materials and device structures. We have also described how large collaborative efforts have lifted the field in terms of credibility and the unifying force that lies in obtaining a consensus. The main reasons for the dramatic improvement in stability gained

in the recent years may be summarized as follows: i) Improved photo-stability of the active polymer materials; ii) the advent of the inverted device structure; iii) use of more stable metal electrodes (e.g., Al → Ag); iv) improved understanding of how each layer may contribute degradation mechanisms; v) improved morphology control; vi) the advent of R2R produced solar cells and their specific stability issues; vii) definition of good measurement practice (ISOS recommendations); viii) interlaboratory studies.

When looking at the imminent challenges with a bearing on stability that will need efficient solutions we highlight development of fast and efficient encapsulation using scalable methodologies such as roll-to-roll methods. The employment of device structures based on only printed layers and no involvement of heat intensive, expensive or scarce materials (e.g. no indium) are likely to present new stability challenges (e.g. consequences of multilayer solution processing). Since the future polymer solar cell is anticipated to enjoy some mechanical flexibility when processed using roll-to-roll methods new failure mechanisms are likely to emerge (e.g. delamination due to poor matching of the thermomechanical properties). One can safely conclude that there is a lot more work to be done but also that the promise of OPV as being a future energy technology is greater than ever.

Acknowledgements

This work has been supported the Danish Strategic Research Council (2104-07-0022), EUDP (j. nr. 64009-0050) and the Danish National Research Foundation. Partial financial support was also received from the European Commission as part of the Framework 7 ICT 2009 collaborative project HIFLEX (Grant No. 248678). From the EU-Indian framework of the "Largecells" project that received funding from the European Commission's Seventh Framework Programme (FP7/2007-2013. Grant No. 261936) and from PV-ERA-NET (project acronym POLYSTAR).

Received: October 31, 2011

Published online: December 29, 2011

- [1] D. M. Chapin, C. S. Fuller, G. L. Pearson, *J. Appl. Phys.* **1954**, 25, 676.
- [2] D. E. Carlson, C. R. Wronski, *Appl. Phys. Lett.* **1976**, 28, 671.
- [3] D. L. Staebler, C. R. Wronski, *Appl. Phys. Lett.* **1977**, 31, 292.
- [4] M. Köntges, I. Kunzen, S. Kajari-Schröder, X. Breitenmoser, B. Bjørneklett, *Sol. Energy Mater. Sol. Cells* **2011**, 95, 1131.
- [5] O. S. Sastry, S. Saurabh, S. K. Shil, P. C. Pant, R. Kumar, A. Kumar, B. Bandopadhyay, *Sol. Energy Mater. Sol. Cells* **2010**, 94, 1463.
- [6] A. W. Czanderna, F. J. Pern, *Sol. Energy Mater. Sol. Cells* **1996**, 43, 101.
- [7] G. J. Jorgensen, K. M. Terwilliger, J. A. DelCueto, S. H. Glick, M. D. Kempe, J. W. Pankow, F. J. Pern, T. J. McMahon, *Sol. Energy Mater. Sol. Cells* **2006**, 90, 2739.
- [8] M. D. Kempe, *Sol. Energy Mater. Sol. Cells* **2006**, 90, 2720.
- [9] M. D. Kempe, G. J. Jorgensen, K. M. Terwilliger, T. J. McMahon, C. E. Kennedy, T. T. Borek, *Sol. Energy Mater. Sol. Cells* **2007**, 91, 315.
- [10] M. D. Kempe, *Sol. Energy Mater. Sol. Cells* **2010**, 94, 246.
- [11] H. Kobayashi, Y. Kasama, T. Fujinaga, M. Takahashi, H. Koinuma, *Solid State Commun.* **2002**, 123, 151.
- [12] H. M. Branz, *Phys. Rev. B* **1999**, 59, 5498.
- [13] B. Yan, G. Yue, J. M. Owens, J. Yang, S. Guha, *Appl. Phys. Lett.* **2004**, 85, 1925.
- [14] J. Meier, R. Flückiger, H. Keppner, A. Shah, *Appl. Phys. Lett.* **1994**, 65, 860.
- [15] L. Yang, L. Chen, A. Catalano, *Appl. Phys. Lett.* **1991**, 59, 840.
- [16] R. S. Crandall, *Phys. Rev. B* **1991**, 43, 4057.
- [17] R. S. Crandall, D. E. Carlson, A. Catalano, H. A. Weakliem, *Appl. Phys. Lett.* **1984**, 44, 200.
- [18] P. J. Zanzucchi, C. R. Wronski, D. E. Carlson, *J. Appl. Phys.* **1977**, 48, 5227.
- [19] B. Rech, H. Wagner, *Appl. Phys. A* **1999**, 69, 155.
- [20] C. Beneking, B. Rech, J. Fölsch, H. Wagner, *Phys. Stat. Sol.* **1996**, 194, 41.
- [21] H. Fritzsche, *Annu. Rev. Mater. Res.* **2001**, 31, 47.
- [22] I. Visoly-Fisher, K. D. Dobson, J. Nair, E. Bezaldel, G. Hodes, D. Cahen, *Adv. Funct. Mater.* **2003**, 13, 289.
- [23] R. Mendoza-Pérez, J. Sastre-Hernandez, G. Contreras-Puente, O. Vigil-Galán, *Sol. Energy Mater. Sol. Cells* **2009**, 93, 79.
- [24] S. S. Hegedus, B. E. McCandless, *Sol. Energy Mater. Sol. Cells* **2005**, 88, 75.
- [25] D. Grecu, A. D. Compaan, D. Young, U. Jayamaha, D. H. Rose, *J. Appl. Phys.* **2000**, 88, 2490.
- [26] K. D. Dobson, I. Visoly-Fisher, G. Hodes, D. Cahen, *Sol. Energy Mater. Sol. Cells* **2000**, 62, 295.
- [27] V. P. Singh, O. M. Erickson, J. H. Chao, *J. Appl. Phys.* **1995**, 78, 4538.
- [28] D. L. Bätzner, A. Romeo, M. Terheggen, M. Döbeli, H. Zogg, A. N. Tiwari, *Thin Solid Films* **2004**, 451-452, 536.
- [29] T. Yanagisawa, T. Kojima, T. Koyanagi, *Microelectron. Reliability* **2004**, 44, 229.
- [30] J. Wennerberg, J. Kessler, L. Stolt, *Sol. Energy Mater. Sol. Cells* **2003**, 75, 47.
- [31] K. H. Lam, J. Close, W. Durisch, *Solar Energy* **2004**, 77, 121.
- [32] F. Kessler, D. Rudmann, *Solar Energy* **2004**, 77, 685.
- [33] G. A. Medvedkin, E. I. Terukov, Y. Hasegawa, K. Hirose, K. Sato, *Sol. Energy Mater. Sol. Cells* **2003**, 75, 127.
- [34] J. F. Guillemoles, *Thin Solid Films* **2002**, 403-404, 405.
- [35] M. Powalla, B. Dimmler, *Thin Solid Films* **2001**, 387, 251.
- [36] C. Radue, E. E. van Dyk, *Physica B* **2009**, 404, 4449.
- [37] W. Durisch, K.-H. Lam, J. Close, *Appl. Energy* **2006**, 83, 1339.
- [38] S. Kijima, T. Nakada, *Appl. Phys. Express* **2008**, 1, 075002.
- [39] M. Yamaguchi, *J. Appl. Phys.* **1995**, 78, 1476.
- [40] J. F. Guillemoles, L. Kronik, D. Cahen, U. Rau, A. Jananek, H.-W. Schock, *J. Phys. Chem. B* **2000**, 104, 4849.
- [41] J. F. Guillemoles, U. Rau, L. Kronik, H.-W. Schock, D. Cahen, *Adv. Mater.* **1999**, 11, 957.
- [42] M. Jørgensen, K. Norrman, F. C. Krebs, *Sol. Energy Mater. Sol. Cells* **2008**, 92, 686.
- [43] G. A. Chamberlain, *Solar Cells* **1983**, 8, 47.
- [44] C. J. Brabec, N. S. Sariciftci, J. C. Hummelen, *Adv. Funct. Mater.* **2001**, 11, 15.
- [45] H. Spanggaard, F. C. Krebs, *Sol. Energy Mater. Sol. Cells* **2004**, 83, 125.
- [46] K. M. Coakley, M. D. McGehee, *Chem. Mater.* **2004**, 16, 4533.
- [47] H. Hoppe, N. S. Sariciftci, *J. Mater. Res.* **2004**, 19, 1924.
- [48] S. Günes, H. Neugebauer, N. S. Sariciftci, *Chem. Rev.* **2007**, 107, 1324.
- [49] B. C. Thompson, J. M. J. Fréchet, *Angew. Chem. Int. Ed.* **2008**, 47, 58.
- [50] B. Saunders, M. L. Turner, *Adv. Coll. Interface Sci.* **2008**, 138, 1.
- [51] G. Dennler, M. C. Scharber, C. J. Brabec, *Adv. Mater.* **2009**, 21, 1323.
- [52] B. Kippelen, J. L. Brédas, *Energy Environ. Sci.* **2009**, 2, 251.
- [53] C. Li, M. Liu, N. G. Pschirer, M. Baumgarten, K. Müllen, *Chem. Rev.* **2010**, 110, 6817.
- [54] W. Cai, X. Gong, Y. Cao, *Sol. Energy Mater. Sol. Cells* **2010**, 94, 954.

- [55] R. Po, M. Maggini, N. Camaioni, *J. Phys. Chem. C* **2010**, *114*, 695.
- [56] C. Winder, N. S. Sariciftci, *J. Mater. Chem.* **2004**, *14*, 1077.
- [57] E. Bundgaard, F. C. Krebs, *Sol. Energy Mater. Sol. Cells* **2007**, *91*, 954.
- [58] R. Kroon, M. Lenes, J. C. Hummelen, P. W. M. Blom, B. De Boer, *Polym. Rev.* **2008**, *48*, 531.
- [59] P.-L. T. Boudreault, A. Najari, M. Leclerc, *Chem. Mater.* **2011**, *23*, 456.
- [60] H. Hoppe, N. S. Sariciftci, *Adv. Polym. Sci.* **2008**, *214*, 1.
- [61] S. Beaupré, P.-L. T. Boudreault, M. Leclerc, *Adv. Mater.* **2010**, *22*, E6.
- [62] A. Facchetti, *Chem. Mater.* **2011**, *23*, 733.
- [63] Y. Liang, L. Yu, *Acc. Chem. Res.* **2010**, *43*, 1227.
- [64] H. Hoppe, N. S. Sariciftci, *J. Mater. Chem.* **2006**, *16*, 45.
- [65] J. Peet, A. J. Heeger, G. C. Bazan, *Acc. Chem. Res.* **2009**, *42*, 1700.
- [66] J. Loos, *Materials Today* **2010**, *13*, 15.
- [67] A. Hadipour, B. De Boer, P. W. M. Blom, *Org. Electron.* **2008**, *9*, 617.
- [68] A. Hadipour, B. De Boer, P. W. M. Blom, *Adv. Funct. Mater.* **2008**, *18*, 169.
- [69] T. Ameri, G. Dennler, C. Lungenschmied, C. J. Brabec, *Energy Environ. Sci.* **2009**, *2*, 347.
- [70] S. Sista, Z. Hong, L.-M. Chen, Y. Yang, *Energy Environ. Sci.* **2011**, *4*, 1606.
- [71] C. J. Brabec, J. R. Durrant, *MRS Bull.* **2008**, *33*, 670.
- [72] F. C. Krebs, *Sol. Energy Mater. Sol. Cells* **2009**, *93*, 394.
- [73] M. Helgesen, R. Søndergaard, F. C. Krebs, *J. Mater. Chem.* **2010**, *20*, 36.
- [74] J. Boucle, P. Ravirajan, J. Nelson, *J. Mater. Chem.* **2007**, *17*, 3141.
- [75] I. Gonzalez-Valls, M. Lira-Cantu, *Energy Environ. Sci.* **2009**, *2*, 19.
- [76] T. Xu, Q. Qiao, *Energy Environ. Sci.* **2011**, *4*, 2700.
- [77] R. Steim, F. R. Kogler, C. J. Brabec, *J. Mater. Chem.* **2010**, *20*, 2499.
- [78] H. Ma, H.-L. Yip, F. Huang, A. K. Y. Jen, *Adv. Funct. Mater.* **2010**, *20*, 1371.
- [79] L.-M. Chen, Z. Xu, Z. Hong, Y. Yang, *J. Mater. Chem.* **2010**, *20*, 2575.
- [80] C. Deibel, V. Dyakonov, *Rep. Prog. Phys.* **2010**, *73*, 096401.
- [81] J. Nelson, *Mater. Today* **2011**, *14*, 462.
- [82] P. G. Nicholson, F. A. Castro, *Nanotechnology*, **2010**, *21*, 492001.
- [83] S. K. Hau, H.-L. Yip, A. K. Y. Jen, *Polymer Rev.* **2010**, *50*, 474.
- [84] F. Zhang, X. Xu, W. Tang, J. Zhang, Z. Zhuo, J. Wang, J. Wang, Z. Xu, Y. Wang, *Sol. Energy Mater. Sol. Cells* **2011**, *95*, 1785.
- [85] T. Gershon, *Mater. Sci. Tech.* **2011**, *27*, 1357.
- [86] C. W. Tang, *Appl. Phys. Lett.* **1986**, *48*, 183.
- [87] G. Yu, C. Zhang, A. J. Heeger, *Appl. Phys. Lett.* **1994**, *64*, 1540.
- [88] M. Glatthaar, M. Niggemann, B. Zimmermann, P. Lewer, M. Riede, A. Hirsch, J. Luther, *Thin Solid Films* **2006**, *491*, 298.
- [89] G. Li, C.-W. Chu, V. Shrotriya, J. Huang, Y. Yang, *Appl. Phys. Lett.* **2006**, *88*, 253503.
- [90] S. Chambon, A. Rivaton, J.-L. Gardette, M. Firon, L. Lutzen, *J. Polym. Sci., Part A: Polym. Chem.* **2007**, *45*, 317.
- [91] S. Chambon, A. Rivaton, J.-L. Gardette, M. Firon, *J. Polym. Sci., Part A: Polym. Chem.* **2009**, *47*, 6044.
- [92] A. Rivaton, S. Chambon, M. Manceau, J.-L. Gardette, N. Lemaître, S. Guillerez, *Polym. Degrad. Stab.* **2010**, *95*, 278.
- [93] S. Chambon, A. Rivaton, J.-L. Gardette, M. Firon, *Polym. Degrad. Stab.* **2011**, *96*, 1149.
- [94] M. Manceau, S. Chambon, A. Rivaton, J.-L. Gardette, S. Guillerez, N. Lemaître, *Sol. Energy Mater. Sol. Cells* **2010**, *94*, 1572.
- [95] H. Hintz, H.-J. Egelhaaf, H. Peisert, T. Chassé, *Polym. Degrad. Stab.* **2010**, *95*, 818.
- [96] M. Manceau, A. Rivaton, J.-L. Gardette, S. Guillerez, N. Lemaître, *Polym. Degrad. Stab.* **2009**, *94*, 898.
- [97] D. E. Motaung, G. F. Malgas, C. J. Arendse, *J. Mater. Sci.* **2011**, *46*, 4942.
- [98] C. J. Brabec, G. Zerza, G. Cerullo, S. De Silvestri, S. Luzzati, J. C. Hummelen, S. Sariciftci, *Chem. Phys. Lett.* **2001**, *340*, 232.
- [99] M. O. Reese, A. M. Nardes, B. L. Rupert, R. E. Larsen, D. C. Olson, M. T. Lloyd, S. E. Shaheen, D. S. Ginley, G. Rumbles, N. Kopidakis, *Adv. Funct. Mater.* **2010**, *20*, 3476.
- [100] J. Schafferhans, A. Baumann, A. Wagenpfahl, C. Deibel, V. Dyakonov, *Org. Electron.* **2010**, *11*, 1693.
- [101] A. Seemann, H.-J. Egelhaaf, C. J. Brabec, J. A. Hauch, *Org. Electron.* **2010**, *10*, 1424.
- [102] A. Aguirre, S. C. J. Meskers, R. A. J. Janssen, H.-J. Egelhaaf, *Org. Electron.* **2011**, *12*, 1657.
- [103] A. Seemann, T. Sauermann, C. Lungenschmied, O. Armbruster, S. Bauer, H.-J. Egelhaaf, J. Hauch, *Sol. Energy* **2011**, *85*, 1238.
- [104] J. Abad, A. Urbina, J. Colchero, *Org. Electron.* **2011**, *12*, 1389.
- [105] J. Abad, N. Espinosa, R. Garcia-Valverde, J. Colchero, A. Urbina, *Sol. Energy Mater. Sol. Cells* **2011**, *95*, 1326.
- [106] R. Grisorio, G. Allegretta, P. Mastroilli, G. P. Suranna, *Macromol.* **2011**, *44*, 7977.
- [107] M. Manceau, E. Bundgaard, J. E. Carlé, O. Hagemann, M. Helgesen, R. Søndergaard, M. Jørgensen, F. C. Krebs, *J. Mater. Chem.* **2011**, *21*, 4132.
- [108] E. Bundgaard, O. Hagemann, M. Manceau, M. Jørgensen, F. C. Krebs, *Macromol.* **2010**, *43*, 8115.
- [109] S. H. Kim, I.-W. Hwang, Y. Jin, S. Song, J. Moon, H. Suh, K. Lee, *Sol. Energy Mater. Sol. Cells* **2011**, *95*, 361.
- [110] Y. Xia, J. Tong, B. Li, C. Wang, H. Liu, *J. Polym. Sci. Part A: Polym. Chem.* **2011**, *49*, 2969.
- [111] J. E. Carlé, M. Jørgensen, M. Manceau, M. Helgesen, O. Hagemann, R. Søndergaard, F. C. Krebs, *Sol. Energy Mater. Sol. Cells* **2011**, *95*, 3222.
- [112] M. Manceau, M. Helgesen, F. C. Krebs, *Polym. Degrad. Stab.* **2010**, *95*, 2666.
- [113] X. Yang, J. K. J. van Duren, R. A. J. Janssen, M. A. Michels, J. Loos, *Macromol.* **2004**, *37*, 2151.
- [114] X. Yang, J. Loos, S. C. Veenstra, W. H. J. Verhees, M. M. Wienk, J. M. Kroon, M. A. J. Michels, R. A. J. Janssen, *Nano Lett.* **2005**, *5*, 579.
- [115] B. Paci, A. Generosi, D. Bailo, V. R. Albertini, R. de Bettignies, *Chem. Phys. Lett.* **2010**, *494*, 69.
- [116] B. Conings, S. Bertho, K. Vandewal, A. Senes, J. D'Haen, J. Manca, R. A. J. Janssen, *Appl. Phys. Lett.* **2010**, *96*, 163301.
- [117] B. Ray, M. A. Alam, *Appl. Phys. Lett.* **2011**, *99*, 033303.
- [118] A. Kumar, Z. Hong, S. Sista, Y. Yang, *Adv. Energy Mater.* **2011**, *1*, 124.
- [119] C. Lin, E.-Y. Lin, F.-Y. Tsai, *Adv. Funct. Mater.* **2010**, *20*, 834.
- [120] S. Ebadian, B. Gholamkhash, S. Shambayati, S. Holdcroft, P. Servati, *Sol. Energy Mater. Sol. Cells* **2010**, *94*, 2258.
- [121] B. Johnson, E. Allagoa, R. L. Thomas, G. Stettler, M. Wallis, J. H. Peel, T. Adalsteinson, B. J. McNelis, R. P. Barber Jr., *Sol. Energy Mater. Sol. Cells* **2010**, *94*, 537.
- [122] B. De Boer, U. Stalmach, P. F. van Hutten, C. Melzer, V. V. Krasnikov, G. Hadziioannou, *Polymer* **2001**, *42*, 9097.
- [123] E. E. Neuteboom, S. C. J. Meskers, P. A. van Hal, J. K. J. van Duren, E. W. Meijer, R. A. J. Janssen, H. Dupin, G. Pourtois, J. Cornil, R. Lazzaroni, J.-L. Brédas, D. Bejonne, *J. Am. Chem. Soc.* **2003**, *125*, 8625.
- [124] K. Sivula, Z. T. Ball, N. Watanabe, J. M. J. Fréchet, *Adv. Mater.* **2006**, *18*, 206.
- [125] S. Miyanishi, Y. Zhang, K. Tajima, K. Hashimoto, *Chem. Comm.* **2010**, *46*, 6723.
- [126] P. D. Topham, A. J. Parnell, R. C. Hiorns, *J. Polym. Sci. Part B: Polym. Phys.* **2011**, *49*, 1131.
- [127] M. Sommer, S. Huettner, M. Thelakkat, *Adv. Polym. Sci.* **2010**, *228*, 123.

- [128] L. Bu, X. Gou, Y. Qu, Z. Xie, D. Yan, Y. Geng, F. Wang, *J. Am. Chem. Soc.* **2009**, *131*, 13242.
- [129] E. J. W. Crossland, M. Kamperman, M. Nedelcu, C. Ducati, U. Wiesner, D.-M. Smilgies, G. E. S. Toombes, M. A. Hillmyer, S. Ludwigs, U. Steiner, H. J. Snaith, *Nano Lett.* **2009**, *9*, 2807.
- [130] M. S. Ryu, J. Jang, *Sol. Energy Mater. Sol. Cells* **2010**, *94*, 1384.
- [131] D. Sahu, H. Padhy, D. Patra, D. Kekuda, C.-W. Chu, I.-H. Chiang, H.-C. Lin, *Polymer* **2010**, *51*, 6182.
- [132] J. Farinhas, Q. Ferreira, R. E. Di Paolo, L. Alcácer, J. Morgado, A. Charas, *J. Mater. Chem.* **2011**, *21*, 12511.
- [133] M. Drees, H. Hoppe, C. Winder, H. Neugebauer, N. S. Sariciftci, W. Schwinger, F. Schöffler, C. Topf, M. C. Scharber, Z. Zhu, R. Gaudiana, *J. Mater. Chem.* **2005**, *15*, 5158.
- [134] B. J. Kim, Y. Miyamoto, B. Ma, J. M. J. Fréchet, *Adv. Func. Mater.* **2009**, *19*, 2273.
- [135] G. Griffini, J. D. Douglas, C. Piliago, T. W. Holcombe, S. Turri, J. M. C. Fréchet, J. L. Mynar, *Adv. Mater.* **2011**, *23*, 1660.
- [136] B. Gholamkhash, S. Holdcroft, *Chem. Mater.* **2010**, *22*, 5371.
- [137] J. Liu, E. N. Kadnikova, Y. Liu, M. D. McGehee, J. M. J. Fréchet, *J. Am. Chem. Soc.* **2004**, *126*, 9486.
- [138] S. A. Gevorgyan, F. C. Krebs, *Chem. Mater.* **2008**, *20*, 4386.
- [139] M. Bjerring, J. S. Nielsen, N. C. Nielsen, F. C. Krebs, *Macromolecules* **2007**, *40*, 6012.
- [140] F. C. Krebs, H. Spanggaard, *Chem. Mater.* **2005**, *17*, 5235.
- [141] F. C. Krebs, K. Norrman, *Prog. Photovoltaics: Research and Appl.* **2007**, *15*, 697.
- [142] F. C. Krebs, K. Norrman, *ACS Appl. Mater. Interfac.* **2010**, *2*, 877.
- [143] M. H. Petersen, S. A. Gevorgyan, F. C. Krebs, *Macromolecules* **2008**, *41*, 8986.
- [144] M. Helgesen, S. A. Gevorgyan, F. C. Krebs, R. A. J. Janssen, *Chem. Mater.* **2009**, *21*, 4669.
- [145] M. Helgesen, F. C. Krebs, *Macromolecules* **2010**, *43*, 1253.
- [146] O. Hagemann, M. Bjerring, N. C. Nielsen, F. C. Krebs, *Sol. Energy Mater. Sol. Cells* **2008**, *92*, 1327.
- [147] T. T. Larsen-Olsen, E. Bundgaard, K. O. Sylvester-Hvid, F. C. Krebs, *Org. Electron.* **2011**, *12*, 364.
- [148] R. Søndergaard, M. Helgesen, M. Jørgensen, F. C. Krebs, *Adv. Energy Mater.* **2011**, *1*, 68.
- [149] T. T. Larsen-Olsen, T. R. Andersen, B. Andreasen, A. P. L. Böttiger, E. Bundgaard, K. Norrman, J. W. Andreasen, M. Jørgensen, F. C. Krebs, *Sol. Energy Mater. Sol. Cells* **2012**, *97*, 43.
- [150] M. Glatthaar, M. Riede, N. Keegan, K. Sylvester-Hvid, B. Zimmermann, M. Niggemann, A. Hinsch, A. Gompert, *Sol. Energy Mater. Sol. Cells* **2007**, *91*, 390.
- [151] M. Glatthaar, N. Mingirulli, B. Zimmermann, T. Ziegler, R. Kern, M. Niggemann, A. Hinsch, A. Gombert, *Phys. Stat. Sol. A* **2005**, *202*, R125.
- [152] F. C. Krebs, T. Tromholt, M. Jørgensen, *Nanoscale* **2010**, *2*, 878.
- [153] F. C. Krebs, R. Søndergaard, M. Jørgensen, *Sol. Energy Mater. Sol. Cells* **2011**, *95*, 1348.
- [154] P. Sullivan, T. S. Jones, *Org. Electron.* **2009**, *9*, 656.
- [155] S. Schäfer, A. Petersen, T. A. Wagner, R. Kniprath, D. Lingenfeller, A. Zen, T. Kirchartz, B. Zimmermann, U. Würfel, X. Feng, T. Mayer, *Phys. Rev. B* **2011**, *83*, 165311.
- [156] Y. Kanai, T. Matsushima, H. Murata, *Thin Solid Films* **2009**, *518*, 537.
- [157] J. Huang, G. Li, Y. Yang, *Adv. Mater.* **2008**, *20*, 415.
- [158] H.-H. Liao, L.-M. Chen, Z. Xu, G. Li, Y. Yang, *Appl. Phys. Lett.* **2008**, *92*, 173303.
- [159] G. Yu, J. Gao, J. C. Hummelen, F. Wudl, A. J. Heeger, *Science* **1995**, *270*, 1789.
- [160] J. Y. Kim, S. H. Kim, H.-H. Lee, A. J. Heeger, *Adv. Mater.* **2006**, *18*, 572.
- [161] D. Gao, M. G. Helander, Z.-B. Wang, D. P. Puzzo, M. T. Greiner, Z.-H. Lu, *Adv. Mater.* **2010**, *22*, 5404.
- [162] K. Kawano, C. Adachi, *Appl. Phys. Lett.* **2010**, *96*, 053307.
- [163] C. Waldauf, M. Morana, P. Denk, P. Schilinsky, K. Coakley, S. A. Choulis, C. J. Brabec, *Appl. Phys. Lett.* **2006**, *89*, 233517.
- [164] R. Steim, A. S. A. Choulis, P. Schilinsky, C. J. Brabec, *Appl. Phys. Lett.* **2008**, *92*, 093303.
- [165] J. Y. Kim, S. H. Kim, H.-H. Lee, K. Lee, W. Ma, X. Gong, A. J. Heeger, *Adv. Mater.* **2006**, *18*, 572.
- [166] J. Li, S. Kim, S. Edington, J. Nedy, S. Cho, K. Lee, A. J. Heeger, M. C. Gupta, J. T. Yates Jr., *Sol. Energy Mater. Sol. Cells* **2011**, *95*, 1123.
- [167] M. Wang, Q. Tang, J. An, F. Xie, J. Chen, S. Zheng, K. Y. Wong, Q. Miao, J. Xu, *ACS Appl. Mater. Interfac.* **2010**, *2*, 2699.
- [168] M. Wang, F. Xie, W. Xie, S. Zheng, N. Ke, J. Chen, N. Zhao, J. B. Xu, *Appl. Phys. Lett.* **2011**, *98*, 183304.
- [169] Y. Wang, L. Yang, C. Yao, W. Qin, S. Yin, F. Zhang, *Sol. Energy Mater. Sol. Cells* **2011**, *95*, 1243.
- [170] S. O. Jeon, J. Y. Lee, *Sol. Energy Mater. Sol. Cells* **2011**, *95*, 1102.
- [171] F.-C. Chen, J.-L. Wu, S. S. Yang, K.-H. Hsieh, W.-C. Chen, *J. Appl. Phys.* **2008**, *103*, 103721.
- [172] L. Yang, H. Xu, H. Tian, S. Yin, F. Zhang, *Sol. Energy Mater. Sol. Cells* **2010**, *94*, 1831.
- [173] H. Jin, M. Tuomikoski, J. Hiltunen, P. Kopola, A. Maaninen, F. Pino, *J. Phys. Chem. C* **2009**, *113*, 16807.
- [174] D. C. Olson, S. E. Shaheen, N. Kopidakis, D. S. Ginley, *Appl. Phys. Lett.* **2006**, *89*, 143517.
- [175] Ü. Özgür, Y. I. Alivov, C. Liu, A. Teke, M. A. Reshchikov, S. Doğan, V. Avrutin, S.-J. Cho, H. Morko, *J. Appl. Phys.* **2005**, *98*, 041301.
- [176] S. J. Pearton, D. P. Norton, K. Ip, Y. W. Heo, *J. Vac. Sci. Tech. B: Microelectron. Nanometer Struct.* **2004**, *22*, 932.
- [177] F. Verbakel, S. C. J. Meskers, R. A. J. Janssen, *Appl. Phys. Lett.* **2006**, *89*, 102103.
- [178] M. R. Lilliedal, A. J. Medford, M. V. Madsen, K. Norrman, F. C. Krebs, *Sol. Energy Mater. Sol. Cells* **2010**, *94*, 2018.
- [179] N. S. Persika, K. J. Stebe, P. C. Searson, *J. Phys. Chem. B* **2003**, *107*, 10412.
- [180] S. R. Ferreira, P. Lu, Y.-J. Lee, R. J. Davis, J. W. P. Hsu, *J. Phys. Chem. C* **2011**, *115*, 13471.
- [181] A. Puetz, T. Stubhan, M. Reinhard, O. Loesch, E. Hammarberg, S. Wolf, C. Feldmann, H. Kalt, A. Colmann, U. Lemmer, *Sol. Energy Mater. Sol. Cells* **2011**, *95*, 579.
- [182] H. Sarenpää, T. Niemi, A. Tukainen, H. Lemmetyinen, N. Tkachenko, *Sol. Energy Mater. Sol. Cells* **2010**, *94*, 1379.
- [183] H. Zhang, J. Ouyang, *Appl. Phys. Lett.* **2010**, *97*, 063509.
- [184] B. Zimmermann, U. Würfel, M. Niggemann, *Sol. Energy Mater. Sol. Cells* **2009**, *93*, 491.
- [185] Y. Lare, B. Kouskoussa, K. Benchouk, S. O. Ouro Djobo, L. Cattin, M. Morsli, F. R. Diaz, M. Gacitua, T. Abachi, M. A. del Valle, F. Armijo, G. A. East, J. C. Bernède, *J. Phys. Chem. Solids* **2011**, *72*, 97.
- [186] M. F. Lo, T. W. Ng, S. L. Lai, F. L. Wong, M. K. Fung, S. T. Lee, C. S. Lee, *Appl. Phys. Lett.* **2010**, *97*, 143304.
- [187] F. C. Krebs, S. A. Gevorgyan, J. Alstrup, *J. Mater. Chem.* **2009**, *19*, 5442.
- [188] M. P. D. Jong, L. J. V. Ijzendoorn, M. J. A. D. Voigt, *Appl. Phys. Lett.* **2000**, *77*, 2255.
- [189] H. Kim, S. Nam, H. Lee, S. Woo, C.-S. Ha, M. Ree, Y. Kim, *J. Phys. Chem.* **2011**, *115*, 13502.
- [190] E. Vitoratos, S. Sakkopoulos, E. Dalas, N. Paliatsas, D. Karageorgopoulos, F. Petraki, S. Kennou, S. A. Choulis, *Org. Electron.* **2009**, *10*, 61.
- [191] E. Voroshazi, B. Verreet, A. Buri, R. Müller, D. Di Nuzzo, P. Heremans, *Org. Electron.* **2011**, *12*, 736.
- [192] E. Voroshazi, B. Verreet, T. Aernouts, P. Heremans, *Sol. Energy Mater. Sol. Cells* **2011**, *95*, 1303.
- [193] R. Betancur, M. Maymó, X. Elias, L. T. Vuong, J. Martorell, *Sol. Energy Mater. Sol. Cells* **2011**, *95*, 735.

- [194] I. Hancox, P. Sullivan, K. V. Chauhan, N. Beaumont, L. A. Rochford, R. A. Hatton, T. S. Jones, *Org. Electron.* **2010**, *11*, 2019.
- [195] P. Qin, G. Fang, Q. He, N. Sun, X. Fan, Q. Zheng, F. Chen, J. Wan, X. Zhao, *Sol. Energy Mater. Sol. Cells* **2011**, *95*, 1005.
- [196] M. T. Lloyd, C. H. Peters, A. Garcia, I. V. Kauvar, J. J. Berry, M. O. Reese, M. D. McGehee, D. S. Ginley, D. C. Olson, *Sol. Energy Mater. Sol. Cells* **2011**, *95*, 1382.
- [197] A. W. Hains, J. Liu, A. B. F. Martinson, M. D. Irwin, T. J. Marks, *Adv. Funct. Mater.* **2010**, *20*, 595.
- [198] K. Norrman, M. V. Madsen, S. A. Gevorgyan, F. C. Krebs, *J. Am. Chem. Soc.* **2010**, *132*, 16883.
- [199] M. F. Lo, T. W. Ng, S. L. Lai, M. K. Fung, S. T. Lee, C. S. Lee, *Appl. Phys. Lett.* **2011**, *99*, 033302.
- [200] B. Gholamkhash, S. Holdcroft, *Sol. Energy Mater. Sol. Cells* **2011**, *95*, 3106.
- [201] A. Moujoud, S. H. Oh, J. J. Hye, H. J. Kim, *Sol. Energy Mater. Sol. Cells* **2011**, *95*, 1037.
- [202] J.-S. Huang, C.-Y. Chou, C.-F. Lin, *IEEE Electron Device Lett.* **2010**, *31*, 332.
- [203] M. Hermenau, M. Riede, K. Leo, S. A. Gevorgyan, F. C. Krebs, K. Norrman, *Sol. Energy Mater. Sol. Cells* **2011**, *95*, 1268.
- [204] K. Norrman, N. B. Larsen, F. C. Krebs, *Sol. Energy Mater. Sol. Cells* **2006**, *90*, 2793.
- [205] K. Norrman, S. A. Gevorgyan, F. C. Krebs, *Appl. Mater. Int.* **2009**, *1*, 102.
- [206] K. Norrman, F. C. Krebs, *Sol. Energy Mater. Sol. Cells* **2006**, *90*, 213.
- [207] M. Lira-Cantu, K. Norrman, J. W. Andreasen, F. C. Krebs, *Chem. Mater.* **2006**, *18*, 5684.
- [208] M. V. Madsen, K. Norrman, F. C. Krebs, *J. Photon. Energy* **2011**, *1*, 011104.
- [209] M. Seeland, R. Rösch, H. Hoppe, *J. Appl. Phys.* **2011**, *109*, 064513.
- [210] F. C. Krebs, *Sol. Energy Mater. Sol. Cells* **2006**, *90*, 3633.
- [211] F. C. Krebs, J. Alstrup, H. Spanggaard, K. Larsen, E. Kold, *Sol. Energy Mater. Sol. Cells* **2004**, *83*, 293.
- [212] G. Dennler, C. Lungenschmied, H. Neugebauer, N. S. Sariciftci, A. Labouret, *J. Mater. Res.* **2005**, *20*, 3224.
- [213] G. Dennler, C. Lungenschmied, H. Neugebauer, N. S. Sariciftci, M. Latréche, G. Czeremuszkin, M. R. Wertheimer, *Thin Solid Films* **2006**, *511–512*, 349.
- [214] P. Madakasira, K. Inoue, R. Ulbricht, S. B. Lee, M. Zhou, J. P. Ferraris, A. A. Zakhidov, *Synth. Met.* **2005**, *155*, 332.
- [215] S. Sarkar, J. H. Culp, J. T. Whyland, M. Garvan, V. Misra, *Org. Electron.* **2010**, *11*, 1896.
- [216] S. Cros, R. de Bettignies, S. Berson, S. Bailly, P. Maise, N. Lemaitre, S. Guillerez, *Sol. Energy Mater. Sol. Cells* **2011**, *95*, S65.
- [217] B. Ecker, J. C. Nolasco, J. Pallarés, L. F. Marsal, J. Posdorfer, J. Parisi, E. von Hauff, *Adv. Funct. Mater.* **2011**, *21*, 2705.
- [218] A. J. Medford, M. R. Lilliedal, M. Jørgensen, D. Aarø, H. Pakalski, J. Fyenbo, F. C. Krebs, *Optics Express* **2010**, *18*, A272.
- [219] F. C. Krebs, J. Fyenbo, D. M. Tanenbaum, S. A. Gevorgyan, R. Andriessen, B. van Remoortere, Y. Galagan, M. Jørgensen, *Energy Environ. Sci.* **2011**, *4*, 4116.
- [220] D. M. Tanenbaum, H. F. Dam, R. Rösch, M. Jørgensen, H. Hoppe, F. C. Krebs, *Sol. Energy Mater. Sol. Cells* **2012**, *97*, 157.
- [221] F. C. Krebs, S. A. Gevorgyan, B. Gholamkhash, S. Holdcroft, C. Schlenker, M. E. Thompson, B. C. Thompson, D. Olson, D. S. Ginley, S. E. Shaheen, H. N. Alshareef, J. W. Murphy, W. J. Youngblood, N. C. Heston, J. R. Reynolds, S. Jia, D. Laird, S. M. Tuladhar, J. G. A. Dane, P. Atienzar, J. Nelson, J. M. Kroon, M. M. Wienk, R. A. J. Janssen, K. Tvingstedt, F. Zhang, M. Andersson, O. Inganäs, M. Lira-Cantu, R. de Bettignies, S. Guillerez, T. Aernouts, D. Cheyns, L. Lutsen, B. Zimmermann, U. Würfel, M. Niggemann, H.-F. Schleiermacher, P. Liska, M. Grätzel, P. Lianos, E. A. Katz, W. Lohwasser, B. Jannon, *Sol. Energy Mater. Sol. Cells* **2009**, *93*, 1968.
- [222] S. A. Gevorgyan, A. J. Medford, E. Bundgaard, S. B. Sapkota, H. Schleiermacher, B. Zimmermann, U. Würfel, A. Chafiq, M. Lira-Cantu, T. Swonke, M. Wagner, C. J. Brabec, O. Haillant, E. Voroshazi, T. Aernouts, R. Steim, J. A. Hauch, A. Elschner, M. Pannone, M. Xiao, A. Langzett, D. Laird, M. T. Lloyd, T. Rath, E. Maier, G. Trimmel, M. Hermenau, T. Menke, K. Leo, R. Rösch, M. Seeland, H. Hoppe, T. J. Nagle, K. B. Burke, C. J. Fell, D. Vak, T. B. Singh, S. E. Watkins, Y. Galagan, A. Manor, E. A. Katz, T. Kim, K. Kim, P. M. Sommeling, W. J. H. Verhees, S. C. Veenstra, M. Riede, M. G. Christoforo, T. Currier, V. Shrotriya, G. Schwartz, F. C. Krebs, *Sol. Energy Mater. Sol. Cells* **2011**, *95*, 1398.
- [223] M. O. Reese, S. A. Gevorgyan, M. Jørgensen, E. Bundgaard, S. R. Kurtz, D. S. Ginley, D. C. Olson, M. T. Lloyd, P. Morvillo, E. A. Katz, A. Elschner, O. Haillant, T. R. Currier, V. Shrotriya, M. Hermenau, M. Riede, K. R. Kirov, G. Trimmel, T. Rath, O. Inganäs, F. Zhang, M. Andersson, K. Tvingstedt, M. Lira-Cantu, D. Laird, C. McGuinness, S. Gowrisanker, M. Pannone, M. Xiao, J. Hauch, R. Steim, D. M. DeLongchamp, R. Rösch, H. Hoppe, N. Espinosa, A. Urbina, G. Yaman-Uzunoglu, J.-B. Bonekamp, A. J. J. M. van Breemen, C. Girotto, E. Voroshazi, F. C. Krebs, *Sol. Energy Mater. Sol. Cells* **2011**, *95*, 1253.
- [224] ISOS-1 <http://www.isos-1.wikispaces.com> (accessed September 2011).
- [225] ISOS-2 <http://www.isos-2.wikispaces.com> (accessed September 2011).
- [226] ISOS-3 <http://indico.conferences.dtu.dk/conferenceDisplay.py?ovw=True&confId=35> (accessed September 2011).
- [227] M. O. Reese, A. K. Sigdel, J. J. Berry, D. S. Ginley, S. E. Shaheen, *Sol. Energy Mater. Sol. Cells* **2010**, *94*, 1254.
- [228] M. Lira-Cantu, A. Chafiq, J. Faissat, I. Gonzalez-Valls, Y. Yu, *Sol. Energy Mater. Sol. Cells* **2011**, *95*, 1362.
- [229] S. A. Gevorgyan, M. Jørgensen, F. C. Krebs, *Sol. Energy Mater. Sol. Cells* **2008**, *92*, 736.
- [230] S. A. Gevorgyan, M. Jørgensen, F. C. Krebs, K. O. Sylvester-Hvid, *Sol. Energy Mater. Sol. Cells* **2011**, *95*, 1389.
- [231] O. Haillant, *Sol. Energy Mater. Sol. Cells* **2011**, *95*, 1284.
- [232] O. Haillant, D. Dumbleton, A. Zielnik, *Sol. Energy Mater. Sol. Cells* **2011**, *95*, 1889.
- [233] R. de Bettignies, F. Leroy, M. Firon, C. Sentein, *Synth. Met.* **2006**, *156*, 510.
- [234] D. Chemisana, *Renewable and Sustainable Energy Reviews* **2011**, *15*, 603.
- [235] T. Tromholt, M. Manceau, M. Helgesen, J. E. Carlé, F. C. Krebs, *Sol. Energy Mater. Sol. Cells* **2010**, *95*, 1308.
- [236] T. Tromholt, E. A. Katz, B. Hirsch, A. Vossier, F. C. Krebs, *Appl. Phys. Lett.* **2010**, *96*, 073501.
- [237] A. Manor, E. A. Katz, T. Tromholt, B. Hirsch, F. C. Krebs, *J. Appl. Phys.* **2011**, *109*, 074508.
- [238] T. Tromholt, A. Manor, E. A. Katz, F. C. Krebs, *Nanotechnology* **2011**, *22*, 225401.
- [239] M. Hermenau, L. Leo, M. Riede, *Organic Photonics IV* (Ed: P. L. Heremans), **2011**, 77220K.
- [240] J. A. Hauch, P. Schilinsky, S. A. Coulis, S. Rajoelson, C. J. Brabec, *Appl. Phys. Lett.* **2008**, *93*, 103306.
- [241] J. Metzendorf, T. Wittchen, K. Heidler, K. Dehne, R. Shimokawa, F. Nagamine, H. Ossenbrink, L. Fornarini, C. Goodbody, M. Davies, K. Emery, R. Deblasio, *IEEE Photovoltaic Specialists Conference* **1990**, 952.
- [242] J. Metzendorf, T. Wittchen, K. Heidler, K. Dehne, R. Shimokawa, F. Nagamine, H. Ossenbrink, L. Fornarini, C. Goodbody, M. Davies, K. Emery, R. Deblasio, The results of the PEP '87 round-robin calibration of reference cells and modules final report PTB technical report PTB-Opt-31 ISBN3-89429-067-6 **1990**.
- [243] C. R. Osterwald, S. Anevsky, A. K. Barua, J. Dubard, K. Emery, D. King, J. Metzendorf, F. Nagamine, R. Shimokawa, N. Udayakumar, Y. X. Wang, W. Zaïman, A. Zastrow, J. Zhang, *IEEE Photovoltaic Specialists Conference* **1996**, 1263.
- [244] C. R. Osterwald, S. Anevsky, K. Bücher, A. K. Barua, P. Chaudhuri, J. Dubard, K. Emery, B. Hansen, D. King, J. Metzendorf, F. Nagamine,

R. Shimokawa, X. Y. Wang, T. Wittchen, W. Zaaiman, A. Zastrow, J. Zhang, *Prog. Photovoltaics* **1999**, 287.

- [245] T. R. Betts, R. Gottschalg, D. G. Infield, W. Kolodenny, M. Prorok, T. Zdanowicz, N. van der Borg, H. de Moor, G. Friesen, A. Guerin de Montgareuil, W. Herrmann, *European Photovoltaic Solar Energy Conference* **2006**, 2447.
- [246] W. Herrmann, S. Mau, F. Fabero, T. Betts, N. van der Borg, K. Kiefer, G. Friesen, W. Zaaiman, *European Photovoltaic Solar Energy Conference* **2007**, 2506.
- [247] D. M. Tanenbaum, M. Hermenau, E. Voroshazi, M. T. Lloyd, Y. Galagan, B. Zimmermann, M. Hösel, H. F. Dam, M. Jørgensen, S. A. Gevorgyan, S. Kudret, W. Maes, L. Lutsen, D. Vanderzande, U. Würfel, R. Andriessen, R. Rösch, H. Hoppe, M. Lira-Cantu, A. Rivaton, G. Y. Uzunoğlu, D. Germack, B. Andreasen, M. V. Madsen, K. Norrman, F. C. Krebs, *RSC Advances* **2012**, <http://dx.doi.org/10.1039/C1RA00686J>.
- [248] J. A. Hauch, P. Schilinsky, S. A. Choulis, R. Childers, M. Biele, C. J. Brabec, *Sol. Energy Mater. Sol. Cells* **2008**, 92, 727.
- [249] F. C. Krebs, M. Jørgensen, K. Norrman, O. Hagemann, J. Alstrup, T. D. Nielsen, J. Fyenbo, K. Larsen, J. Kristensen, *Sol. Energy Mater. Sol. Cells* **2009**, 93, 422.
- [250] F. C. Krebs, T. D. Nielsen, J. Fyenbo, M. Wadstrøm, M. S. Pedersen, *Energy Environ. Sci.* **2010**, 3, 512.
- [251] F. C. Krebs, J. Alstrup, M. Biancardo, H. Spanggaard, *Large Area Polymer Solar Cells. Proc. SPIE.* **2005**, 5938, 593804.
- [252] F. C. Krebs, H. Spanggaard, T. Kjær, M. Biancardo, J. Alstrup, *Large Area Plastic Solar Cell Modules. Mater. Sci. Eng. B* **2007**, 138, 106.
- [253] S. R. Dupont, M. Oliver, F. C. Krebs, R. H. Dauskardt, *Sol. Energy Mater. Sol. Cells.* **2012**, 97, 171.
- [254] J. Alstrup, M. Jørgensen, A. J. Medford, F. C. Krebs, *ACS Appl. Mater. Interfaces* **2010**, 2, 2819.

Cite this: *Phys. Chem. Chem. Phys.*, 2012, **14**, 11780–11799

www.rsc.org/pccp

PAPER

TOF-SIMS investigation of degradation pathways occurring in a variety of organic photovoltaic devices – the ISOS-3 inter-laboratory collaboration

Birgitta Andreasen,^a David M. Tanenbaum,^{ab} Martin Hermenau,^c Eszter Voroshazi,^d Matthew T. Lloyd,^e Yulia Galagan,^f Birger Zimmernann,^g Suleyman Kudret,^h Wouter Maes,^h Laurence Lutsen,ⁱ Dirk Vanderzande,^h Uli Würfel,^g Ronn Andriessen,^f Roland Rösch,^j Harald Hoppe,^j Gerardo Teran-Escobar,^k Monica Lira-Cantu,^k Agnès Rivaton,^l Gülşah Y. Uzunoglu,^m David S. Germack,ⁿ Markus Hösel,^a Henrik F. Dam,^a Mikkel Jørgensen,^a Suren A. Gevorgyan,^a Morten V. Madsen,^a Eva Bundgaard,^a Frederik C. Krebs^a and Kion Norrman^{*a}

Received 30th May 2012, Accepted 4th July 2012

DOI: 10.1039/c2cp41787a

The present work is the fourth (and final) contribution to an inter-laboratory collaboration that was planned at the 3rd International Summit on Organic Photovoltaic Stability (ISOS-3). The collaboration involved six laboratories capable of producing seven distinct sets of OPV devices that were degraded under well-defined conditions in accordance with the ISOS-3 protocols. The degradation experiments lasted up to 1830 hours and involved more than 300 cells on more than 100 devices. The devices were analyzed and characterized at different points of their lifetimes by a large number of non-destructive and destructive techniques in order to identify specific degradation mechanisms responsible for the deterioration of the photovoltaic response. Work presented herein involves time-of-flight secondary ion mass spectrometry (TOF-SIMS) in order to study chemical degradation in-plane as well as in-depth in the organic solar cells. Various degradation mechanisms were investigated and correlated with cell performance. For example, photo-oxidation of the active material was quantitatively studied as a function of cell performance. The large variety of cell architectures used (some with and some without encapsulation) enabled valuable comparisons and important conclusions to be drawn on degradation behaviour. This comprehensive investigation of OPV stability has significantly advanced the understanding of degradation behaviour in OPV devices, which is an important step towards large scale application of organic solar cells.

^a Department of Energy Conversion and Storage, Technical University of Denmark, Frederiksborgvej 399, DK-4000, Roskilde, Denmark. E-mail: kino@dtu.dk

^b Department of Physics and Astronomy, Pomona College, Claremont, CA 91711, USA

^c Arbeitsgruppe Organische Solarzellen (OSOL), Institut für Angewandte Photophysik, Technische Universität Dresden, 01062, Dresden, Germany

^d IMEC, Kapeldreef 75, 3000 Leuven, Belgium and Katholieke Universiteit Leuven, ESAT, Kasteelpark Arenberg 10, 3000, Leuven, Belgium

^e National Renewable Energy Laboratory, Golden, CO 80401, USA

^f Holst Centre, High Tech Campus 31, 5656 AE Eindhoven, The Netherlands

^g Fraunhofer Institute for Solar Energy Systems ISE, Heidenhofstrasse 2, D-79110 Freiburg, Germany

^h Hasselt University, Campus, Agoralaan 1, Building D, WET/OBPC, B-3590 Diepenbeek, Belgium

ⁱ IMEC, IMOMECA Associated Laboratory, Campus University of Hasselt, Wetenschapspark 1, B-3590, Diepenbeek, Belgium

^j Institute of Physics, Ilmenau University of Technology, Weimarer Str. 32, 98693, Ilmenau, Germany

^k Centre d'Investigació en Nanociència i Nanotecnologia (CIN2, CSIC), Laboratory of Nanostructured Materials for Photovoltaic Energy, ETSE, Campus UAB, Edifici Q, 2nd Floor, E-08193, Bellaterra (Barcelona), Spain

^l Clermont Université, Université Blaise Pascal, Laboratoire de Photochimie Moléculaire et Macromoléculaire (LPMM), BP10448, F-63000 Clermont-Ferrand, France

^m CNRS, UMR6505, LPMM, F-63177, Aubière, France

ⁿ Condensed Matter Physics, Brookhaven National Lab, Building 510B Upton, NY, 11973, USA

1. Introduction

Organic photovoltaics (OPV) constitute an attractive alternative to silicon-based solar cells, manifested in fast processing and extremely low cost.^{1–3} The OPV research field has vastly increased in the past decade, covering a large number of focus areas such as photoelectric conversion efficiency (PCE), processing techniques, new materials, device configuration, and lifetime and stability. Exceptional progress has been made within PCE optimization and lifetime and stability. The PCE is ~10% for small laboratory cells^{4,5} and ~2% for roll-to-roll (R2R) cells.⁶ The lifetime has been optimized from minutes to a few years under outdoor conditions. Lifetime and stability are determined by the magnitude and multitude of degradation mechanisms occurring throughout the OPV device during operation and storage.^{7–9} A detailed understanding of the degradation mechanisms is of utmost importance if acceptable lifetimes are to be achieved, which is a prerequisite for large-scale application and thus commercialization.³ OPV degradation is highly complex and constitutes an analytical challenge due to the multitude of materials, interfaces, and device architectures that are constantly being modified and optimized.^{10–13}

The work presented in this article is part of a large inter-laboratory study that resulted from the 3rd International Summit on Organic Photovoltaic Stability (ISOS-3).¹⁴ The collaboration involved six laboratories (Table 1) capable of manufacturing OPV devices, which produced seven distinct sets of OPV devices. The devices were all shipped to Risø DTU where they were degraded under identical well-defined conditions. Three different degradation conditions were used in accordance with the ISOS-3 protocols: accelerated full sun simulation; low level indoor fluorescent lighting; and dark storage with daily monitoring of the photovoltaic parameters.¹⁴ These conditions will be referred to as “full sun”, “fluorescent” and “dark”, respectively. The devices were analyzed and characterized at different points of their lifetime by a large number of non-destructive and destructive techniques. The terminology used for a lifetime of a device extracted from the degradation experiment is “TXX”, where XX denotes the percentage which the PCE has declined to from the initially measured PCE, *i.e.* T100 is the initial measurement, T80 is when PCE has declined to 80% of its initial value *etc.* The original goal was to extract the devices from the degradation experiment at T100, T80, T50, and T10, which more or less

was achieved (some devices never reached T10 within the timeframe of the project). Once a device was extracted it was not reused, and since some of the characterization methods are destructive, it was necessary to manufacture a large number of devices. The degradation experiments lasted up to 1830 hours and involved more than 100 devices with more than 300 cells (a device can contain several cells).

The ISOS-3 inter-laboratory study has produced a vast amount of results, which so far has resulted in three articles, hereafter termed ISOS-3 reports.^{15–17} The different device manufacturing methods along with the degradation procedures and electrical characterization have been presented in the first ISOS-3 report.¹⁵ The second ISOS-3 report describes work using a suite of imaging techniques to map specific degradation mechanisms.¹⁶ The following imaging techniques were employed: laser-beam induced current (LBIC), photoluminescence imaging (PLI), electroluminescence imaging (ELI) and lock-in thermography (LIT). In addition to analyzing the ISOS-3 devices at specified T-values (in this case corresponding to different devices and thus cells), selected devices were cycled in order to monitor the evolution of spatial defects on the same cell. In the third article incident photon-to-electron conversion efficiency (IPCE) and *in situ* IPCE were employed to describe various degradation mechanisms.¹⁷ The most important conclusions regarding degradation mechanisms based on the previous ISOS-3 reports are summarized in the following.

The combination of the imaging techniques LBIC, PLI, ELI and LIT suggested that the main degradation mechanisms were the following:¹⁶

- Formation of aluminium oxide (at the aluminium electrode).
- Formation of blocking contacts due to silver oxide formation or ZnO dedoping.
- Electro-migration of silver (especially at the edges due to enhanced electric fields).
- Water and oxygen ingress through pinholes and from the edges of the cells.
- Water release from highly conductive PEDOT:PSS.

The overall conclusion based on the imaging results is that OPV device stability is mostly controlled by the instability of the charge collecting electrodes. It should be emphasized that these imaging analyses alone do not directly reveal degradation mechanisms, complementary information is often necessary to come to plausible conclusions. Ideally it would make

Table 1 Cell configurations used in the ISOS-3 inter-laboratory study

Laboratory ^a	Cell configuration	Encapsulation and/or substrate (back–front)
IAPP	Al–BPhen–C ₆₀ –ZnPc:C ₆₀ –MeO–TPD:C ₆₀ F ₃₆ –ITO ^b	Glass–glass
Holst	Al–LiF–P3HT:PCBM–PEDOT:PSS–SiN, Ag ^c	Stainless steel–glass
ISE	Au–PEDOT:PSS–P3HT:PCBM–Cr–Al–Cr	Glass–glass
NREL	Al–Ag–PEDOT:PSS–P3HT:PCBM–ZnO–ITO	None–glass
IMEC	Al–Ag–MoO ₃ –P3HT:PCBM–ZnO–ITO	None–glass
Risø DTU	Ag–PEDOT:PSS–P3HT:PCBM–ZnO–ITO	UV filter barrier–PET, UV filter barrier ^e
Risø DTU	Ag–PEDOT:PSS–P3HT- <i>co</i> -P3AcET:PCBM–ZnO–ITO ^d	UV filter barrier–PET, UV filter barrier

^a See author addresses for details on the laboratories. ^b C₆₀ is Buckminsterfullerene, ZnPc is zinc-phthalocyanine, BPhen is 4,7-diphenyl-1,10-phenanthroline, MeO-TPD is *N,N'*-diphenyl-*N,N'*-bis(3-methylphenyl)-[1,1'-biphenyl]-4,4'-diamine. ^c P3HT is poly(3-hexylthiophene), PCBM is phenyl-C₆₁-butyric acid methyl ester, PEDOT is poly(3,4-ethylenedioxythiophene), PSS is poly(styrenesulfonate). ^d P3HT-*co*-P3AcET is poly(3-hexylthiophene-*co*-3-(2-acetoxyethyl)thiophene). ^e PET is a 130 μm thick poly(ethylene terephthalate), the UV filter barrier is a 90 μm thick multi-laminate with a UV-filter (Alcan) with a pressure sensitive adhesive (467MPF, 3 M).

sense to combine the analyses with techniques that produce direct chemical information.

Because the IPCE and *in situ* IPCE analyses were conducted in both ambient and N₂ atmospheres it was possible to identify the materials more susceptible to degradation caused by molecular oxygen and water. The result of the IPCE and *in situ* IPCE analyses resulted in the following major conclusions/comments regarding degradation:¹⁷

- For some of the encapsulated devices the degradation could possibly be initiated at the Ag or Au/PEDOT:PSS interface by the formation of a chemical bond between the Ag (or Au) and the PEDOT:PSS, which can occur in the absence of oxygen and water.

- The devices without encapsulation were highly dependent on atmospheric conditions and water uptake was a major problem attributed to the hygroscopic nature of PEDOT:PSS and semiconductor oxides.

- For the devices without encapsulation the water uptake was observed to be random and reversible.

- For the devices without encapsulation water will primarily degrade the electrodes of the cell.

- The cells within a device (a device can contain several cells) degraded differently depending on the position of the cell in the device.

The present work constitutes the fourth and final report in the series of reports that resulted from the ISOS-3 inter-laboratory study. The main analytical technique used in this work is time-of-flight secondary ion mass spectrometry (TOF-SIMS), a technique producing direct chemical information. The secondary technique is X-ray photoelectron spectroscopy (XPS), which also produces direct (but complementary) chemical information. The basic information of TOF-SIMS is mass spectral information, *i.e.* chemical information. TOF-SIMS imaging has an exceptional low probe depth of 1–2 nm, and is able to obtain surface images based on the mass spectral information. Furthermore, material can be sputtered away from the surface during the TOF-SIMS imaging analysis, *i.e.* a microscopic hole can be made that when combined with the imaging capability produces a depth profile, *i.e.* mass spectral-based images as a function of depth. The principle of TOF-SIMS depth profiling is schematically shown in Fig. 1. The fact that TOF-SIMS produces direct chemical information from any given point in the cell makes it, in principle, an ideal technique to either directly identify a degradation mechanism,

or complement the analysis results described in the previous ISOS-3 reports.^{15–17} However, there are certain limitations such as a poor depth resolution, which makes it challenging to detect interface phenomena. Furthermore, the depth profiling properties used are such that all molecular information is destroyed leaving only atomic ions and small fragment ions to be monitored. Finally, the data interpretation can be very challenging due to the enormous amount of mass spectral peaks generated during a TOF-SIMS analysis, which is problematic if one does not know specifically what one is looking for, *i.e.* “looking for a needle in a haystack situation”.

The main focus of the work presented herein is to study the degradation of the active bulk material monitored by the oxygen incorporation that will be correlated with loss in performance for the various ISOS-3 devices. Furthermore, the oxygen incorporation will be quantified by correlating the TOF-SIMS results with results obtained by the quantitative XPS technique. Furthermore, degradation mechanisms suggested in the previous ISOS-3 reports will be correlated with information extracted from the TOF-SIMS depth profiling analyses. Finally, trends between loss in cell performance and information extracted from the TOF-SIMS depth profiling data will be described and discussed.

2. Experimental

Experimental details pertaining to manufacture of the ISOS-3 devices, the degradation experiments, and characterization of the photovoltaic parameters can be found in the first ISOS-3 report.¹⁵ Relevant information regarding the present work is that seven distinct device types (Table 1) were degraded under three different conditions: full sun, fluorescent, and dark (as mentioned previously in the text). The devices were extracted from the degradation tests at different lifetimes corresponding to (more or less) T100, T80, T50 and T10, and subsequently shipped to the participating laboratories around the world for analysis. The destructive analyses were obviously performed last and when Risø DTU (that initially performed the degradation experiments) received the devices for the destructive TOF-SIMS analysis, they were placed in a glove box in a dry nitrogen atmosphere. Devices that were encapsulated had the encapsulation removed. A TOF-SIMS depth profiling analysis cannot penetrate the thick encapsulation. The Risø DTU cells were laminated and when delaminated the layers detached at the PEDOT:PSS/P3HT:PCBM interface, which turned out to be fortunate (will be evident later in the text). The devices and partial devices were placed on a TOF-SIMS sample holder in the glove box that was then placed in a specially designed transfer vessel that can sustain a controlled atmosphere long enough for the transfer vessel to be inserted into the vacuum chamber of the TOF-SIMS instrument. The encapsulated devices were thus never exposed to ambient air between the degradation experiments and the TOF-SIMS analysis. After the TOF-SIMS analysis the devices were transferred back to the glove box and stored until possible reanalysis.

TOF-SIMS analyses were performed on six out of the seven distinct devices. The IAPP device was omitted since the main objective in this study was to compare the oxygen incorporation in the active material as a function of loss in performance.

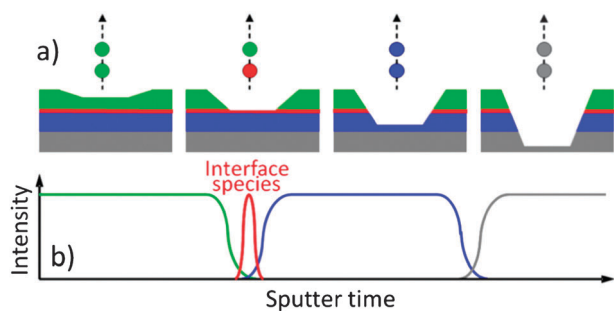


Fig. 1 (a) Schematic cross-section of an OPV device at various stages of depth profiling. (b) Schematic depth profile showing the intensity of various materials as a function of sputter time (*i.e.* depth).

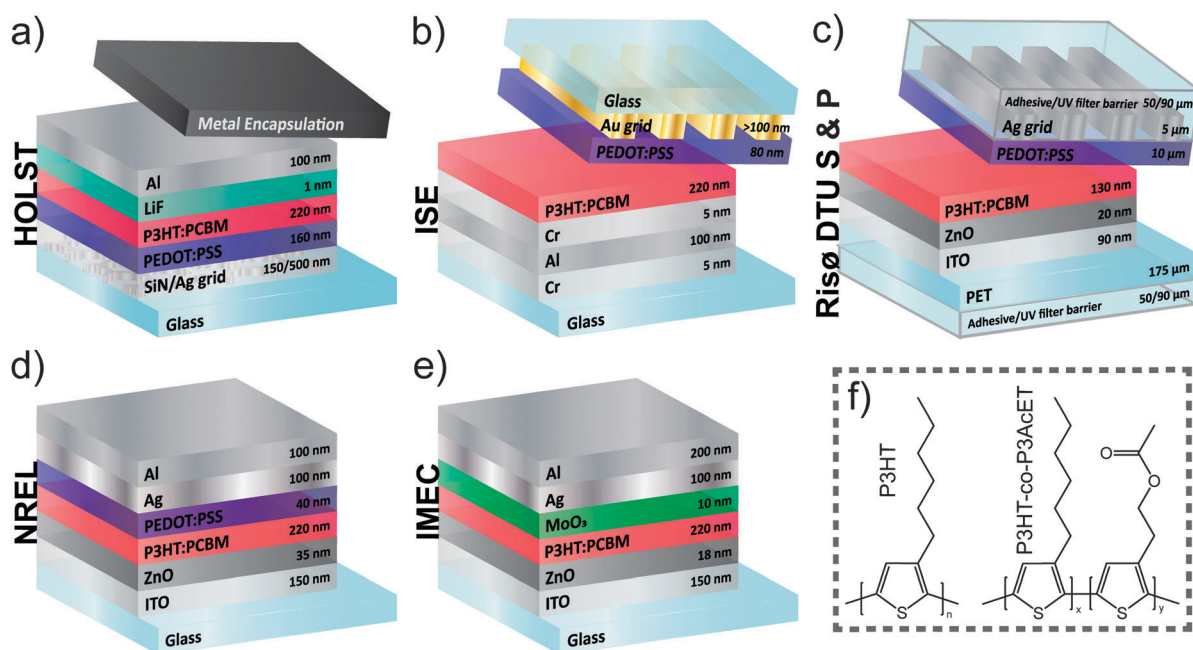


Fig. 2 (a)–(e) illustrate the different device layer structures (materials and thicknesses) investigated in this work. The tilted sections on devices (a)–(c) indicate where the devices were opened/delaminated, thus making the TOF-SIMS analysis possible. The active layers of all the devices consisted of P3HT:PCBM except the Risø DTU S device that had the slightly modified P3HT polymer P3HT-co-P3AcET. The molecular structures of P3HT and P3HT-co-P3AcET are shown in (f).

The IAPP device is the only device not using P3HT:PCBM as the active material. The intensity of a mass spectral marker can only be compared for the same material when different cells are compared due to the response factors that are material dependent in a TOF-SIMS analysis. Another problem with the IAPP device was the long lifetime that by far exceeded the 1830 hours that the degradation experiments lasted. However, the IAPP device has previously been extensively studied at Risø DTU.¹⁸ In that particular study the device was exposed to controlled atmospheres without encapsulation and illuminated ($AM1.5G$, 330 W m^{-2} , $49 \text{ }^\circ\text{C}$). T50 was found to be ~ 2700 hours in a N_2 atmosphere, 74 hours in an $\text{O}_2 : \text{N}_2$ atmosphere, and 11 hours in a $\text{H}_2\text{O} : \text{N}_2$ atmosphere. It was found that water significantly causes the device to degrade. The two most significant water-induced degradation mechanisms were found to be: (i) diffusion of water through the aluminium electrode in between the grains, resulting in formation of aluminium oxide at the BPhen/Al interface, and (ii) diffusion of water into the active layer ($\text{ZnPc} : \text{C}_{60}$), where ZnPc, but not C_{60} , becomes oxidized. Fig. 2 shows schematics of the devices that were studied in this work, and associated layer thicknesses.

2.1 TOF-SIMS analysis

The TOF-SIMS analyses were performed using a TOF-SIMS IV (ION-TOF GmbH, Münster, Germany). 25 ns pulses of 25 keV Bi^+ (primary ions) were bunched to form ion packets with a nominal temporal extent of < 0.9 ns at a repetition rate of 10 kHz, yielding a target current of 0.7 pA. These primary ion conditions were used to obtain mass spectra, ion images, and depth profiles. Depth profiling was performed using an analysis area of $200 \times 200 \text{ } \mu\text{m}^2$ centred in a sputter area of $300 \times 300 \text{ } \mu\text{m}^2$. 30 nA of 3 keV Xe^+ was used as sputter ions.

An encapsulated IMEC device was analyzed in a slightly different way: the encapsulation was removed and the Al–Ag– MoO_3 stack was partly removed. $11 \times 8 \text{ mm}^2$ surface areas were then imaged, each covering four cells on the device. These images were cropped to sizes corresponding to the individual cells ($5.2 \times 2.7 \text{ mm}^2$). Depth profiling was performed on the encapsulated IMEC device at various surface locations using an analysis area of $500 \times 500 \text{ } \mu\text{m}^2$ centred in a sputter area of $750 \times 750 \text{ } \mu\text{m}^2$. For all analyses electron bombardment (20 eV) was used to minimize charge built-up at the surface. Desorbed secondary ions were accelerated to 2 keV, mass analyzed in the flight tube, and post-accelerated to 10 keV before detection.

The relative degree of oxygen incorporation (*i.e.* degradation) in the bulk active material is extracted from the depth profiling data by evaluating the depth profiles in order to pinpoint the sputter time window that corresponds only to the bulk P3HT:PCBM material. This is exemplified by the NREL device that exhibits illustrative depth profiles (Fig. 3) that demonstrate the principle.

Careful selection of more or less specific mass spectral markers enables distinction between the individual layers. Within the sputter time window for the P3HT:PCBM material the goal was to pinpoint where all the signal intensities are constant/parallel, *i.e.* without interference from other species. The oxygen depth profile (O^-) in Fig. 3 shows that in that particular case there is only a limited sputter time window available due to interference from ZnO and ITO that contributes to the oxygen depth profile (O^-). In this case the interference is probably caused by a small degree of interlayer mixing, which is not caused by the sputter process that acts in the opposite direction. Furthermore, a depth profile only makes physical sense if the lateral plane of the probed volume is homogeneous, so to ensure lateral homogeneity the ion

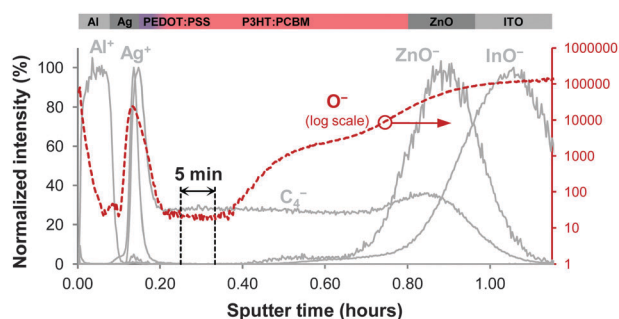


Fig. 3 TOF-SIMS depth profiles of a T100 NREL device (the layer structure is indicated at the top of the figure). Various carefully selected mass spectral markers identify the different layers (grey lines). The oxygen profile (dashed red line) and the indicated sputter time window corresponding to the bulk of the P3HT:PCBM material show from where the information is extracted. The thin PEDOT:PSS layer is defined by the Na^+ profile (not shown) and does not overlap with the 5 minute sputter time window in question.

images were carefully analyzed and any abnormalities such as spatially localized contaminants (*e.g.* particles) were bypassed in the dataset, which ensured that only the photo-oxidation was probed. The depth profiles in Fig. 3 also demonstrate the unfortunate poor depth resolution that worsens for longer sputter times. It should be emphasized that different materials have different sputter rates, so there is no correlation between relative sputter time windows and relative layer thicknesses. To ensure that the extracted information could be compared within and across the different devices some simple measures had to be taken during the data interpretation. It is not a problem to maintain the experimental analysis conditions over short periods of time, however, due to the large amount of devices that were analyzed over a very long time it was impossible to reproduce the experimental conditions accurately. The signal intensity is sensitive towards some instrumental parameters, so in order to eliminate the instrument effects and maintain the comparability the following procedure was adapted: in each case equally sized sputter time windows corresponding to 30 scans were chosen. More importantly, the oxygen signal intensity was normalized against the sum of most of the abundant signals within the same sputter time window, which constituted (for the sputter conditions in question) the following signals: C_n^- ($n = 2-4; 6-10$). The peak C_5^- was omitted due to significant peak overlap and C_1^- was omitted because it, for unknown reasons, worsened the reproducibility. It was thus $\text{Int}(\text{O}^-)/\text{Int}(\text{C}_n^-, n = 2-4; 6-10)$ that was extracted from each depth profile (the ratio was multiplied by a factor of 1000 for practical reasons), which provides a semi-quantitative measure of the relative oxygen incorporation in the active layer for various devices at different lifetimes (T100, T80, T50, T10).

2.2 XPS analysis

XPS was employed to convert the semi-quantitative TOF-SIMS information into quantitative XPS information by correlating XPS data with TOF-SIMS data, *i.e.* creating a calibration curve. The XPS analyses were performed on a K-alpha (Thermo Electron Limited, Winsford, UK) using

a monochromatic Al-K α X-ray source and a take-off angle of 90° from the surface plane. Atomic concentrations were determined from surface spectra (100–600 eV, 200 eV detector pass energy, 5 scans) and were calculated by determining the relevant integral peak intensities using a Shirley type background. All XPS analyses were repeated at least three times on different surface locations.

3. Results and discussion

3.1 Quantification of TOF-SIMS depth profiling data

When studying oxygen incorporation/uptake in P3HT:PCBM (*i.e.* degradation) it is obviously interesting to attempt to quantify how much oxygen is incorporated. This turned out to be far from simple. The first approach was to create a series of calibration samples from which a calibration curve could be obtained. P3HT:PCBM was spin-coated onto ITO-coated glass substrates (ITO improved the quality of the mass spectral peak shapes) and illuminated for varying amounts of time. The idea was then to perform non-quantitative TOF-SIMS depth profiling on these calibration samples, extract the normalized oxygen intensities and then perform quantitative XPS depth profiling on the same samples, and subsequently correlate the data. This was, however, not possible because during the XPS depth profiling analysis the oxygen becomes underestimated due to a sputter phenomenon. The same phenomenon applies for the TOF-SIMS depth profiling but that is of less importance since TOF-SIMS is not quantitative to start out with, the only effect is a decrease in sensitivity towards oxygen during TOF-SIMS depth profiling. This problem was solved by performing XPS spectroscopy directly on the surfaces (*i.e.* not depth profiling) of the calibration samples and correlating these results with the TOF-SIMS depth profiling data. This is only justified because the surface chemistry appears to be equivalent with the bulk chemistry (often not the case), which is documented in Fig. 4 for a spin-coated P3HT:PCBM sample. As is evident from Fig. 4 all the profiles

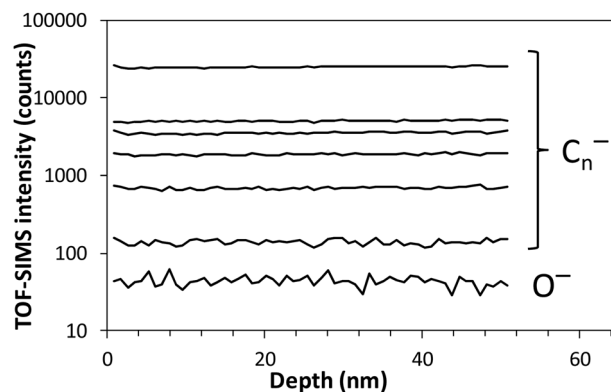


Fig. 4 TOF-SIMS depth profiles of a spin-coated P3HT:PCBM sample. The sample was spun from dichlorobenzene ($20 : 20 \text{ mg ml}^{-1}$) at 800 rpm for one minute producing a $208 \pm 3 \text{ nm}$ film thickness (measured by AFM profilometry). The sputter process is in increments of 10 s using 3 keV Xe^+ (30 nA) over a $300 \times 300 \mu\text{m}^2$ surface area and the analysis covers the central $200 \times 200 \mu\text{m}^2$ part using 0.7 pA Bi^+ . The sputter time scale was converted to a depth scale from a measured sputter rate of $5.26 \pm 0.08 \text{ nm min}^{-1}$ (only valid for P3HT:PCBM).

have a constant intensity from the first scan, which suggests that the surface chemistry in this case is equivalent to the bulk chemistry. It is therefore justified to correlate surface obtained XPS data with bulk obtained TOF-SIMS data.

The second problem was caused by a well-described phenomenon. P3HT has the ability to interact with molecular oxygen resulting in the formation of a charge transfer complex (eqn (1)).^{19–21} The process is reversible and is thus sometimes referred to as reversible degradation:



Abdou *et al.*¹⁹ described the phenomenon for poly(3-alkylthiophenes) and found that $\sim 1\%$ of the π -conjugated segments and $\sim 30\%$ of the dissolved molecular oxygen form a charge transfer complex, which corresponds to a charge transfer complex concentration of $\sim 1.3 \times 10^{-3}$ M. They found that the complex is weakly bound ($\Delta H^\circ = -10.6$ kJ mol⁻¹) and possesses a distinct absorption band in the visible region. The electronic properties of the material are affected by the complex depending on the oxygen pressure. The authors found that the complex causes the carrier concentration to increase, the conductivity to increase, and the charge carrier mobility to be lowered, and the complex is a fluorescence quencher of mobile polaronic excitons.

In a recent publication Guerrero *et al.*²⁰ studied the phenomenon in OPV devices with the configuration Ag–Ca–P3HT:PCBM–PEDOT:PSS–ITO. The authors showed that the complex is present in complete cells and that it is responsible for photocurrent reduction and loss in photo-voltage. Furthermore, it was found that irreversible degradation induced by molecular oxygen is attributed to calcium oxide formation.

Aguirre *et al.*²¹ demonstrated that illuminating P3HT in the presence of air induces persistent radical cations on the P3HT chains. They found that the photo-induced charges are stable at room temperature for several hours, but recombine quickly if the air is removed from the atmosphere. The authors postulate, that the persistency of the photo-induced charges is possible due to the existence of an energy barrier separating the excited charge transfer state from the ground state charge transfer complex. The barrier is proposed to be a result of stabilization of the excited charge transfer state and possibly a result of chemical interaction between P3HT and molecular oxygen, resulting in a so-called relaxed charge transfer state. Finally, it was found that lowering the pressure of air in the chamber was sufficient to break up the charge pair.

In the present work the afore-mentioned calibration samples were spin-coated in ambient air and stored for ~ 20 hours in darkness in ambient air before being transferred to the vacuum chambers of the TOF-SIMS and XPS instrument. It became evident that the charge transfer complex had to be considered.

When extracting the normalized oxygen intensities from the calibration samples an effect of time was observed. This is demonstrated in Fig. 5 for various spin-coated P3HT:PCBM samples exposed to various experimental conditions. All samples exhibit the same behaviour, which is a decrease in normalized oxygen intensity (oxygen content in the material, *i.e.* not in the gas phase) as a function of time. This phenomenon is not

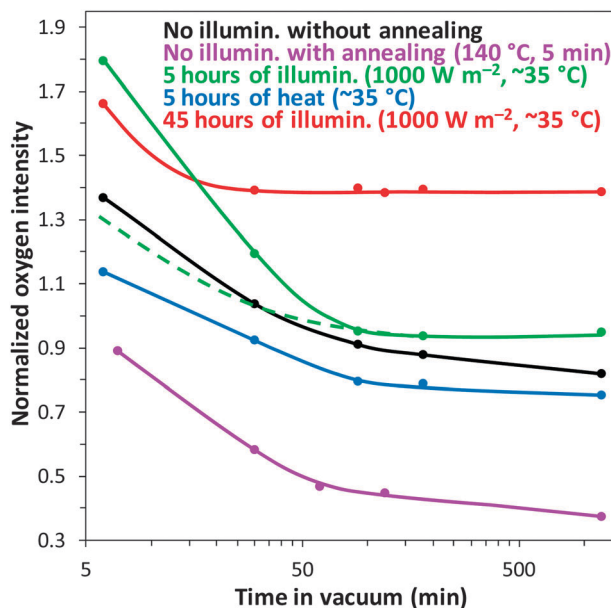


Fig. 5 Normalized oxygen intensity of the film as a function of time in vacuum for spin-coated P3HT:PCBM films. The probe depth was ~ 25 nm. The samples were spun from dichlorobenzene ($20 : 20$ mg ml⁻¹) at 800 rpm for one minute. All illuminated samples were not annealed prior to illumination. The normalized oxygen intensity was extracted from TOF-SIMS depth profiles as described earlier in the text. All samples were introduced into the vacuum chamber approximately 20 hours after spin coating. It took 3 minutes to pump down and an additional 3 minutes to set up the analysis before data could be collected. The green dashed line indicates the sample that is illuminated for 5 hours and then reanalyzed after storing in darkness in ambient air.

related to simple diffusion of solubilized molecular oxygen out of the material, which is a process that takes place within a few minutes at the most. It is presumably an effect of the reversible formation of the charge transfer complex (eqn (1)). Once the samples are placed in a vacuum the equilibrium follows Le Chatelier's principle and shifts towards removal of molecular oxygen from the complex, *i.e.* depletion of the charge transfer complex.

The plots in Fig. 5 contain a lot of interesting information. If the result obtained for the non-annealed non-illuminated sample (black line) is compared with the annealed non-illuminated sample (purple line), it is clear that a significant drop is observed in the normalized oxygen intensity. This has been confirmed by XPS that shows a 30% drop in oxygen content. Furthermore, it is consistent with the findings by Mattis *et al.*²² that concluded that an annealing temperature above 120 °C is required to promote oxygen desorption. The sample that was heated for five hours (blue line) was put under the simulated sun wrapped in aluminium foil so that it would receive the heat (~ 35 °C) but not the light. Five hours at ~ 35 °C must be considered as a very gentle annealing compared to five minutes at 140 °C (purple line), which is consistent with the relative result observed in Fig. 5. For the illuminated samples (green and red lines) a significant increase in normalized oxygen intensity is observed. The illumination promotes the generation of the persistent radicals enabling the charge

transfer complex to be formed, which partly explains the elevated normalized oxygen intensities. In addition, the harsh conditions will inevitably photo-oxidize the material forming covalently bound degradation products, *i.e.* an irreversible process. It appears that the more the photo-oxidation present the shorter the time to level out, *i.e.* faster depletion of the charge transfer complex. This is intuitively what one would expect based on the fact that photo-oxidation reduces the number of molecular sites available for charge transfer complex formation. The sample that had undergone the following procedure: stored in darkness for ~ 20 hours, illuminated for five hours, stored in darkness for ~ 20 hours, analyzed, stored in darkness for ~ 20 hours, reanalyzed, correspond to the solid green and dashed green lines, respectively (Fig. 5). The reanalyzed sample has an initial value that is significantly lower compared to the first time it was analyzed, but levels out to the photo-oxidation level that was also observed during the first analysis. This observation suggests that once the material has been depleted for the charge transfer complex it requires light to restore it to the original charge transfer complex concentration. Assuming that the plots in Fig. 5 were correctly interpreted, it means that the charge transfer complex is formed to some degree without illumination or, alternatively, because the samples unavoidably received some degree of low level illumination during handling. The findings presented in Fig. 5 agree fairly well with what has been described in regard to the charge transfer complex using alternative techniques.^{19–21} However, the timescale for depletion of the charge transfer complex in a vacuum is somewhat surprising and unpractical.

A calibration curve could now be constructed based on samples that were stored in the XPS and TOF-SIMS vacuum chambers for at least 20 hours prior to analysis in order to remove/minimize the charge transfer complex to an acceptable degree (not shown). At this point the third problem revealed itself. The calibration curve (not shown) produced unrealistic results when applied to the ISOS-3 depth profiling results. After numerous systematic experiments it became clear that annealing had a crucial effect on the calibration curve, more precisely on the normalized oxygen intensities obtained by TOF-SIMS, which is presumably a matrix effect caused by the annealing that presumably changes the crystallinity. All the ISOS-3 devices were annealed during fabrication, which therefore requires calibration samples that are annealed under the same conditions. The TOF-SIMS depth profiling results are clearly very sensitive to experimental conditions, which raised some concern about whether the fact that the calibration samples were exposed to ambient air during illumination could have an effect, *i.e.* the P3HT:PCBM material in the ISOS-3 devices was sandwiched between various barrier layers and electrodes. Due to the clearly complex nature of these calibration experiments an alternative (more safe) approach was chosen that was simpler but rougher. It was decided to use some of the ISOS-3 cells that were stored in darkness in a glove box after the degradation experiments and analyses. Since XPS depth profiling was not an option (discussed earlier in the text) the choice of cells was limited to those that were delaminated, *i.e.* with the P3HT:PCBM exposed (Fig. 2). The ISE and the Risø DTU cells fulfilled this criterion.

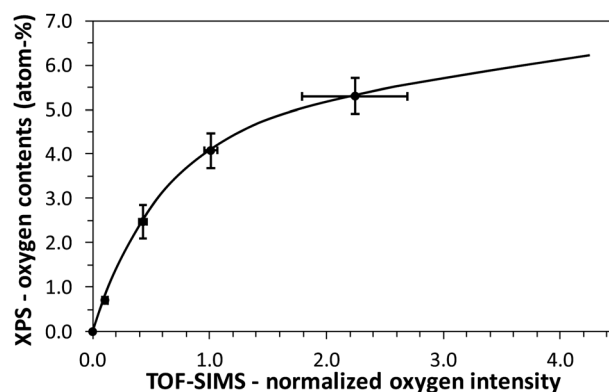


Fig. 6 Calibration curve between TOF-SIMS depth profiling data and XPS data. The TOF-SIMS data were normalized from $\text{Int}(\text{O}^-)/\text{Int}(\text{C}_n^-)$, $n = 2-4; 6-10$ and multiplied by a factor of 1000 for practical reasons. Each point is an average of at least three points on different surface locations. All samples were placed in the vacuum chamber at least 20 hours prior to analysis in order to remove the weakly bound charge transfer complex between molecular oxygen and P3HT. The probe depth was ~ 25 nm.

The ISE was encapsulated with glass during the degradation experiments, so it is expected to have experienced a minimum of oxygen incorporation or none at all. The Risø DTU cells were encapsulated with a semi-impermeable organic barrier film, which previously was shown not to be 100% efficient.³⁰ Risø DTU T100 and T10 cells (full sun) were used for the calibration curve. The cells were stored at least 20 hours in the vacuum chambers of the TOF-SIMS and XPS instruments prior to analysis. The calibration curve is shown in Fig. 6.

It is very fortunate that a modified version of P3HT (P3HT-*co*-P3AcET:PCBM) is used in the Risø DTU S device as it contains native oxygen in the form of an ester group (Fig. 2f) that will help spread the points in the calibration curve. The lowest point is obviously (0.0) and the highest point is (2.2, 5.3) that originates from the Risø DTU S T10 cell, so any measurements acquired above this value will be based on extrapolation.

The need for storing the samples for at least 20 hours in the TOF-SIMS vacuum chambers prior to analysis was realized after all the ISOS-3 devices were analyzed, which obviously raised some concern. However, upon further reflection it turned out not to be a problem. All the glass/metal encapsulated cells were never exposed to ambient air at any point, so there is no concern about oxygen uptake. The Risø DTU cells were exposed to oxygen and water to some extent due to inferior encapsulation, and the non-encapsulated were obviously directly exposed to ambient air during the degradation experiments and during the non-destructive analysis in the various laboratories. After testing they were all sent back to Risø DTU and placed in a glove box. The devices were then prepared for analysis (removal of encapsulation) and 13–18 samples were placed on the TOF-SIMS sample holder, a procedure that took most of a day. The sample holder was then typically transferred *via* a transfer vessel containing an inert atmosphere to the TOF-SIMS analysis chamber late in the day so that it would be ready for analysis the next morning. So by tracing back the working procedures it could be concluded that all the ISOS-3 devices were exposed to the nitrogen atmosphere in the

glove box and the vacuum in the TOF-SIMS instrument for such a long time that it is safe to assume that the charge transfer complex had been depleted.

3.2 Oxygen incorporation and its effect on device degradation

It should be clear by now that oxygen incorporation in P3HT:PCBM is described by two processes: (i) formation of a charge transfer complex (reversible degradation), and (ii) photo-oxidation (irreversible degradation). Both processes are well-described in the literature and constitute an analytical challenge when present at the same time. However, due to the fortunate timescale of the analyses of the ISOS-3 devices we can assume that only irreversible photo-oxidation is probed. P3HT and P3HT:PCBM are well-described in terms of photo-oxidation both as materials but also as components in photovoltaic devices. In this study photo-oxidation of the active materials in the ISOS-3 devices was quantified using XPS calibrated TOF-SIMS depth profiling data, which has never been attempted before.

Photo-oxidation of the active material (P3HT:PCBM) was then compared to loss of photovoltaic performance, which is not necessarily an easy comparison since other degradation mechanisms are in play. The ultimate challenge in studying degradation phenomena in OPV devices is to quantify the contribution from each degradation mechanism to the overall degradation of the photovoltaic performance.

In terms of photo-oxidation it makes sense to group the six different devices (Table 1 and Fig. 2) according to the encapsulation, well-knowing that we thereby do not consider possible internal photo-oxidation caused by metal oxides. The encapsulation used can be split up into three groups: (i) glass/metal encapsulation (ISE and Holst), (ii) UV filter (flexible) encapsulation (Risø DTU S and P), and (iii) non-encapsulated (IMEC and NREL). The groups are listed here according to permeability with respect to molecular oxygen and water.

3.2.1 Comments on reproducibility for devices and TOF-SIMS analyses. As described in the first ISOS-3 report devices were extracted from the degradation experiments at various degrees of performance, more or less corresponding to T100, T80, T50, and T10.¹⁵ Because some of the analyses were destructive it was not possible to follow loss of performance from the beginning to the end for one particular device, it had to be four devices that each represented T100, T80, T50, and T10, respectively. However, this will consequently result in strict requirements in terms of reproducibility when manufacturing the devices, which seems challenging considering the delicate device architectures requiring multiple processes to finally become a device. This was clearly seen in the third report that focused on IPCE analyses revealing significant differences in IPCE between equivalent devices and between cells in a device/module.¹⁷

Oxygen incorporation in the active material is expected to be zero or close to zero in the impermeable encapsulated devices and modest in the others according to previous experience.²⁹ Furthermore, the sputter process reduces the sensitivity profoundly, so detecting small changes with inferior sensitivity requires a good reproducibility with respect to device manufacturing since aberrations will result in chemical

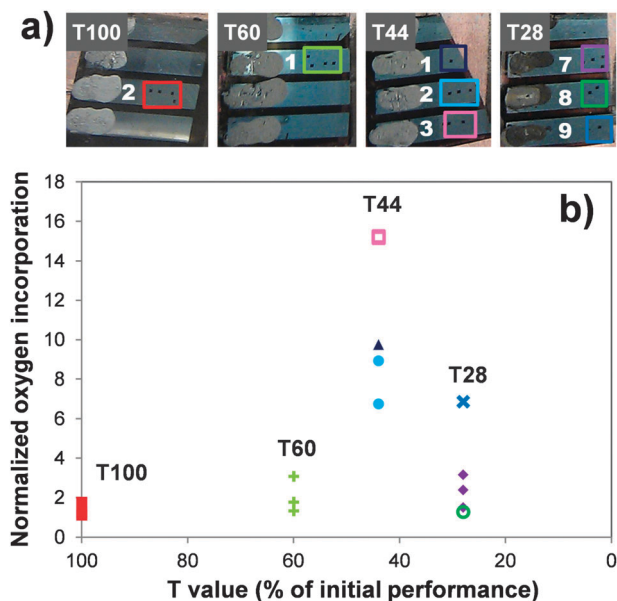


Fig. 7 (a) Photographs of pieces of IMEC devices (full sun) showing the TOF-SIMS depth profiling holes. The devices were cut in pieces so that they could be analyzed using various destructive methods. The colored squares indicate which analyses were associated with this test. (b) Normalized oxygen incorporation corresponding to cell surface locations shown in (a) as a function of performance loss. The TOF-SIMS data were normalized from $\text{Int}(\text{O}^-)/\text{Int}(\text{C}_n^-)$, $n = 2-4;6-10$ and multiplied by a factor of 1000 for practical reasons.

inhomogeneities that will consequently affect the relative results and thus the quality of the work.

In order to assess the reproducibility associated with the ISOS-3 cells a test was performed on four IMEC devices (full sun) corresponding to T100, T60, T44, and T28, respectively (Fig. 7a). Multiple analyses were performed on one single cell, and multiple cells were analyzed within the same device in order to measure the point-to-point variation within the same cell as well as the cell-to-cell variation. The result is shown in Fig. 7.

Several interesting observations can be extracted from Fig. 7. The reproducibility is observed to significantly deteriorate for lower T-values, which suggests that the oxygen incorporation becomes more inhomogeneous for increasing degree of photo-oxidation. In addition, the highest T44 and T28 values originate from the central parts of the devices (not obvious from Fig. 7a), which, however, could be a coincidence considering the limited data. Finally, the result suggests that the cell-to-cell variation is significantly larger than the point-to-point variation on the same cell, which is surprising. No explanation was found for this observation. The magnitude of the relative (reverse) result of the T28 and T44 devices suggested that one of the devices was erroneous somehow. A comparison of the IV degradation characteristics revealed that the T28 IMEC device showed a clear inconsistency and was consequently omitted.

It is obvious from the reproducibility test that a certain degree of noise in the data is expected for especially the low T-value devices due to the fact that an apparent inhomogeneity is introduced for an increased degree of degradation in

the active material. Inhomogeneous degradation patterns were observed in the work described in the second ISOS-3 report.¹⁶

3.2.2 Full sun, fluorescent, and dark degradation conditions.

After the TOF-SIMS depth profiling analyses were complete the effects in terms of oxygen incorporation were observed to be very subtle for the devices degraded under a full sun, *i.e.* the harshest condition compared to fluorescent and dark conditions. The results for the fluorescent and dark conditions were therefore, as expected, even more subtle, to a degree where the point-to-point variation caused by the material inhomogeneity is far greater. The following discussion will thus focus on devices degraded under full sun conditions.

3.2.3 Glass/metal encapsulation – ISE and Holst devices.

The ISE and Holst devices were encapsulated by glass–glass and glass–metal, respectively, and sealed with epoxy. These two devices thus had so-called impermeable encapsulation, which is expected to reflect in the analysis results. Fig. 8a and b presents the measured oxygen contents as a function of loss of performance and illumination time for the ISE and Holst devices.

Because of the impermeable encapsulation no oxygen incorporation was expected during the degradation experiments, which is consistent with the fact that no detectable trend is observed in Fig. 8a and b. However, the results are very scattered, which makes it impossible to detect possible subtle trends. The scattered nature of the points in the graphs suggests that the oxygen content to some extent is inhomogeneously distributed in the active material. How is this at all possible? The native oxygen comes exclusively from PCBM. A possible phase separation between P3HT and PCBM seems unlikely and would have to occur on a macroscopic scale, which is unlikely. An alternative explanation could be varying degree of internal oxidation caused by materials already present in the cells, *e.g.* water residues in the hygroscopic PEDOT:PSS, which then diffuses into the active material and causes oxidation. It is also possible that the excess PSS (always present in PEDOT:PSS) diffuses into the active material and contributes to the oxygen content (PSS contains $-\text{SO}_3\text{H}$ groups). The two suggested explanations could possibly explain why the measured average oxygen contents (~ 4 atom%) are elevated compared to the calculated values of 2.2 atom% (ISE) and 2.4 atom% (Holst). The calculated values are based on the theoretical element compositions and the P3HT:PCBM compositions, which are 1 : 0.7 for the ISE device and 1 : 1 for the Holst device. Since the T100 cells also have ~ 4 atom% oxygen, the phenomena (if the assumption is correct) must have happened in the time window between fabrication and analysis, which corresponded to months.

Fig. 8c shows loss of performance as a function of time (logarithmic time-scale). The ISE device exhibits an exponential decay (or close to within the accuracy) in performance with time, *i.e.* straight line behaviour on a logarithmic time-scale (Fig. 8c). The Holst device has a non-linear behaviour that suddenly drops significantly after 21 hours, resulting in a relatively low lifetime (T8 after 122 hours). For comparison the ISE device reaches T13 after 1822 hours. It was suggested in one of the earlier ISOS-3 reports that the rapid degradation of

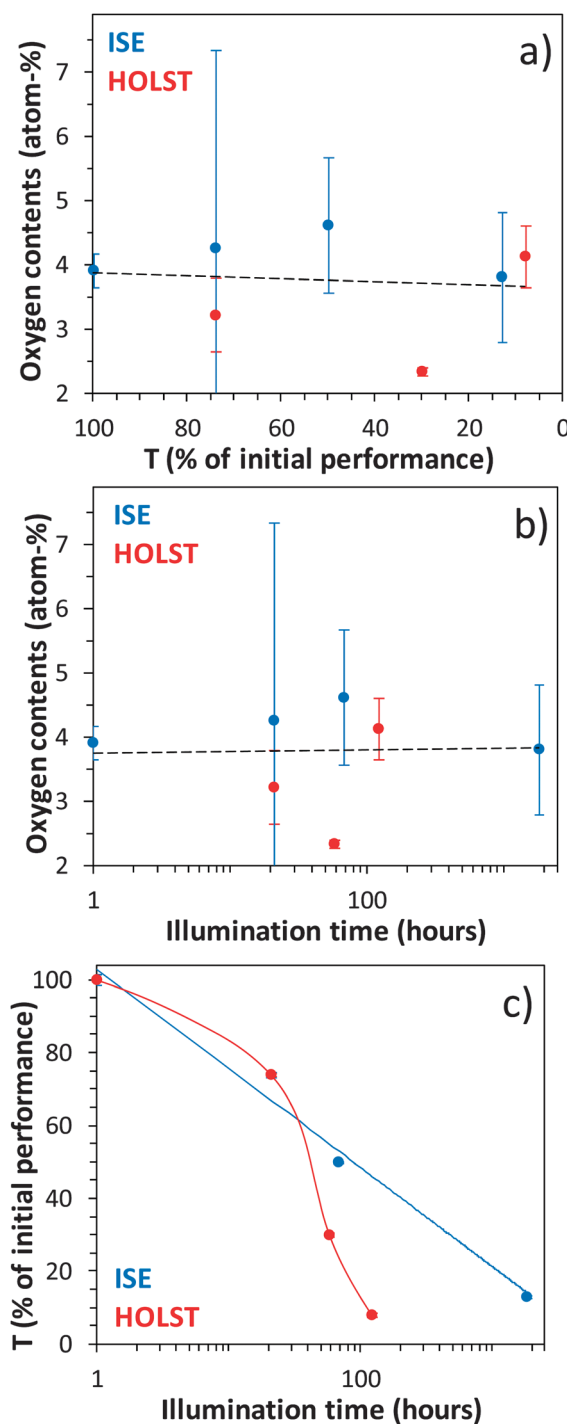


Fig. 8 (a)–(b) Oxygen contents in the bulk of the active material extracted from the TOF-SIMS depth profiling analysis of the ISE and Holst devices under full sun degradation conditions. The dashed line is a straight guide line through all points in the graph. Each point is an average of three measurements on different surface locations. The T100 Holst sample was lost. (a) Oxygen contents as a function of loss in performance. (b) Oxygen contents as a function of illumination time (AM 1.5G, 1000 W m^{-2} , $85 \pm 5 \text{ }^\circ\text{C}$, metal halide lamp, KHS Solar Constant 1200). Zero was substituted with one on the logarithmic axis for practical purposes. (c) Loss of performance as a function of illumination time.

the Holst device under full sun simulation is caused by a thermal instability at $75 \text{ }^\circ\text{C}$, which correlates well with the fact

that under full sun conditions the temperature is $85 \pm 5 \text{ }^\circ\text{C}$ (AM1.5G, 1000 W m^{-2}).¹⁵ Furthermore, under dark conditions the temperature corresponds to room temperature, and under fluorescent conditions the temperature is $\sim 45 \text{ }^\circ\text{C}$ (100 W m^{-2}), which further correlates well with the fact that the performance of these particular ISE and Holst devices did not deteriorate to any significant degree during more than 1830 hours of testing. The relative temporal behaviour in performance and the significant difference in lifetimes suggest a significant difference in degradation behaviour, which is not surprising, considering the different architectures (Fig. 2a and b).

The degradation mechanisms that are in play in the ISE and Holst devices are not related to oxygen incorporation (*i.e.* photo-oxidation) in the active material, or at least not to any detectable degree. It should be emphasized that the interpretation is complicated by the scatter in the results. If photo-oxidation was not an important factor for the overall degradation, then other factors must have been in play for the ISE and Holst devices such as those suggested in the second and third ISOS-3 reports.^{16,17}

In the second ISOS-3 report it was suggested that for the Holst device elevated temperatures ($85 \pm 5 \text{ }^\circ\text{C}$) caused by the sun simulator and additional heating of the cell due to current collection within the PEDOT:PSS could result in water being released from the highly conductive PEDOT:PSS, which consequently would react with the Al electrode, forming aluminium oxide.¹⁶ Furthermore, in the third ISOS-3 report an additional degradation mechanism was proposed for the Holst device. It was suggested that during the degradation experiment Ag reacts/interacts almost spontaneously with PEDOT:PSS, leading to degradation of the device performance. In addition, it was suggested that Ag possibly also (or alternatively) reacts with P3HT, which induces a slow but steady degradation by migration of Ag into PEDOT:PSS and oxidation of the Ag electrode. It was furthermore proposed that oxidation of the LiF/Al electrode could be a possible degradation mechanism.¹⁷ Additional TOF-SIMS analyses from this work (described later in the text) on the Holst and ISE devices did not reveal any chemical changes during the degradation experiments. However, that does not necessarily mean that the degradation phenomena in question are not occurring (discussed later in the text).

With respect to the ISE device the conclusion from the second ISOS-3 report states that one possible degradation mechanism is water being homogeneously released from PEDOT:PSS that consequently reacts with Cr–Al–Cr forming chromium and aluminium oxide.¹⁶ The third ISOS-3 report has the same conclusion including possible degradation of the Au electrodes.¹⁷ Lira-Cantu *et al.* propose these degradation mechanisms based on the fact that metals like Ag, Cu, and Au are known to interact with the S-atom of polymers like P3HT and PEDOT, and suggests that it is thus possible that the Cr/P3HT:PCBM interface reacts in a similar way as well as the Au/PEDOT:PSS interface.¹⁷

In summary, due to the impermeable encapsulation no trends were expected. However, it was not possible to detect possible subtle trends due to significant point-to-point variation for both devices. The erratic nature of the measured

oxygen contents suggests that oxygen to some extent is inhomogeneously distributed in the active material, which could be the result of (i) internal oxidation caused by water originating from PEDOT:PSS or (ii) diffusion of excess PSS from PEDOT:PSS. Both of these explanations could possibly explain the elevated (on average) oxygen content compared to the calculated contents. Water release from PEDOT:PSS was suggested in the previous ISOS-3 reports.^{16,17} The relative performance over time suggests significantly different degradation behaviour for the two devices, which is further supported by significantly different lifetimes. Photo-oxidation was most likely not an important factor for the overall device degradation, so other factors must have been in play for the ISE and Holst devices such as for example the degradation mechanisms proposed in the second and third ISOS-3 reports.^{16,17}

3.2.4 UV-filter encapsulation – Risø DTU P and Risø DTU S devices. The flexible UV filter encapsulation used is to some extent permeable with respect to molecular oxygen and water (*i.e.* so-called semi-impermeable encapsulation), so some degree of photo-oxidation is expected. Fig. 9 displays the measured oxygen contents as a function of loss of performance and illumination time for the Risø DTU P and Risø DTU S devices. The only difference between the Risø DTU P and Risø DTU S devices is that the Risø DTU S device uses a modified version of P3HT in the active material, *i.e.* P3HT-*co*-P3AcET instead of P3HT (see Fig. 2f for the molecular structures). The results in Fig. 9 are the most convincing, manifested in a relatively low degree of scatter.

Oxygen incorporation is observed for both devices for an increase in illumination time or for decreasing performance. The apparent linear relationship suggests that photo-oxidation could be the dominant degradation mechanism for these devices in particular. The increased level of oxygen contents in the Risø DTU S device compared to the Risø DTU P devices is due to fact that P3HT-*co*-P3AcET contains an ester group (Fig. 2f). Fig. 9c reveals an exponential decay in performance over time, which was also observed for the ISE device. However, this relationship does not necessarily suggest equivalent degradation mechanisms.

The two Risø DTU devices seem to have similar degradation behaviour, but there are notable differences. The slope of the Risø DTU P device in terms of oxygen incorporation is steeper than for the Risø DTU S device, which is manifested in an oxygen increase of 3.0 atom% compared to 1.8 atom% during the degradation experiments. Furthermore, the Risø DTU S device exhibited a slightly better stability as it took more than 200 hours longer to degrade, which is consistent with a lower degree of oxygen incorporation (1.8 compared to 3.0 atom%) during testing.

The results indicate that the use of P3HT-*co*-P3AcET instead of P3HT induces stability. The increased stability could in principle be because P3HT-*co*-P3AcET has a higher resistance towards molecular oxygen and/or water, but that seems unlikely since the molecular difference is only on the side chain, *i.e.* not the active part of the molecule. However, the side chain affects the morphology, so it is more likely that P3HT-*co*-P3AcET induces a morphological stability compared to P3HT.

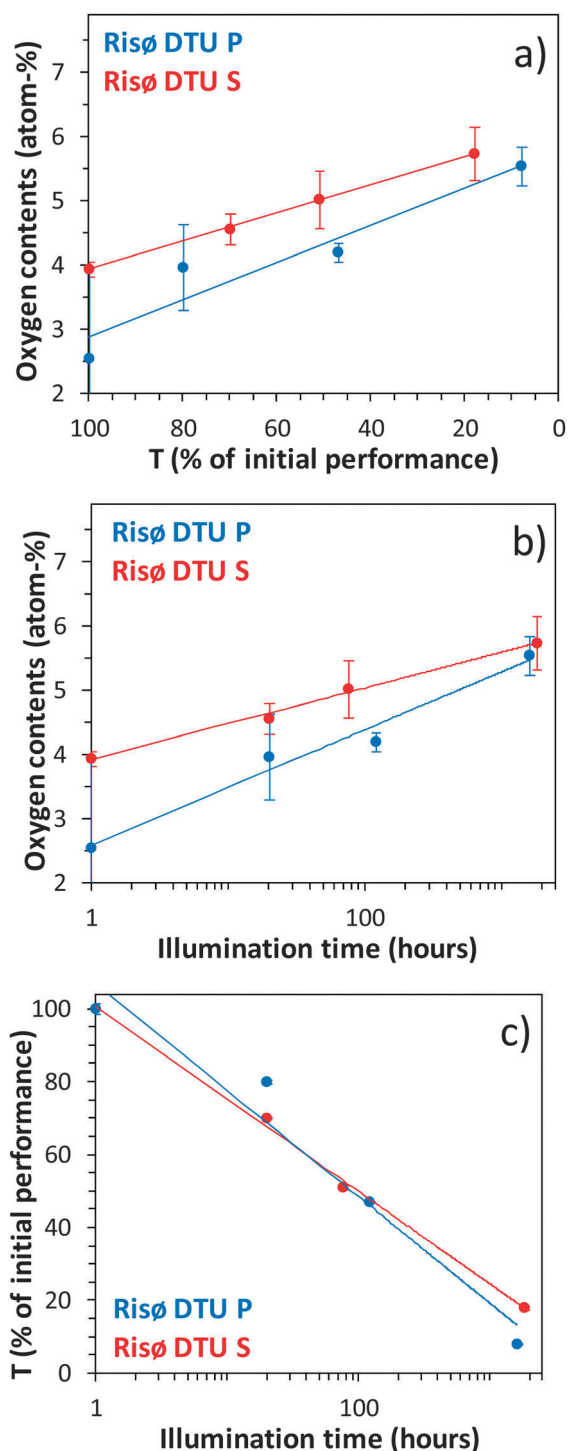


Fig. 9 (a)–(b) Oxygen contents in the bulk of the active material extracted from the TOF-SIMS depth profiling analysis of the Risø DTU P and Risø DTU S devices under full sun degradation conditions. Each point is an average of three measurements on different surface locations. (a) Oxygen contents as a function of loss in performance. (b) Oxygen contents as a function of illumination time (AM 1.5G, 1000 W m^{-2} , $85 \pm 5 \text{ }^\circ\text{C}$, metal halide lamp, KHS Solar Constant 1200). Zero was substituted with one on the logarithmic axis for practical purposes. (c) Loss of performance as a function of illumination time.

In the work described in the second ISOS-3 report the population of shunts was observed to increase over time

during the degradation experiments, which were suggested to be driven by electro-migration of Ag at places where the electric field was enhanced.¹⁶ It was furthermore proposed that oxidation of Ag or ZnO de-doping results in subtle blocking contact features. In addition, during the degradation experiments an increase in the series resistance of the devices was observed that was assigned to morphological changes/degradation, whereas a current decrease was assigned to photo-oxidation of the active material. One notable difference was observed between the Risø DTU P and the Risø DTU S device. The latter exhibited practically no increase in series resistance, which was assigned to a more stable morphology in the active material.

In the work described in the third ISOS-3 report it was found that under dark conditions both devices are susceptible to moisture.¹⁷ However, consistent with the findings in the present work it was found that the Risø DTU S device has a higher resistance against moisture. The moisture effect was not observed under full sun or fluorescent testing conditions, *i.e.* where light and heat are present. This is however inconsistent with the findings in the present work, where oxygen incorporation was detected under full sun conditions only, which suggests that the moisture under dark conditions is involved in degradation mechanisms other than photo-oxidation of the active material. This is consistent with the proposed mechanisms in the third ISOS-3 report that include oxidation of the Ag electrode and migration of Ag provoked by PEDOT due to well-documented Ag–S interactions.¹⁷ It was proposed that the higher stability of the Risø DTU S device is caused by an impeding effect of having used P3HT-*co*-P3AcET in the reaction with Ag, which will inhibit degradation of the electrodes. Finally, it was suggested that it is the degradation of the electrodes that initially is responsible for the overall degradation of performance and not degradation of the active materials.

In summary, because a so-called semi-impermeable encapsulation was used some degree of photo-oxidation was expected for the Risø DTU P and Risø DTU S devices, which was indeed also observed. An apparent linear relationship is observed for oxygen incorporation as a function of loss in performance and an exponential increase of oxygen incorporation as a function of time, suggesting that photo-oxidation could be the dominant degradation mechanism. Using P3HT-*co*-P3AcET instead of P3HT induces stability, which is most likely morphological stability causing less oxygen to be incorporated resulting in a longer lifetime. Conclusions on the relative stability are supported by the findings in the previous ISOS-3 reports.^{16,17}

3.2.5 No encapsulation – NREL and IMEC devices. The NREL and IMEC devices have no encapsulation and are thus expected to be significantly photo-oxidated during full sun testing conditions. The device architectures (Fig. 2d and e) are very similar, the only significant difference is the hole transport layer that consists of PEDOT:PSS (NREL device) or MoO_3 (IMEC device). Any observed differences in degradation behaviour should therefore be directly related to the difference in the hole transport layer used.

Fig. 10 displays the measured oxygen contents as a function of loss of performance and illumination time for the NREL

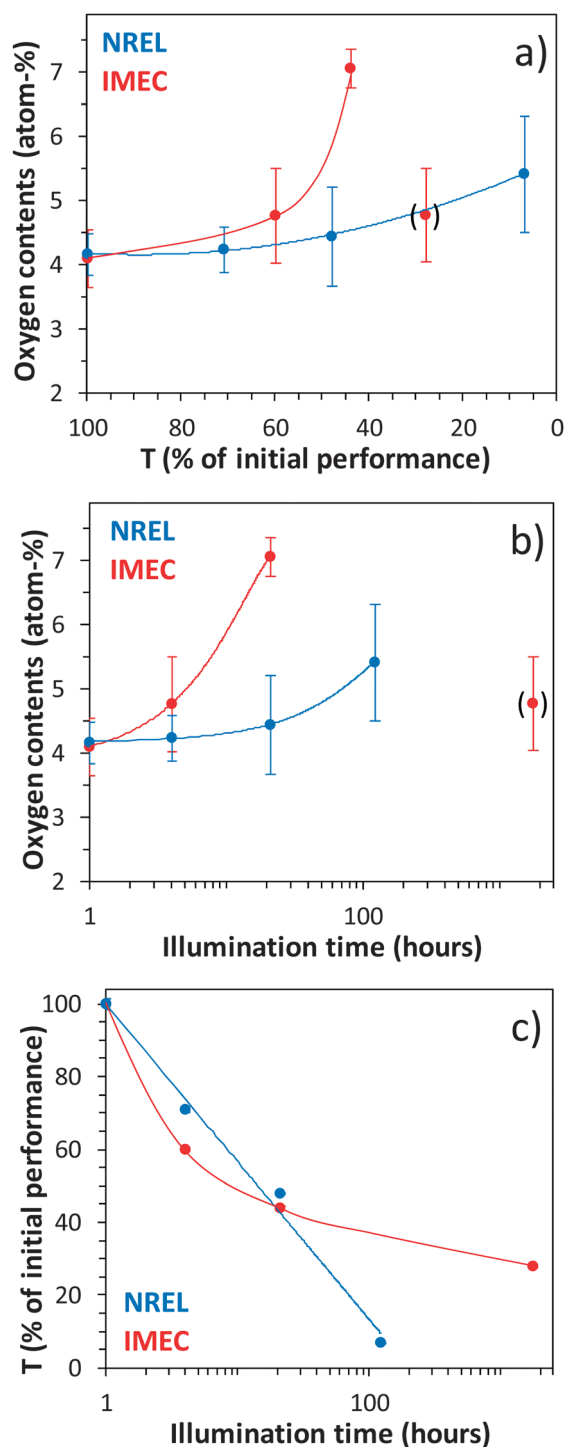


Fig. 10 (a)–(b) Oxygen contents in the bulk of the active material extracted from the TOF-SIMS depth profiling analysis of the NREL and IMEC devices under full sun degradation conditions. Each point is an average of three measurements on different surface locations. (a) Oxygen contents as a function of loss in performance. (b) Oxygen contents as a function of illumination time (AM 1.5G, 1000 W m^{-2} , $85 \pm 5 \text{ }^\circ\text{C}$, metal halide lamp, KHS Solar Constant 1200). Zero was substituted with one on the logarithmic axis for practical purposes. (c) Loss of performance as a function of illumination time.

and IMEC devices. The oxygen incorporation is observed as expected to increase for a decrease in performance or increase

in illumination time (Fig. 10a and b). The T28 IMEC sample was erroneous, which was documented from a comparison of the IV degradation characteristics that showed a clear inconsistency for the T28 IMEC sample that consequently was omitted.

Considering that these devices had no encapsulation during the full sun illumination it is surprising that such a small amount of oxygen was incorporated. The oxygen content increased by 1.3 atom% for the NREL device and by 3.0 atom% for the IMEC device, the latter being equivalent to the Risø DTU P device that had a so-called semi-impermeable encapsulation. Both devices start out with a slow oxygen incorporation that later on accelerates, which is a completely different situation compared to the Risø DTU devices that exhibited a linear increase.

Fig. 10c shows an exponential decay in performance over time for the NREL device, which was also observed for the ISE and Risø DTU devices. The NREL device reaches T7 within 122 hours, which is relatively fast and equivalent to the Holst device. However, in terms of performance loss over time the Holst device (Fig. 8c) has a significantly different behaviour, suggesting that different degradation mechanisms are in play. The performance loss over time for the IMEC device (Fig. 10c) is interesting since the behaviour is the opposite compared to the Holst device. Initially the performance for the IMEC device drastically decreases but levels out and surprisingly (since no encapsulation is used) ends up having a long lifetime (reaches T28 after 1751 hours). The IMEC device is the fastest to incorporate oxygen in the active material, but has a lifetime comparable with the encapsulated devices (except for the Holst device). It is tempting to assign the significantly different degradation behaviour of the IMEC device compared to the NREL device to the different hole transport layer (MoO_3 instead of PEDOT:PSS). However, another difference is the 200 nm thick Al electrode on the IMEC device compared to only 100 nm on the NREL device, which must be significant in terms of the barrier properties. Having said that, the MoO_3 layer must also have different barrier properties than PEDOT:PSS. MoO_3 is well-known to induce better stability towards ambient atmosphere compared to PEDOT:PSS.²³ One thing is clear, the IMEC device has a complex degradation behaviour that calls for complementary analysis results.

The second ISOS-3 report offers a lot of discussion on possible degradation mechanisms in the IMEC device.¹⁶ The degradation mechanisms are described as initially being two competing processes involving Ag penetration into MoO_3 and oxidation of Ag. The acting work function in direct vicinity to active layer becomes reduced at the place where Ag penetration is occurring. Later on blocking contact features start to occur. It was suggested that diffusion of molecular oxygen and/or water into the device could result in increasing barriers for charge injection and extraction by formation of Ag_2O or by doping at the ZnO layer.

The degradation behaviour of the NREL device is also described in the second ISOS-3 report.¹⁶ It was found that a massive degree of shunting developed over large parts of the NREL device mainly at the places where injection remained possible after oxidation of Ag, *i.e.* around pinholes and at the

edges of the metal electrode. It was concluded that electro-migration of Ag resulted in penetration of the PEDOT:PSS layer, which was proposed to be significantly less dense than the MoO₃ layer.²³

The third ISOS-3 report describes significant problems in characterizing the NREL device using IPCE.¹⁷ It was not possible to detect possible trends due to an erratic response from the IPCE analysis. The erratic response was believed to be caused by a reversible uptake of water in the hygroscopic PEDOT:PSS that highly depended on the relative humidity at the time and place of analysis. It was nevertheless possible to detect an interaction between Ag and the sulphur in PEDOT:PSS, which together with the water uptake was taken as an indication that degradation takes place at the electrodes consequently reducing the flux of current throughout the cell over time. The combined degradation phenomenon affected the cells inhomogeneously, which was manifested in a significant variation in the IPCE results within the same cell on the device/substrate and between different cells on the same device/substrate. The erratic response was also observed in the present work for the NREL device (large error bars in Fig. 10a and b), but that is not necessarily the same phenomenon since the erratic response is also observed for the impermeable encapsulated devices (Fig. 8a and b) in the present work.

In an *in situ* IPCE analysis on the NREL device the charge transfer complex was identified and it was possible to monitor the release of molecular oxygen over time. The reversible formation of the charge transfer complex will unavoidably contribute to the erratic response when analyzing devices without encapsulation. As described earlier in the text this phenomenon was not significant in the present work. From the *in situ* IPCE analysis it was furthermore possible to monitor release of oxygen from the ZnO crystalline structure. Finally, The IPCE analyses supported the findings from the second ISOS-3 report that electro-migration of Ag into the PEDOT:PSS layer occurs.¹⁶

A lot of the features found in the NREL device were also found in the IMEC device including the charge transfer complex. However, one important observation was a significantly smaller degree of erratic response in the IMEC device that supported the conclusion that PEDOT:PSS was a significant contributor to the erratic response. However, at longer times in the degradation experiment a non-uniform effect of the cell position on the device/substrate started to emerge. By comparing the IPCE results from an encapsulated IMEC device and one without encapsulation it was concluded that the ambient atmosphere is modifying the properties of MoO₃ and ZnO. When the IPCE analysis was performed in a nitrogen atmosphere on the IMEC and NREL devices, oxygen was observed to release from MoO₃ and ZnO, which is a well-known phenomenon for semiconductor oxides. The oxygen release from MoO₃ and ZnO will change the properties of the materials (including the photovoltaic properties) and provide a source of oxygen that can react with the organic materials such as the active layer (*i.e.* internal oxidation).

In summary, without encapsulation the NREL and IMEC devices were expected to be significantly photo-oxidated during full sun testing conditions, but surprisingly the level of photo-oxidation in the active material corresponded to the

semi-encapsulated devices. A slow oxygen incorporation is observed initially that accelerates at longer times. The IMEC device has a surprisingly long lifetime compared to the NREL device, which is attributed to the only significant difference between the devices, which is the hole transport layer that consisted of PEDOT:PSS (NREL) and MoO₃ (IMEC). MoO₃ is well-known to induce better stability compared to PEDOT:PSS towards ambient atmosphere.²³

3.3 Correlating LBIC and TOF-SIMS data

LBIC visualizes the relative light-beam induced current typically over the entire solar cell area, which is useful for pinpointing where the current is low or zero in the lateral plane of the cell. However, the LBIC analysis contains no in-depth information that would otherwise reveal in which layer or interface the phenomenon causing the loss of current is located. In the second ISOS-3 report LBIC was employed and correlated with related techniques such as photoluminescence imaging (PLI), electroluminescence imaging (ELI), and lock-in thermography (LIT) that each provides useful complementary in-plane information based on different sensing characteristics.¹⁶ The strength of this approach lies in the multitude of techniques (*i.e.* sensing characteristics) used to conclude on specific degradation mechanisms, which compensates for the indirect nature of the information (*i.e.* lack of in-depth information).

In this work an attempt was made to correlate LBIC data with TOF-SIMS data. TOF-SIMS provides three-dimensional chemical information, *i.e.* direct chemical information in-plane as well as in-depth. However, this comparison is not necessarily straightforward since the LBIC detected cell degradation could be caused by a missing contact, *i.e.* not a chemical phenomenon. Furthermore, if the degradation is caused by an interface phenomenon (often the case) the limited depth resolution of the in-depth analysis could be an issue. Diffusion of water and molecular oxygen into the device resulting in photo-oxidation is a degradation mechanism that has been described thoroughly in the past and is the focus of this present work.^{18,24–30} An available glass-encapsulated IMEC device was therefore chosen for the comparison, which should exclude this specific well-described degradation mechanism.

The grey images in Fig. 11 represent the LBIC images for the IMEC device in question (see Fig. 2e for cell configuration). The device consists of 12 cells of which cells 1–3 were defective and 7 and 8 were apparently interconnected (equivalent LBIC images). After the LBIC analysis the device was transferred to a glove box where the glass encapsulation was removed. An attempt was made to peel off the Al–Ag–MoO₃ stack of the cells in order to access the MoO₃/P3HT:PCBM interface. It is usually very easy to peel off the upper electrode on pristine cells, but illuminated/heated cells typically either do not peel off or only partly peel off depending on the cell configuration and the degree of illumination/heating. It is thus interesting that the peel off process was almost complete for the defective cells (1–3). The partially delaminated cells (4–12) were then transferred in an inert atmosphere to the TOF-SIMS instrument. A TOF-SIMS imaging analysis was performed on cells 4–12.

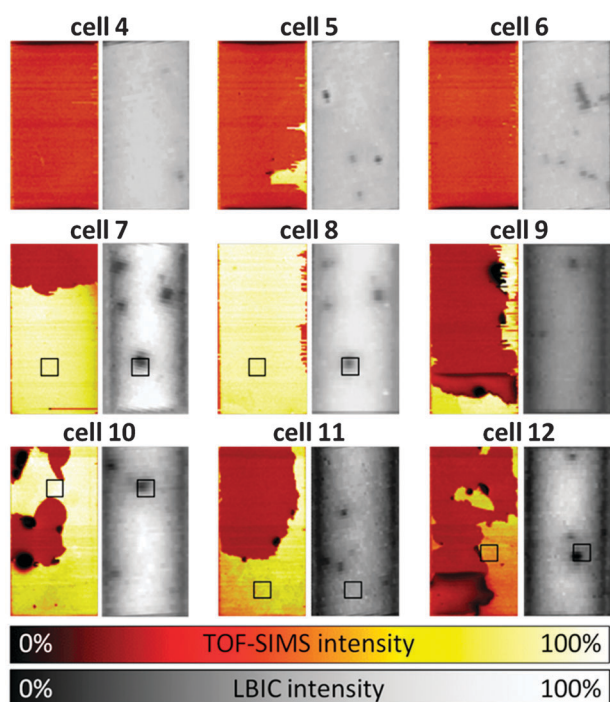


Fig. 11 Analytical results of cells 4–12 (1–3 were defective) from an encapsulated IMEC device. The grayscale images are LBIC images and the color images are the corresponding TOF-SIMS total ion images ($5.2 \times 2.7 \text{ mm}^2$). The squares indicate areas ($500 \times 500 \mu\text{m}^2$) that were analyzed with TOF-SIMS depth profiling. The Al–Ag–MoO₃ layers were partly removed prior to TOF-SIMS analysis (the yellow/white areas correspond to the Al surface).

The coloured images in Fig. 11 represent the total ion images of the cell surfaces. The high intensity areas (yellow/white) correspond to the Al surface and the dark red areas correspond to the exposed P3HT:PCBM surface (*i.e.* MoO₃/P3HT:PCBM interface). The total ion signal is a convenient way to screen for chemical contrast on the surface. As is evident from Fig. 11 there are no correlations between the LBIC images and the TOF-SIMS total ion images. The TOF-SIMS images are actually extremely homogeneous. The dark spots are instrument effects caused by flakes of upward-banded Al–Ag–MoO₃ causing loss of signal. It can now be concluded that localized loss of current in the cells (black spots in the LBIC images) is not related to a chemical phenomenon at the MoO₃/P3HT:PCBM interface. However, it is not possible to conclude anything about a possible missing contact between MoO₃ and P3HT:PCBM from the TOF-SIMS ion images in Fig. 11.

The next step was to study the remaining layers and interfaces in the cells. TOF-SIMS depth profiling was performed on surface locations indicated by the squares in Fig. 11. In a TOF-SIMS depth profiling analysis ion images are acquired as a function of depth. Ion images from 100 of the most abundant mass spectral markers were monitored as a function of depth in order to find a possible correlation between the LBIC image and the TOF-SIMS ion images. The depth profiling analyses were started at surface locations that partly covered (to get chemical contrast) the dark spots in the corresponding LBIC images with one exception (cell 11, reference LBIC location).

All ion images were monitored through all layers and interfaces, *i.e.* from the Al surface to the bulk of the ITO. Unfortunately all ion images were extremely homogenous in all depths, which means that the degradation mechanism in question was not detectable by TOF-SIMS depth profiling.

3.4 Correlating loss of performance with various TOF-SIMS information

The primary objective of the TOF-SIMS investigation of the ISOS-devices was to correlate the photo-oxidation of the active layer with loss of cell performance. However, as documented in the previous ISOS-3 reports, photo-oxidation of the active material is not the only degradation mechanism in play during operation of the organic solar cells.^{16,17} The different cell architectures enable a variety of degradation mechanisms to contribute to the overall degradation of the cell. When the TOF-SIMS depth profiling analyses were performed relevant information was extracted from the raw data so that the photo-oxidation could be adequately described. The raw data consist of mass spectral data, which contain an overwhelming amount of information. This is one of the reasons that the TOF-SIMS technique is so attractive, but it is also the reason why it is often very complicated to interpret the results. It is tremendously less complicated if one knows what to look for. However, it should be emphasized that it is not possible to detect all degradation mechanisms. The raw data consist of mass spectral information, and mass spectral markers are typically chosen to represent a species that somehow is involved in the degradation mechanism or to support conclusions made on other mass spectral markers. The problem is that not all mass spectral markers are unique. One good example of a situation where it was not possible to extract direct information is the proposed mechanism involving migration of water from the PEDOT:PSS. Water produces mass spectral markers that are the same for all species containing oxygen, *i.e.* no unique markers. It is possible to detect the resulting oxidation, *i.e.* indirect information that requires assumption to be made. It is not impossible to study migration of water out of PEDOT:PSS, however, that would require a specially designed experiment where isotopically labelled water is used (H₂¹⁸O), which produces unique mass spectral markers. It has previously been shown that H₂¹⁸O is easily tracked in OPV devices from its reaction/degradation products.²⁵

The secondary goal of this study was to carefully study the raw data in detail in order to ascertain whether trends related to loss of performance could be extracted and possibly related to specific degradation mechanisms such as those suggested in the previous ISOS-3 reports.^{16,17} This was partially achieved and the result is presented and discussed in the following.

3.4.1 The IMEC device. The IMEC device is by far the most complex system to analyze in terms of degradation mechanisms. The cell configuration is Al–Ag–MoO₃–P3HT:PCBM–ZnO–ITO and mass spectral information is obtained throughout the entire device starting from the outer aluminium surface and ending somewhere in the bulk of the ITO layer. Due to the poor depth resolution that gets worse for longer sputter times it is difficult to extract certain types of information from deeper layers, *e.g.* interface phenomena

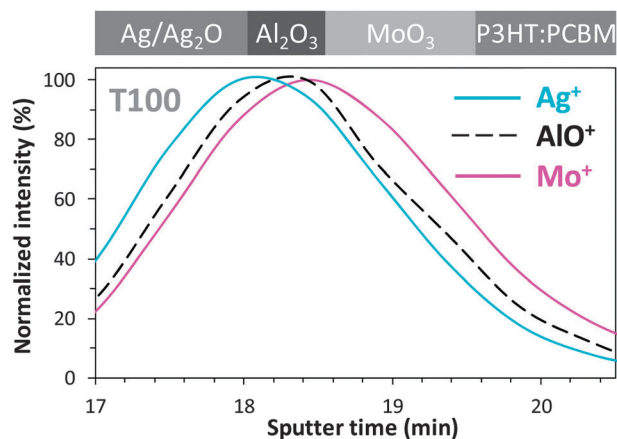


Fig. 12 TOF-SIMS depth profiles for a T100 IMEC cell that was exposed to full sun conditions without encapsulation. The sputter time window is chosen to emphasize the existence of a thin Al_2O_3 layer at the Ag/MoO₃ interface, which is present in all the IMEC devices. The indicated ions are mass spectral markers chosen to represent the individual layers. The schematic on top of the plot illustrates the part of the layer stack the data were extracted from.

occurring at P3HT:PCBM/ZnO and ZnO/ITO that produces weak possible generic mass spectral markers. Since the active layer was thoroughly investigated in the primary work described herein, it made sense to focus on the upper layers (Al–Ag–MoO₃).

Upon close inspection of the raw data from the upper layers one surprising observation was made, which is presented in Fig. 12. A layer of Al_2O_3 is present at the Ag/MoO₃ interface. Fig. 12 shows a narrow sputter time window around that interface. The dashed line representing Al_2O_3 is located exactly between the Ag and MoO₃ layers and is presumably very thin. The reason that the MoO₃ layer (10 nm) appears so thick compared to the Ag layer (100 nm) is the poor depth resolution and a large detector response from MoO₃. This is a more plausible explanation rather than possible differences in sputter rates. The profiles in Fig. 12 are extracted from a T100 device, so the phenomenon must have occurred during fabrication or in the time between fabrication and analysis. The Al_2O_3 at the Ag/MoO₃ interface could be the result of aluminium migration from the Al electrode through the Ag layer and subsequent oxidation somehow. Alternatively, it could be Al_2O_3 migration from MoO₃ that (like ZnO) contains trace amounts of various metal oxides. Al_2O_3 is not observed at the MoO₃/P3HT:PCBM interface, so if the latter explanation is correct the phenomenon must be catalyzed by the adjacent Ag layer.

Fig. 13 displays the profiles for the mass spectral marker AlO^- representing Al_2O_3 over a sputter time window covering Al–Ag–MoO₃. As is evident from Fig. 13 Al_2O_3 is present in the T100 cell through the entire Al electrode and is accumulated at the air/Al interface and at the Al/Ag interface (and in the unintentional Al_2O_3 layer). The intensity of AlO^- clearly increases for decreasing cell performance consistent with Al_2O_3 formation as a result of molecular oxygen and water diffusing into the cell (*i.e.* no encapsulation) that consequently reacts with Al. This is one of the proposed degradation mechanisms presented in the second and third ISOS-3 reports.^{16,17} It should be noted that one other phenomenon can affect the

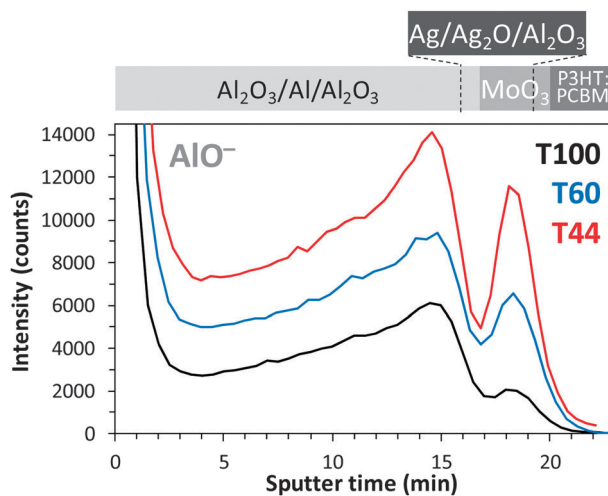


Fig. 13 TOF-SIMS depth profiles for IMEC cells exposed to full sun conditions without encapsulation. The profiles show a massive build-up of aluminum oxide in the Al–Ag–MoO₃ region of the cells for decreasing cell performance. AlO^- is the mass spectral marker chosen to represent aluminum oxide. The schematic on top of the plot illustrates the part of the layer stack the data were extracted from.

intensity of a mass spectral marker. If the physical properties of the material change it could affect the detector response, *e.g.* crystallinity, electric conductivity, *etc.* However, these possible effects are small compared to the intense signal boost you get for an increase in Al_2O_3 concentration.

The clear correlation between accumulation of Al_2O_3 and loss of cell performance suggests that this phenomenon is at least partly responsible for the degradation of the photovoltaic response. Unfortunately it is not possible to quantify how much this degradation mechanism is contributing to the overall degradation of the photovoltaic response. Furthermore, it is not possible to determine how much the Al_2O_3 at the Ag/MoO₃ interface contributes compared to the Al_2O_3 at the Al/Ag interface, but it is possible to conclude that Al_2O_3 accumulation at the Ag/MoO₃ interface is faster than at the Al/Ag interface.

The comparison between LBIC images and TOF-SIMS data involved an encapsulated IMEC device. The availability of an encapsulated IMEC device makes it obvious to compare the TOF-SIMS depth profiling data with and without encapsulation. Fig. 14 sums the results of that comparison. The T44 device without encapsulation was illuminated in ambient air for 21 hours, and the T50 device with encapsulation (glass) was illuminated for 2600 hours, which demonstrates the strength of glass encapsulation.

The first interesting observation is the lack of Al_2O_3 at the Al/Ag interface for the device with encapsulation. Half way through the Al electrode the AlO^- profiles are practically the same, but then the concentration of Al_2O_3 decreases to zero. Unfortunately it was not possible to obtain a T100 device with encapsulation, which would have been an interesting comparison. It appears that the encapsulated device was fabricated with no Al_2O_3 at all at the Al/Ag interface, which is impressive from a technical point of view.

The second interesting observation is the intensity of the Al_2O_3 at the Ag/MoO₃ interface, which is significantly elevated

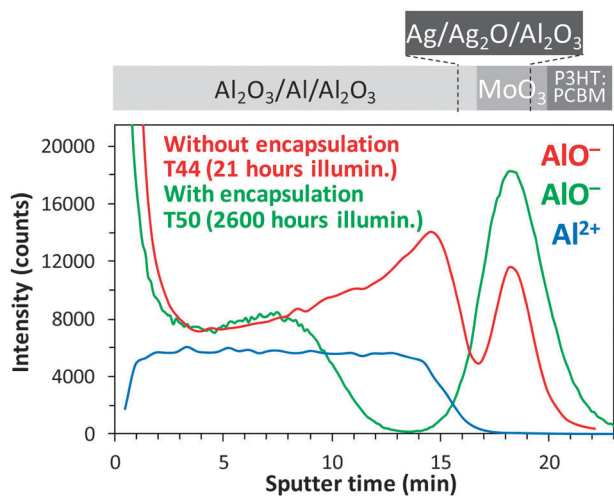


Fig. 14 TOF-SIMS depth profiles for IMEC cells exposed to full sun conditions with and without encapsulation (glass). The device without encapsulation was illuminated for 21 hours (T44), and the encapsulated device was illuminated for 2600 hours (T50). The profiles show the relative build-up of aluminium oxide in the Al–Ag–MoO₃ region of the cells. AlO[−] is the mass spectral marker chosen to represent aluminium oxide. The Al²⁺ profile (T100 device without encapsulation) was included to define the exact sputter time window for the Al electrode. Different sputter properties were used for the encapsulated device, so the sputter time was corrected such that the AlO[−] peak at the Ag/MoO₃ interface was aligned. The schematic on top of the plot illustrates the part of the layer stack the data were extracted from.

for the encapsulated device compared to the device without encapsulation. This is somewhat difficult to speculate on considering the lack of ambient air for the encapsulated device. It is still possible that Al₂O₃ originates from migration from the MoO₃ layer (as an impurity). A more farfetched explanation could be that Al₂O₃ migrates from the Al/Ag interface, which could explain why no Al₂O₃ is present at the Al/Ag interface (*i.e.* depletion). Since the encapsulated device has only reached T50 after 2600 hours it would seem that the presence of Al₂O₃ at the Ag/MoO₃ interface is not deteriorating the photovoltaic performance, which is surprising. The Al²⁺ profile (T100 device without encapsulation) was included in Fig. 14 to define the exact sputter time window for the Al electrode. The shape of the Al²⁺ profile did not change as a function of loss of cell performance.

The encapsulated IMEC device revealed another difference when compared to the corresponding device without encapsulation (Fig. 15). The mass spectral marker OH[−] is typically formed (during the ionization part of the analysis) in metal oxides with limited intensity compared to O[−]. However, on metal oxide surfaces exposed to an atmosphere the M–OH groups will typically be abundant resulting in a very intense OH[−] signal intensity. The mass spectral marker OH[−] is detected at the Ag/MoO₃ interface (Fig. 15) for both devices, which is not as interesting as the fact that it is also detected at the Al₂O₃/Ag interface, but only for the encapsulated device. The OH[−] profile for the encapsulated device appears to be wider than the corresponding profiles for the device without encapsulation, which could be due to the fact that other

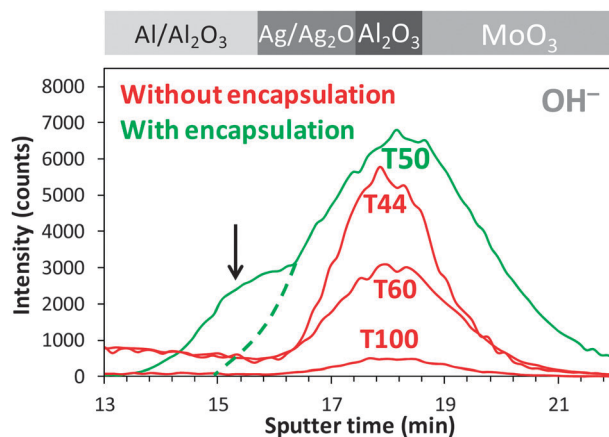


Fig. 15 TOF-SIMS depth profiles for IMEC cells exposed to full sun conditions with (green) and without (red) encapsulation (glass). The device without encapsulation was illuminated for 21 hours (T44), and the encapsulated device was illuminated for 2600 hours (T50). The intensity of the mass spectral marker OH[−] increases (like AlO[−] and O[−]) in the unintentional aluminium oxide layer for decreasing cell performance. An additional OH[−] peak indicated by the arrow is observed for the device without encapsulation at the Al₂O₃/Ag interface. The dashed line is drawn to clarify that the additional OH[−] profile peak (arrow) for the encapsulated device overlaps with the other OH[−] profile peak and takes the form of a “shoulder”. Different sputter properties were used for the encapsulated device, so the sputter time was corrected such that the AlO[−] peak at the Ag/MoO₃ interface was aligned. The schematic on top of the plot illustrates the part of the layer stack the data were extracted from.

sputter properties were used for the encapsulated device (the sputter time axis was corrected to allow comparison). It is difficult to speculate on what type of chemistry would explain the additional OH[−] signal (arrow in Fig. 15) at the Al₂O₃/Ag interface. Since the phenomenon is observed on the stable device (T50 after 2600 hours) it is unlikely that it is related to degradation of the photovoltaic performance.

In the second and third ISOS-3 reports silver migration and silver oxidation were suggested to be involved in degradation mechanisms.^{16,17} The mass spectral marker AgO[−] representing silver oxide was detected on all the IMEC devices at the Ag/Al₂O₃ interface (Fig. 16). As is evident from Fig. 16 the AgO[−] intensity is observed to increase for decreasing cell performance. However, it should be noted that the intensity is extremely weak (barely detectable). The apparent trace amount of Ag₂O is observed starting from all surface locations. It was not possible to detect silver migration. However, it should be emphasized that the TOF-SIMS depth profiling analyses are performed on random surface locations, *i.e.* not necessarily at lateral surface positions where degradation is more pronounced as described in the second ISOS-3 report where various imaging techniques were employed to visualize the lateral degradation patterns.¹⁶

3.4.2 The NREL device. The NREL device has the architecture Al–Ag–PEDOT:PSS–P3HT:PCBM–ZnO–ITO. As mentioned earlier in the text, the device differs only by the hole transport layer compared to the IMEC device, *i.e.* PEDOT:PSS instead of MoO₃. At first one would thus expect the degradation

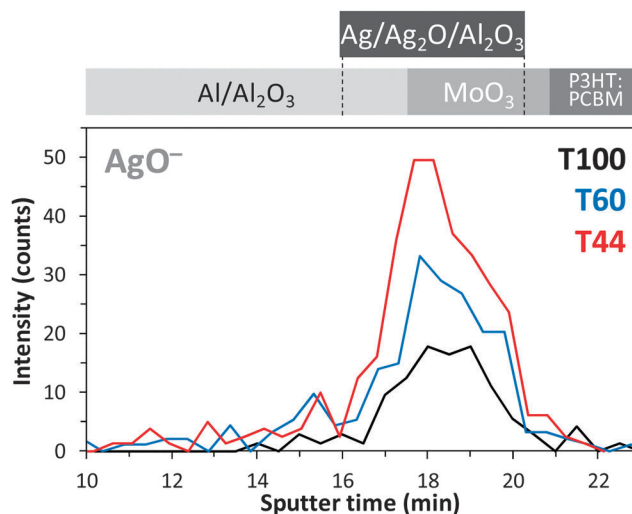


Fig. 16 TOF-SIMS depth profiles for IMEC cells exposed to full sun conditions. The profiles show a very subtle increase in the intensity of the mass spectral marker AgO^- for decreasing cell performance, which most likely corresponds to a small degree of silver oxide formation. The schematic on top of the plot illustrates the part of the layer stack the data were extracted from.

mechanisms to be similar. It turns out that besides similarities there are also surprising differences.

The first observation is the same as that for the IMEC device (with no encapsulation), that Al_2O_3 is observed to accumulate for decreasing cell performance (not shown), which was expected based on the fact that no encapsulation was employed. Formation of Al_2O_3 is consistent with conclusions drawn in the previous ISOS-3 reports.^{16,17} The second observation is the lack of the additional (unintentional) Al_2O_3 layer (see Fig. 12), which suggests that its existence in the IMEC device is related to MoO_3 one way or the other.

Fig. 17 reveals another interesting phenomenon not observed in the IMEC device. The profiles representing the Ag, Al_2O_3 , and PEDOT:PSS layers are observed to systematically widen for decreasing cell performance. In addition, Al_2O_3 and Ag have exactly the same sputter times (not shown), so it looks like the Al_2O_3 from the Al/Ag interface is dissolving in the Ag layer that consequently thickens the Ag layer (Fig. 17a). When Al_2O_3 expands into the Ag layer the result will be a widening of the AlO^- profile as shown in Fig. 17b.

The Al^{2+} T100 profile shown Fig. 17d is consistent with the IMEC device, *i.e.* the expected depth profile for a normal Al electrode. However, unlike the IMEC device, this profile changes drastically for decreasing cell performance. The Al^{2+} signal is systematically lost at the Al/Ag interface for decreasing cell performance. This supports the proposed phenomenon of Al_2O_3 and apparently also Al dissolving in the Ag layer. This is not observed for the IMEC device, suggesting that PEDOT:PSS is involved in the phenomenon, possibly from migration of water or acid from PEDOT:PSS to the Al/Ag interface.

Fig. 17c displays the Na^+ profiles that also widen for decreasing cell performance. Na^+ is a native component in PEDOT:PSS and is thus representative for PEDOT:PSS. The same trend is observed for the SO_x^- profiles, which are also representative of PEDOT:PSS (less pronounced trend though, not shown). The Na^+ profile is not just widening but also shifting to higher sputter times, suggesting that PEDOT:PSS is

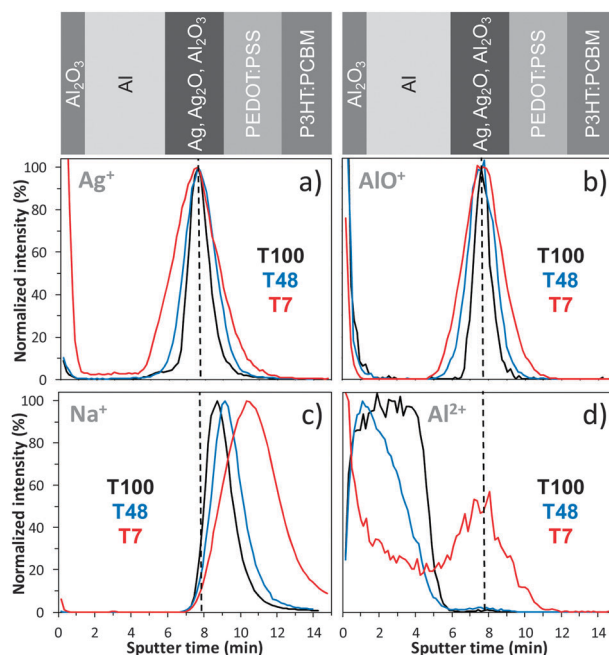


Fig. 17 (a)–(d) TOF-SIMS depth profiles for NREL cells exposed to full sun conditions. (a)–(c) The profiles of the mass spectral markers Ag^+ , AlO^+ , Na^+ exhibit a widening in the sputter time window for decreasing cell performance. (b) The AlO^+ intensities increase (not shown) for decreasing cell performance, *i.e.* accumulation of aluminum oxide. (c) Na^+ is a native component in PEDOT:PSS, and is thus used as a marker for PEDOT:PSS. (d) Al^{2+} defines the non-oxide form of the aluminum electrode, which is observed to become oxidated and to dissolve in the silver layer for decreasing cell performance. The schematics on top of the plots illustrate the part of the layer stack the data were extracted from.

partly dissolving in P3HT:PCBM, a phenomenon that was not observed for MoO_3 in the IMEC device.

3.4.3 The Risø DTU devices. The layer composition of the Risø DTU P device is Ag–PEDOT:PSS–P3HT:PCBM–ZnO–ITO

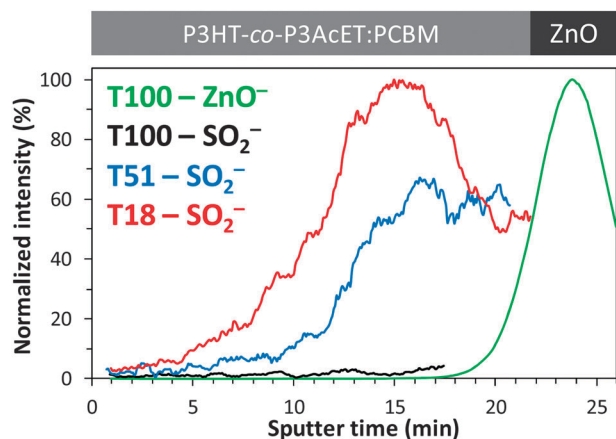


Fig. 18 TOF-SIMS depth profiles for Risø DTU S cells exposed to full sun conditions. SO_2^- is a mass spectral marker for an unknown R- SO_x species that is increasing in intensity and evolving at the P3HT-co-P3AcET:PCBM/ZnO interface. ZnO^- is a mass spectral marker for ZnO and is included to define the ZnO layer for clarity. The schematic on top of the plot illustrates the part of the layer stack the data were extracted from.

and the Risø DTU S device differs only by using P3HT-co-P3AcET instead of P3HT. Due to the thick plastic encapsulation it was necessary to delaminate the device prior to analysis. The device delaminated at the PEDOT:PSS/P3HT:PCBM interface, which left the device without the upper electrode. It was not possible to analyze the peeled off encapsulation-Ag-PEDOT:PSS layer stack because of the thickness of the Ag layer (5 μm) and the PEDOT:PSS layer (10 μm), which is too thick to be analyzed with the sputter properties in question. That leaves the P3HT:PCBM(P3HT-co-P3AcET)-ZnO-ITO layer stack to be analyzed. No trends were observed for any of the mass spectral markers with respect to cell performance for the Risø DTU P device. However, for the Risø DTU S device one trend was observed, which is shown in Fig. 18 for a sputter time window corresponding to the P3HT-co-P3AcET-ZnO layer stack.

The mass spectral marker SO_2^- for the Risø DTU S device is observed to increase systematically with decreasing cell performance. The shape of the profiles suggests that the phenomenon originates from within the ZnO layer. The species responsible for the mass spectral marker SO_2^- must be a R- SO_x species (R = H, organic, or metal). The ZnO layer contains trace amounts of a variety of inorganic and organic impurities.

However, it makes little sense that migration of that species into the active material should be affected by whether P3HT-co-P3AcET or P3HT is used in the active material. A less likely explanation could be oxidation of the thiophene sulphur by something very reactive originating from within the ZnO layer (e.g. O_2H^-), but it makes little sense that P3HT is not equally affected by it. The Risø DTU S device turned out to be more stable than Risø DTU P, i.e. it took 200 hours longer to degrade. It is difficult to conclude on how much the phenomenon described in Fig. 18. affects the cell performance, or whether it affects it at all.

3.4.4 The Holst and ISE devices. The cell configuration of the Holst cell is Al-LiF-P3HT:PCBM-PEDOT:PSS-SiN,Ag

and the ISE cell configuration is Au-PEDOT:PSS-P3HT:PCBM-Cr-Al-Cr. The ISE device was unavoidably delaminated leaving the P3HT:PCBM-Cr-Al-Cr part of the layer stack for analysis. The raw depth profiling data were carefully investigated for both devices in order to extract possible trends between mass spectral marker intensities and cell performance. No trends were found in any of the layers and interfaces.

As stated earlier in the text no oxygen incorporation could be detected in the active materials, and no other chemical changes are observed in the devices for decreasing cell performance. No electrode oxidation was observed, no layer thickening was observed, and no interlayer mixing was observed. Apparently it is not possible to detect the cause of degradation, suggesting that the phenomenon or phenomena are not chemical in nature (e.g. delamination at interfaces) or simply too subtle to detect using this analytical technique.

4. Conclusions

The work presented in this article is part of a large inter-laboratory study that resulted from the 3rd International Summit on Organic Photovoltaic Stability (ISOS-3). The collaboration involved six laboratories that produced seven distinct sets of OPV devices that were degraded under identical conditions in accordance with the ISOS protocols. The degradation experiments lasted 1830 hours and involved more than 300 cells on more than 100 devices. The devices were analyzed and characterized at different points of their lifetime by a large number of non-destructive and destructive techniques in order to describe specific degradation mechanisms responsible for the deterioration of the photovoltaic activity that lead to insufficient lifetimes.

The present work is a systematic study of the ISOS-3 devices using TOF-SIMS in order to identify specific degradation mechanisms responsible for the deterioration of the photovoltaic activity. It was only possible to detect degradation in cells that were exposed to the harshest conditions (AM1.5G, 1000 W m^{-2} , 85 ± 5 $^\circ\text{C}$). Two devices had impermeable encapsulations and it was not even possible under the harshest conditions to detect any form of chemical degradation as a function of cell performance, which suggests that degradation is not chemical in nature or too subtle to detect using the technique in question.

Photo-oxidation of the active layer (P3HT:PCBM) used in six of the seven devices was quantitatively monitored as a function of cell performance by correlating surface obtained XPS data with bulk obtained TOF-SIMS data. This calibration was complicated by various factors such as being sensitive towards experimental conditions, and the occurrence of a charge transfer complex between molecular oxygen and P3HT. No photo-oxidation could be detected in the two devices with impermeable encapsulations consistent with expectations. Two devices had so-called semi-impermeable encapsulations and both exhibited an apparent linear relationship in oxygen incorporation for decreasing cell performance, which suggests that photo-oxidation of the active material could be the dominant degradation mechanism. Using P3HT-co-P3AcET instead of P3HT in the devices with semi-permeable encapsulation induces stability, which is believed to be morphological stability causing less

oxygen to be incorporated resulting in a longer lifetime. Two devices had no encapsulation and exhibited, at first, slow photo-oxidation of the active material that accelerated later in the degradation tests. Photo-oxidation behaviour with respect to the active layer was different for the two types of encapsulation, but the degree of photo-oxidation was surprisingly on the same order of magnitude.

Attempts were made to correlate degradation patterns in LBIC images and TOF-SIMS total ion images for an encapsulated IMEC device with the architecture Al–Ag–MoO₃–P3HT:PCBM–ZnO–ITO. It was concluded that localized loss of current in the cells as described by the LBIC images is not related to a chemical phenomenon at the MoO₃/P3HT:PCBM interface. No correlations could be found in any of the other layers and interfaces, which suggests that the degradation mechanism in question is not detectable by the technique used.

The raw depth profiling data were screened in order to extract possible correlations between the mass spectral data and loss in cell performance that could assist in identifying specific degradation mechanisms and possibly support conclusions drawn in the first three ISOS-3 reports. Several trends were discovered that could be contributing to the overall degradation of the photovoltaic performance.

The trends for the IMEC device were observed to be:

- Increased migration of Al₂O₃ from either the Al/Ag interface or from the bulk MoO₃ layer to the Ag/MoO₃ interface for decreasing cell performance.
- The additional Al₂O₃ layer and the Al₂O₃ from the Al interfaces accumulate for increasing illumination time and thus for decreasing cell performance.
- When the IMEC device is encapsulated no Al₂O₃ is found at the Al/Ag interface, but the additional Al₂O₃ layer is still present.
- Trace amounts of Ag₂O were detected that exhibited a very weak increase for decreasing cell performance.

The trends for the NREL device were found to be:

- Accumulation of Al₂O₃ for decreasing cell performance.
- Dissolution of Al and Al₂O₃ in the Ag electrode for decreasing cell performance possibly catalyzed by water or acid from PEDOT:PSS.
- Thickening of the Ag electrode for decreasing cell performance due to the addition of Al₂O₃.
- Partly dissolution of PEDOT:PSS in the active layer (P3HT:PCBM) for decreasing cell performance.

One trend was found for the Risø DTU S device:

- The concentration of an unknown R–SO_x species migrating out from within the ZnO layer increases for decreasing cell performance, but it is uncertain whether it contributes to the overall degradation.

The present study and the previous studies in this inter-laboratory collaboration clearly demonstrate the strength of combining complementary analysis techniques on systematically prepared OPV devices in order to gain improved knowledge of the dominant degradation mechanisms responsible for loss of photovoltaic response. The extensive investigation on OPV stability presented in the series of ISOS-3 reports has significantly improved the understanding of degradation behaviour in OPV devices, which is a vital step towards large scale application of organic solar cells.

Acknowledgements

This work has been supported by the Danish Strategic Research Council (2104-07-0022), EUDP (j.no. 64009-0050, 64009-0051) and the Danish National Research Foundation. Partial financial support was also received from the European Commission as part of the Framework 7 ICT 2009 collaborative project HIFLEX (grant no. 248678), partial financial support from the EU Indian framework of the “Largecells” project that received funding from the European Commission’s Seventh Framework Programme (FP7/2007–2013, grant no. 261936), partial financial support was also received from the European Commission as part of the Framework 7 ICT 2009 collaborative project ROTROT (grant no. 288565) and from PVERA-NET (project acronym POLYSTAR). are due to CONACYT (México) for the PhD scholarship awarded to G. T.-E; to the Spanish Ministry of Science and Innovation, MICINN-FEDER project ENE2008-04373; to the Consolider NANOSELECT project CSD2007-00041; to the Xarxa de Referència en Materials Avançats per a l’Energia, XaRMAE of the Catalonia Government (Spain). RR and HH are grateful for financial support from the Thuringian Ministry of Culture and the German Federal Ministry of Education and Research in the frameworks of FIPV II and PPP (contract number 13N9843), respectively. DMT acknowledges generous support from the Inger and Jens Bruun Foundation through The American-Scandinavian Foundation.

References

- 1 *Polymeric Solar Cells: Materials, Design, Manufacture*, ed. F. C. Krebs, DEStech Publications, 2010.
- 2 *Polymer Photovoltaics: A Practical Approach*, ed. F. C. Krebs, SPIE Press Monograph, 2008.
- 3 T. D. Nielsen, C. Cruickshank, S. Foged, J. Thorsen and F. C. Krebs, *Sol. Energy Mater. Sol. Cells*, 2010, **94**, 1553–1571.
- 4 M. A. Green, K. Emery, Y. Hishikawa, W. Warta and E. D. Dunlop, *Prog. Photovoltaics*, 2011, **19**, 565–572.
- 5 R. F. Service, *Science*, 2011, **332**, 293.
- 6 F. C. Krebs, J. Fyenbo, D. M. Tanenbaum, S. A. Gevorgyan, R. Andriessen, B. Remoortere, Y. Galagand and M. Jørgensen, *Energy Environ. Sci.*, 2011, **4**, 4116–4123.
- 7 M. Jørgensen, K. Norrman and F. C. Krebs, *Sol. Energy Mater. Sol. Cells*, 2008, **92**, 686–714.
- 8 M. Jørgensen, K. Norrman, S. A. Gevorgyan, T. Tromholt, B. Andreasen and F. C. Krebs, *Adv. Mater.*, 2012, **24**, 580–612.
- 9 *Stability and Degradation of Organic and Polymer Solar Cells*, ed. F. C. Krebs, Wiley, 2012.
- 10 A. Seemann, T. Sauermann, C. Lungenschmied, O. Armbruster, S. Bauer, H. J. Egelhaaf and J. Hauch, *Sol. Energy*, 2011, **85**, 1238–1249.
- 11 M. T. Lloyd, C. H. Peters, A. Garcia, I. V. Kauvar, J. J. Berry, M. O. Reese, M. D. McGehee, D. S. Ginley and D. C. Olson, *Sol. Energy Mater. Sol. Cells*, 2011, **95**, 1382–1388.
- 12 D. M. Tanenbaum, H. F. Dam, R. Rösch, M. Jørgensen, H. Hoppe and F. C. Krebs, *Sol. Energy Mater. Sol. Cells*, 2012, **97**, 157–170.
- 13 M. Seeland, R. Rösch and H. Hoppe, *J. Appl. Phys.*, 2011, **109**, 064513.
- 14 M. O. Reese, S. A. Gevorgyan, M. Jørgensen, E. Bundgaard, S. R. Kurtz, D. S. Ginley, D. C. Olson, M. T. Lloyd, P. Morvillo, E. A. Katz, A. Elschner, O. Haillant, T. R. Currier, V. Shrotriya, M. Hermenau, M. Riede, K. Kirov, G. Trimmel, T. Rath, O. Inganäs, F. Zhang, M. Andersson, K. Tvingstedt, M. Lira-Cantu, D. Laird, C. McGuinness, S. Gowrisanker, M. Pannone, M. Xiao, J. Hauch, R. Steim, D. F. M. DeLongchamp, R. Rösch, H. Hoppe, N. Espinosa, A. Urbina, G. Yaman-Uzunoglu,

- J.-B. Bonekamp, A. J. J. M. van Breemen, C. Giroto, E. Voroshazi and F. C. Krebs, *Sol. Energy Mater. Sol. Cells*, 2011, **95**, 1253–1267.
- 15 D. M. Tanenbaum, M. Hermenau, E. Voroshazi, M. T. Lloyd, Y. Galagan, B. Zimmermann, M. Hösel, H. F. Dam, M. Jørgensen, S. A. Gevorgyan, S. Kudret, W. Maes, L. Lutsen, D. Vanderzande, U. Würfel, R. Andriessen, R. Rösch, H. Hoppe, G. Teran-Escobar, M. Lira-Cantu, A. Rivaton, G. Y. Uzunoğlu, D. Germack, B. Andreasen, M. V. Madsen, K. Norrman and F. C. Krebs, *RSC Adv.*, 2012, **2**, 882–893.
- 16 R. Rösch, D. M. Tanenbaum, M. Jørgensen, M. Seeland, M. Bärenklau, M. Hermenau, E. Voroshazi, M. T. Lloyd, Y. Galagan, B. Zimmermann, U. Würfel, M. Hösel, H. F. Dam, S. A. Gevorgyan, S. Kudret, W. Maes, L. Lutsen, D. Vanderzande, R. Andriessen, G. Teran-Escobar, M. Lira-Cantu, A. Rivaton, G. Y. Uzunoğlu, D. Germack, B. Andreasen, M. V. Madsen, K. Norrman, H. Hoppe and F. C. Krebs, *Energy Environ. Sci.*, 2012, **5**, 6521–6540.
- 17 G. Teran-Escobar, D. Tanenbaum, E. Voroshazi, M. Hermenau, K. Norrman, M. T. Lloyd, Y. Galagan, B. Zimmermann, M. Hösel, H. F. Dam, M. Jørgensen, S. A. Gevorgyan, S. Kudret, W. Maes, L. Lutsen, D. Vanderzande, U. Würfel, R. Andriessen, R. Rösch, H. Hoppe, A. Rivaton, G. Y. Uzunoğlu, D. S. Germack, B. Andreasen, M. V. Madsen, E. Bundgaard, F. C. Krebs and M. Lira-Cantu, *Phys. Chem. Chem. Phys.*, 2012, DOI: 10.1039/C2CP40821J.
- 18 M. Hermenau, M. Riede, K. Leo, S. A. Gevorgyan, F. C. Krebs and K. Norrman, *Sol. Energy Mater. Sol. Cells*, 2011, **95**, 1268–1277.
- 19 M. S. A. Abdou, F. P. Orfino, Y. Son and S. Holdcroft, *J. Am. Chem. Soc.*, 1997, **119**, 4518–4524.
- 20 A. Guerrero, P. P. Boix, L. F. Marchesi, T. Ripolles-Sanchis, E. C. Pereira and G. Garcia-Belmonte, *Sol. Energy Mater. Sol. Cells*, 2012, **100**, 185–191.
- 21 A. Aguirre, S. C. J. Meskers, R. A. J. Janssen and H.-J. Egelhaaf, *Org. Electron.*, 2011, **12**, 1657–1662.
- 22 B. A. Mattis, P. C. Chang and V. Subramanian, *Synth. Met.*, 2006, **156**, 1241–1248.
- 23 E. Voroshazi, B. Verreet, A. Buri, R. Müller, D. Di Nuzzo and P. Heremans, *Org. Electron.*, 2011, **12**, 736–744.
- 24 K. Norrman, N. B. Larsen and F. Krebs, *Sol. Energy Mater. Sol. Cells*, 2006, **90**, 2793–2814.
- 25 K. Norrman, S. A. Gevorgyan and F. C. Krebs, *ACS Appl. Mater. Interfaces*, 2009, **1**, 102–112.
- 26 F. C. Krebs and K. Norrman, *Prog. Photovoltaics*, 2007, **15**, 697–712.
- 27 K. Norrman and F. Krebs, *Sol. Energy Mater. Sol. Cells*, 2006, **90**, 213–227.
- 28 M. Lira-Cantu, K. Norrman, J. W. Andreasen and F. C. Krebs, *Chem. Mater.*, 2006, **18**, 5684–5690.
- 29 K. Norrman, M. V. Madsen, S. A. Gevorgyan and F. C. Krebs, *J. Am. Chem. Soc.*, 2010, **132**, 16883–16892.
- 30 M. V. Madsen, K. Norrman and F. C. Krebs, *J. Photonics Energy*, 2011, **1**, 011104.

Aqueous Processing of Low-Band-Gap Polymer Solar Cells Using Roll-to-Roll Methods

Thomas R. Andersen, Thue T. Larsen-Olsen, Birgitta Andreasen, Arvid P. L. Böttiger, Jon E. Carlé, Martin Helgesen, Eva Bundgaard, Kion Norrman, Jens W. Andreasen, Mikkel Jørgensen, and Frederik C. Krebs*

Solar Energy Programme, Risø National Laboratory for Sustainable Energy, Technical University of Denmark, Frederiksborgvej 399, DK-4000 Roskilde, Denmark

Aqueous processing of polymer solar cells presents the ultimate challenge in terms of environmental friendliness and has only been reported in a few instances. The approaches to solubilization of the conjugated and active material in water fall in three categories: solubilization through (1) ionic side chains such as sulfonic acid, carboxylic acid, or ammonium, (2) nanoparticle dispersions of hydrophobic polymers in water, or (3) nonionic alcohol and glycol side chains. The latter approach is the most recent and most successful in terms of performance where PCEs of up to 0.7% have been reached on indium tin oxide (ITO) substrates with aqueous processing of the four subsequent layers in the solar cell stack (including the printed metal back electrode).¹ The approach employing ionic side chains is perhaps conceptually the most appealing as it opens up for layer-by-layer assembly of the films or interface layers² but has so far not been employed successfully for the active layer itself. The nanoparticle dispersion approach developed by Landfester *et al.*^{3–7} is particularly appealing as it allows for control of the nanoparticle size and for processing using pure water as solvent for common hydrophobic conjugated polymers. In terms of development of the polymer and organic photovoltaic (OPV) technology, the latter point is of some significance since the large body of polymers available today has been developed for processing in organic solvents such as chlorobenzene, 1,2-dichlorobenzene, *etc.* One could envisage a complete redesign of the chemistry as described above¹ (method 3) but it will require a complete rediscovery of the solvent–material interaction and morphology relationships. While this may be necessary, in

ABSTRACT Aqueous nanoparticle dispersions of a series of three low-band-gap polymers poly[4,8-bis(2-ethylhexyloxy)benzo(1,2-b:4,5-b')dithiophene-alt-5,6-bis(octyloxy)-4,7-di(thiophen-2-yl)(2,1,3-benzothiadiazole)-5,5'-diyl] (P1), poly[(4,4'-bis(2-ethylhexyl)dithieno[3,2-b:2',3'-d]silole)-2,6-diyl-alt-(2,1,3-benzothiadiazole)-4,7-diyl] (P2), and poly[2,3-bis-(3-octyloxyphenyl)quinoxaline-5,8-diyl-alt-thiophene-2,5-diyl] (P3) were prepared using ultrasonic treatment of a chloroform solution of the polymer and [6,6]-phenyl-C₆₁-butyric acid methyl ester ([60]PCBM) mixed with an aqueous solution of sodium dodecylsulphate (SDS). The size of the nanoparticles was established using small-angle X-ray scattering (SAXS) of the aqueous dispersions and by both atomic force microscopy (AFM) and using both grazing incidence SAXS (GISAXS) and grazing incidence wide-angle X-ray scattering (GIWAXS) in the solid state as coated films. The aqueous dispersions were dialyzed to remove excess detergent and concentrated to a solid content of approximately 60 mg mL⁻¹. The formation of films for solar cells using the aqueous dispersion required the addition of the nonionic detergent FSO-100 at a concentration of 5 mg mL⁻¹. This enabled slot-die coating of high quality films with a dry thickness of 126 ± 19, 500 ± 25, and 612 ± 22 nm P1, P2, and P3, respectively for polymer solar cells. Large area inverted polymer solar cells were thus prepared based on the aqueous inks. The power conversion efficiency (PCE) reached for each of the materials was 0.07, 0.55, and 0.15% for P1, P2, and P3, respectively. The devices were prepared using coating and printing of all layers including the metal back electrodes. All steps were carried out using roll-to-roll (R2R) slot-die and screen printing methods on flexible substrates. All five layers were processed using environmentally friendly methods and solvents. Two of the layers were processed entirely from water (the electron transport layer and the active layer).

KEYWORDS: roll-to-roll coating polymer solar cells · organic solar cells · slot-die coating · aqueous inks · nanoparticle dispersions

the end it is of interest to simply adapt the large body of materials at hand to an aqueous process. It is also of critical importance to replace the organic solvents if one has the ambition to manufacture polymer solar cells on a gigawatt scale.

There are several concerns associated with the use of chlorinated and aromatic solvents on a very large scale. Concern for the people working at the manufacturing machine is crucial both in terms of toxicity and, in the case of aromatic solvents,

* Address correspondence to frkr@risoe.dtu.dk.

Received for review March 11, 2011 and accepted April 14, 2011.

Published online April 22, 2011
10.1021/nn200933r

© 2011 American Chemical Society

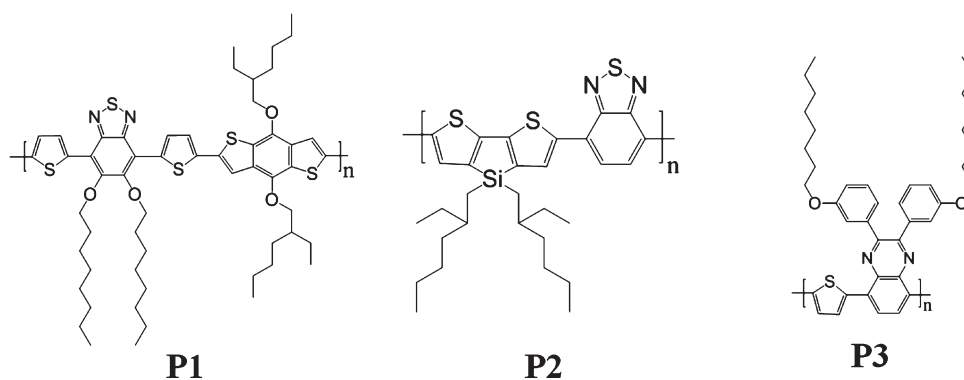


Figure 1. The structure for the three polymers used, P1, P2, and P3 (see text for the systematic names).

flammability. In the case of the chlorinated solvents the environmental concern is large, and it is unlikely that large scale manufacturing using such solvents is possible in a European setting. As an example, the current state of the art based on ProcessOne⁸ would involve approximately 16 million liters of chlorobenzene for the production of 1 GW_p of polymer solar cell. An additional concern is the cumulative energy needed for raw materials production, where a poor choice of processing method and processing materials can severely affect the energy payback time (EPBT) of the solar cell. Life cycle analysis has confirmed that water is the solvent that is most beneficial to use, requiring only a small electrical energy input for production.⁹ The cumulative thermal energy in materials production of chlorobenzene alone, as given in the example above, would be 880 TJ, adding 10 days to the EPBT. In contrast the use of water as the solvent would require only 17 TJ, adding only 4 h to the EPBT.

In terms of active materials the most successful approach so far has been the use of low-band-gap materials based on the donor–acceptor approach as shown in Figure 1. The UV–vis spectra of the three polymers **P1**, **P2**, and **P3** were recorded, and the optical band gaps were determined to be 1.8, 1.5, and 1.8 eV, respectively (Figure 2).

In this work we prepared aqueous nanoparticle dispersions of the known low-band-gap polymers poly[4,8-bis(2-ethylhexyloxy)benzo(1,2-b:4,5-b')dithiophene-alt-5,6-bis(octyloxy)-4,7-di(thiophen-2-yl)(2,1,3-benzothiadiazole)-5,5'-diyl] (**P1**),¹⁰ poly[(4,4'-bis(2-ethylhexyl)-dithieno[3,2-b:2',3'-d]silole)-2,6-diyl-alt-(2,1,3-benzothiadiazole)-4,7-diyl] (**P2**),¹¹ and poly[2,3-bis(3-octyloxyphenyl)-quinoxaline-5,8-diyl-alt-thiophene-2,5-diyl] (**P3**)¹² (Figure 1) in mixtures with [60]PCBM. We developed an aqueous R2R manufacturing process for flexible polymer solar cells through careful ink formulation and processing.

RESULTS AND DISCUSSION

Overview. The polymer solar cell has grown from a laboratory experiment to an emerging technology

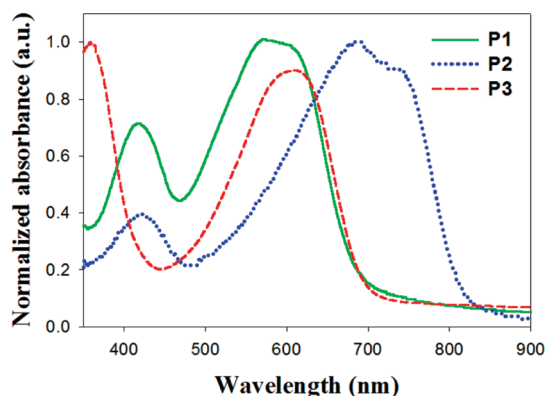


Figure 2. The UV–vis spectra of P1, P2, and P3. The optical band gap was determined to be 1.8, 1.5, and 1.8 eV for P1, P2, and P3, respectively.

with great potential to significantly contribute to future energy production. Currently, polymer solar cells can be prepared using industrial roll-to-roll methods⁸ and are sufficiently stable for demonstration products. They have for instance been employed as a low cost lighting solution for developing countries.¹³ While upscaling has been described successfully their current potential should be viewed critically^{14,15} and compared to existing thin film solar cell technologies such as CdTe and amorphous silicon. The polymer solar cell is currently the poorest performing PV technology (in existence) in terms of power conversion efficiency, while it has distinct advantages of high speed production, adaptability, and an abundance of raw materials. Recent work on the life cycle analysis from several groups⁹ have highlighted the potential of the technology and in one case, where the source of data was fully public, revealed EPBTs in the range of 1.35–2.02 years.⁹ As outlined in the introduction there is an urgent need for processes and processing materials that lower the embedded energy and the process energy, as this is a necessary method for lowering the EPBT. This should of course go in hand with an increase in efficiency. In this work where we aim at replacing the organic solvent for processing of the active area with water there is a direct gain at the site of manufacture but it should be emphasized that solvents and large amounts of

detergent are required for the manufacture of the nanoparticle dispersions. It is assumed that those can be recycled to fully benefit from the aqueous processing of hydrophobic materials that has already been developed. If this is not the case then there might not be any gain in the cumulative energy for raw materials production but there will still be a large gain in terms of human safety and lower emission of chlorinated or aromatic solvent into the environment because the preparation of the nanoparticle dispersions inherently allows for containment and reuse of solvents. A detailed life cycle analysis of the inks is thus warranted and until this has been carried out a complete comparison is not possible. At this point however the benefits of an aqueous ink are large enough to justify research in this direction.

Formation of Nanoparticle Dispersions. The generic method developed by Landfester *et al.* in a series of original research papers during the period from 1999 to 2004 was followed and found to be directly applicable with minor modifications.^{3–7} A significantly larger amount of SDS was found to be needed than reported previously for a given nanoparticle size. The correlation between the size of the nanoparticles and the amounts of solvent, water, and SDS seem to be depending on the properties of the individual polymers. We found that a 100 mM SDS solution and a solid content in the organic phase of $\sim 40 \text{ mg mL}^{-1}$ reproducibly gave nanoparticles with a size below 150 nm as established with SAXS measurements. We also found that the nanoparticles were conserved in the coated films (*vide supra*). The observed discrepancy in particle size as a function of SDS content could also be linked to the

method of particle size determination where light scattering was employed previously. The reported method for the removal of the excess detergent comprises dialysis and centrifugal dialysis. These methods however allow for the preparation of only small quantities of ink. In our case large volumes ($>100 \text{ mL}$) of inks with a high solid content was needed, and we initially attempted using a large basket centrifuge allowing for the continuous addition of water but finally settled on a Millipore filter system with a processing volume of 500 mL. Using this method, ink volumes of 100 mL with a solid content of 60 mg mL^{-1} could be prepared in a few hours. The inks were diluted 625 times corresponding to a final SDS concentration in the ink of 0.16 mM.

Particle Size and Crystalline Order. SAXS was employed on both the aqueous dispersions and on the solid films to determine particle sizes. AFM images of the films were analyzed to determine particle size distributions and gave similar results.

GIWAXS data showed poorly developed crystalline order of polymers **P2** and **P3**, with only weak first order reflections corresponding to lamellar spacings of 18.2 and 24.0 Å, respectively, and a broad peak at $\sim 1.34 \text{ \AA}^{-1}$ that we ascribe to packing of disordered side chains. **P1** showed very weak scattering, with no features that may be attributed to crystalline order of the polymer (the wide peak at high q values is the background signal from the glass substrate). All three films show a weak peak at $\sim 0.69 \text{ \AA}^{-1}$ that we ascribe to nanocrystalline [60]PCBM (Table 1 and Figures 3 and 4).

Inks and Roll-to-Roll Coating. The spin coating of thin films was possible, whereas large area films with the thickness/coverage required for making functional OPV devices was not possible. It was further found impossible to successfully coat these inks even with very fast web speeds and fast drying on a heated roller and a short distance (18 cm) between the coating head and the oven. Web speeds as high as 8 m min^{-1} were employed with a roller temperature of $80 \text{ }^\circ\text{C}$. By heating the foil just after coating, quick drying was possible (within seconds), but significant dewetting was still observed (see Supporting Information).

TABLE 1. The Average Particle Diameter in P1, P2, and P3 As Determined by SAXS and AFM. The Standard Deviation Is Given in the Brackets

polymer	SAXS (dispersions)	AFM (films)	GISAXS (films)
P1	130(38) nm	<i>a</i>	<i>a</i>
P2	32(10) nm	69(47) nm	32(22) nm
P3	87(21) nm	120(82) nm	107(72) nm

^a Not possible to establish due to aggregation in the sample.

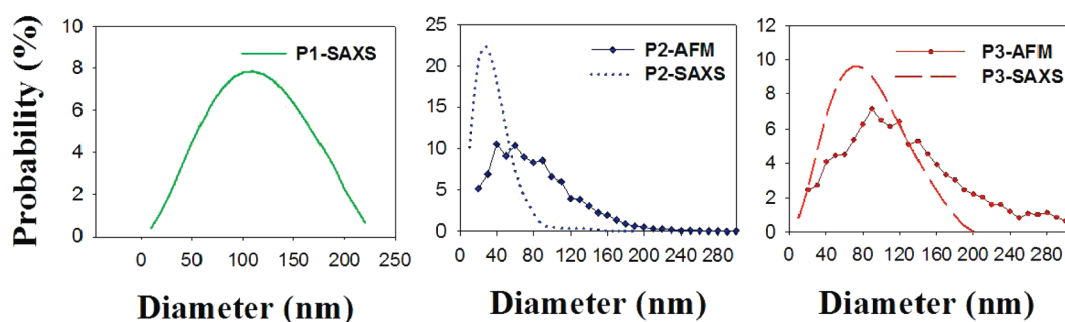


Figure 3. Size distributions of the particles P1 (left), P2 (middle), P3 (right) measured by AFM and SAXS. The SAXS measurements were performed with the particles in a water suspension, and the AFM was measured from spin-coated films. The distribution of P1 could not be determined by AFM due to aggregation of the particles.

Careful inspection of the wetting behavior revealed that the ink initially wets the surface and then dewets leaving a thin film (possibly comprising a single layer of nanoparticles). We ascribe this to the initial wetting and drying followed by lowering of the surface energy of the first layer and subsequent dewetting of the higher surface tension solution.

This phenomenon is quite well-known in the area of coating technology and is in essence a result of poisoning the otherwise wettable surface by the surface active properties of the ink itself. To solve this problem, the addition of a nonionic fluorosurfactant (FSO-100) was found to be necessary. The amount added was critical, and with too little material dewetting was still observed,

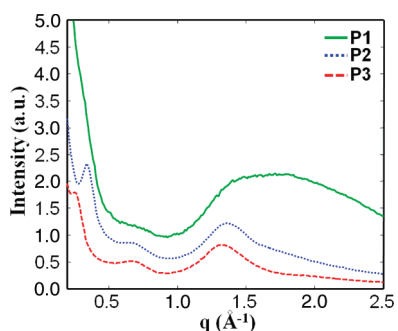


Figure 4. GIWAXS patterns of the three polymers, spin-coated on glass. No texture was observed, and the 2D patterns were thus azimuthally averaged as a function of q . The patterns are scaled for clarity.

whereas too much led to films with extremely poor adhesion. A concentration of 5 mg mL^{-1} was found to be the best compromise between coatability and adhesion. Films prepared in this manner passed the tape test.¹⁶ The age of the meniscus was found to be of critical importance for efficient wetting and good adhesion of the dried film. This phenomenon is well-known in the area of coating technology, where shear induced in the ink as a result of the coating process itself leads to depletion of surfactant at the surface of the ink. In the case of water based inks this implies that the surface tension of the ink in the region of coating increases to a level where dewetting occurs. In such cases the speed of the coating process must be decreased to a level where the surfactant has time to diffuse to the surface and maintain the lower surface tension. Web speeds of 1 m min^{-1} were found to present the best conditions even though web speeds as high as 1.6 m min^{-1} could also be employed. A web speed of 0.6 m min^{-1} was used in all experiments to fabricate the devices presented in this work. Examples of dewetting during coating can be seen in the Supporting Information, and correct wettings are shown in Figure 5. The thickness of the dry active layers of **P1**, **P2**, and **P3** were measured by AFM profilometry and were found to be 126 ± 19 , 500 ± 25 , and $612 \pm 22 \text{ nm}$, respectively.

The devices were completed by slot-die coating poly-(3,4-ethylenedioxythiophene) poly(styrenesulfonate) (PEDOT:PSS) on top of the active layer and interestingly

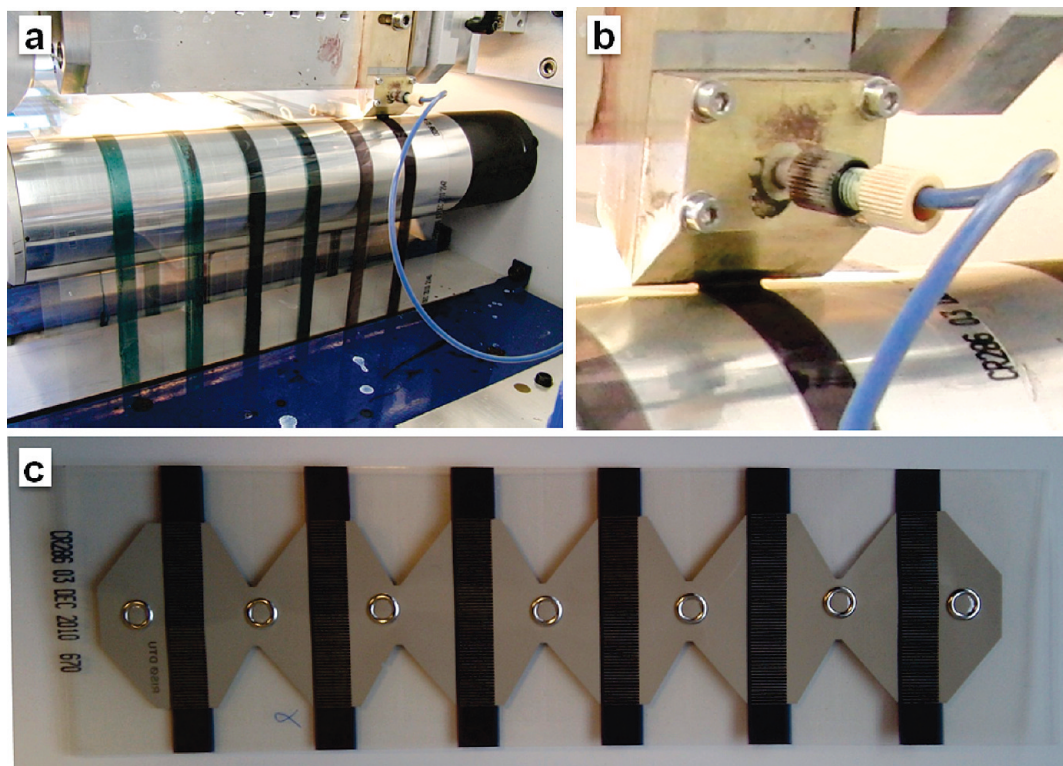


Figure 5. (a) Slot-die coating of the active layer using the aqueous nanoparticle dispersions and (b) an enlargement of the coating head, coating bead and wet film, and (c) showing a complete device with six individual solar cells.

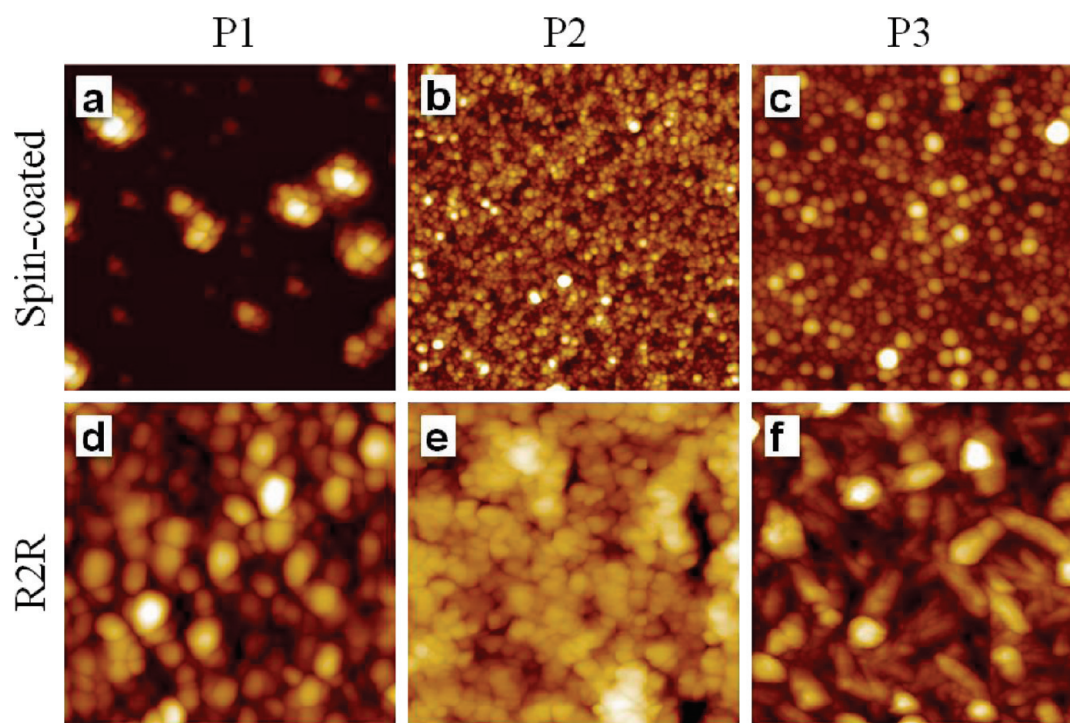


Figure 6. AFM topography images of spin-coated (a–c) and R2R (d–f) prepared samples of P1, P2, and P3. All the images were taken at $5 \times 5 \mu\text{m}^2$.

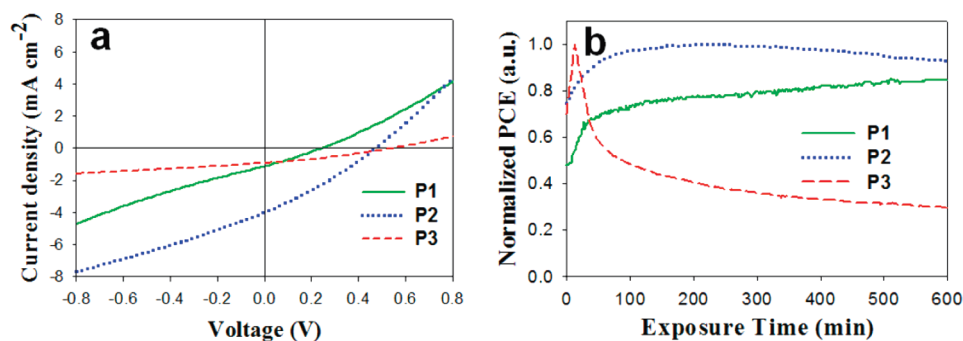


Figure 7. (a) *IV*-curves for the devices based on the three different polymers, at peak performance (AM1.5G , 1000 W m^{-2} , $85 \pm 5 \text{ }^\circ\text{C}$). (b) The development of the solar cell PCE during the initial 10 h of the exposure to 1 sun is shown for the three different polymers. Values are normalized to the corresponding peak value for each polymer (see Table 2).

no prewetting of the active layer with isopropyl alcohol was needed. We ascribe this to a fortuitous interaction between the fluorosurfactants in the PEDOT:PSS formulation and in the coated active layer. The devices were completed by screen printing a silver ink onto the PEDOT:PSS electrode. The devices were finally encapsulated using a simple barrier foil as described earlier and tested using an automated roll-to-roll IV-tester.^{8,14,15}

Morphology. The morphology differences between spin-coated and R2R prepared samples and between the different sample materials can clearly be observed in the AFM images in Figure 6. On the spin-coated samples the individual nanoparticle shapes can be observed (with exception of **P1**, which looks like agglomerates made up of smaller particles). In the R2R samples the nanoparticles can no longer be clearly

distinguished; instead it looks like the nanoparticles have merged in places. The different morphologies observed across the R2R samples could be caused by the “harsh” process conditions, where annealing at high temperatures is involved, and due to the different thermal properties of the polymers.

When the R2R coated samples in Figure 6 panels d, e, and f are compared, it looks like the particles are increasingly merged ($d < f < e$). This could be because these samples were prepared at slightly different conditions with the annealing time increasing ($d < f < e$). Each roll-to-roll experiment (a roll of foil) comprises six coated stripes as described earlier.¹⁵ The first coated stripe will thus pass the oven a total of eight times, whereas that last coated stripe will pass the oven a total of three times (including the two passages when

coating PEDOT:PSS and printing the silver back electrode).

Device Performance. The freshly prepared devices were put under a calibrated solar simulator (AM1.5G, 1000 W m^{-2}) and *IV*-scans were recorded every 1 min, for up to 36 h (according to the ISOS-L-1 procedure²⁶ using a temperature of $85 \pm 5 \text{ }^\circ\text{C}$). For all devices an initial steady increase in PCE during exposure to sunlight was generally observed.

However the optimum period of light exposure was significantly different for the three photoactive polymers, as can be seen in Figure 7. The PCE increase was caused by improvement of both the short circuit current and open circuit voltage, while the fill-factor was relatively constant. This behavior is not unique for these cells prepared from water-dispersed nanoparticles, but is readily observed for other polymer solar cells, having the same layer structure but an active layer processed from organic solvents such as chlorobenzene.¹⁵ It is ascribed to a combination of effects such as photodoping of the zinc oxide layer by UV-light, accompanied by beneficial morphological changes in the active layer due to the relatively high temperature ($85 \pm 5 \text{ }^\circ\text{C}$).¹⁴

The devices prepared from the aqueous dispersions show poorer performance compared to earlier reported efficiencies for devices based on **P1**, **P2**, and **P3**, prepared using chlorobenzene as solvent (Figure 7).^{10–12} The source of this most likely shunts across the active layer. Because of the particle nature of the active layers (Figure 6), the film will be somewhat porous and thus susceptible to shunting by the subsequent processing of PEDOT:PSS. It is thus likely that the amount of shunts should be dependent on the layer thickness relative to the particle diameters. When the obtained PCEs for the different polymers are

compared, it is observed that thicker layers and smaller particle size seem to give a higher performance. Apart from these suspected microscopic shunts, there are some larger shunts for some devices due to incomplete coverage evident from optical inspection of the film and even more so from the light beam induced current (LBIC) scan shown in Figure 8 where (blue) dots within the (red/green) active area reveal such shunts. Furthermore, effects from the significant amount of fluorosurfactant present in the ink along with the residual SDS bound to the surface of the nanoparticles have not been determined. This does however show that it is possible to prepare devices from water with a non-negligible performance, and worth noting that a large part of the relatively low performance of these devices prepared from water could be due to coating technicalities that are bound to become less pronounced as further experience is gained.

Directions for Future Work. The possibility of achieving aqueous processing and operator safety and avoiding the emission of environmentally harmful solvents to the environment was demonstrated, and while this is a great step forward it was achieved at the expense of using a fluorinated surfactant. There is a well-documented concern over release of fluorinated surfactants to the environment where extremely harmful effects have been documented.¹⁷ In our case the surfactant is not released directly to the environment but will follow the solar cell until the end of its life cycle, where it should be properly disposed. The identification of existing environmentally friendly surface active materials or the development of new ones for coating should be researched actively to avoid the use of fluorinated detergents while maintaining the advantages of aqueous processing of OPV.

The relationship between the chemical disposition of the polymer materials and nanoparticle size in the final ink will have to be established along with the relationship between the size of the nanoparticles and the performance of the solar cell printed from them. Since this requires quite large quantities of conjugated polymer material, the type of materials that perform best should be identified followed by replacement of the fluorinated surfactant. Once the truly environmentally friendly ink with the best performance has been identified the ink can be finally optimized with respect to nanoparticle size, solid content, drying time, etc.

TABLE 2. The Photovoltaic Properties Obtained for the Devices When Processed from Water^a

polymer	V_{oc} (V)	J_{sc} (mA cm^{-2})	FF (%)	PCE (%)
P1	0.24	1.10	27.5	0.07
P2	0.47	3.99	29.3	0.55
P3	0.54	0.92	30.8	0.15

^aThe device geometry was PET/ITO/ZnO/polymer-[60]PCBM/PEDOT:PSS/Ag-(printed), and the active area of the devices was 4 cm^2 . The testing conditions were AM1.5G, 1000 W m^{-2} , $85 \pm 5 \text{ }^\circ\text{C}$.

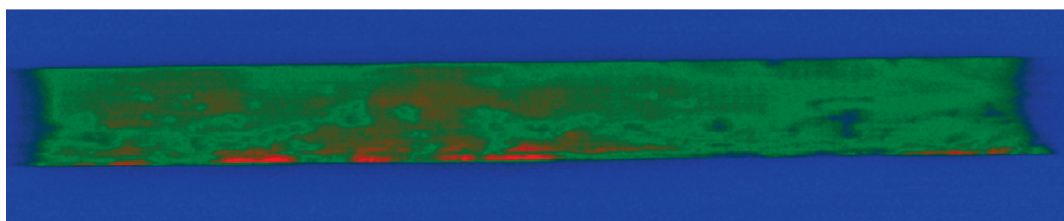


Figure 8. The LBIC image for a mapping of a P2 cell. The intensity scale is going from blue with no intensity over green to red with high intensity.

In our case **P2** proved to work best and further optimization using this class of materials should be pursued.

CONCLUSIONS

We have successfully prepared aqueous nanoparticle dispersions of three low-band-gap polymers and formulated inks for roll-to-roll processing into polymer solar cells on a flexible substrate which resulted in PCEs of 0.55, 0.15, and 0.07% for poly[(4,4'-bis(2-ethylhexyl)dithieno[3,2-b:2',3'-d]silole)-2,6-diyl-alt-(2,1,3-benzothiadiazole)-4,7-diyl], poly[2,3-bis-(3-octyloxyphenyl)-quinoxaline-5,8-diyl-alt-thiophene-2,5-diyl], and poly[4,8-bis(2-ethylhexyloxy)benzo(1,2-b:4,5-b')

dithiophene-alt-5,6-bis(octyloxy)-4,7-di(thiophen-2-yl)(2,1,3-benzothiadiazole)-5,5'-diyl], respectively. We analyzed the nanoparticles in aqueous dispersion using SAXS and in solid film using GISAXS, GIWAXS, and AFM. The ink formulation and roll-to-roll processing was found to be challenging, however a reproducible method giving homogeneous films that adhered well to the surface of the zinc oxide based electron transport layer was obtained. The relatively poor device performance is ascribed to shunting and non-optimum morphology. Further work should be directed at improving coating condition and ink formulation as this has been successful in the case of organic solvent systems.

METHODS

Materials. The polymers were prepared as described in the literature.^{10–12} They had values for M_n , M_w , and polydispersities of, respectively, 11.0 kDa, 28.7 kDa, and 2.6 for **P1**, 6.0 kDa, 10.9 kDa and 1.8 for **P2**, and 21.0 kDa, 89.0 kDa, and 4.2 for **P3**. [60]PCBM, SDS and chloroform were purchased in standard grade. An aqueous precursor solution for the zinc oxide was prepared as described in the literature.¹ PEDOT:PSS was based on EL-P 5010 from Agfa that was diluted with isopropyl alcohol to a viscosity of 200 mPa·s. The printable silver back electrode was PV410 from Dupont.

Nanoparticle Preparation. The typical recipe for small scale production, the polymer material (0.3 g) was together with [60]PCBM (0.3 g) dissolved in chloroform (15.5 mL) and mixed with an aqueous 100 mM SDS solution (50 mL) in a large beaker. The mixture was stirred vigorously for 1 h and then subjected to ultrasound (1 kW) for 5 min using an UIP 1000hd transducer from Hielscher ultrasound technology fitted with a booster head. The mixture was then stirred on a hot plate at 65 °C for 3 h until all the chloroform had evaporated. For small scale preparations, the aqueous dispersion was then dialyzed in dialysis tubing against 2×10 L pure water. In the final step the suspensions were concentrated to have a solid content of approximately 60 mg mL⁻¹.

For large scale preparations, the aqueous dispersion was dialyzed using a Millipore system with a capacity of 500 mL. The mixture was concentrated by dialysis from a volume of 500 mL to a volume of 100 mL with a forward pressure of 1.4 bar and a pressure gradient across the filter of 0.7 bar. Pure water (400 mL) was then added and the procedure was repeated 4 times corresponding to a dilution of the solution by a factor of 625. In the final step the suspensions were concentrated to have a solid content of 60 mg mL⁻¹.

X-ray Scattering. The SAXS and grazing incidence SAXS (GISAXS) experiments were performed at a laboratory setup using a rotating Cu-anode operating at 46 kV and 46 mA as X-ray source. The SAXS instrument was configured for a fully evacuated sample to detector distance of 4579 mm covering a q -range of $2.5 \times 10^{-3} < q < 0.12 \text{ \AA}^{-1}$, where the length of the scattering vector $q = 4\pi \sin(\theta)/\lambda$, with θ equal to half the scattering angle, and λ being the X-ray wavelength for Cu K α (1.5418 Å). The X-rays are monochromated and collimated by two-dimensional multilayer optics and detected by a 2D "Gabriel"-type gas-proportional delay line detector.¹⁸ The nanoparticle dispersions were measured in 1 mm borosilicate capillaries, sealed with epoxy glue for the SAXS experiments, and GISAXS of films spin-coated on glass were measured by orienting the substrate at an X-ray incidence angle of 0.5°. The 2D scattering images of the randomly oriented particles in dispersion were reduced to 1D cross sections by azimuthal

averaging, whereas the GISAXS scattering were reduced to 1D curves by taking projections through the Yoneda peak¹⁸ at constant q_z . The reduced 1D data were analyzed by using the Bayesian inverse Fourier transform (BIFT).¹⁹

GIWAXS of spin-coated films on glass were acquired by orienting the substrate surface just below the critical angle for total reflection with respect to the incoming X-ray beam (0.18°), maximizing scattering from the deposited film with respect to scattering from the substrate. In the wide scattering angle range ($>5^\circ$), the X-ray scattering is sensitive to crystalline structure. For the experiment we used a camera comprising an evacuated sample chamber with an X-ray photosensitive image plate as detector and a rotating Cu-anode operating at 50 kV/200 mA as X-ray source, focused and monochromatized (Cu K α , $\lambda = 1.5418 \text{ \AA}$) by a 1D multilayer.¹⁹ The samples were mounted 120 mm from the detector. The GIWAXS data were analyzed by reducing the acquired 2D data by azimuthal averaging of intensity as a function of scattering vector length, q , to determine the characteristic d -spacings of the polymers, using the software SimDiffraction.²⁰

Atomic Force Microscopy. AFM imaging was performed on an N8 NEOS (Bruker Nano GmbH, Herzogenrath, Germany) operating in an intermittent contact mode using PPP-NCLR cantilevers (NANOSENSORS, Neuchatel, Switzerland). Images were recorded at a scan speed of 0.8 lines min⁻¹. The images were analyzed using the image processing software package SPIP 5.1.5 (Image Metrology A/S, Hørsholm, Denmark).

The samples were first delaminated by ripping the plastic laminate off in a swift motion and thereafter placed on a glass slide using double sided tape.

It is well-known that AFM can at times overestimate particle sizes in the lateral plane and therefore the height z is often used as a measure for the diameter of spherical particles.^{21–23} However, since the particles in the samples at hand are closely packed the height measurements of individual particles would be too time-consuming and inaccurate.²⁴ Therefore the best estimate to determine the particle size was to employ the Particle & Pore Analysis module included in the SPIP 5.1.5 software. The size was analyzed on at least two different positions of the sample analyzing a minimum of 2000 particles on each sample.

The thicknesses of the dry films were measured by AFM profilometry, see Figure 9. The thickness was measured at a minimum of three different positions on each film, with each position consisting of at least three individual measurements.

Light Beam Induced Current (LBIC) Mapping. The LBIC experiments were carried out using a custom-made setup with 410 nm laser diode (5 mW output power, 100 μ m spot size ($\approx 65 \text{ W/cm}^2$), ThorLabs) mounted on a computer controlled XY-stage and focused to a spot size of $<100 \mu$ m. The short circuit current from the device under study was measured using a computer

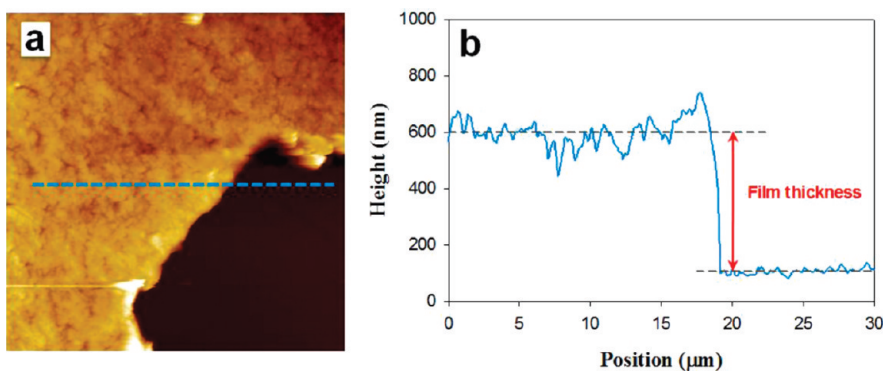


Figure 9. (a) $30 \times 30 \mu\text{m}^2$ AFM topography image indicating where the thickness was measured. (b) line profile extracted from the AFM image (dashed line).

controlled source measure unit (Keithley 2400), and mapped by raster scanning across the device. Further details are available elsewhere.²⁵

Ink Formulation. The nonionic fluorosurfactant (FSO-100) was added to the dialyzed aqueous suspension of the polymer/[60]PCBM nanoparticles. The concentration of fluorosurfactant was 5 mg mL^{-1} and the polymer/[60]PCBM concentration was 60 mg mL^{-1} . This solution was employed directly for slot-die coating.

Roll-to-Roll Coating. A PET substrate with an ITO pattern was prepared and cleaned as described earlier.^{13–15} The zinc oxide precursor solution was prepared as described earlier¹ and comprised $\text{Zn}(\text{OAc})_2 \cdot 2\text{H}_2\text{O}$ (100 mg mL^{-1}), $\text{Al}(\text{OH})(\text{OAc})_2$ (2 mg mL^{-1}), and FSO-100 (2 mg mL^{-1}) in water. This solution was microfiltered immediately prior to use ($0.45 \mu\text{m}$) and then slot-die coated at a speed of 2 m min^{-1} with a wet thickness of $4.9 \mu\text{m}$. After the initial drying of the precursor film it was converted into an insoluble film by passage through an oven at a temperature of $140 \text{ }^\circ\text{C}$ with a speed of 0.2 m min^{-1} (oven length = 4 m). This gave an insoluble doped zinc oxide film with a thickness of $25 \pm 5 \text{ nm}$. The aqueous polymer/[60]PCBM nanoparticle dispersion was then slot-die coated at a speed of 1 m min^{-1} with a wet thickness of 30.4 , 17.6 , and $20.8 \mu\text{m}$ for **P1**, **P2**, and **P3**, respectively. The coating speed and the time between application of the wet film and the drying were critical for successful formation of a homogeneous film without dewetting. The slot-die coating head had a temperature of $60 \text{ }^\circ\text{C}$, the coating roller had a temperature of $80 \text{ }^\circ\text{C}$, and the temperature of the foil was kept at $80 \text{ }^\circ\text{C}$ until it reached the oven at $140 \text{ }^\circ\text{C}$. The distance from the point of coating to the oven entry was 18 cm . PEDOT:PSS was then applied by slot-die coating at a speed of 0.2 m min^{-1} and dried at $140 \text{ }^\circ\text{C}$ (oven length = 2 m). It was found unnecessary to wet the film surface prior to coating the PEDOT:PSS and this might be due to the beneficial interaction between the fluorosurfactants in the active layer film and in the PEDOT:PSS. Finally the device was completed by roll-to-roll screen printing a silver grid electrode and drying at $140 \text{ }^\circ\text{C}$. The devices were encapsulated using roll-to-roll lamination of a simple food packaging barrier with a pressure sensitive adhesive onto both sides of the foil.^{13–15}

IV-Characterization. In each coated stripe that represents one set of experiments a total of 150 solar cells were prepared (900 cells for each roll). The devices were light soaked with continuous sweeping of the *IV*-curve until a constant performance was reached. Typically the performance dropped rapidly during the first 10 min of light soaking followed by a slow improvement in performance over 4–6 h where a stable level of performance was reached. The data reported is for the stable regime. The devices were initially tested using a roll-to-roll tester and the functional devices were the recovered for further testing using a calibrated solar simulator (AM1.5G , 1000 W m^{-2} , $85 \pm 5 \text{ }^\circ\text{C}$). The prolonged testing was made according to the ISOS-L-1 procedure.²⁶

Acknowledgment. This work was supported by the Danish National Research Foundation. We gratefully acknowledge the

assistance of Steen Hansen with modifying the BIFT algorithm for use with polydisperse systems and Lasse Gorm Jensen for creating graphical illustrations.

Supporting Information Available: Details of the GISAXS analysis of solid films, with data and the description of the data reduction procedure; details of dewetting during coating. This material is available free of charge via the Internet at <http://pubs.acs.org>.

REFERENCES AND NOTES

- Søndergaard, R.; Helgesen, M.; Jørgensen, M.; Krebs, F. C. Fabrication of Polymer Solar Cells Using Aqueous Processing for All Layers Including the Metal Back Electrode. *Adv. Eng. Mater.* **2011**, *1*, 68–71.
- Rider, D. A.; Worfolk, B. J.; Harris, K. D.; Lalany, A.; Shahbazi, K.; Fleischauer, M. D.; Brett, M. J.; Buriak, J. M. Stable Inverted Polymer/Fullerene Solar Cells Using a Cationic Polythiophene Modified PEDOT:PSS Cathodic Interface. *Adv. Funct. Mater.* **2010**, *20*, 2404–2415.
- Landfester, K. The Generation of Nanoparticles in Miniemulsions. *Adv. Mater.* **2001**, *13*, 765–768.
- Kietzke, T.; Neher, D.; Landfester, K.; Montenegro, R.; Güntner, R.; Scherf, U. Novel Approaches to Polymer Blends Based on Polymer Nanoparticles. *Nat. Mater.* **2003**, *2*, 408–412.
- Piok, T.; Gamerith, S.; Gadermaier, C.; Plank, H.; Wenzl, F. P.; Patil, S.; Montenegro, R.; Kietzke, T.; Neher, D.; Scherf, U.; *et al.* Organic Light-Emitting Devices Prepared from Semiconducting Nanospheres. *Adv. Mater.* **2003**, *15*, 800–804.
- Kietzke, T.; Neher, D.; Kumke, M.; Montenegro, R.; Landfester, K.; Scherf, U. A Nanoparticle Approach to Control the Phase Separation in Polyfluorene Photovoltaic Devices. *Macromolecules* **2004**, *37*, 4882–4890.
- Antonietti, M.; Landfester, K. Polyreactions in Miniemulsions. *Prog. Polym. Sci.* **2002**, *27*, 689–757.
- Krebs, F. C.; Gevorgyan, S. A.; Alstrup, J. A Roll-to-Roll Process to Flexible Polymer Solar Cells: Model Studies, Manufacture, and Operational Stability Studies. *J. Mater. Chem.* **2009**, *19*, 5442–5442.
- Espinosa, N.; Garcia-Valverde, R.; Urbina, A.; Krebs, F. C. A Life Cycle Analysis of Polymer Solar Cell Modules Prepared Using Roll-to-Roll Methods Under Ambient Conditions. *Sol. Energy Mater. Sol. Cells* **2011**, *95*, 1293–1302.
- Bundgaard, E.; Hagemann, O.; Jørgensen, M.; Krebs, F. C. Low-Band-Gap Polymers for Roll-to-Roll Coated Organic Photovoltaics Design, Synthesis and Characterization. *Green* **2011**, *1*, 55–64.
- Hou, J.; Chen, H. Y.; Zhang, S.; Li, G.; Yang, Y. Synthesis, Characterization, and Photovoltaic Properties of a Low Band Gap Polymer Based on Silole-Containing Polythiophenes and 2,1,3-Benzothiadiazole. *J. Am. Chem. Soc.* **2008**, *130*, 16144–16145.
- Wang, E.; Hou, L.; Wang, Z.; Hellström, S.; Zhang, F.; Inganäs, O.; Andersson, M. R. An Easily Synthesized Blue

- Polymer for High-Performance Polymer Solar Cells. *Adv. Mater.* **2010**, *22*, 5240–5244.
13. Krebs, F. C.; Nielsen, T. D.; Fyenbo, J.; Wadstrøm, M.; Pedersen, M. S. Manufacture, Integration and Demonstration of Polymer Solar Cells in a Lamp for the “Lighting Africa” Initiative. *Energy Environ. Sci.* **2010**, *3*, 512–512.
 14. Krebs, F. C.; Tromholt, T.; Jørgensen, M. Upscaling of Polymer Solar Cell Fabrication Using Full Roll-to-Roll Processing. *Nanoscale* **2010**, *2*, 873–886.
 15. Alstrup, J.; Medford, A. J.; Jørgensen, M.; Krebs, F. C. Ultrafast and Parsimonious Materials Screening for Polymer Solar Cells Using Differentially Pumped Slot-Die Coating. *ACS Appl. Mater. Interfaces* **2010**, *2*, 2819–2827.
 16. ASTM INTERNATIONAL Standards Worldwide. Standard Test Methods for Measuring Adhesion by Tape Test. p. 8.
 17. Renner, R. Growing Concern over Perfluorinated Materials. *Environ. Sci. Technol.* **2001**, *35*, 154A–160A.
 18. Yoneda, Y. Anomalous Surface Reflection of X-Rays. *Phys. Rev.* **1963**, *131*, 2010–2013.
 19. Apitz, D.; Bertram, R.; Benter, N.; Hieringer, W.; Andreasen, J.; Nielsen, M.; Johansen, P.; Buse, K. Investigation of Chromophore-Chromophore Interaction by Electro-optic Measurements, Linear Dichroism, X-ray Scattering, and Density-Functional Calculations. *Phys. Rev. E* **2005**, *72*, 036610-1–036610-10.
 20. Breiby, D. W.; Bunk, O.; Andreasen, J. W.; Lemke, H. T.; Nielsen, M. M. Simulating X-ray Diffraction of Textured Films. *J. Appl. Crystallogr.* **2008**, *41*, 262–271.
 21. Villarrubia, J. Algorithm for Scanned Probe Microscope Image Simulation, Surface Reconstruction, and Tip Estimation. *J. Res. Natl. Inst. Stand. Technol.* **1997**, *102*, 425–454.
 22. Hoo, C. M.; Starostin, N.; West, P.; Mecartney, M. L. A Comparison of Atomic Force Microscopy (AFM) and Dynamic Light Scattering (DLS) Methods to Characterize Nanoparticle Size Distributions. *J. Nanopart. Res.* **2008**, *10*, 89–96.
 23. Boyd, R. D.; Cuenat, A. New Analysis Procedure for Fast and Reliable Size Measurement of Nanoparticles from Atomic Force Microscopy Images. *J. Nanopart. Res.* **2011**, *13*, 105–113.
 24. Dias, A.; Buono, V. T. L.; Vilela, J. M. C.; Andrade, M. S.; Lima, T. M. Particle Size and Morphology of Hydrothermally Processed MnZn Ferrites Observed by Atomic Force Microscopy. *J. Mater. Sci.: Mater. Med.* **1997**, *32*, 4715–4718.
 25. Krebs, F. C.; Søndergaard, R.; Jørgensen, M. Printed Metal Back Electrodes for R2R Fabricated Polymer Solar Cells Studied Using the LBIC Technique. *Sol. Energy Mater. Sol. Cells* **2011**, *95*, 1348–1353.
 26. Reese, M. O.; Gevorgyan, S. A.; Jørgensen, M.; Bundgaard, E.; Kurtz, S. R.; Ginley, D. S.; Olson, D. C.; Lloyd, M. T.; Morvillo, P.; Katz, E. A.; *et al.* Consensus Stability Testing Protocols for Organic Photovoltaic Materials and Devices. *Sol. Energy Mater. Sol. Cells* **2011**, *95*, 1253–1267.

Comparative studies of photochemical cross-linking methods for stabilizing the bulk hetero-junction morphology in polymer solar cells†

Jon Eggert Carlé, Birgitta Andreasen, Thomas Tromholt, Morten V. Madsen, Kion Norrman, Mikkel Jørgensen and Frederik C. Krebs*

Received 3rd July 2012, Accepted 14th August 2012

DOI: 10.1039/c2jm34284g

We are here presenting a comparative study between four different types of functionalities for cross-linking. With relatively simple means bromine, azide, vinyl and oxetane could be incorporated into the side chains of the low band-gap polymer **TQ1**. Cross-linking of the polymers was achieved by UV-light illumination to give solvent resistant films and reduced phase separation and growth of PCBM crystallites in polymer:PCBM films. The stability of solar cells based on the cross-linked polymers was tested under various conditions. This study showed that cross-linking can improve morphological stability but that it has little influence on the photochemical stability which is also decisive for stable device operation under constant illumination conditions.

Introduction

Research on polymer solar cells (PSC) has reportedly delivered an increase in the power conversion efficiency to some 10% by optimization of each component and especially in the case of the active layer composed of a light harvesting polymer and a molecular acceptor.^{1,2} Another aspect that needs to be addressed is the stability of these devices, which has also improved by several orders of magnitude during the last decade.³ Modern PSC rely on a so-called bulk hetero-junction where the polymer–acceptor mixture in the active layer is micro-phase segregated to form a bi-continuous structure with channels for both electron and hole transport. A key issue is that the excitons formed upon irradiation with light have a limited diffusion length in these materials of 10–20 nm, which means that this is also the optimal physical dimension of the domains in the hetero-junction. Unfortunately, this is not usually the thermodynamic equilibrium (*i.e.* the material is metastable), which is manifested in a growth of PCBM acceptor crystallites that erodes the optimal morphology.^{4,5}

Several strategies have been developed to mitigate this problem. One of the first proposed was to combine the donor polymer with the acceptor part to create block-copolymers that form stable bi-continuous networks by supra-molecular forces.^{6–8} This approach has not been so successful, presumably due to the formidable synthetic challenges. Another strategy is to cross-link the active layer after it has been deposited by a cross-linking reaction. One possibility that has been explored is to use side chains that are attached to the polymer with tertiary ester

groups that can be cleaved off by a thermal treatment of the processed films. The residual carboxylic acid groups then form hydrogen bonds resulting in a very stiff matrix that also immobilizes the acceptor part.⁹ Yet another approach that is also explored in this work is to incorporate cross-linkable groups in some of the polymer side chains. Several different photo-curable groups have been used for this purpose such as oxetane groups,¹⁰ alkyl-bromide,^{11,12} azide^{13–15} and vinyl.^{16,17} The idea is once again that the cross-linking immobilizes the structure inhibiting further growth of domains.

Previous studies have each focused on one specific cross-linking reaction only. This study compares four different types of functionalities for cross-linking attached to a low band-gap polymer **TQ1**.^{18,19} Furthermore, experiments have been carried out in an inert atmosphere and with hot dark storage between measurements to enhance the thermally induced morphological instability. Finally, different experimental conditions aimed for degradation were compared in order to investigate the importance of morphological stability compared to photochemical stability.

Experimental

Synthesis

2,5-Bis-(trimethylstannyl)-thiophene,²⁰ 3,3'-(5,8-dibromoquinoline-2,3-diyl)diphenol (**1**) and **TQ1** were synthesized according to the procedures described in the literature.¹⁸

5,8-Dibromo-2,3-bis(3-(8-bromooctyloxy)phenyl)quinoxaline (2b). Compound **1** (1 g, 2.118 mmol), 1,8-dibromooctane (5.76 g, 21.18 mmol) and potassium carbonate (1.464 g, 10.59 mmol) were dissolved in DMSO (20 ml). The mixture was stirred at 50 °C under argon overnight. Water was added and the organic phase was

Department of Energy Conversion and Storage, Technical University of Denmark, Frederiksborgvej 399, DK-4000 Roskilde, Denmark. E-mail: fkr@dtu.dk

† Electronic supplementary information (ESI) available. See DOI: 10.1039/c2jm34284g

extracted with ethyl acetate. The organic phase was washed three times with water and dried over MgSO_4 . The crude product was added to a silica column and eluted with heptane–ethyl acetate to give the product as a solid. Yield 32.1% (580 mg, 0.679 mmol). ^1H NMR (500 MHz, CDCl_3) δ 7.92 (s, 2H), 7.30–7.20 (m, 4H), 7.16 (m, 2H), 6.99–6.85 (m, 2H), 3.87 (t, $J = 6.5$ Hz, 4H), 3.42 (t, $J = 6.8$ Hz, 4H), 1.93–1.79 (m, 4H), 1.79–1.64 (m, 4H), 1.50–1.27 (m, 16H). ^{13}C NMR (126 MHz, CDCl_3) δ 159.05, 154.00, 139.32, 139.17, 133.11, 129.32, 123.72, 122.60, 116.54, 115.77, 77.27, 77.02, 76.77, 68.02, 33.95, 32.80, 29.17, 29.08, 28.72, 28.12, 25.94.

5,8-Dibromo-2,3-bis(3-(undec-10-enyloxy)phenyl)quinoxaline (2c). Prepared as for **2b**: compound **1** (500 mg, 1.059 mmol), 11-bromoundec-1-ene (617 mg, 2.65 mmol) and potassium carbonate (1464 mg, 10.59 mmol) were dissolved in DMSO (10 ml). Yield 87% (715 mg, 0.921 mmol). ^1H NMR (500 MHz, CDCl_3) δ 7.93 (s, 2H), 7.29–7.23 (m, 4H), 7.23–7.17 (m, 2H), 6.96 (m, 2H), 5.84 (dd, $J = 17.0$, 10.3 Hz, 2H), 5.06–4.90 (m, 4H), 3.88 (t, $J = 6.6$ Hz, 4H), 2.07 (dd, $J = 14.5$, 6.8 Hz, 4H), 1.83–1.68 (m, 4H), 1.50–1.21 (m, 26H). ^{13}C NMR (126 MHz, CDCl_3) δ 159.09, 154.03, 139.33, 139.18, 133.06, 129.30, 123.74, 122.56, 116.61, 115.82, 114.13, 68.15, 33.79, 29.54, 29.44, 29.35, 29.13, 28.95, 26.02.

5,8-Dibromo-2,3-bis(3-(6-((3-ethyloxetan-3-yl)methoxy)hexyloxy)phenyl)quinoxaline (2d). Prepared as for **2b**: compound **1** (500 mg, 1.059 mmol), 3-((6-bromohexyloxy)methyl)-3-ethyloxetane (739 mg, 2.65 mmol) and potassium carbonate (1464 mg, 10.59 mmol) were dissolved in DMSO (10 ml). Yield 80% (740 mg, 0.852 mmol). ^1H NMR (500 MHz, CDCl_3) δ 7.91 (s, 2H), 7.24 (m, 4H), 7.19–7.11 (m, 2H), 7.00–6.84 (m, 2H), 4.45 (d, $J = 5.8$ Hz, 4H), 4.37 (d, $J = 5.8$ Hz, 4H), 3.88 (t, $J = 6.5$ Hz, 4H), 3.53 (s, 4H), 3.47 (t, $J = 6.6$ Hz, 4H), 1.74 (q, $J = 7.4$ Hz, 8H), 1.66–1.58 (m, 4H), 1.50–1.35 (m, 8H), 0.89 (t, $J = 7.5$ Hz, 6H). ^{13}C NMR (126 MHz, CDCl_3) δ 159.09, 153.98, 139.30, 139.20, 133.08, 129.28, 123.73, 122.61, 116.53, 115.82, 78.57, 73.55, 71.51, 68.02, 43.50, 29.54, 29.12, 26.80, 25.97, 25.89, 8.15.

General procedure for the Stille cross-coupling polymerization

Monomer **2a** and one of the monomers **2b**, **2c** or **2d** (9 : 1 molar ratio) and 2,5-bis(trimethylstannyl)thiophene were mixed in degassed toluene to give a 0.04 M solution. To this was added a catalyst mix of 2 mol% tris(dibenzylideneacetone)dipalladium(0) and 8 mol% tri-*o*-tolylphosphine. The solution was stirred at 100 °C for at least 48 hours to complete the polymerization. The crude polymer was then precipitated by adding the reaction mixture to a large volume of methanol. The polymers were purified by Soxhlet extraction, first with methanol, then with hexane and finally with chloroform. The chloroform fraction was then precipitated by pouring it into 10 times the volume of methanol. The precipitate was filtered off and dried in vacuum to give the purified polymer.

Polymer TQ-Br. Monomers **2b** (100 mg, 0.117 mmol), **2a** (734 mg, 1.053 mmol) and 2,5-bis(trimethylstannyl)thiophene (480 mg, 1.170 mmol). Yield 620 mg (83%).

Polymer TQ-Vinyl. Monomers **2c** (50 mg, 0.064 mmol), **2a** (404 mg, 0.579 mmol) and 2,5-bis(trimethylstannyl)thiophene (264 mg, 0.644 mmol). Yield 370 mg (91%).

Polymer TQ-Oxetane. Monomers **2d** (50 mg, 0.058 mmol), **2a** (361 mg, 0.518 mmol) and 2,5-bis(trimethylstannyl)thiophene (236 mg, 0.576 mmol). Yield 330 mg (90%).

Polymer TQ-N₃. **TQ-Br** (300 mg, 0.483 mmol) was dissolved in toluene (100 ml) at 100 °C and sodium azide (314 mg, 4.83 mmol) in DMF (100 ml) was added slowly. The mixture was stirred at 100 °C under argon for 48 hours. The solvents were removed under reduced pressure and the polymer redissolved in chloroform and precipitated in methanol. The polymer was purified by Soxhlet extraction first with methanol then with chloroform and finally precipitated in methanol. Yield: 290 mg (95%).

Device fabrication

The polymers **TQ1**, **TQ-Br**, **TQ-Vinyl**, **TQ-Oxetane** or **TQ-N₃** and [60]PCBM (Solenne b.v., The Netherlands) were dissolved separately in chlorobenzene (20 mg ml⁻¹) and stirred overnight at 50 °C. The polymer and PCBM solutions were mixed and further stirred at 50 °C and then filtered (1 μm pore size). To the **TQ-Oxetane** blend was added 5% (by weight) of the photoacid generator (bis(4-*tert*-butylphenyl)iodonium *p*-toluenesulfonate) (Sigma-Aldrich). The prefabricated ITO coated glass substrates were first ultrasonically cleaned in water and then in 2-propanol. Zinc oxide nanoparticles (ZnO), prepared according to the literature,²¹ were spin-coated from water onto the ITO covered substrate at 1000 rpm and annealed at 140 °C for 10 minutes. The active layer, composed of the polymer:PCBM solution, was spin-coated at 700 rpm onto the ZnO layer followed by UV-irradiation at 254 nm with a laboratory lamp (commonly employed for thin layer chromatography) for 10 minutes in a glove box to cross-link the polymer. A PEDOT:PSS (Agfa EL-P 5010) solution was then spin-coated on top at 2800 rpm followed by annealing at 110 °C for 2 minutes. The devices were transferred to a vacuum chamber where silver electrodes were applied by thermal evaporation at a pressure below 10⁻⁶ mbar. The active area of the devices was 0.25 cm².

Optical microscopy

Blends (1 : 1 by weight) of the polymers and [60]PCBM in chlorobenzene (20 mg ml⁻¹) were spin-coated on glass slides at 700 rpm. The samples were then treated with UV-irradiation (254 nm) for 10 minutes in a glove box using a hand held lamp. The samples were then annealed in ambient air for 13 hours at 150 °C. Optical micrographs of the samples were acquired before and after the annealing procedure.

Photochemical degradation studies

Photochemical stabilities were evaluated using a fully automated, high capacity degradation setup with an AM1.5G spectrum in the ambient atmosphere at 1000 W m⁻² described elsewhere.²² Each polymer was spin-coated on glass substrates from a chlorobenzene solution. The spin coating parameters were adjusted in order to obtain a film thickness of around 60 nm.

Quantification of the degradation rate was based on the evolution of the gradual decrease of UV-visible absorbance, which was recorded at 20 min intervals.

Results and discussion

Synthesis of cross-linkable versions of TQ1

We selected the low band gap polymer **TQ1** for creating cross-linkable versions. The typical octyloxy side chains on the diphenyl-quinoxaline monomer can easily be substituted with alkyl groups adorned with azide, bromine, vinyl or oxetane functionalities that can be used for photocross-linking reactions. These types of cross-linking functionalities have previously been investigated with the purpose of stabilizing the morphology in other types of PSC.^{10–16}

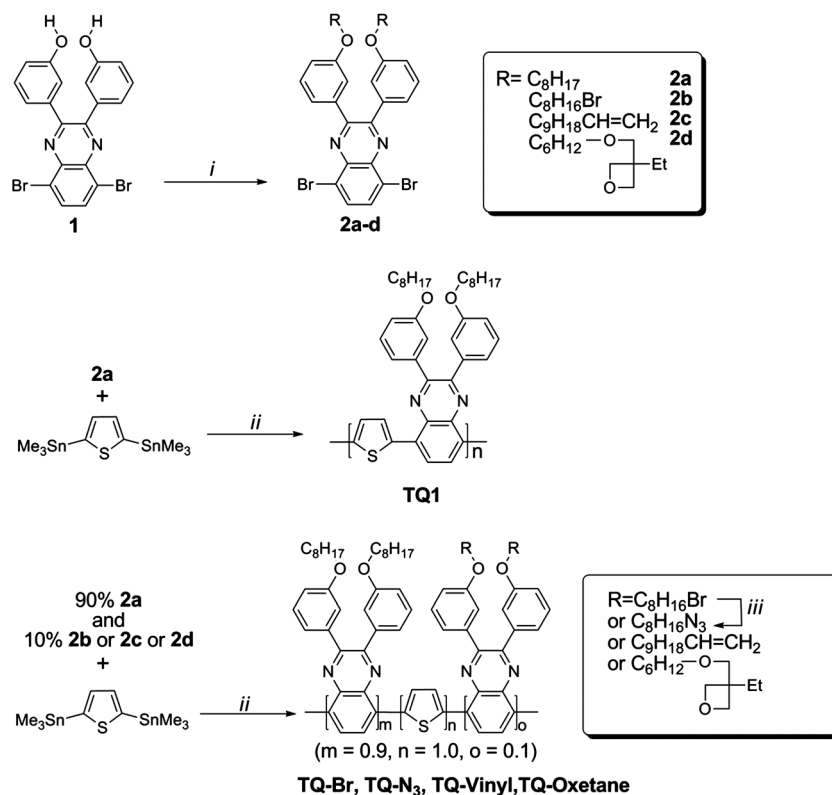
The syntheses of the monomers and the polymerization of the five polymers studied in this work are outlined in Scheme 1.

One of the reasons for choosing the **TQ1** system for this work was the relatively straightforward preparation of the functionalized monomers. The key was the synthesis of the starting material quinoxaline 3,3'-(5,8-dibromoquinoxaline-2,3-diyl)diphenol (**1**) that is common to all the monomers, which is prepared from the known 5,8-dibromo-2,3-bis(3-methoxyphenyl)quinoxaline¹⁸ by cleaving of the methyl groups with concentrated hydrobromic acid. The different quinoxaline monomers were then prepared by alkylation at the phenolate functions with either 1-bromooctane or a substituted alkyl bromide as shown in Scheme 1. Polymerization reactions to give either **TQ1** or the co-polymers **TQ-Br**,

TQ-Vinyl and **TQ-Oxetane** were performed through a Stille coupling either between pure **2a** and 2,5-bis(trimethylstannyl)-thiophene or using a mixture of **2a** and one of the monomers **2b–d**. A monomer feed ratio of **2b–d** to **2a** was chosen to be 1 : 9 which should secure several cross-linkable groups per polymer chain. The synthesis of **TQ-N₃** was carried out by treating **TQ-Br** with sodium azide in hot toluene–DMF, replacing bromine with an azide group. This transformation is clearly observed by ¹H NMR of the polymers. The polymers were characterized by size exclusion chromatography (SEC) with THF as the eluent, using polystyrene as the standard (see Table 1), and also by ¹H NMR (see ESI Fig. S1–5†).

Cross-linking experiments

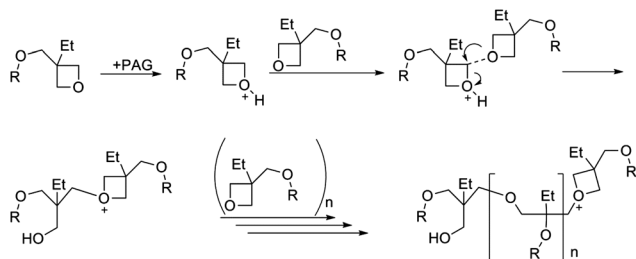
The four different photoactive groups used in this study are expected to cross-link *via* different chemical reaction mechanisms when initiated by UV exposure (254 nm). The bromo-alkyl group is presumably cleaved homolytically to give an alkyl radical and a bromine atom²³ while the alkyl azide group splits off molecular nitrogen (N₂) leaving an alkyl nitrene.^{24,25} The highly reactive nitrene can then react with either the polymer or the fullerene in the bulk through an addition reaction to double bonds.²⁶ The reactions of the vinyl and the oxetane groups are slightly more speculative. The oxetane ring undergoes cross-linking initiated by a photoacid generator (PAG). The propagation probably involves ring-opening of the oxetane through an attack of another oxetane group, as shown in Scheme 2.²⁷



Scheme 1 Synthesis of the monomers **2a–d** and subsequent polymerization with 2,5-bis-(trimethylstannyl)-thiophene to give the polymers with different functionalities in the side chains. **TQ1**, **TQ-Br**, **TQ-N₃**, **TQ-Vinyl** and **TQ-Oxetane**. i: K₂CO₃, DMSO; ii: Pd(PPh₃)₄, toluene; and iii: NaN₃, toluene, DMF.

Table 1 Molecular weight and optical data for the five polymers

Polymer	M_n (kDa)	M_w (kDa)	PD	λ_{\max} (nm)	E_g^{opt} (eV)	λ_{\max} (nm) cross-linked	E_g^{opt} (eV) cross-linked
TQ1	37.7	174.8	4.6	364/623	1.7	364/622	1.7
TQ-Br	20.7	67.0	3.23	364/624	1.7	363/618	1.7
TQ-N₃	22.7	92.2	4.1	360/621	1.7	363/620	1.7
TQ-Vinyl	23.7	86.8	3.66	361/623	1.7	364/620	1.7
TQ-Oxetane	22.1	90.1	4.1	361/623	1.7	364/622	1.7

**Scheme 2** A possible mechanism for cross-linking of oxetane through a ring opening polymerization. Et = ethyl, R = polymer and PAG = photoacid generator.

In all cases reactive intermediates are formed that can react fast with neighboring groups in the film. These may be on other polymer strands giving rise to cross-linking of the polymer matrix and/or with PCBM cross-linking the donor–acceptor domains.

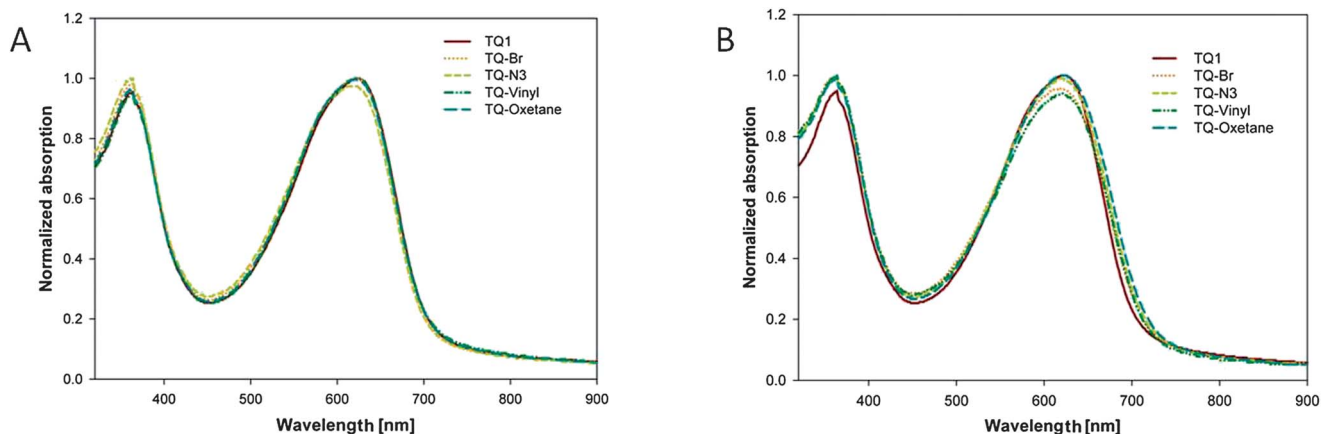
Each of the five polymers was spin-coated onto glass substrates from chloroform solution and dried to give thin films. The films were then irradiated at 254 nm using a mercury lamp UV-lamp for 10 minutes to induce photochemical cross-linking, which was then investigated by a solvent resistance test. The glass substrates with the polymer films were immersed in hot 1,2-dichlorobenzene where only the **TQ1** film could be dissolved proving that cross-linking had taken place for the **TQ-Br**, **TQ-N₃**, **TQ-Vinyl** and **TQ-Oxetane** films. Thin films prepared from blends of the polymers with PCBM in a 1 : 1 ratio (by weight) were tested in the same way. The **TQ1**:PCBM film was fully soluble while the thin films with **TQ-Br**, **TQ-N₃**, **TQ-Vinyl** and

TQ-Oxetane showed partial solvent resistance. PCBM has a strong absorption in the 254 nm range and therefore absorbs part of the UV light used for cross-linking. This could be a reason for the lower solvent resistance.

Absorption spectra of each polymer were acquired as thin films before and after cross-linking by illumination of the films with UV light. Incorporation of the functional groups does not change the absorption spectra of the polymers when compared to **TQ1** (Fig. 1). The spectra of the polymers all have similar features with a $\pi \rightarrow \pi^*$ transition at *ca.* 360 nm and a charge transfer transition at \sim 620 nm (band gap at 1.7 eV). The absorption spectra of the polymers were essentially unchanged after photocross-linking, showing the same transitions and band gaps as before UV-illumination, which suggests that none of the four different cross-linking reactions damaged the conjugated polymer backbone.

Stability investigations

Photochemical stability. The photochemical stability of conjugated polymers is dependent on several different parameters such as oxygen concentration, temperature, and the molecular structure.²⁸ Incorporation of different functionalities into the polymer could change its stability. Photochemical stabilities of the five polymers were therefore evaluated using a fully automated, high capacity degradation setup with an AM1.5G spectrum in the ambient atmosphere at 1000 W m⁻² at ambient temperature.²² The gradual decrease of UV-vis absorption of the \sim 60 nm polymer thin films was spectroscopically monitored during ageing. The normalized absorption *versus* irradiation time

**Fig. 1** UV-vis spectra of **TQ1**, **TQ-Br**, **TQ-N₃**, **TQ-Vinyl** and **TQ-Oxetane** films before (A) and after (B) cross-linking by UV irradiation for 10 minutes at 254 nm.

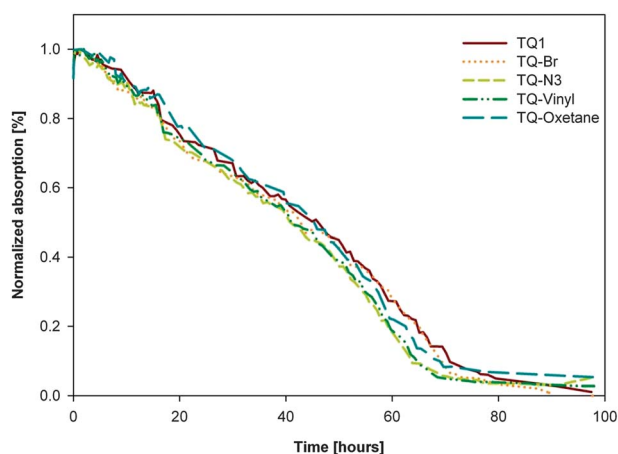


Fig. 2 Photochemical stability of the five polymers as thin films. Normalized absorption *versus* time under constant illumination ($AM1.5G$, 1000 W m^{-2}).

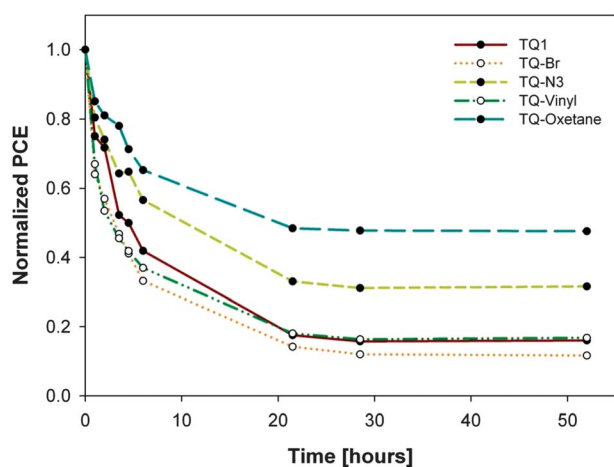


Fig. 3 Efficiencies of devices containing TQ1, TQ-Br, TQ-N₃, TQ-Vinyl or TQ-Oxetane during thermal annealing at $100 \text{ }^\circ\text{C}$ in the dark in an ambient atmosphere (normalized).

for the five polymers is shown in Fig. 2. The degradation rates of the five polymers are almost identical and total bleaching of the films is reached after about 70 hours of illumination. This suggests that incorporation of the functionalities does not affect the photochemical stability of these polymers.

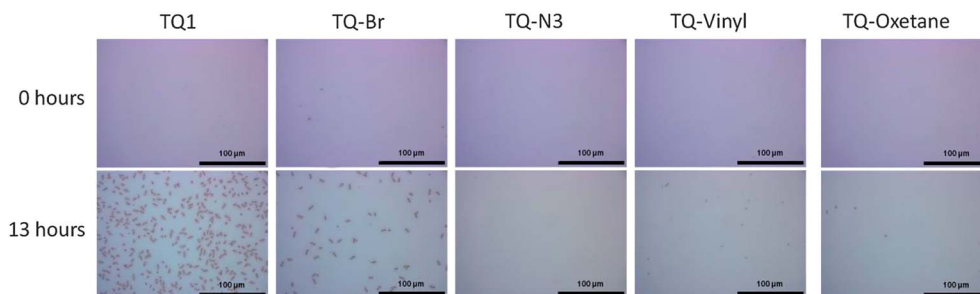


Fig. 4 Optical micrographs ($195 \times 260 \mu\text{m}^2$) of spin-coated thin films of the five polymers blended with PCBM (1 : 1 wt) before (0 hours) and after annealing at $150 \text{ }^\circ\text{C}$ for 13 hours. All the thin films have been irradiated with UV light at 254 nm for 10 minutes before recording images. The dark areas correspond to PCBM rich domains.

Dark thermal degradation in an ambient atmosphere. One of the tests that has been used to prove the increased stability of devices with cross-linked active layers is thermal annealing with intermittent testing under illumination. This test brings out the degradation due to thermally induced morphology changes such as growth of PCBM domains. Devices with an inverted type geometry (ITO/ZnO/active layer/PEDOT/Ag) were prepared for each of the five polymers and subjected to thermal annealing at $100 \text{ }^\circ\text{C}$ for 50 hours. At intervals the *IV* curves of the devices were measured under illumination ($AM1.5G$, 1000 W m^{-2}). As seen in Fig. 3 the devices with TQ-N₃ and TQ-Oxetane degraded to a lesser degree and stabilized at a higher power conversion level than TQ1, TQ-Vinyl and TQ-Br.

The active layer of these devices was further investigated by optical microscopy and atomic force microscopy (AFM) (the AFM images are available in the ESI†). Each blend was imaged before and after annealing at $150 \text{ }^\circ\text{C}$ for 13 hours (see Fig. 4). As expected, large PCBM crystallites formed in the TQ1:PCBM film similar to what has been observed for annealing of P3HT:PCBM.^{4,5} Blends containing TQ-Vinyl, TQ-N₃ and TQ-Oxetane showed either none or only very little phase segregation while the blend containing TQ-Br showed some phase segregation but not to the extent seen for TQ1:PCBM. This confirms that the cross-linking has taken place for all the polymers with incorporated functional groups and that the cross-linking stabilizes the morphology of the BHJ layer towards thermal annealing as has been reported earlier.^{11–16}

Constant illumination in ambient atmosphere versus inert atmosphere. Dark thermal degradation reduces the effect of illumination so it is also obvious to investigate device degradation under constant illumination. The results from a study carried out in the ambient atmosphere are shown in Fig. 5a where a similar exponential decay over 17 hours from a maximum to almost no residual efficiency is observed. The cross-linking does not seem to infer any added stability in this case indicating that the dominant degradation mode in this test is photochemical. This observation is consistent with the outcome of the photochemical degradation experiments performed on the pure polymer films that were also unaffected by the cross-linking.

When this study was repeated under inert atmosphere (Fig. 5b), however, the overall rate of degradation was retarded and some differences between the polymers became apparent. A fast initial decay in the performance was once again observed,

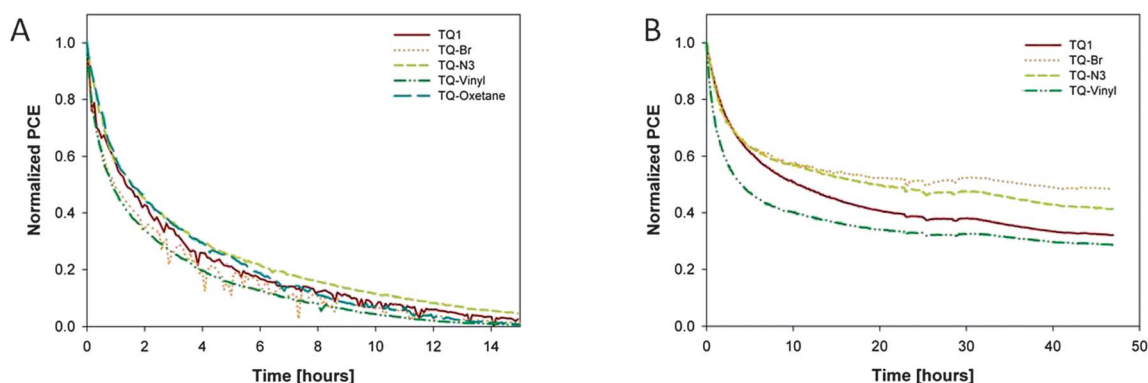


Fig. 5 Deterioration of the power conversion efficiencies of the devices under constant illumination in (A) ambient atmosphere, and in (B) inert atmosphere (normalized).

which could be due to the fact that the devices were fabricated under ambient conditions, which means that they contained a residual amount of oxygen–water. After about 5 hours the decay rate slowed and clear differences in the performance between the different polymers were observed in the order: **TQ-Br** > **TQ-N₃** > **TQ1** > **TQ-Vinyl**.

Conclusions

This study has shown that different types of cross-linking moieties can be incorporated into the side chains of the low band gap **TQ1** type polymer by relatively simple means. The cross-linking reaction could be achieved by UV-irradiation of the pure polymer films to give insoluble products. When PCBM was included the cross-linking was less efficient presumably due to the optical absorption band of PCBM. Some solvent resistance was however observed in this case indicating some degree of cross-linking.

The UV-vis spectra of the polymer films were not affected proving that the cross-linking reaction did not damage the conjugated backbone of the polymers even though widely different reaction types are expected for the four different types of side chain functionalities: bromide, azide, vinyl and oxetane.

Cross-linking was shown to inhibit excessive phase separation and growth of PCBM crystallites in polymer:PCBM films during dark thermal annealing as shown by optical microscopy. This resulted in improved solar cell device stability under the conditions in question. It did, however, not improve the device stability under constant illumination in an ambient atmosphere, which is probably dominated by photochemical degradation rather than by thermal mechanisms. When oxygen–water was excluded by employing an inert atmosphere the stability increased somewhat and more importantly, some differences in stability became apparent between the polymers with **TQ-Br** and **TQ-N₃** giving the most stable devices. At present no explanation is provided for this observed difference, but it could be ascribed to different cross-linking mechanisms and also to different reaction rates.

This study shows that cross-linking can improve morphological stability, but that other factors such as photochemical degradation might be more important for device stability under constant illumination conditions.

Acknowledgements

This work has been supported by the Danish Strategic Research Council (2104-07-0022), EUDP (j.no. 64009-0050 and 64011-0002), the Danish National Research Foundation, and from PVERA-NET (project acronym POLYSTAR).

Notes and references

- 1 T. Chu, J. Lu, S. Beaupré, Y. Zhang, J. Pouliot, S. Wakim, J. Zhou, M. Leclerc, Z. Li, J. Ding and Y. Tao, *J. Am. Chem. Soc.*, 2011, **133**, 4250.
- 2 H. Chen, J. Hou, S. Zhang, Y. Liang, G. Yang, Y. Yang, L. Yu, Y. Wu and G. Li, *Nat. Photonics*, 2009, **3**, 649.
- 3 M. Jørgensen, K. Norrman, S. A. Gevorgyan, T. Tromholt, B. Andreasen and F. C. Krebs, *Adv. Mater.*, 2012, **24**, 580.
- 4 S. Bertho, G. Janssen, T. J. Cleij, B. Conings, W. Moons, A. Gadisa, J. D'Haen, E. Goovaerts, L. Lutsen, J. Manca and D. Vanderzande, *Sol. Energy Mater. Sol. Cells*, 2008, **92**, 753.
- 5 M. Drees, H. Hoppe, C. Winder, H. Neugebauer, N. S. Sariciftci, W. Schwinger, F. Schäßler, C. Topf, M. C. Scharber, Z. Zhu and R. Gaudiana, *J. Mater. Chem.*, 2005, **15**, 5158.
- 6 P. D. Topham, A. J. Parnell and R. C. Hiorns, *J. Polym. Sci., Part B: Polym. Phys.*, 2011, **49**, 1131.
- 7 G. Ren, P.-T. Wu and S. A. Jenekhe, *Chem. Mater.*, 2010, **22**, 2020.
- 8 E. J. W. Crossland, M. Kamperman, M. Nedelcu, C. Ducati, U. Wiesner, D. M. Smilgies, G. E. S. Toombs, M. A. Hillmyer, S. Ludwigs, U. Steiner and H. J. Snaith, *Nano Lett.*, 2009, **9**, 2807.
- 9 J. Liu, E. N. Kadnikova, Y. Liu, M. D. McGehee and J. M. J. Fréchet, *J. Am. Chem. Soc.*, 2004, **126**, 9486.
- 10 J. Farinhas, Q. Ferreira, R. E. Di Paolo, L. Alcácer, J. Morgado and A. Charas, *J. Mater. Chem.*, 2011, **21**, 12511.
- 11 B. J. Kim, Y. Miyamoto, B. Ma and J. M. J. Fréchet, *Adv. Funct. Mater.*, 2009, **19**, 2273.
- 12 G. Griffini, J. D. Douglas, C. Piliago, T. W. Holcombe, S. Turri, J. M. J. Fréchet and J. L. Mynar, *Adv. Mater.*, 2011, **23**, 1660.
- 13 B. Gholamkhash and S. Holdercroft, *Chem. Mater.*, 2010, **22**, 5371.
- 14 H. J. Kim, A. R. Han, C. H. Cho, H. Kang, H. H. Cho, M. Y. Lee, J. M. J. Fréchet, J. H. Oh and B. J. Kim, *Chem. Mater.*, 2012, **24**, 215.
- 15 C. Y. Nam, Y. Qin, Y. S. Park, H. Hlaing, X. Lu, B. M. Ocko, C. T. Black and R. B. Grubbs, *Macromolecules*, 2012, **45**, 2338.
- 16 C. H. Hsieh, Y. J. Cheng, P. J. Li, C. H. Chen, M. Dubosc, R. M. Liang and C. S. Hsu, *J. Am. Chem. Soc.*, 2010, **132**, 4887.
- 17 U. R. Lee, T. W. Lee, M. H. Hoang, N. S. Kang, J. W. Yu, K. H. Kim, K. G. Lim, T. W. Lee, J. I. Jin and D. H. Choi, *Org. Electron.*, 2011, **12**, 269.
- 18 T. Yamamoto, B. L. Lee, H. Kokubo, H. Kishida, K. Hirota, T. Wakabayashi and H. Okamoto, *Macromol. Rapid Commun.*, 2003, **24**, 440.
- 19 E. Wang, L. Hou, Z. Wang, S. Hellström, F. Zhang, O. Inganäs and M. R. Andersson, *Adv. Mater.*, 2010, **22**, 5240.
- 20 M. Helgesen, S. A. Gevorgyan, F. C. Krebs and R. A. J. Janssen, *Chem. Mater.*, 2009, **21**, 4669.

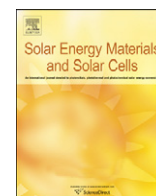
- 21 W. J. E. Beek, M. M. Wienk, M. Kemerink, X. Yang and R. A. J. Janssen, *J. Phys. Chem. B*, 2005, **109**, 9505.
- 22 T. Tromholt, M. V. Madsen, J. E. Carlé, M. Helgesen and F. C. Krebs, *J. Mater. Chem.*, 2012, **22**, 7592.
- 23 K. S. Lee, K. Y. Yeon, K. H. Jung and S. K. Kim, *J. Phys. Chem. A*, 2008, **112**, 9312.
- 24 R. F. Klima and A. D. Gudmundsdóttir, *J. Photochem. Photobiol., A*, 2004, **162**, 239.
- 25 K. A. Murray, A. B. Holmes, S. C. Moratti and G. Rumbles, *J. Mater. Chem.*, 1999, **9**, 2109.
- 26 N. Yasuda, S. Yamamoto, Y. Wada and S. Yanagida, *J. Polym. Sci., Part A: Polym. Chem.*, 2001, **39**, 4196.
- 27 S. Feser and K. Meerholz, *Chem. Mater.*, 2011, **23**, 5001.
- 28 M. Manceau, E. Bundgaard, J. E. Carlé, O. Hagemann, M. Helgesen, R. Søndergaard, M. Jørgensen and F. C. Krebs, *J. Mater. Chem.*, 2011, **21**, 4132.



ELSEVIER

Contents lists available at [SciVerse ScienceDirect](http://www.sciencedirect.com)

Solar Energy Materials & Solar Cells

journal homepage: www.elsevier.com/locate/solmat

Simultaneous multilayer formation of the polymer solar cell stack using roll-to-roll double slot-die coating from water

Thue T. Larsen-Olsen, Birgitta Andreasen, Thomas R. Andersen, Arvid P.L. Böttiger, Eva Bundgaard, Kion Norrman, Jens W. Andreasen, Mikkel Jørgensen, Frederik C. Krebs*

Risø National Laboratory for Sustainable Energy, Technical University of Denmark, Frederiksborgvej 399, DK-4000 Roskilde, Denmark

ARTICLE INFO

Available online 23 September 2011

Keywords:

Double slot-die coating
Organic solar cells
Roll-to-roll coating polymer solar cells
Simultaneous multilayer formation
Slot-die coating

ABSTRACT

Double slot-die coating using aqueous inks was employed for the simultaneous coating of the active layer and the hole transport layer (HTL) in fully roll-to-roll (R2R) processed polymer solar cells. The double layer film was coated directly onto an electron transport layer (ETL) comprising doped zinc oxide that was processed by single slot-die coating from water. The active layer comprised poly-3-hexylthiophene:Phenyl-C₆₁-butyric acid methyl ester (P3HT:PCBM) as a dispersion of nanoparticles with a radius of 46 nm in water characterized using small-angle X-ray scattering (SAXS), transmission electron microscopy (TEM), and atomic force microscopy (AFM). The HTL was a dispersion of poly(3,4-ethylenedioxythiophene) poly(styrenesulfonate) (PEDOT:PSS) in water. The films were analyzed using time-of-flight secondary ion mass spectrometry (TOF-SIMS) as chemical probe and X-ray reflectometry as physical probe, confirming the identity of the layered structure. The devices were completed with a back electrode of either Cu tape or evaporated Ag. Under standard solar spectrum irradiation (AM1.5G), current–voltage characterization (*J*–*V*) yielded an open-circuit voltage (V_{oc}), short-circuit current (J_{sc}), fill factor (*FF*), and power conversion efficiency (*PCE*) of 0.24 V, 0.5 mA cm^{−2}, 25%, and 0.03%, respectively, for the best double slot-die coated cell. A single slot-die coated cell using the same aqueous inks and device architecture yielded a V_{oc} , J_{sc} , *FF*, and *PCE* of 0.45 V, 1.95 mA cm^{−2}, 33.1%, and 0.29%, respectively.

© 2011 Elsevier B.V. All rights reserved.

1. Introduction

Flexible polymer solar cells can be manufactured by roll-to-roll (R2R) processes, which are inherently faster than batch processing of solar cells [1]. The manufacture of polymer solar cells using R2R processing has been reported demonstrating high speed of manufacture even on a small scale [2–4]. Thus, polymer solar cell modules with the size of an A4 sheet of paper have total processing times in the range of one minute (45–90 s) [3]. This period of time is from the moment the fresh carrier substrate enters the process until the completed, encapsulated, and tested polymer solar cell module exits the process as a finished product. It is impossible to envisage such throughput speeds with any process that handles the solar cell as a discrete unit. The above example employed relatively simple R2R processing equipment and low web speeds in the range of 0.3–2 m min^{−1} processing one layer at a time by subsequent single passes through the machinery. In order to improve throughput speed there are a few

routes, which can be followed. One obvious route is to increase the processing speed, which puts significant requirements on the drying equipment. The faster the web speed, the larger and more complex the ovens and driers become. Another option is to make an inline printing and coating machine where the same web passes through several printing stations with each station representing each layer in the solar cell stack. This method has the advantage of minimizing handling damage of the web. The method does put some constraints on the chosen printing and coating methods as they all have to operate in the same window of web speed and the final web speed will be determined by the slowest process. A final route is the simultaneous formation of several layers of the solar cells stack. This method is in many ways ideal as it lowers the number of passages through the processing equipment thus lowering the handling damage, increases the processing speed significantly without increasing the web speed and thus does not necessarily require more complex drying technology. In addition, there are advantages in the context of life cycle analysis and the method provides a path to a reduction of the energy payback time (EPBT) by significantly reducing the direct process energy involved in the manufacture [5]. The approach also introduces a massive challenge in

* Corresponding author. Tel.: +45 46 77 47 99.

E-mail address: frkr@risoe.dtu.dk (F.C. Krebs).

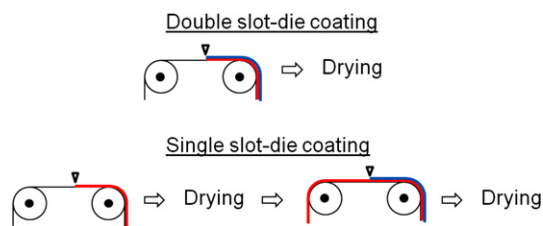


Fig. 1. Illustration of the double slot-die coating of the active layer (red) and the HTL (blue) in a R2R process, compared to the equivalent process using single slot-die coating. (For interpretation of the references to color in this figure legend, the reader is referred to the web version of this article).

the ink formulation for the layers that are coated simultaneously as the formation and drying of a wet multilayer film is highly complex. The successful application of the technique is however rewarding in terms of processing speed and simplicity, see Fig. 1.

In this work we demonstrate the simultaneous formation of two of the layers in the polymer solar cell stack by double slot-die coating of the active layer and the hole transporting layer (HTL) from aqueous dispersions. We describe the ink formulation and the required steps to efficiently design inks that give stable bilayer structures in the wet film and during drying.

2. Experimental

2.1. Materials

P3HT (Sepiolid P-200 from BASF) was employed as the donor polymer and technical grade PCBM was employed as the acceptor material (Solenne BV). An aqueous precursor solution for the ZnO was prepared as described earlier [6] and comprised $\text{Zn}(\text{OAc})_2 \cdot 2\text{H}_2\text{O}$ (100 mg mL^{-1}), $\text{Al}(\text{OH})(\text{OAc})_2$ (2 mg mL^{-1}), and the non-ionic fluorosurfactant (FSO-100) (2 mg mL^{-1}) in water. PEDOT:PSS was based on an aqueous dispersion (2:1 w/w) of Orgacon EL-P 5010 from Agfa that was used directly as received. The electrode material was either Cu tape or evaporated silver. The substrate was a $130 \mu\text{m}$ poly(ethylene terephthalate) (PET) substrate with a patterned ITO layer (nominally $60 \Omega \text{ square}^{-1}$) (acquired from IST).

2.2. Nanoparticle preparation and ink

P3HT (4 g, Sepiolid P200, BASF) and PCBM (4 g, 99%, Solenne B.V.) were dissolved in chloroform (268 g, Spectrophotometric grade, Sigma-Aldrich) and mixed with an aqueous 100 mM sodium dodecyl sulfate (SDS) solution (480 mL) (99%, Sigma-Aldrich) in a large beaker. The mixture was stirred vigorously for one hour and then subjected to ultrasound (0.9 kW) for 6.5 min using an UIP 1000 hd transducer from Hielscher ultrasound technology fitted with a booster head. The mixture was then stirred on a hot plate at 65°C for three hours until all the chloroform had evaporated. The aqueous dispersion was dialyzed to remove SDS using a Millipore system with a capacity of 500 mL. The mixture was concentrated by dialysis from a volume of 500 mL to a volume of 100 mL with a forward pressure of 1.4 bar and a pressure gradient across the filter of 0.7 bar. Pure water (400 mL) was then added and the procedure was repeated 4 times corresponding to a dilution of the solution by a factor of 625. In the final step the suspension were concentrated to have a solid content of 60 mg mL^{-1} . FSO-100 was added to the dialyzed aqueous suspension of the P3HT:PCBM nanoparticles. The concentration of fluorosurfactant was 5 mg mL^{-1} and the P3HT:PCBM concentration was 60 mg mL^{-1} . This solution was employed directly for slot-die coating.

2.3. TOF-SIMS

Depth profiling analysis was performed using a TOF-SIMS IV (ION-TOF GmbH, Münster, Germany). 25-ns pulses of 25-keV Bi^+ (primary ions) were bunched to form ion packets with a nominal temporal extent of $< 0.9 \text{ ns}$ at a repetition rate of 10 kHz yielding a target current of 1 pA. Depth profiling was performed using an analysis area of $100 \times 100 \mu\text{m}^2$ and a sputter area of $300 \times 300 \mu\text{m}^2$. 30 nA of 3-keV Xe^+ was used as sputter ions. Electron bombardment (20 eV) was used to minimize charge build-up at the surface. Desorbed secondary ions were accelerated to 2 keV, mass analyzed in the flight tube, and post-accelerated to 10 keV before detection.

2.4. SAXS

The X-ray source for the SAXS measurements was a Cu rotating anode (Rigaku H3R), collimated and monochromatized by 2D multilayer optics (K_α radiation, $\lambda = 1.5418 \text{ \AA}$). The anode was operated in fine focus mode at 46 kV/46 mA and the beam diameter was collimated by 3 pinholes to 1.0 mm diameter at the sample position. An $18 \times 18 \text{ cm}^2$ 2D position sensitive gas detector was used for collecting the scattering data, and a 4 mm beamstop was placed in front of the gas detector, situated 4579 mm from the sample.

2.5. Reflectometry

The reflectometry measurement was made on setup with a rotating Cu-anode (Rigaku RU-200) operated at 50 kV/200 mA as X-ray source, focused and monochromatized by a 1D multilayer optic (K_α radiation, $\lambda = 1.5418 \text{ \AA}$).

2.6. AFM

The P3HT:PCBM nanoparticle dispersion was spin-coated on a glass substrate. The AFM imaging was performed on an N8 Neos (Bruker Nano GmbH, Herzogenrath, Germany) operating in an intermittent contact mode using PPP-NCLR cantilevers (NANO-SENSORS, Neuchatel, Switzerland). The images were recorded at a scan speed of 0.8 lines s^{-1} .

2.7. Substrate preparation

A PET substrate with an ITO pattern was prepared and cleaned as described earlier [2]. The ZnO solution was microfiltered immediately prior to use (filter pore size of $0.45 \mu\text{m}$) and then slot-die coated at a speed of 2 m min^{-1} with a wet thickness of $4.9 \mu\text{m}$. After the initial drying of the precursor film it was converted into an insoluble film by passage through an oven at a temperature of 140°C with a speed of 0.2 m min^{-1} (oven length = 4 m). This gave an insoluble doped zinc oxide film with a thickness of $25 \pm 5 \text{ nm}$.

2.8. Double slot-die coating

The web was forwarded at a speed of 1 m min^{-1} when the aqueous P3HT:PCBM nanoparticle dispersion was pumped into the first chamber of a double slot-die coating head. The aqueous PEDOT:PSS dispersion was pumped into the second chamber of the double slot-die coating head. The double film was then slot-die coated at a nominal wet thickness of $23 \mu\text{m}$ for both the P3HT:PCBM film and the PEDOT:PSS dispersion. The slot-die coating head and the coating roller had temperatures of 60°C and 80°C , respectively. The temperature of the foil was kept at

80 °C until it reached the oven at 140 °C. The distance from the point of coating to the oven entry was 18 cm.

2.9. Device characterization

The devices were placed under simulated sunlight in a solar simulator with the following specifications: 1000 W m⁻², AM1.5G, 85 ± 2 °C, and 45 ± 5% relative humidity. The *J*-*V* curves were measured here were carried out at 85 °C by scanning both forwards and backwards in steps of 20 mV ensuring that no hysteresis was present. The scanning speed was 0.1 V s⁻¹.

3. Results and discussion

The simultaneous multilayer formation by roll coating methods has been achieved with only a few techniques such as curtain coating, slide coating, and slot-die coating [1]. The two former are only operational in the very high speed regime (typically > 4 m s⁻¹) and require relatively viscous solutions. In return, they offer the simultaneous formation of many layers. Slot-die coating has been explored for multilayer film formation with up to three layers (in triple slot-die coating) or in combination with the slide coating technique in slot-slide coating. In the context of polymer solar cells the simultaneous multilayer formation has not been reported so far.

There are many good reasons for double slot-die coating not having been employed for polymer solar cells. Firstly, the multilayer formation requires that the same solvent is used for the coated layers and that the layer coated first has the highest surface tension. Secondly, the drying has to be sufficiently fast to minimize diffusion of solutes between the layers. For a bilayer film with a total wet thickness of 100 μm, diffusion of solutes such as small molecules and ions are exceptionally fast unless the viscosity is high. In our case we employ water and the viscosity of the solutions are low (< 25 mPa s) implying that it would be difficult to prevent interlayer diffusion. The mean displacement for a molecule such as phenyl-C₆₁-butyric acid methyl ester (PCBM) is on the order of 30 μm s⁻¹ and with wet thicknesses on the order of ≪ 100 μm this would imply that drying should be completed on timescales much faster than a second to avoid complete interlayer mixing by diffusion. We estimated the diffusion lengths using the Einstein equation [7] where we have the diffusion constant and mean displacement, as follows:

$$D = \frac{k_B T}{6\pi\eta r}, \lambda_{1d} = \sqrt{2Dt}.$$

here k_B is boltzman's constant, T is absolute temperature, η is the viscosity (of the ink), r is the particle radius, and t is time. Eliminating D , we get the following mean displacement, during 1 s diffusion, for a C₆₀ molecule (taken to be similar to PCBM) at 80 °C:

$$\lambda_{C60} = \sqrt{\frac{k_B}{3\pi} \times \frac{1 \text{ s} \times 353 \text{ K}}{1 \text{ mPa s} \times 0.5 \text{ nm}}} = 3.22 \times 10^{-5} \text{ m}.$$

For $r = 50 \text{ nm}$ particle

$$\lambda_{np} = \sqrt{\frac{k_B}{3\pi} \times \frac{1 \text{ s} \times 353 \text{ K}}{1 \text{ mPa s} \times 50 \text{ nm}}} = 3.22 \times 10^{-6} \text{ m}.$$

here we have assumed a constant viscosity of 1 mPa s, which should be considered a conservative estimate, as it is likely to be higher and will increase as the drying proceeds. In our case, the inks P3HT:PCBM, and poly(3,4-ethylenedioxythiophene):poly(styrenesulfonate) (P3HT:PCBM and PEDOT:PSS) are both aqueous dispersions of large aggregates with average sizes 50–100 times larger than the PCBM molecule, hence interlayer mixing due to

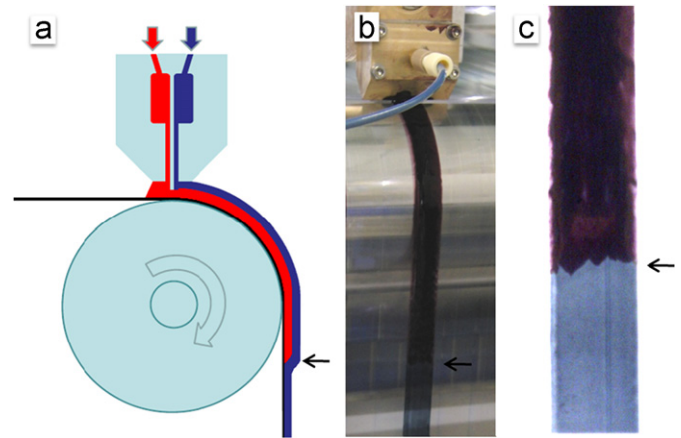


Fig. 2. Double slot-die coating experiment at an instance where the film changes appearance going from a single layer of PEDOT:PSS (blue) to a simultaneous coating of P3HT:PCBM (red) and PEDOT:PSS. The transition is marked by the arrows going from (a) a schematic of the experimental situation, to (b) a photograph of the experiment, and to (c) a close-up photograph of the same foil piece, taken after the coating experiment. (For interpretation of the references to color in this figure legend, the reader is referred to the web version of this article.)

diffusion of the particles between the two layers would be 1–2 orders of magnitude slower, thus enabling drying without detrimental interlayer mixing. At the same time a limited amount of interdiffusion should be advantageous as it gives a diffusive interface between the coated layers with much higher adhesion, possibly lowering device degradation due to layer delamination. Experience gained from the actual coating experiments suggests that the process is very parameter sensitive. However, a stable operation regime was found and a very illustrative example of the simultaneous bilayer formation from the coating experiment is shown in Fig. 2, where it was possible to turn on and off the flow of one of the inks, thus revealing a sharp transition from single- to bilayer.

3.1. Nanoparticle characterization

3.1.1. X-ray scattering

The aqueous ink was studied by small angle X-ray scattering (SAXS) in order to determine the size of the particles. The ink was placed in 1 mm capillaries and sealed with epoxy glue, and the data were analyzed using the Bayesian Indirect Fourier Transform [8]. The average particle radius was found to be 46 nm, see Fig. 3.

3.1.2. Microscopy

The drop-cast and spin-coated samples of the nanoparticles were imaged using transmission electron microscopy (TEM) (Fig. 3b) and atomic force microscopy (AFM) (Fig. 3c), respectively. The image documented that spherical nanoparticles had formed.

3.2. Bilayer characterization

3.2.1. Time-of-flight secondary ion mass spectrometry (TOF-SIMS) depth profiling analysis

The obvious concern when performing double slot-die coating is whether the expected bilayer is formed, or whether complete mixing of the layers had occurred. An experiment was designed to resolve this issue. A piece of double slot-die coated sample was submerged in a sodium hydroxide solution in order to facilitate delamination (Fig. 4b). After a while a discrete PEDOT:PSS film simply floated off the top of the surface leaving a P3HT:PCBM film

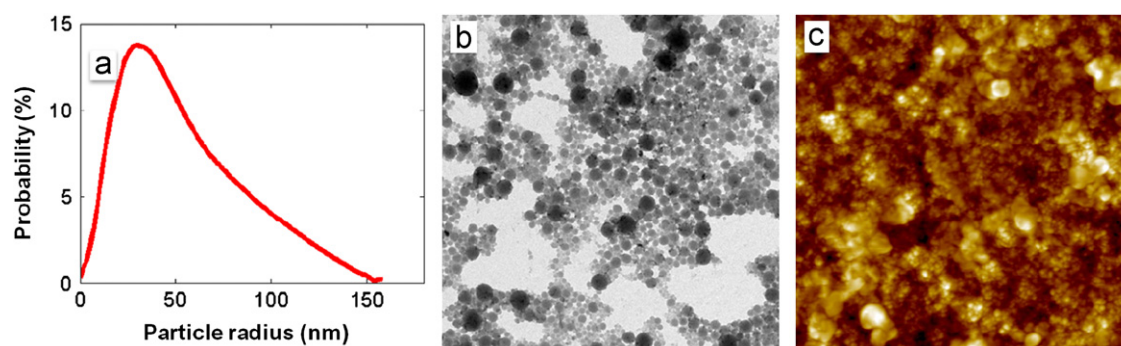


Fig. 3. (a) Volume weighted size distribution of the nanoparticles calculated from the SAXS measurement. (b) TEM image ($5 \times 5 \mu\text{m}^2$) of a drop-cast sample. (c) AFM image ($5 \times 5 \mu\text{m}^2$) of a spin-coated sample.

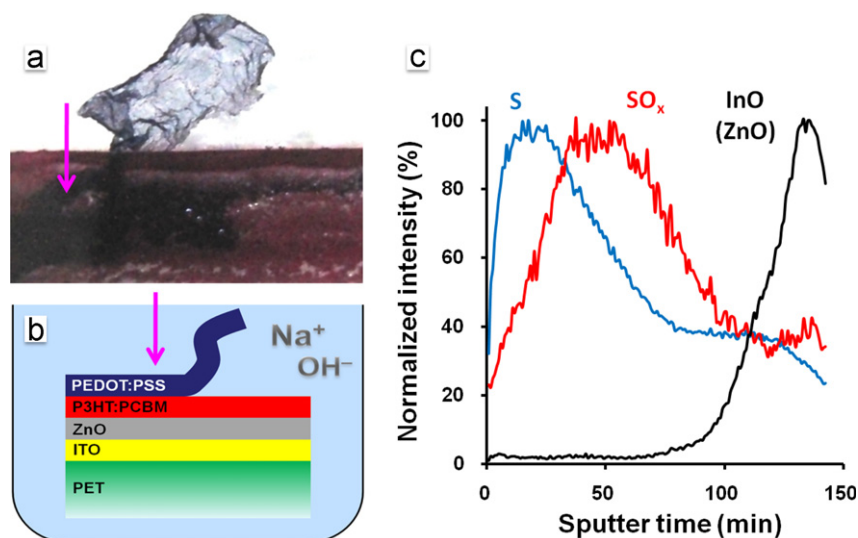


Fig. 4. (a) Photograph showing a $18 \times 7 \text{ mm}^2$ film section delaminated from the double slot-die coated film in NaOH (aq). (b) Schematic of the submerged sample showing the surface location (purple arrow) for the TOF-SIMS depth profiling analysis. (c) TOF-SIMS depth profiles in negative ion mode confirming that the double slot-die coated film has formed a bilayer. The ZnO layer was so thin that the resulting profile was too noisy, so it was left out for clarity. The noisy ZnO profile is superimposed (due to the thin nature of the film) on the InO⁻ profile.

on the substrate surface (Fig. 4a). This is clear visual evidence that the double slot-die coating experiment yields a discrete bilayer film. The observations were confirmed by chemical analysis using TOF-SIMS.

TOF-SIMS depth profiling was in addition employed to support the observation and to further document that a bilayer had indeed formed during the double slot-die coating process. Fig. 4a–b shows the surface location where the depth profiling analysis was carried out. Several factors complicate the depth profiling analysis: (i) the sputter depth resolution (under the conditions in question) in soft materials is very poor (compared to hard materials, e.g. metals), and (ii) depth profiles are typically based on unique mass spectral markers that consist of molecular fragment ions or atomic ions, but no unique mass spectral markers are formed under the given experimental conditions. However, due to the fact that equivalent mass spectral markers originating from different molecular environments will produce a different signal response, the different materials may still be uniquely resolved. It turns out that the signal intensities for the S⁻ and SO_x⁻ fragment ions (formed in both layers) are extremely dependent on their origin. S⁻ is intense in PEDOT:PSS and relatively weak in P3HT:PCBM whereas SO_x⁻ exhibits the opposite behavior. Fig. 4c shows the depth profiles using S⁻ and SO_x⁻ as mass spectral markers. In spite of the complicated experimental conditions it was still possible to confirm that a bilayer was formed during the double slot-die coating process. In addition, a

depth profile was acquired at a surface location where delamination had occurred that showed the presence of the expected one layer (see Fig. S1 in supporting information). Due to the aforementioned factors affecting the analysis it is not possible to conclude anything about the extent of interlayer mixing that was a consequence of the coating process. From the delamination experiment shown in Fig. 4 we however assume that the interface is discrete when viewed on the scale of the film thickness and probably resembles the roughness that an individual film of the P3HT:PCBM nanoparticles would.

3.2.2. Reflectometry

The coated films were studied with reflectometry in order to determine whether the two double slot-die coated liquids had mixed. Two samples were measured, a double slot-die coated PEDOT:PSS/P3HT:PCBM bilayer and a single slot-die coated PEDOT:PSS layer, both on a ZnO/ITO/PET substrate. The top layer of the two samples showed the critical angle for total reflection at the same position corresponding to the same electron density for the top layer in both preparations, see Fig. 5.

3.3. Device performance

The *J*–*V* characteristics of the freshly prepared solar cells are shown in Fig. 6 together with a reference device, also processed using the aqueous P3HT:PCBM nanoparticle ink as active layer

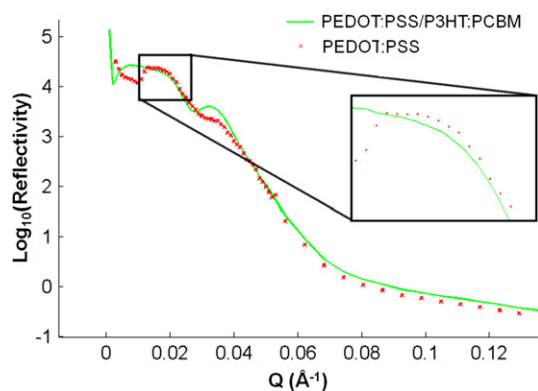


Fig. 5. Reflected intensity for two coated samples. One with PEDOT:PSS and one double slot-die coated PEDOT:PSS/P3HT:PCBM bilayer. The critical angle (θ_c) for total reflection is at 0.176° for both films corresponding to a scattering vector Q_c of 0.025 \AA^{-1} ($Q = 4 \pi \sin \theta / \lambda$, $\lambda = 1.5418 \text{ \AA}$).

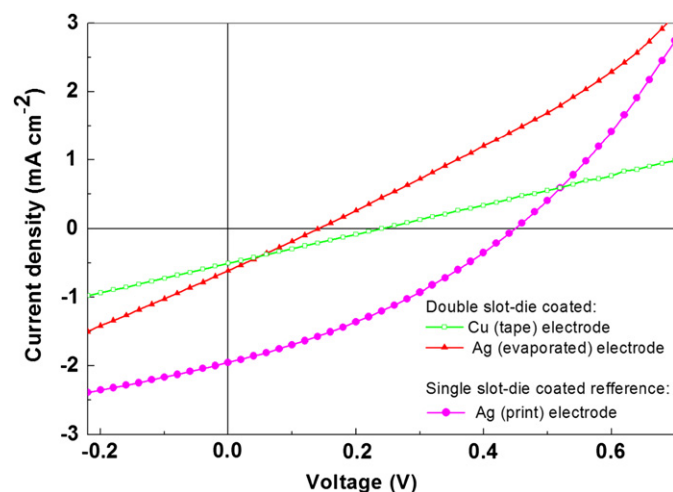


Fig. 6. J - V curves of the double slot-die coated devices shown in comparison with a device of similar layer structure processed by standard single slot-die coating.

Table 1
Summary of the J - V characterization.

Cell ID	PCE (%)	J_{sc} (mA cm^{-2})	V_{oc} (V)	FF (%)
Double slot-die (Cu tape)	0.03	0.5	0.24	25.0
(Ag evaporated)	0.02	0.61	0.14	25.6
Single slot-die	0.29	1.95	0.45	33.1

and PEDOT:PSS as HTL, but prepared by two sequential single slot-die coating steps (i.e. one layer at the time). The use of this nanoparticle ink constitutes a unique route for aqueous processing of large area low band gap polymer solar cells recently demonstrated by our group [9]. The extracted photovoltaic parameters are summarized in Table 1. As is evident the photovoltaic response is significantly lower for the double slot-die coated devices compared to the reference device with respect to all photovoltaic parameters. One notable feature is the linearity of the J - V curves within the active quadrant (FF of 25%), which suggests that the operation of the cells is dominated by the internal resistances in the devices, i.e. a low shunt resistance and a high series resistance. A low shunt resistance can be ascribed to two possible effects: (1) from the complex dynamic nature of the simultaneous bilayer formation, as it is likely that PEDOT:PSS forms percolation paths through the active layer during formation, which, in turn, will short the device. (2) It could also be

linked to the known photoinduced defects in ZnO as reported recently [10].

Furthermore, the devices having the evaporated Ag electrode display the lowest shunt resistances and consequently lowest V_{oc} , probably due to shunts being formed during evaporation, while the Cu-tape avoids shunts by preferentially contacting the top-most part of the bilayer film, suggesting a somewhat inhomogeneous film. However, the higher series resistance for the devices utilizing a Cu-tape electrode hints to a large contact resistance at the PEDOT:PSS/Cu interface.

We also constructed the reference (blank) devices comprising ITO/ZnO/P3HT:PCBM/Cu-tape, and ITO/ZnO/PEDOT:PSS/Cu-tape, where ITO is indium tin oxide. The corresponding J - V curves under standard illumination conditions revealed no photovoltaic response thus documenting the photovoltaic properties of double slot-die coated films. The relatively poor performance of the double slot-die coated devices possibly also has its roots in the large areas we explore (several cm^2) compared to relative film inhomogeneity for the double slot-die coated films. Also the shunts might be located at the edges as is evident from the photograph in Fig. 4a where the PEDOT:PSS has the possibility to overspill the undercoat of P3HT:PCBM and thus short circuit the device. By further tuning the coating conditions, surface tensions for the inks and substrate surface energies it should be possible to minimize these effects.

4. Conclusions

We have successfully demonstrated double slot-die coated polymer solar cells processed roll-to-roll, using two aqueous inks for the simultaneous formation of both the active layer (P3HT:PCBM) and hole transporting layer (PEDOT:PSS). The devices performed relatively poor compared to similar devices processed by single slot-die coating. This is ascribed to far from perfect layer separation due to the complex nature of the bilayer formation process; resulting in shunts and low current extraction efficiencies. This convincingly demonstrates a possible route for lowering the energy payback time of polymer solar cells, which is an important factor in a possible future scenario of large scale energy production.

Acknowledgements

This work was supported by the Danish National Research Foundation. We also thank Dr. T. Kasama at DTU Center for Electron Nanoscopy for TEM measurements.

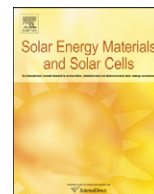
Appendix A. Supporting information

Supplementary data associated with this article can be found in the online version at doi:10.1016/j.solmat.2011.08.026.

References

- [1] F.C. Krebs, Fabrication and processing of polymer solar cells. A review of printing and coating techniques, *Solar Energy Materials and Solar Cells* 93 (2009) 394–412.
- [2] F.C. Krebs, T. Tromholt, M. Jørgensen, Upscaling of polymer solar cell fabrication using full roll-to-roll processing, *Nanoscale* 2 (2010) 873–886.
- [3] F.C. Krebs, T.D. Nielsen, J. Fyenbo, M. Wadstrøm, M.S. Pedersen, Manufacture, integration and demonstration of polymer solar cells in a lamp for the Lighting Africa initiative, *Energy & Environmental Science* 3 (2010) 512–525.
- [4] F.C. Krebs, J. Fyenbo, M. Jørgensen, Product integration of compact roll-to-roll processed polymer solar cell modules: methods and manufacture using flexographic printing, slot-die coating and rotary screen printing, *Journal of Materials Chemistry* 20 (2010) 8994–9001.

- [5] N. Espinosa, R. García-Valverde, A. Urbina, F.C. Krebs, A life cycle analysis of polymer solar cell modules prepared using roll-to-roll methods under ambient conditions, *Solar Energy Materials and Solar Cells* 95 (2010) 1293–1302.
- [6] R. Søndergaard, M. Helgesen, M. Jørgensen, F.C. Krebs, Fabrication of polymer solar cells using aqueous processing for all layers including the metal back electrode, *Advanced Energy Materials* 1 (2011) 68–71.
- [7] A. Einstein, On the motion of small particles suspended in liquids at rest required by the molecular-kinetic theory of heat, *Annalen Der Physik* 17 (1905) 549–560.
- [8] S. Hansen, Bayesian estimation of hyperparameters for indirect Fourier transformation in small-angle scattering, *Journal of Applied Crystallography* 33 (2000) 1415–1421.
- [9] T.R. Andersen, T.T. Larsen-Olsen, B. Andreasen, A.P.L. Böttiger, J.E. Carle, M. Helgesen, E. Bundgaard, K. Norrman, J.W. Andreasen, M. Jørgensen, F.C. Krebs, Aqueous processing of low-band-gap polymer solar cells using roll-to-roll methods, *ACS Nano* 5 (2011) 4188–4196.
- [10] A. Manor, E.A. Katz, T. Tromholt, F.C. Krebs, Electrical and photo-induced degradation of ZnO layers in organic photovoltaics, *Advanced Energy Materials* (2011) 836–843.



Roll-to-roll processed polymer tandem solar cells partially processed from water

Thue T. Larsen-Olsen, Thomas R. Andersen, Birgitta Andreasen, Arvid P.L. Böttiger, Eva Bundgaard, Kion Norrman, Jens W. Andreasen, Mikkel Jørgensen, Frederik C. Krebs*

Risø National Laboratory for Sustainable Energy, Technical University of Denmark, Frederiksborgvej 399, DK-4000 Roskilde, Denmark

ARTICLE INFO

Available online 21 September 2011

Keywords:

Roll-to-roll processing
Tandem solar cells
Polymer solar cells
Printing and coating
Aqueous processing

ABSTRACT

Large area polymer tandem solar cells completely processed using roll-to-roll (R2R) coating and printing techniques are demonstrated. A stable tandem structure was achieved by the use of orthogonal ink solvents for the coating of all layers, including both active layers. Processing solvents included water, alcohols and chlorobenzene. Open-circuit voltages close to the expected sum of sub cell voltages were achieved, while the overall efficiency of the tandem cells was found to be limited by the low yielding back cell, which was processed from water based ink. Many of the challenges associated with upscaling the multilayer tandem cells were identified giving valuable information for future experiments and development.

© 2011 Elsevier B.V. All rights reserved.

1. Introduction

The ultimate efficiency of polymer solar cells is inherently limited by the narrow absorption bands of the chromophores that constitute the photoactive layer of the solar cells. One obvious route to circumvent this is to stack several junctions having complementary absorption bands, thus increasing the spectral overlap of the solar cell and the terrestrial solar spectrum. The benefits of the tandem architecture over single junction cells have been thoroughly studied and reviewed [1–4], and within reasonable assumptions it has been found that a tandem architecture can increase the ultimate efficiency of polymer solar cells with 20–50%, where the highest increase is seen in the case where the single junction cells perform under their ultimate potential [1,2].

The most advantageous approach to polymer solar cell fabrication, with respect to application as an energy technology, is to allow for fast processing of all layers relying on as few coating/printing methods as possible using roll-to-roll (R2R) processing. With regards to tandem polymer solar cells the most obvious device is an all solution processed monolithic tandem cell where the sub cells are connected in series rather than parallel. This naturally presents some challenges in multilayer coating where the typical number of layers required in a tandem cell is around 6–8. All these layers (some of them very thin) have to be coated on top of each other without having subsequent coating steps adversely affecting already coated layers. The traditional laboratory approach to building up the stack is thus not expected to be easily scalable

since it often employs vacuum deposition of many of the layers and a rational choice in the order of application. With the boundary condition that all layers have to be processed in air without vacuum, using only solution based printing and coating techniques, it becomes very challenging to realize functional tandem structures. So far only one report has documented vacuum free solution processing of all layers, including the printed metal back electrode [5], while large stacks by solution processing (and vacuum deposited back electrodes) have been reported [6]. Most tandem solar cell reports today employ one or more vacuum coating steps.

In this report we demonstrate R2R processing of tandem polymer solar cells on flexible substrates and show that there are many challenges associated not only with solution processing of entire tandem solar cell stacks, but also with the transfer from laboratory scale batch processing on rigid substrates to a full R2R only process on flexible films.

2. Experimental section

2.1. Materials

Poly-3-hexylthiophene (P3HT) was commercially available and had an M_n of ~ 20000 Da and an $M_w \sim 40000$ Da. Phenyl- C_{61} -butyric acid methyl ester (PC[60]BM) had a purity of 99%. Poly-[thiophene-2,5-diyl-*alt*-(2,3-bis(3-octyloxyphenyl)quinoxaline-5,8-diyl)] (TQ-1) was synthesized according to the method described in the literature [7] and had an M_n of ~ 29000 Da and an $M_w \sim 89000$ Da.

The ink used for the front bulk heterojunction (BHJ) active layer comprised PC[60]BM as the acceptor material (18 mg mL^{-1}) and

* Corresponding author. Tel.: +45 46 77 47 99.
E-mail address: frkr@risoe.dtu.dk (F.C. Krebs).

P3HT as the donor polymer (22 mg mL^{-1}) dissolved in chlorobenzene. For the back BHJ active layer an aqueous ink [8] comprising an aqueous dispersion of nanoparticles consisting of the low band gap polymer TQ-1 (Fig. 1) and PC[60]BM prepared as described earlier [8]. An aqueous precursor solution for the zinc oxide (ZnO) used as electron transporting layer (ETL) was prepared as described earlier [9] and comprised $\text{Zn}(\text{OAc})_2 \cdot 2\text{H}_2\text{O}$ (100 mg mL^{-1}), $\text{Al}(\text{OH})(\text{OAc})_2$ (2 mg mL^{-1}) and FSO-100 (2 mg mL^{-1}) in water. Vanadium(V)oxide (V_2O_5) employed as hole transporting layer (HTL) was prepared by diluting a base solution of vanadium(V)-oxoisopropoxide with isopropanol to a concentration of 25 mg mL^{-1} , following recommendations of earlier studies [10,11]. Poly(3,4-ethylenedioxythiophene) poly(styrenesulfonate) (PEDOT:PSS) was based on Orgacon EL-P 5010 from Agfa diluted 2:1 (w:w) with isopropanol. The printable silver back electrode was PV410 from Dupont. The substrate was a 130 micron PET substrate with a patterned ITO layer (nominally $60 \Omega \text{ square}^{-1}$).

2.2. Slot-die coating

The bottom electron contact was prepared directly on the PET/ITO substrate, prepared and cleaned as described earlier [12]. The zinc oxide precursor solution was microfiltered immediately prior

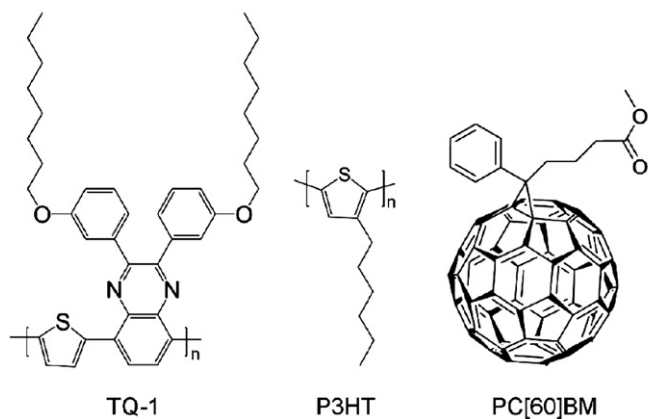


Fig. 1. Structure of poly-[thiophene-2,5-diyl-*alt*-(2,3-bis(3-octyloxyphenyl)quinoxaline-5,8-diyl)] (TQ-1), poly-3-hexylthiophene (P3HT), and phenyl- C_{60} -butyric acid methyl ester (PC[60]BM).

to use (filter pore size of $0.45 \mu\text{m}$) and then slot-die coated at a speed of 2 m min^{-1} with a wet thickness of $4.9 \mu\text{m}$. After the initial drying of the precursor film it was converted into an insoluble film by passage through an oven at a temperature of $140 \text{ }^\circ\text{C}$ with a speed of 0.2 m min^{-1} (oven length = 4 m). This gave an insoluble doped zinc oxide film with a thickness of $25 \pm 5 \text{ nm}$. The P3HT:PC[60]BM ink described above was microfiltered and slot die-coated with at a web speed of 1.6 m min^{-1} and a wet thickness of $11.2 \mu\text{m}$. The film was dried by passage through an oven (2 m) at $140 \text{ }^\circ\text{C}$. The recombination layer comprised a $\text{V}_2\text{O}_5/\text{ZnO}$ stack that was slot-die coated in two steps. The V_2O_5 layer was slot-die coated directly on top of the dried P3HT:PC[60]BM layer, with a web speed of 2 m min^{-1} and a wet thickness of $8 \mu\text{m}$. The film was dried by passage through an oven (2 m) at $140 \text{ }^\circ\text{C}$. The second zinc oxide layer was prepared exactly as the first (anode) layer, directly on the V_2O_5 layer. The back cell was prepared by slot-die coating an aqueous TQ-1:PC[60]BM nanoparticle dispersion (Fig. 2) at a web speed of 0.2 m min^{-1} and a wet thickness of $30 \mu\text{m}$. The wet film was dried at $140 \text{ }^\circ\text{C}$ (oven length = 2 m) as described earlier [8]. The back electrode was prepared by applying PEDOT:PSS by slot-die coating at a speed of 0.2 m min^{-1} with drying at $140 \text{ }^\circ\text{C}$ (oven length = 2 m). It was found unnecessary to wet the film surface prior to coating the PEDOT:PSS and this might be due to the beneficial interaction between the fluorosurfactants in the aqueous nanoparticle dispersion and in the PEDOT:PSS. Finally, the device was completed by R2R screen printing a silver grid electrode and drying at $140 \text{ }^\circ\text{C}$. The devices were encapsulated using R2R lamination of a simple food packaging barrier with a pressure sensitive adhesive onto both sides of the foil [12b].

2.3. TOF-SIMS depth profiling analysis

Time-of-flight secondary ion mass spectrometry (TOF-SIMS) was employed to perform a depth profiling analysis. The experiments were conducted using a TOF-SIMS IV (ION-TOF GmbH, Münster, Germany). 25-ns pulses of 25-keV Bi^+ (primary ions) were bunched to form ion packets with a nominal temporal extent of $< 0.9 \text{ ns}$ at a repetition rate of 10 kHz yielding a target current of 1 pA. These primary ion conditions were used to obtain depth profiles in both negative and positive ion mode. Depth profiling was performed using an analysis area of $100 \times 100 \mu\text{m}^2$

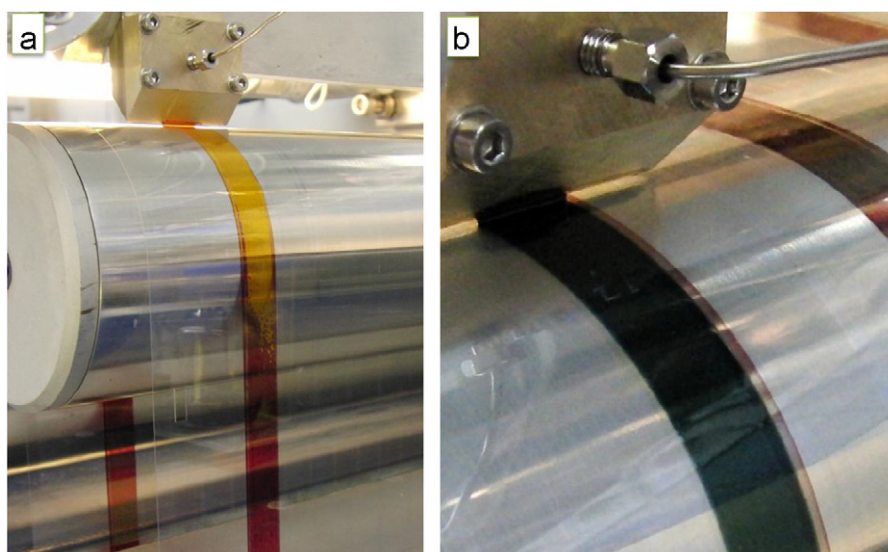


Fig. 2. Photographs of the actual R2R coating experiment in progress. (a) Coating of the front BHJ material (the drying process of the film is visible). (b) Coating of the back BHJ material.

and a sputter area of $300 \times 300 \mu\text{m}^2$. 30 nA of 3-keV Xe^+ were used as sputter ions. Electron bombardment (20 eV) was used to minimize charge build-up at the surface. Desorbed secondary ions were accelerated to 2 keV, mass analyzed in the flight tube, and post-accelerated to 10 keV before detection.

2.4. *J–V* characterization

The final devices were put under simulated sunlight at 1000 W m^{-2} , $85 \pm 5 \text{ }^\circ\text{C}$, $40 \pm 10\%$ relative humidity (rh) (AM1.5G). *J–V* curves were recorded by sweeping from -1 V to $+1 \text{ V}$ in steps of 20 mV and a rate of 0.1 V s^{-1} to ensure that no dynamic effects resulted in over/under estimation of J_{sc} and V_{oc} . The time evolution of the photovoltaic performance was recorded by continuously illuminating the device under the above conditions while recording complete IV data every one minute according to ISOS-L-1 [13].

3. Results and discussion

3.1. The tandem cell

This study describes the transfer of a laboratory scale tandem solar cell process on rigid glass substrates to a R2R process on flexible plastic substrates. The laboratory process was described previously [11] and was developed with an aim of being compatible with R2R processing. The tandem solar cell structure comprised a multilayer stack with the composition PET/ITO/ZnO/front-BHJ/ V_2O_5 /ZnO/back-BHJ/PEDOT:PSS/Ag, where PET is poly(ethylene terephthalate) (substrate), ITO is indium tin oxide (transparent front electrode), ZnO is the electron transport layer, front-BHJ is the front bulk heterojunction consisting of P3HT:PC[60]BM (active layer 1), V_2O_5 /ZnO is the recombination layer, back-BHJ consists of TQ-1:PC[60]BM (active layer 2), PEDOT:PSS is the hole transport layer, and Ag is the back electrode. Illustrative photographs of the coating process are shown in Fig. 2.

The first attempts resulted in very poorly performing devices typically showing open-circuit voltages around what is expected for single junction devices. Optical inspection of the completed devices revealed the possible origin of this malfunction to be cracks in the V_2O_5 part of the recombination layer (Fig. 3). It was found that these cracks form at some point during the processing of the V_2O_5 layer, possibly due to the heat treatment and/or bending of the substrate as it passes through the R2R equipment. As is also hinted in Fig. 3 these cracks persist after processing of the ZnO layer thus rendering the recombination layer penetrable to the solute of the back BHJ

as this is coated. This would most likely solubilize the front BHJ and thus seriously compromise the integrity of the serial connection of the two sub cells. This situation is schematically described in Fig. 4a. Such a short-circuiting of the recombination layer would make the two active layers effectively function as one poorly performing active layer, in turn, explaining the single junction-like low open-circuit voltage observed for these devices.

However, it was possible to work around this issue by utilizing an aqueous ink for the processing of the back BHJ using a method recently described by Andersen et al. [8]. This presented a unique opportunity for orthogonal processing since water cannot solubilize the front BHJ. From the photomicrographs shown in Fig. 4 it is evident that the back cell looks less affected by the cracks in the recombination layer when water based processing is employed (Fig. 4b compared to Fig. 4a).

3.2. TOF-SIMS depth profiling analysis

TOF-SIMS depth profiling analysis was employed in both negative and positive ion mode in order to document the layer stack order. The encapsulation film is too thick for a depth profiling analysis, so it was necessary to delaminate the tandem solar cell. TOF-SIMS mass spectra of the exposed surfaces revealed that delamination took place at the PEDOT:PSS/back BHJ interface.

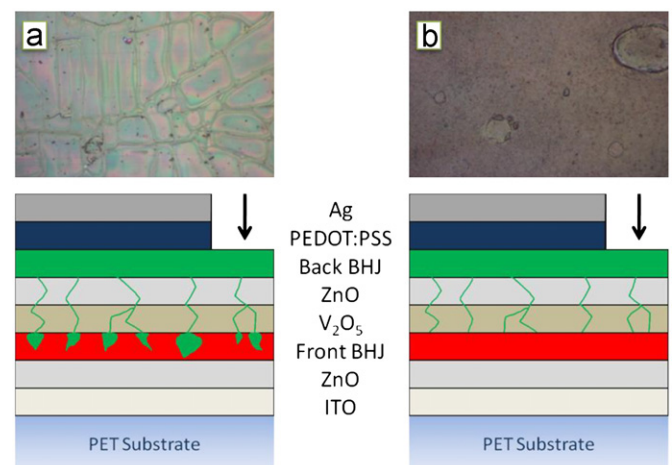


Fig. 4. Schematics of the tandem solar cell under study and photomicrographs ($230 \times 150 \mu\text{m}^2$) obtained at the indicated positions (black arrows), which illustrates the proposed consequence of the observed cracks in the recombination layer when using (a) a non-orthogonal solvent (chloroform) and (b) an orthogonal solvent (water), for the processing of the back BHJ.

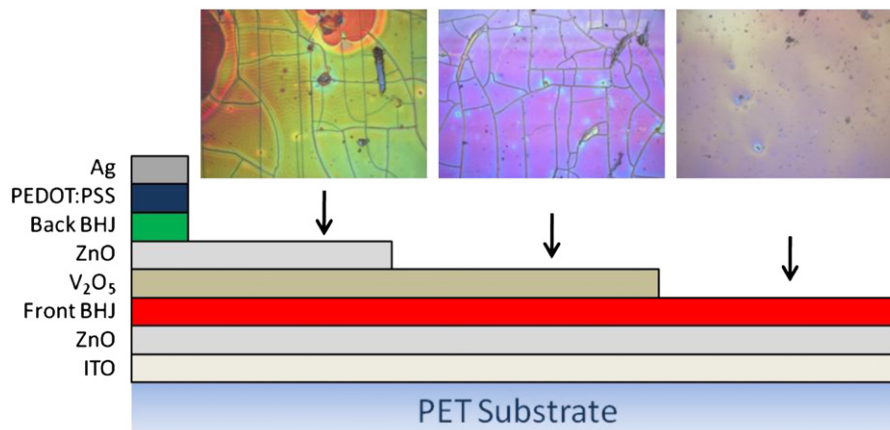


Fig. 3. Schematic of the tandem solar cell under study and photomicrographs ($260 \times 195 \mu\text{m}^2$) revealing cracks in the V_2O_5 layer, which persist through the ZnO layer.

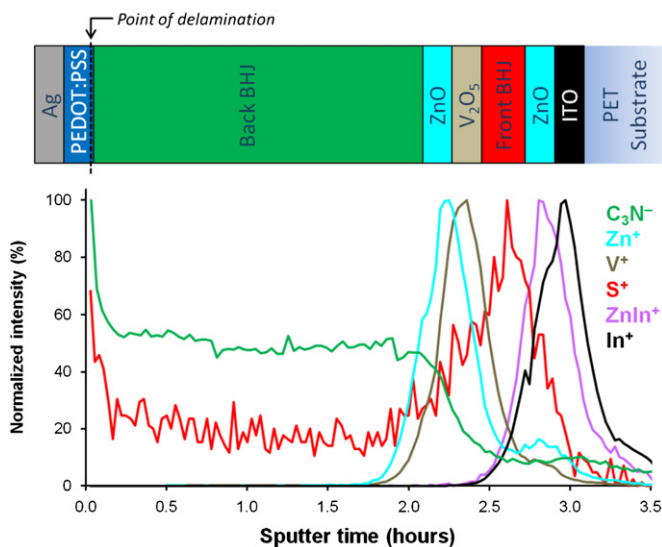


Fig. 5. TOF-SIMS depth profiles through the delaminated tandem solar cell. C_3N^- is a marker for the back BHJ obtained from a depth profile run in negative mode, Zn^+ is a marker for the ZnO , V^+ is a marker V_2O_5 , S^+ is a marker for both front and back BHJ, and $ZnIn^+$ (formed during the ionization step of the analysis) is a marker for the front ZnO and In^+ is a marker for ITO.

Fig. 5 shows the results of the depth profile analysis. Various factors complicated the analysis, such as interface roughness, which is well known phenomenon in R2R processing (e.g. compared to spin coating). Furthermore, depth profiling in soft materials is associated with an inferior depth resolution (under the given sputter conditions), compared to hard materials (e.g. metals). These conditions constitute a challenge especially when it comes to performing depth profiling on very thin layers such as the ZnO (~ 25 nm) and V_2O_5 (~ 15 nm) layers present in this device. However, as is evident from **Fig. 5** it was quite possible, in spite of the conditions, to document the multilayer stack composition in the tandem solar cell device. Residual PEDOT:PSS was present in the PEDOT:PSS/back BHJ interface after the delamination process presumably due to a small degree of interlayer mixing that resulted in presumably a matrix effect, which is observed as initially elevated signals from the back BHJ material (i.e. at the beginning of the sputter time window). During the ionization process the Zn^+ signal is discriminated due to the formation of the $ZnIn^+$ cluster ion caused by the close vicinity of the ITO (i.e. an ionization phenomenon). Finally, a significantly long sputter time window is observed for the back BHJ compared to the front BHJ, which suggests that the back BHJ is significantly thicker (assuming similar sputter rates) than the front BHJ consistent with an expected layer thickness of ~ 600 nm [8] for the back BHJ as compared to the thickness of the front BHJ ~ 200 nm.

3.3. Electrical characterization

J - V characteristics for the best performing tandem device are shown in **Fig. 6**, (blue triangles) together with representative J - V curves for both tandem and back cell reference devices with and without photo-annealing (800 min). The key photovoltaic parameters are summarized in **Table 1**, while the dynamic evolutions of the short circuit current (I_{sc}) and open-circuit voltage (V_{oc}) are shown in **Fig. 7**. By summing the V_{oc} values from the sub cell reference devices (**Table 1**) it is possible to estimate that the perfect tandem device would have an open-circuit voltage close to 1 V. As is clear from the presented data in **Table 1**, the actual tandem devices gave, at best, a V_{oc} around 0.9 V while V_{oc} values

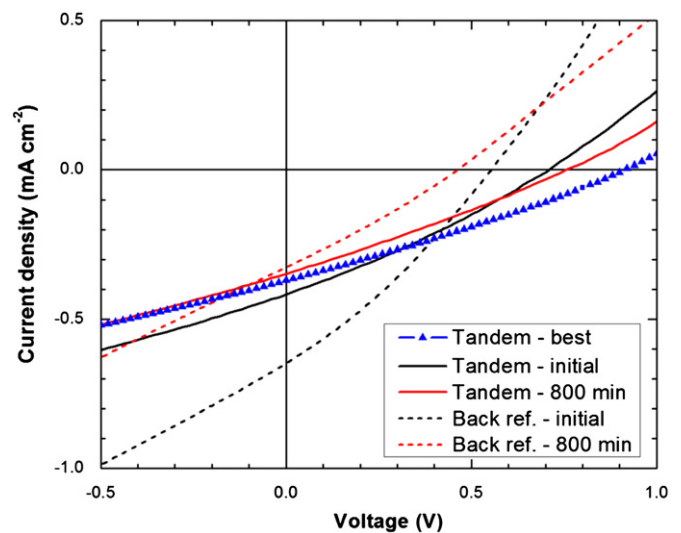


Fig. 6. J - V characteristics (AM1.5G 1000 W m^{-2}) for the best performing tandem cells. Also shown is a more average cell, before (initial) and after (800 min) photo-annealing.

Table 1

Summary of the J - V characterization.

Cell	PCE (%)	J_{sc} (mA cm^{-2})	V_{oc} (V)	FF (%)
Tandem ^(a)				
(Initial)	0.09	-0.42	0.71	28.8
(800 min)	0.07	-0.35	0.76	27.5
(Best)	0.10	-0.37	0.91	28.2
Back cell ^(a)				
(Initial)	0.11	-0.65	0.55	30.2
(800 min)	0.04	-0.33	0.46	27.7
Front cell (Ref. [11])	1.32	-7.17	0.50	36.9

^a Cell active area of 4 cm^2 .

around 0.75 V were readily measured, hence between 0.1 and 0.25 V less than the expected ideal value.

Various loss mechanisms can influence the tandem voltage, of which most are related to the nature of the sub cell interconnection, i.e. the recombination layer. In this case it is highly probable that the before mentioned observed defects (**Fig. 3**) are likely to have a negative influence on V_{oc} if the mechanism schematically shown in **Fig. 4b** is considered, i.e. shunts across the recombination layer would lower the tandem V_{oc} . Furthermore, the results show that the front and back reference cells both exhibit a decreasing V_{oc} during the dynamic evolution J - V experiment as observed in **Fig. 7** and S7 (see e-component). For the tandem devices the trend is opposite, i.e. increasing V_{oc} over time. Both reference cells display saturation at around 0.45 V, which fits well with the peak value of the best tandem cell.

It appears that the sub cell interconnection improves over time, possibly due to burning of shunts across the recombination layer, originally formed as a consequence of the defects. With respect to the I_{sc} it is noticeable that the tandem device and the back cell reference device have rather similar I_{sc} values. This should be compared to the front cell I_{sc} , which is a factor of 10 to 20 times larger. Thus the tandem device is severely current limited by the poor performing back cell.

This significant current mismatch is likely to influence the current-voltage characteristics of the tandem cell. Hadipour et al. [14] found that the excess current will cause the surplus of free holes to pile up at the middle electrode (recombination layer), which will result in a lowering of the effective internal field in the

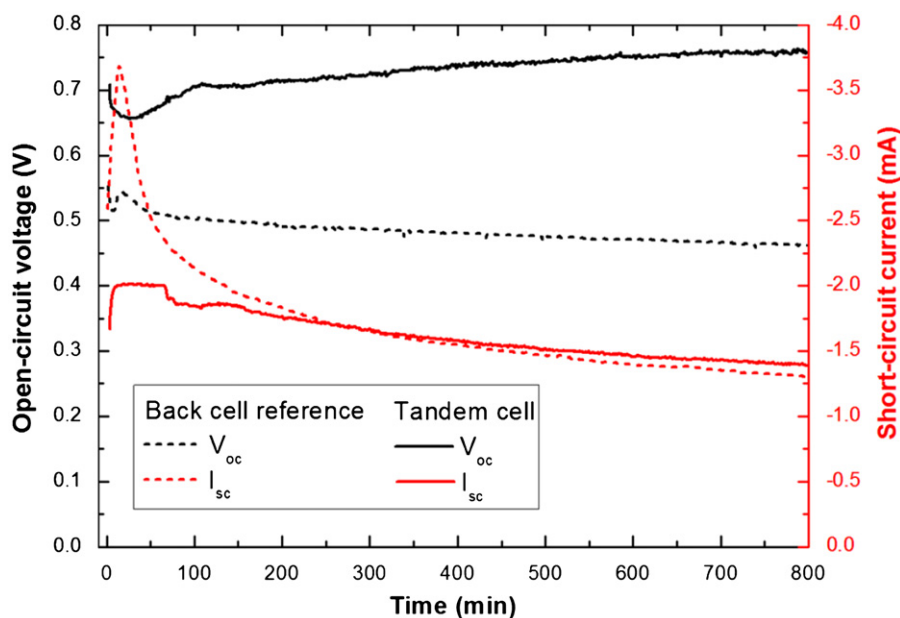


Fig. 7. Time evolution of the open-circuit voltage and short-circuit current during the 800 min of photo-annealing ($AM1.5G\ 1000\ W\ m^{-2}$) of the tandem cell, and a corresponding single junction reference cell mimicking the current-limiting back cell.

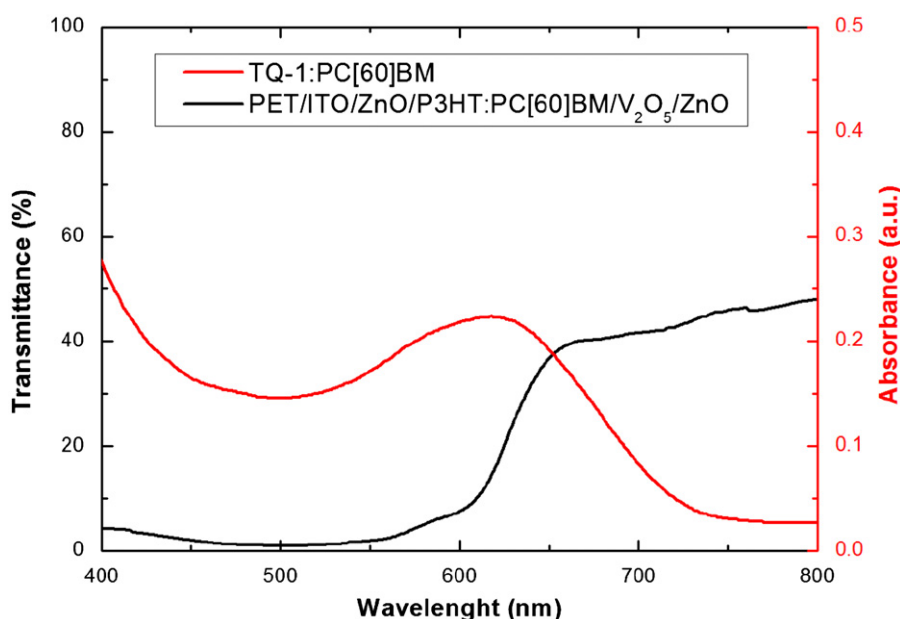


Fig. 8. Transmittance of the front cell and the recombination layer relative to the absorbance of the back cell active layer.

front sub cell, while for the back sub cell the opposite will be the case and the internal field will increase.

Hence the sub cell currents will equilibrate at some intermediate value, resulting in a higher I_{sc} value for the tandem device compared to the expected current of the limiting sub cell reference device. How the tandem current equilibrates is very much dependent on the slope of the $J-V$ curves of the sub cells around short-circuit as well as the degree of current mismatch, as recently pointed out by Braun et al. [15] for the case of an inorganic tandem cell. This can be easily understood, e.g. in the case of the current limiting sub cell; as the reverse biasing caused by the current mismatch will only result in a significant increase in current if the $J-V$ curve of the sub cell has a non zero slope in reverse bias, which is the case for the cells under study here. Furthermore, according to Fig. 8 the tandem back cell will suffer

from an obvious poor spectral matching with the front cell transmission spectrum, and thus receive a significantly lower photon flux than the reference cell. From this, a significant lowering of the back cell current would be expected. However, as the $J-V$ data shows that the I_{sc} of the tandem is not lower but rather comparable to that of the current limiting back cell reference device this would in fact imply a combination of the spectral mismatch and the increased quantum efficiency of the tandem back cell due to current mismatch (the effect described in Refs. [14 and 15]). To support this, we construct the ideal tandem curve from the two reference sub cells by summing voltages at equal currents, as described in Ref. [14]. We take into account the spectral mismatch by a mismatch factor S , which is simply multiplied with the current of the back cell reference. These can be seen in Fig. 9, for the case of $S=1$ and $S=0.5$, together with the

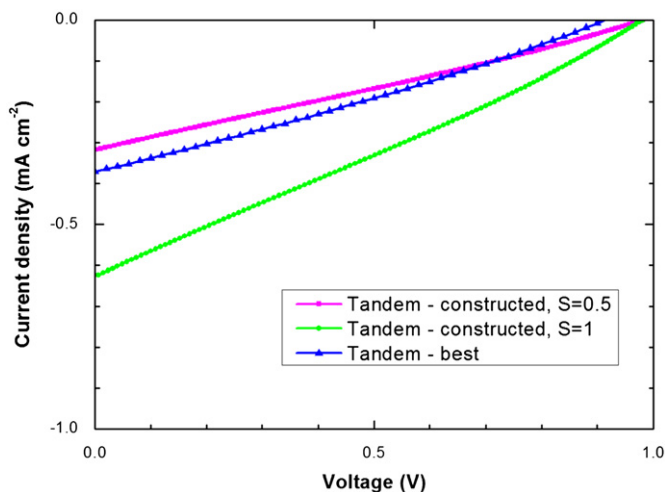


Fig. 9. Constructed tandem J - V characteristics with spectral mismatching ($S=0.5$) and without ($S=1$), compared with the best measured tandem device.

best tandem curve. As can be seen, it is likely that severe spectral mismatching is the cause of the low short-circuit current of the tandem cell, while the discrepancy between the model and the measurement can be explained by the somewhat crude model, such as negligence of V_{oc} dependence on light intensity [16], and the assumption of a perfect ohmic connection between the sub cells, e.g. a perfect recombination layer.

3.4. Future developments

The tandem approach within polymer photovoltaics has so far been utilized in an attempt to maximize efficiency, i.e. without constraints on materials and fabrication methods. The present work, however, demonstrates the fragility of the tandem device approach from a solution processing point of view, and in doing so, stresses the importance of having certain constraints in mind when assessing a given set of materials and processing methods. In this regard especially the recombination layer presents an all-determining weak-point of the tandem cell; a perfect recombination layer would be insoluble and solvent impenetrable, being either a pn-junction preferably a highly doped tunnel junction or alternatively having metal like characteristics. This has so far been achieved only for small area devices using rigid substrates [6,11,17–21]. Lee et al. [22] successfully demonstrated a small area tandem device on a flexible substrate but using vacuum deposition. However, as for upscaling of the fabrication, it is the view of the authors that a stable and highly reliable solution process for polymer tandem solar cells can only be ensured by a completely orthogonalized process in which none of the processing steps can seriously harm any of the previously processed layers. This has to do with the inherently rough nature of a high throughput R2R process, during which cracks and small coating imperfections would act as solvent paths leading to partial dissolution of underlying layers. The aqueous emulsion approach utilized in this work is one possible solution presenting both a stable and possibly environmentally friendly fabrication process. At the same time it allows for the use of the large amount of existing polymers. However, the success of this technique of course depends on whether significantly better device performance can be achieved. Another foreseeable solution would be a process where the layers by some in-line post process are rendered insoluble, for instance using thermal- or light-induced thermocleavage of the solubilizing groups as demonstrated earlier [5,23,24]. This would be very desirable as it ensures free choice of solvent for the subsequent layers, and also removes constraints

on the recombination layer in terms of materials and layer thicknesses, thus opening for a wider range of tweakable parameters.

4. Conclusions

We have successfully demonstrated large area flexible polymer tandem solar cells with all layers processed entirely from solution, and partially from water. The multilayer stack on flexible PET substrate comprised a cathode of ITO/ZnO, a recombination layer of V_2O_5 /ZnO, and a PEDOT:PSS/Ag (printed) anode. The two serially connected BHJs was comprised of a P3HT:PC[60]BM front cell processed from chlorobenzene and a back cell processed from an aqueous dispersion of poly[2,3-bis-(3-octyl oxyphenyl)-quinoxaline-5,8-diyl-alt-thiophene-2,5-diyl]:PC[60]BM nanoparticles. The composition and integrity of the multilayer stack was confirmed by TOF-SIMS depth profiling. The V_{oc} of the best tandem device was 0.9 V, while both the corresponding single junction reference devices had a V_{oc} around 0.5 V. This confirms a serial connection of the sub cells while the observed voltage losses are ascribed to visible defects in the recombination layer and a non-ohmic connection of the two sub cells.

Acknowledgment

This work was supported by the Danish National Research Foundation. We gratefully acknowledge Lasse Gorm Jensen for creating graphical illustrations and Jon E. Carlé and Martin Helgesen for preparing polymer materials.

Appendix A. Supplementary materials

Supplementary data associated with this article can be found in the online version at doi:10.1016/j.solmat.2011.08.025.

Details of GIWAXS measurements and time evolution for the back reference cell.

References

- [1] T. Ameri, G. Dennler, C. Lungenschmied, C.J. Brabec, Organic tandem solar cells: a review, *Energy & Environmental Science* 2 (2009) 347–363.
- [2] G. Dennler, M.C. Scharber, T. Ameri, P. Denk, K. Forberich, C. Waldauf, C.J. Brabec, Design rules for donors in bulk-heterojunction tandem solar cells. Towards 15% energy-conversion efficiency, *Advanced Materials* 20 (2008) 579–583.
- [3] J.D. Kotlarski, P.W.M. Blom, Ultimate performance of polymer: fullerene bulk heterojunction tandem solar cells, *Applied Physics Letters* 98 (2011) 053301.
- [4] Y.M. Nam, J. Huh, W.H. Jo, A computational study on optimal design for organic tandem solar cells, *Solar Energy Materials and Solar Cells* 95 (2011) 1095–1101.
- [5] O. Hagemann, M. Bjerring, N.C. Nielsen, F.C. Krebs, All solution processed tandem polymer solar cells based on thermocleavable materials, *Solar Energy Materials and Solar Cells* 92 (2008) 1327–1335.
- [6] J. Gilot, M.M. Wienk, R.A.J. Janssen, Double and triple junction polymer solar cells processed from solution, *Applied Physics Letters* 90 (2007) 143512.
- [7] E. Wang, L. Hou, Z. Wang, S. Hellström, F. Zhang, O. Inganäs, M.R. Andersson, An easily synthesized blue polymer for high-performance polymer solar cells, *Advanced Materials* 22 (2010) 5240–5244.
- [8] T.R. Andersen, T.T. Larsen-Olsen, B. Andreasen, A.P.L. Böttiger, J.E. Carlé, M. Helgesen, E. Bundgaard, K. Norrman, J.W. Andreasen, M. Jørgensen, F.C. Krebs, Aqueous processing of low-band-gap polymer solar cells using roll-to-roll methods, *ACS Nano* 5 (2011) 4188–4196.
- [9] R. Søndergaard, M. Helgesen, M. Jørgensen, F.C. Krebs, Fabrication of polymer solar cells using aqueous processing for all layers including the metal back electrode, *Advanced Energy Materials* 1 (2011) 68–71.
- [10] N. Espinosa, H.F. Dam, D.M. Tanenbaum, J.W. Andreasen, M. Jørgensen, F.C. Krebs, Roll-to-roll processing of inverted polymer solar cells using hydrated vanadium(V)oxide as a PEDOT:PSS replacement, *Materials* 4 (2011) 169–182.

- [11] T.T. Larsen-Olsen, E. Bundgaard, K.O. Sylvester-Hvid, F.C. Krebs, A solution process for inverted tandem solar cells, *Organic Electronics* 12 (2011) 364–371.
- [12] a) F.C. Krebs, T. Tromholt, M. Jørgensen, Upscaling of polymer solar cell fabrication using full roll-to-roll processing, *Nanoscale* 2 (2010) 873–886; b) J. Alstrup, M. Jørgensen, A.J. Medford, F.C. Krebs, Ultra fast and parsimonious materials screening for polymer solar cells using differentially pumped slot-die coating, *ACS Applied Materials & Interfaces* 2 (2010) 2819–2827.
- [13] M.O. Reese, S.A. Gevorgyan, M. Jørgensen, E. Bundgaard, S.R. Kurtz, D.S. Ginley, D.C. Olson, M.T. Lloyd, P. Morvillo, E.A. Katz, A. Elschner, O. Haillant, T.R. Currier, V. Shrotriya, M. Hermenau, M. Riede, K.R. Kirov, G. Trimmel, T. Rath, O. Inganäs, F. Zhang, M. Andersson, K. Tvingstedt, M. Lira-Cantu, D. Laird, C. McGuinness, S. Gowrisanker, M. Pannone, M. Xiao, J. Hauch, R. Steim, D.M. DeLongchamp, R. Rösch, H. Hoppe, N. Espinosa, A. Urbina, G. Yaman-Uzunoglu, J.-B. Bonekamp, A.J.J.M. van Breemen, C. Girotto, E. Voroshazi, F.C. Krebs, Consensus stability testing protocols for organic photovoltaic materials and devices, *Solar Energy Materials and Solar Cells* 95 (2011) 1253–1267.
- [14] A. Hadipour, B. de Boer, P.W.M. Blom, Device operation of organic tandem solar cells, *Organic Electronics* 9 (2008) 617–624.
- [15] A. Braun, N. Szabo, K. Schwarzburg, T. Hannappel, E. Katz, J.M. Gordon, Current-limiting behavior in multijunction solar cells, *Applied Physics Letters* 98 (2011) 223506.
- [16] T. Tromholt, E. Katz, B. Hirsch, A. Vossier, F.C. Krebs, Effects of concentrated sunlight on organic photovoltaics, *Applied Physics Letters* 96 (2010) 073501.
- [17] A. Hadipour, B. de Boer, J. Wildeman, F.B. Kooistra, J.C. Hummelen, M.G.R. Turbiez, M.M. Wienk, R.A.J. Janssen, P.W.M. Blom, Solution-processed organic tandem solar cells, *Advanced Functional Materials* 16 (2006) 1897–1903.
- [18] J.Y. Kim, K. Lee, N.E. Coates, D. Moses, T.-Q. Nguyen, M. Dante, A.J. Heeger, Efficient tandem polymer solar cells fabricated by all-solution processing, *Science* 317 (2007) 222–225.
- [19] S. Sista, M.-H. Park, Z. Hong, Y. Wu, J. Hou, W.L. Kwan, G. Li, Y. Yang, Highly efficient tandem polymer photovoltaic cells, *Advanced materials* 22 (2010) 380–383.
- [20] D.J.D. Moet, P. de Bruyn, P.W.M. Blom, High work function transparent middle electrode for organic tandem solar cells, *Applied Physics Letters* 96 (2010) 153504.
- [21] C.-H. Chou, W.L. Kwan, Z. Hong, L.-M. Chen, Y. Yang, A. Metal-Oxide, Interconnection layer for polymer tandem solar cells with an inverted architecture, *Advanced Materials* 23 (2011) 1282–1286.
- [22] B.J. Lee, H.J. Kim, W. -ik Jeong, J.-J. Kim, A transparent conducting oxide as an efficient middle electrode for flexible organic tandem solar cells, *Solar Energy Materials and Solar Cells* 94 (2010) 542–546.
- [23] T. Tromholt, S.A. Gevorgyan, M. Jørgensen, F.C. Krebs, K.O. Sylvester-Hvid, Thermocleavable materials for polymer solar cells with high open circuit voltages – a comparative study, *ACS applied materials & interfaces* 1 (2009) 2768–2777.
- [24] F.C. Krebs, K. Norrman, Using light induced thermocleavage in a roll-to-roll process for polymer solar cells, *ACS applied materials & interfaces* 2 (2010) 877–887.